**Czech Technical University in Prague**

**Faculty of Nuclear Sciences and Physical Engineering**

DISSERTATION

**Novel Schemes in Ion Acceleration**

**Driven by High-Intensity Lasers**

Prague 2023                                    Martin Matys

# Bibliografický záznam

|  |  |
|---:|:---|
| Autor: | Ing. Martin Matys<br>České vysoké učení technické v Praze, Fakulta jaderná a fyzikálně inženýrská, Katedra fyzikální elektroniky |
| Název práce: | Nová schémata pro urychlování iontů pomocí vysoce intenzivních laserových impulzů |
| Studijní program: | Aplikace přírodních věd |
| Studijní obor: | Fyzikální inženýrství |
| Školitel: | doc. Ing. Jan Pšikal, Ph.D.<br>České vysoké učení technické v Praze, Fakulta jaderná a fyzikálně inženýrská, Katedra fyzikální elektroniky |
| Školitel specialista: | Prof. Sergei Vladimirovich Bulanov<br>The Extreme Light Infrastructure ERIC, ELI Beamlines facility |
| Akademický rok: | 2022/2023 |
| Počet stran: | 158 |
| Klíčová slova: | interakce laseru s plazmatem, urychlování iontů, plazmová závěrku, částicové simulace |

# Bibliographic entry

| | |
|---:|:---|
| Author: | Ing. Martin Matys |
| | Czech Technical University in Prague, Faculty of Nuclear Sciences and Physical Engineering, Department of Physical Electronics |
| Title of dissertation: | Novel Schemes in Ion Acceleration Driven by High-Intensity Lasers |
| Degree programme: | Applications of Natural Sciences |
| Field of study: | Physical Engineering |
| Supervisor: | doc. Ing. Jan Pšikal, Ph.D. |
| | Czech Technical University in Prague, Faculty of Nuclear Sciences and Physical Engineering, Department of Physical Electronics |
| Supervisor specialist: | Prof. Sergei Vladimirovich Bulanov |
| | The Extreme Light Infrastructure ERIC, ELI Beamlines facility |
| Academic year: | 2022/2023 |
| Number of pages: | 158 |
| Keywords: | laser-plasma interaction, ion acceleration, plasma shutter, particle-in-cell simulation |

**Prohlášení/Declaration**

Prohlašuji, že jsem předloženou práci vypracoval samostatně a že jsem uvedl veškerou použitou literaturu.

I hereby declare that I carried out this work independently, and only with the cited sources, literature and other professional sources.

V Praze dne/In Prague on 3. 3. 2023

........................................
Ing. Martin Matys

# Abstrakt

Urychlování iontů pomocí laserových impulzů se těší zvláštní pozornosti pro svoje významné aplikace, jako je hadronová terapie v onkologii, jaderná fúze a použití v materiálové a jaderné fyzice. Cílem této práce je teoretická studie nových schémat urychlování iontů pomocí vysokointenzivních laserových impulsů, s použitím particle-in-cell (PIC) simulací. Aplikace těchto schémat zlepšuje vlastnosti generovaného iontového svazku, jako je snížení jeho divergence a/nebo dosažení vyšší maximální energie urychlených iontů. V experimentech na urychlování iontů pomocí laseru v současnosti dominuje použití relativně tlustých terčů využívajících mechanismus nazývaný Target Normal Sheath Acceleration (TNSA), zejména k urychlování uhlovodíkových nečistot na zadní straně terče. Urychlování iontů lze v principu vylepšit pomocí tří druhů úprav: (1) Použitím jiných urychlovacích mechanismů, jako je např. urychlování pomocí radiačního tlaku záření (Radiation Pressure Acceleration - RPA), které se projeví při zvýšení intenzity laserových impulzů (a/nebo snížením hustoty a tloušťky terče); (2) Použitím speciální geometrie a složení terče; (3) Tvarováním profilu laserového impulsu.

V této práci je pomocí PIC simulací demonstrována: dominance RPA mechanismu pro urychlování protonovů při interakci kryogenního vodíkového terče s vysoce intenzivními multi-PW laserovými impulzy, relevantními pro laserové systémy jako je např. ELI Beamlines; generace kvazi-monoenergetického iontového svazku s nízkou divergencí pomocí vysokointenzivního laserového impulsu se strmě stoupající náběžnou hranou a dvouvrstvého terče se zvlněným rozhraním mezi dvěma vrstvami; lokální zvýšení intenzity a generace impulzu se strmě stoupající náběžnou hranou při použití velmi tenké pevnolátkové fólie (tzv. plazmatické závěrky - plasma shutter) a její aplikaci pro urychlení iontů z velmi tenkého stříbrného terče, což má za následek zvýšení maximální energie iontů a snížení divergence generovaného iontového svazku. S dalšími vědeckými skupinami jsme také spolupracovali na vizualizaci našich výsledků ve virtuální realitě, na kombinaci hydrodynamických a PIC simulací a na návrhu konstrukce dvojité plazmové závěrky pro efektivní urychlování iontů.

# Abstract

Laser-driven ion acceleration is very attractive for its highly important applications, like hadron therapy in oncology, controlled nuclear fusion, and use in material and nuclear physics. The aim of this work is theoretical study of novel schemes of laser-driven ion acceleration, available via the use of high-intensity laser pulses, with the help of particle-in-cell (PIC) simulations. The application of these schemes advances ion acceleration in the sense of improving the generated ion beam properties like lowering its divergence and/or achieving higher maximal ion energy. The laser-driven ion acceleration experiments are currently dominated by the use of relatively thick targets employing Target Normal Sheath Acceleration (TNSA) mechanism to preferably accelerate hydrocarbon contaminants at the target rear side. The ion acceleration can be improved by three essential modifications: (1) Employing different acceleration mechanisms, like the Radiation Pressure Acceleration (RPA), with increasing laser pulse intensities (and/or lowering the target density and thickness); (2) Using special target geometry and composition; (3) Shaping the laser pulse profile.

In this work we demonstrated with the help of PIC: the dominance of RPA mechanism for proton acceleration from cryogenic hydrogen target interaction with high-intensity multi-PW laser pulses relevant to laser systems like ELI Beamlines; generation of quasi-monoenergetic ion beam with low divergence using a high-intensity laser pulse with a steep-rising front and a double-layer target with initial corrugation on the interface between two layers; local intensity increase and steep-front generation of a high-intensity laser pulse burning through an ultra-thin solid foil (so-called plasma shutter) and its application for ion acceleration using ultra-thin silver target, resulting in increase of maximal ion intensity and reduction of generated beam divergence. We also collaborated with other groups on Virtual Reality visualization of our results, combination of hydrodynamic simulations with PIC ones and design of a double shutter scenario for efficient ion acceleration.

# Contents

# Chapter 1

# Introduction

## 1.1 Historical development and state of the art

Laser-driven ion acceleration is one of the most promising and widely studied features of ultra-intense laser-matter interaction [1–4], receiving particular attention for its highly important applications, like hadron therapy in oncology [1; 5; 6], controlled nuclear fusion [7–9], use in material science as a radioisotope source and a stage to explore exotic nuclei [10; 11], in nuclear science involving heavy ion collisions, e.g., for hot and dense matter research [12] and schemes like fission-fusion nuclear reaction [13; 14], production of PET (positron emission tomography) medical isotopes [15], proton imaging [16], proton-induced X-ray emission spectroscopies (PIXE) [17; 18] (e.g., for cultural heritage diagnostics), and generation of ultrashort neutron pulses [19; 20].

The collective acceleration of charged particles using electric fields excited in plasma media was proposed in 1950s by V. I. Veksler, Ya. B. Fainberg and G. I. Budker [21; 22]. The invention of the laser in 1960 [23] marked a new stage in this effort. The follow-up invention of techniques like Q-switching [24], mode-locking [25], cavity dumping [26] and chirped pulse amplification [27] enabled generation of short, high-power and high-intensity laser pulses. Subsequently, the ion acceleration in the plasma media driven by such laser pulses was excessively studied in nineties [2]. The laser-plasma interaction of these times was mainly connected with electron heating at the front side of the target. These electrons then propagate through the target and cause ion acceleration at the rear side of the target. This behavior is described by the so-called Target Normal Sheath Acceleration (TNSA) mechanism [28]. This effort culminated in 2000, when energy of 58 MeV was reached for protons using a PW laser [29]. Since then only a relatively slow improvement of maximal reached energy was announced, e.g., 67.5 MeV in 2011 [30] using flat-top hollow micro-cones and 85 MeV in 2016 [31] reducing the target thickness to micrometer level. The most straightforward way to increase the maximal ion energy is to increase the laser pulse power and intensity. However, this increase is in principle limited by the square-root (ponderomotive) scaling of the TNSA mechanism [3]. Therefore, an employment of novel acceleration schemes in combination with the use of different acceleration mechanisms is needed to reach higher ion energies in a faster pace.

One of the promising mechanisms is Radiation Pressure Acceleration (RPA) [32; 33], which may get involved especially in combination with the use of ultrathin or low-density targets. Its experimental indications have already been observed [34–37]. Usually several ion acceleration mechanisms take place during the laser-target interaction. The interplay

between them depends on the target and laser parameters [38]. For example, the increase of laser intensity for relatively low-density solid targets, like cryogenic hydrogen [39], can result in the shift of the origin of the ions accelerated to the highest energies from the target rear side towards its interior, as demonstrated by our group in Ref. [40]. It was also demonstrated in experiment, that energies per nucleon of the bulk carbon ions can reach significantly higher values than the energies of contaminant protons [41]. The radiation pressure also plays a role in directing the electron flow in Directed Coulomb Explosion (DCE) [42] and in creation of low-density regions required for the onset of Relativistic Induced Transparency (RIT) [43] in solid targets. This results in occurrence of several hybrid and intermediate mechanisms like a hybrid RPA-TNSA regime [44; 45] and Break-out Afterburner [46; 47]. The hybrid RPA-TNSA mechanism (influenced by the onset of RIT) set a new record in proton acceleration, reaching energy over 94 MeV in experiment conducted in 2018 [45]. With the advent of multi-petawatt laser systems like ELI Beamlines (Czech Republic) [48–50], ELI NP [51; 52], APOLLON (France) [53] or SEL (China) [54] the laser pulses will reach intensities over $10^{23}$ W/cm$^2$, entering the acceleration regimes dominated by the radiation pressure, promising new records in proton/ion acceleration.

The demonstration of RPA regime for acceleration of heavy ions is also expected in future. Currently the highest energies are being achieved by using ultra-thin targets, e.g., the recent record for gold ion acceleration (exceeding 7 MeV/nucleon) was achieved with lowering the target thickness down to 25 nm [14]. For silver ions, energy exceeding 20 MeV/nucleon was achieved lowering the target thickness down to 50 nm [55].

## 1.2 Aims and motivation

The aim of this dissertation is to investigate the novel schemes of ion acceleration, available via the use of high-intensity laser pulses, with the help of particle-in-cell (PIC) simulations. The application of these schemes should advance ion acceleration in the sense of improving the generated ion beam properties like lowering its divergence or/and achieving higher maximal ion energy. The ion acceleration can be improved by three essential modifications marking the main topics of this dissertation: (1) Employing different acceleration mechanisms, like the Radiation Pressure Acceleration (RPA), by increasing laser pulse intensities (and/or lowering the target density and thickness); (2) Using special target geometry and composition, like double-layer target with interface corrugation; (3) Shaping the laser pulse profile, e.g., by employing a plasma shutter (an ultra-thin foil placed in front of the target).

The first topic is focused on proton acceleration via interaction of high-power and high-intensity laser pulse (relevant to L4 laser at ELI Beamlines [50]) with low-density cryogenic (solid) hydrogen targets. These targets provide interesting medium for ion acceleration as they can be made relatively thin, with low density, lacking contaminants, debris-free and can be used in high-repetition laser-target experiments [39; 56–58]. The combination of high laser intensity (over $10^{22}$ W/cm$^2$ ) with very low (but still overdense) target density provides perfect conditions for demonstration of efficiency of different acceleration mechanisms(apart from the classical TNSA) like the RPA and the influence of the RIT on ion acceleration.

In addition to increasing the laser pulse intensity and changing the target thickness, the use of structured targets can also improve the maximum energy and quality of laser-accelerated ions. Various target were proposed for ion acceleration, e.g., double-layer [59–64], with nano-structures at its surface [65], nano-holes [66; 67] or a specific geometry, like a transverse Gaussian shape [68], a dual parabola [69], with a few micron-size holes [70] and a pizza-cone target [30].

Moreover, the target shape can influence the development of hydrodynamic-like instabilities arising from the laser-target interaction (e.g. Rayleigh-Taylor-like instability [71; 72]). This can result into fracturing the target into high-density ion bunches, which exhibit quasi-monoenergetic behavior [73; 74]. The instability development can be (partially) controlled by the imprinted corrugation on the target surface as demonstrated in [75].

In the second topic we continued in this idea using double-layer targets with corrugation on the interface between two layers. We assumed a steep-front laser pulse, aiming to produce rather impulsive instability with Richtmyer-Meshkov-like features [76; 77], which could be more reliable for bunch generation, as its growth rate is rather linear compared to Rayleigh-Taylor-like instability with exponential rate [78]. Together with the use of a high-power laser pulse one can expect generation of high-energy ion beams with low divergence.

After modifying the target shape and composition, and increasing the laser intensity, the next logical step for study of the novel schemes of ion acceleration is the shaping of the laser pulse profile. The generation of a steep-front laser pulse is a desirable feature affecting laser-plasma dynamics [79]. This feature can be achieved by the nonlinear evolution of the laser pulse as it propagates (or burns) through an underdense plasma [80–82], a near critical density plasma [83; 84] or an overdense plasma [43; 85]. The overdense approach is especially interesting as such foils can be also used for improvement of the laser pulse contrast, as demonstrated in experiments [86; 87]. This kind of ultra-thin solid foil is often referred to as the plasma shutter [85–87]. It represents an interesting addition to techniques like double planar plasma mirrors [88], already implemented in the laser systems. An additional advantage of the use of the ultra-thin foil is the generation of a relativistic plasma aperture and diffraction of the laser pulse affecting the electron [89] and ion dynamics [90].

In the last topic we investigated the possibility of locally increase of the laser pulse intensity using the relativistic plasma aperture generated by the interaction of high-intensity laser pulse with the ultra-thin plasma shutter and the generation of the steep-front pulse. Subsequently, we study the effect of the pulse shaping on ion acceleration from the additional target located behind the plasma shutter, aiming to improve both the maximal ion energy and the divergence of the produced ion beam.

## 1.3 Author's role and contributions

The author's personal role, contributions, training and skill development are described in this section. Therefore, the pronouns *I* and *my* are used in this section instead of the words *author* and *author's* for the sake of simplicity.

My doctoral training was supervised by doc. Ing. Jan Pšikal, Ph.D. and Prof. Sergei V. Bulanov. It took place at the Department of Physical Electronics, Faculty of Nuclear Sciences and Physical Engineering, Czech Technical University in Prague and at The Extreme Light Infrastructure ERIC, ELI Beamlines Facility. I was an active member of two scientific teams: the computational physics group of Prof. Jiří Limpouch at CTU in Prague and HIFI team of Prof. Sergei V. Bulanov at ELI Beamlines. The topic of this dissertation reflects my involvement in three scientific projects:

- Ultra-intense laser interaction with specially-designed targets as a source of energetic particles and radiation - GA15-02964S - from Czech Science Foundation
  Principal Investigator: doc. Ing. Jan Pšikal, Ph.D. from Czech Technical University in Prague

- The High Field Initiative - CZ.02.1.01/0.0/0.0/15_003/0000449 - from European

Regional Development Fund
Principal Investigator: Prof. Sergei V. Bulanov from ELI Beamlines

- Plasma optics for ultra-intense laser physics experiments - GA18-09560S - from Czech Science Foundation
Principal Investigator: doc. Ing. Ondřej Klimo, Ph.D. from Czech Technical University in Prague

I actively collaborated on the research included in this dissertation with all three Principal Investigators, the members of the scientific teams at ELI Beamlines and CTU in Prague, and with professors Katsunobu Nishihara and Kunioki Mima from Institute of Laser Engineering, Osaka University, Japan. I also participated in courses, summer schools and study stays at other institutions including: the stay at Queen's University Belfast in March 2018 (ERASMUS+ training: O2/LTT-C2: High Power Laser Matter Interactions / High Energy Density Physics - Theory and Experiments); the 8th Summer School on Atoms and Plasmas in Super-Intense Laser Fields, in Erice Italy 2017 and short visit of Kansai Photon Science Institute, Kizugawa, Japan with invited presentation in September 2019 [91].

Due to the outbreak of covid-19 pandemic, I participated in other international activities in the online form, including: ELI Summer School 2020, in Szeged Hungary 2020; LaPlaSS2021 - Experimental methods in High Intensity Laser-Plasma processes, Laser-Plasma Summer School organized by the CLPU Laser-Plasma Chair of the University of Salamanca, in Salamanca Spain 2021; 28th Laser Summer School, in Osaka Japan 2021. In addition, I attended several certificated courses in the Czech Republic, including: Introduction to MPI, at IT4Innovations in Ostrava 2021; Introduction to Machine and Deep Learning, at IT4Innovations in Ostrava 2022; Several courses in Czech language provided by FZU - Institute of Physics of the Czech Academy of Sciences focused on presentation and communication skills, and popularization of science.

My PhD training was focused on preparation, running and processing computationally demanding particle-in-cell simulations of high-intensity laser irradiation of various solid targets relevant to laser centers like ELI Beamlines, and subsequent analysis, theoretical explanation and visualization of the huge amount of produced data, often amounting to several (tens of) Terabytes for a single 3D simulation. I learned how to work independently and in a team, participate in multidisciplinary projects, e.g., combining PIC simulations with hydrodynamic ones, discussing the shutter design with team members and contacting possible manufacturer for further discussions, and collaborating on Virtual Reality visualizations of our results. I gained experiences in preparation and submission of the manuscripts of scientific papers, serving as a corresponding author and preparation of a basic grant applications. That includes open access grant competitions for computer time at IT4Innovations National Supercomputing Center and student chapter activity grant applications of SPIE society. I have been a principal investigator of 10 computational projects at IT4Innovations receiving together several millions of core-hours for our team.

Several educational activities were part of my PhD training, including giving tutorials for the undergraduate course *Numerical methods* at the Czech Technical University in Prague and being a supervisor of 2-day scientific mini-projects for high school students at event *Week of science at FNSPE* organized by our faculty in years 2017-2019 and 2022 with mini-projects: *Simulations of ion acceleration by ELI laser and their visualization in Virtual Reality* and *Monte Carlo simulation of virus spreading.* I served as a chapter officer in the student club *SPIE CTU in Prague Student Chapter* for 6 terms (2x as a chapter president), actively co-organizing the chapter seminars, dealing with outside communication, funding grants applications and reports to SPIE supervisors. I was also involved in popularization of science

to general public at ELI Beamlines, mostly using the virtual reality stations, containing, among others, visualizations of my simulations. The activities ranged from small-group school excursion to large events like International Day of Light and Researcher's night.

The research done during my PhD training resulted in 5 papers in peer-reviewed journals, 9 conference proceedings and invited chapters in two books, see the full list in Appendix A. The core of this doctoral thesis is based on the following five selected publications:

I. M. Matys, J. Psikal, K. Nishihara, O. Klimo, M. Jirka, P. Valenta and S. V. Bulanov (2023). High-quality laser-accelerated ion beams from structured targets. *Photonics* **10**, 61.

II. J. Psikal and M. Matys (2018). Dominance of hole-boring radiation pressure acceleration regime with thin ribbon of ionized solid hydrogen. *Plasma Physics and Controlled Fusion* **60**, 044003.

III. M. Matys, K. Nishihara, M. Kecova, J. Psikal, G. Korn, S. V. Bulanov (2020). Laser-driven generation of collimated quasi-monoenergetic proton beam using double-layer target with modulated interface. *High Energy Density Physics* **36**, 100844.

IV. M. Jirka, O. Klimo and M. Matys (2021) Relativistic plasma aperture for laser intensity enhancement. *Physical Review Research* **3**, 033175.

V. M. Matys, S. V. Bulanov, M. Kucharik, M. Jirka, J. Nikl, M. Kecova, J. Proska, J. Psikal, G. Korn and O. Klimo (2022). Design of plasma shutters for improved heavy ion acceleration by ultra-intense laser pulses. *New Journal of Physics* **24**, 113046.

These selected papers will be referred in text by the Roman numerals for easy distinguishing. The research was presented on several scientific conferences and workshops, e.g., the oral presentations at the 63rd Annual Meeting of the APS Division of Plasma Physics in 2021, SPIE Optics&Optoelectronics 2021, and a key-note presentation at 3rd Users' Conference of IT4Innovations in 2019, the full list is presented in Appendix A.2. The paper I. was selected by the editors as the cover of the January 2023 issue of Photonics [92].

During my doctoral training I also participated on other projects, collaborations and employments not included in this dissertation. Namely, subcontract of AFOSR project *Directed High Energy Radiation and Particle Beams Generated Using Extreme Magnetic Fields* (sub award agreement 12248263) supervised by Dr. Georg Korn at the side of ELI Beamlines. We also collaborated with groups from TAE Technologies, Inc., Ecole Polytechnique, University of Szeged and ELI-ALPS on simulation studies of proton and deuteron acceleration using mJ-Class few-cycle high-repetition lasers for neutron generation (collaboration acknowledged, e.g., in [93; 94] ). We worked on the topic of light ion acceleration for hadron therapy using multi-layer targets with shutter, which was presented (together with our previous shutter results) at the conference Flash Radiotherapy & Particle Therapy Conference (FRPT 2022) in Barcelona. I further broadened my computer knowledge at the beginning of my doctoral training, when I was partially employed as a network administrator at the faculty.

# Chapter 2

# Theoretical background

*In this chapter, Gaussian c.g.s. units are used. Furthermore, the temperature $T$ of the particle type $\alpha$ is expressed in the electronvolt unit $T_\alpha[eV]$, instead of Kelvin $T'_\alpha[K]$, i.e. $T_\alpha = k_B T'_\alpha$, where $k_B$ is the Boltzmann constant.*

## 2.1 High-intensity laser interaction with overdense plasma

### 2.1.1 Basic theoretical background

The high-intensity laser interaction with overdense plasma presents specific conditions of initially quasi-neutral medium of free charged particles with collective behavior combined with strong external and internal (generated) electromagnetic fields, provided by the laser itself and by the plasma interaction with it. The charge of a single particle is efficiently shielded in plasma on distances longer than the so-called Debye length by the cloud of charged particles surrounding it. For electrons with charge $q = -e$, density $n_e$ and temperature $T_e$ the Debye length can be expressed as

$$\lambda_{D_e} = \sqrt{\frac{T_e}{4\pi n_e e^2}} \tag{1}$$

The electric potential $\varphi$ of the point charge $q$ in plasma then decreases by the factor of $\mathrm{e_N}^{-1}$ (Euler number) at the distance of $r = \lambda_{D_e}$:

$$\varphi = \frac{q}{r} exp\left(\frac{-r}{\lambda_{D_e}}\right). \tag{2}$$

The quasi-neutrality of the initial target can be expressed via the relation between the electron $n_e$ and ion $n_i$ density via the average charge state of ions $Z$ as $n_e = Z n_i$. The distortion of the quasi-neutrality leads to electron oscillation over ions, its frequency is called the plasma electron frequency and is expressed as:

$$\omega_{pe} = \sqrt{\frac{4\pi e^2 n_e}{m_e}}, \tag{3}$$

where $m_e$ and $e$ denotes the electron mass and charge.

The electron density in laser-target interaction is often used in multiplies of the critical

density $n_c$ relevant to the laser angular frequency $\omega$

$$n_c = \frac{m_e \omega^2}{4\pi e^2}. \tag{4}$$

In the non-relativistic case, the laser pulse with the given $\omega$ reflects from the plasma with density higher than the critical one (so-called overdense plasma), which is implied from the corresponding dispersion relation of an electromagnetic wave propagating in plasma is [95]:

$$\omega^2 = \omega_{pe}^2 + (kc)^2, \tag{5}$$

where $c$ is the speed of light in vacuum and $k$ is the wave number. Under this conditions the laser pulse can efficiently propagate to overdense plasma only via the skin effect into the skin layer defined as:

$$l_s = \frac{c}{\omega_{pe}}. \tag{6}$$

Another fundamental characteristic of the laser pulse is its intensity, defined as the energy flux density averaged over the field oscillations:

$$I(\vec{r}, t) = \left\langle \left| \frac{c}{4\pi} \vec{E} \times \vec{B} \right| \right\rangle = \frac{c}{8\pi} |E_o(\vec{r}, t)|^2 \tag{7}$$

where $\vec{E}$ denotes the electric field vector, $E_0$ the electric field amplitude and $\vec{B}$ the magnetic field vector.

It is often useful to express the laser strength and combination of the target density and thickness in dimensionless variables like dimensionless amplitude of the laser electric field $a_0$ and the areal density of the target $\epsilon_0$

$$a_0 = \frac{eE_0}{m_e \omega c} \approx 0.85 \sqrt{\frac{I\lambda^2}{10^{18} \text{ W cm}^{-2}\mu\text{m}^2}}; \qquad \epsilon_0 = \frac{\lambda l}{4\pi l_s^2} = \pi \frac{n_e}{n_c} \frac{l}{\lambda}, \tag{8}$$

where $E_0$ is the electric field amplitude, $\lambda$ is the wavelength of the incident laser pulse, $l$ is the thickness of the target. The factor $l/l_s^2$ can be interpreted as the characteristic length related to the foil surface density $\sigma = ln_e$ [43].

The amplitude $a_0$ is used to express the relativistic Lorentz factor of laser field:

$$\gamma_L = \begin{cases} \sqrt{1 + a_0^2} & \text{for circular polarization} \\ \sqrt{1 + \dfrac{a_0^2}{2}} & \text{for linear polarization} \end{cases} \tag{9}$$

The linear polarization has different representations in 2D and 3D simulations. In the 2D case, one needs to specify, if the laser is linearly p-polarized (electric field lies in the plane of incidence, sometimes called transverse-magnetic) or linearly s-polarized (electric field is perpendicular to the plane of incidence, sometimes called transverse-electric). The 3D case then contains both parts and is behaving differently in these two planes as is demonstrated in the papers in Appendix C.

The motion of charged particles in electromagnetic field is described by the the Lorentz force $F_L$

$$F_L = q(\vec{E} + \vec{v} \times \vec{B}), \tag{10}$$

where $\vec{v}$ is the velocity of the charged particle. The $\vec{v} \times \vec{B}$ component of the Lorentz force becomes significant for relativistic laser-plasma interaction, described in the next section.

### 2.1.2 Relativistic effects and transparency

The laser-plasma interaction is considered to be relativistic for $a_0 > 1$. [96].

The factor $\gamma_L$ given by Eq. (9) starts to significantly differ from unity. Electrons now oscillate in the laser wave with the relativistic quiver velocity [97]

$$v_{osc} \approx \frac{eE_0}{\gamma_L m_e \omega} = \frac{ca_0}{\gamma_L} \tag{11}$$

If the average electron momentum is much lower than the oscillation momentum (i.e. $a_0 \gg 1$), then the $\gamma$ factor for electron

$$\gamma \approx \gamma_L > 1 \tag{12}$$

Which brings the need for relativistic corrections of several equations and parameters. The dispersion relation given by Eq. (5) becomes:

$$\omega^2 = \frac{\omega_{pe}^2}{\gamma} + (kc)^2, \tag{13}$$

Therefore, the laser pulse can now propagate into plasma in regions for which $\omega > \omega_{pe}/\sqrt{\gamma}$, i.e., up to electron densities $n_e = n_c \gamma > n_c$. This phenomenon is called relativistic (induced) transparency. Comparing the relations in Eq. (8), thin overdense plasma becomes relativistically transparent to parts of incident laser pulse fulfilling the condition $a_0 \gg \epsilon_0$ [43]. On the other hand, the laser-target parameters around $a_0 = \epsilon_0$ provides suitable conditions for efficient pushing / expelling of target electrons, which is beneficial for several acceleration mechanisms described in section 2.2.

The skin effect is affected correspondingly and the skin depth given by Eq. (6) is relativistically corrected into:

$$l_{sc} = \sqrt{\gamma} \frac{c}{\omega_{pe}}. \tag{14}$$

An analogous dimensionless amplitude to Eq. (8) can be defined using the ion mass $m_i$ instead of $m_e$: $a_i = eE_0/m_i \omega c$. Assuming acceleration of protons with $m_i \approx 1836\, m_e$, the laser intensity required to reach $a_i = 1$ is $I_i \approx 5 \times 10^{24}\ \mathrm{W \cdot cm^{-2}} (\mu m)^2$. This value exceeds the recent experimental record of reached intensity by an order of magnitude [98]. Therefore, the ion acceleration is currently mostly realized indirectly through the interaction with relativistic electrons via charge-separation fields as will be discussed in the next section 2.2.

## 2.2 Ion acceleration mechanisms

In this section, three main ion acceleration mechanisms using overdense plasma (generated by the laser interaction with solid targets) are described. Namely Target Normal Sheath Acceleration (TNSA), Radiation Pressure Acceleration (RPA) and Coulomb Explosion (CE). They accelerates ions via generation of strong charge-separation electric fields at different parts of the targets: TNSA at the target rear side, RPA at the front side and CE in the whole target volume, where electrons were expelled from. More than one mechanisms usually

occur during the laser–target interaction, and their interplay depends on the target and laser parameters [38].

Several intermediate mechanisms were also described, e.g., the hybrid RPA-TNSA mechanism [44; 45], directed Coulomb explosion [42] and break-out afterburner [46; 47], which accelerate ions to high energies around the onset of the relativistic transparency. In the near critical density plasma Magnetic Vortex Acceleration mechanism [99] can occur, if the laser pulse is intense enough to penetrate through the target to form a density channel. This results in generation of a strong azimuthal magnetic field, which has the form of a dipole vortex in 2D and toroidal vortex in 3D. Its expansion results in a strong quasi-static electric field accelerating ions.

### 2.2.1   Target Normal Sheath Acceleration (TNSA)

The most commonly applied mechanism in experiments is TNSA. In this scenario, the laser irradiation of the target front side results in generation of hot electron population. These electrons can propagate through the target and reach its rear side, as their losses through collisions are minimal (they have significantly higher energy compared to the bulk electrons) and their current is compensated by the return current of the cold electrons in the opposite direction [100; 101]. The electrons can escape the target and form an electron sheath (which is normal to the target) at its rear side, producing a strong quasi-static charge-separation electric field accelerating ions (see the scheme in Fig. 1). The sheath can be enhanced by the electron recirculation around the target [102], which happens as the electrons crossing the vacuum-target boundary get subsequently deaccelerated and attracted back to the target by the arising quasistatic field. Protons and other hydrocarbon impurities are primarily accelerated, as they have the most optimal charge to mass ratio. Using the techniques like target heating and ablation [103; 104], the thickness of the impurities can be controlled for either their efficient acceleration or cleaning of the target for acceleration of the heavier bulk ions.
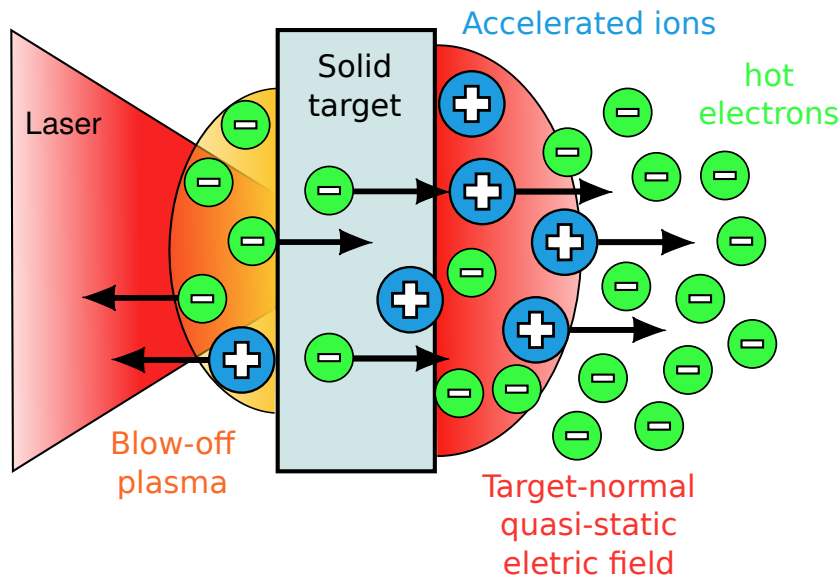


**Figure 1:** The scheme of the TNSA mechanism. Source: author's master thesis [105].

The basic model of the sheath at the target rear side with initial electron density $n_{0,e}$ is given by the assumptions of ions with charge number $Z$ and density $n_i$ being initially at rest and having a sharp step-like density profile at the rear side of the target (located at the position $x = 0$), which can be described using the Heaviside function $\Theta$ as:

$$n_i = \frac{n_{0,e}}{Z} \Theta(-x). \tag{15}$$

On the contrary, the electrons with charge $e$ and temperature $T_e$ can move and their density $n_e$ redistributes according to the Boltzmann distribution with electrostatic potential $\phi$:

$$n_e = n_{0,e} \exp(e\phi/T_e), \tag{16}$$

The Poisson's equation then can be expressed as [2]:

$$\mathrm{d}_x^2 \phi = 4\pi e [n_e - Z n_i] \tag{17}$$

The plasma is considered neutral apart from this sheath region which thickness is of the order of the Debye length $\lambda_D$ (1). The initial longitudinal electric field in this layer is [2]:

$$E_{sheath,0} = \sqrt{\frac{2}{\mathrm{e_N}}} \frac{T_e}{e\lambda_D} = \sqrt{\frac{8\pi}{\mathrm{e_N}} n_e T_e}, \tag{18}$$

where $\mathrm{e_N}$ is the Euler number.

The maximal ion energy $\mathcal{E}_{i,max}$ (at the front of the expanding ion cloud) of ions with mass $m_i$ can be expressed using the 1D expansion model [106]:

$$\mathcal{E}_{i,max}(t) = 2 Z T_e \ln^2\left(\tau + \sqrt{\tau^2 + 1}\right), \tag{19}$$

where $\tau = \omega_{pi} t / \sqrt{2\mathrm{e}_N}$ with the ion plasma frequency $\omega_{pi} = \sqrt{4\pi e^2 Z n_{0,e}/m_i}$.

Another approach is the strong charge-separation field model [107–109]. Here the acceleration of a small number of light particles (considered as test particles) is described solving equations (16) and (17). The ion energy is expressed using their position $x_i$ along the target normal [2]:

$$\mathcal{E}_{i,max}(x_i) = 2 Z T_e \ln\left(\frac{C_1 + x_i/\lambda_D}{\sqrt{2}}\right), \tag{20}$$

where constant $C_1 \approx 2$.

In principle, both models (19) and (20) predict unlimited energy gain with increasing acceleration time or ion position in the accelerating field, which does not correspond to reality. Therefore, the acceleration time $t_{acc}$ or distance $x_{acc}$ needs to be limited. For example limiting the $t_{acc}$ to the order of the laser pulse duration $\tau_0$ (i.e., $t_{acc} \approx 1.3 \cdot \tau_0$) was found relevant to many experiments and simulations [110].

In paper II. we compared our simulation results with the relativistic model for light ions with finite acceleration length given in [111; 112]. Here the electron sheath at the rear side of the target is assumed to consist of only plasma-bound electrons. The electrons with highest energy can escape this region and do not contribute to generation of the acceleration field. The maximum energy of the light ions described by this model is:

$$\mathcal{E}_{i,max} = Z T_e \frac{e^{\varphi^*}(\varphi^* - 1) + 1}{e^{\varphi^*} - 1}, \tag{21}$$

where $\varphi^* = \mathcal{E}_{e,max}/T_e$ is the normalized maximum energy of plasma-bound electrons. Therefore, the model requires two values ($T_e$ and $\mathcal{E}_{e,max}$), which need to be measured in the experiments (derived from the simulation results) or fitted by a relevant approximation. For a wide range of laser parameters, the electron temperature $T_e$ can be approximated by the ponderomotive potential [113; 114]:

$$T_e = \Phi_{pond} = m_e c^2 \left[ \sqrt{1 + a_0^2} - 1 \right], \tag{22}$$

and $\varphi^* = \mathcal{E}_{e,max}/T_e$ can be fitted by the empirical formula [111]:

$$\varphi^*_{fit} = 4.8 + 0.8 \ln\left(E_L(J)\right), \tag{23}$$

where $E_L$ is the laser energy in Joule.

The TNSA models are usually isothermal, assuming the electron temperature equal to the ponderomotive potential. The ion energy spectrum is given by theory [106] as:

$$\frac{\mathrm{d}N_i}{\mathrm{d}\mathcal{E}_i} = \frac{n_{0,i} c_s t_{acc}}{\sqrt{2\mathcal{E}_i ZT_e}} \exp\left(-\sqrt{\frac{2\mathcal{E}_i}{ZT_e}}\right), \qquad \mathcal{E}_i \leqslant \mathcal{E}_{i,max}(t), \tag{24}$$

where $N_i$ and $\mathcal{E}_i$ is the number of ions and their energy, and $c_s = \sqrt{ZT_e/m_i}$ is the ion acoustic velocity. Therefore, the TNSA mechanism provides mostly broad and exponentially decreasing ion energy spectra with a cut-off energy. Its energy scaling is dominated by the ponderomotive potential (Eq. 22), which provides square root dependence on increasing intensity. Therefore, different mechanisms, which can provide narrower energy spectrum and more efficient energy scaling are being assumed for ion acceleration.

## 2.2.2   Radiation Pressure Acceleration (RPA)

Another promising mechanism is the Radiation Pressure Acceleration (RPA) [32], which is becoming more and more relevant in the experimental conditions with the increasing laser intensity and the decreasing target areal density. High-intensity laser becomes strong enough to push the electrons into the target. In turn a strong charge separation field arises, accelerating ions behind in the layer depleted from the electrons (i.e., the electron depletion layer). Two main scenarios can occur. For a relatively thin targets, the area around the laser focal spot can be pinched out from the target and accelerated as a compact structure transferring the laser energy into the electron layer and subsequently into the ion layer following it through the charge-separation field. For the relatively thick target, the laser pulse is pushing electrons through the target like a plow or a piston, efficiently boring a hole through the target, which is described as the Hole Boring (HB) regime [113; 115–117].

On the contrary to the TNSA mechanism, the relevant electrons in the RPA do not propagate deeper into the target, but piled up and are kept near the front side of the target (or near the ion layer in the case of thin foil) by the strong electrostatic field, as the equilibrium between the radiation and electrostatic pressure is reached. This can be expressed assuming the maximal reflectivity of the laser pulse from the target as [118]

$$\frac{1}{8\pi}E_{es}^2 = \frac{2}{c}I, \tag{25}$$

where the amplitude of the electrostatic field in the depletion layer (with thickness $l_{ed}$) can

be obtained from the Poisson equation as

$$E_{es}(l_{ed}) = 4\pi e n_{e,0} l_{ed},$$ (26)

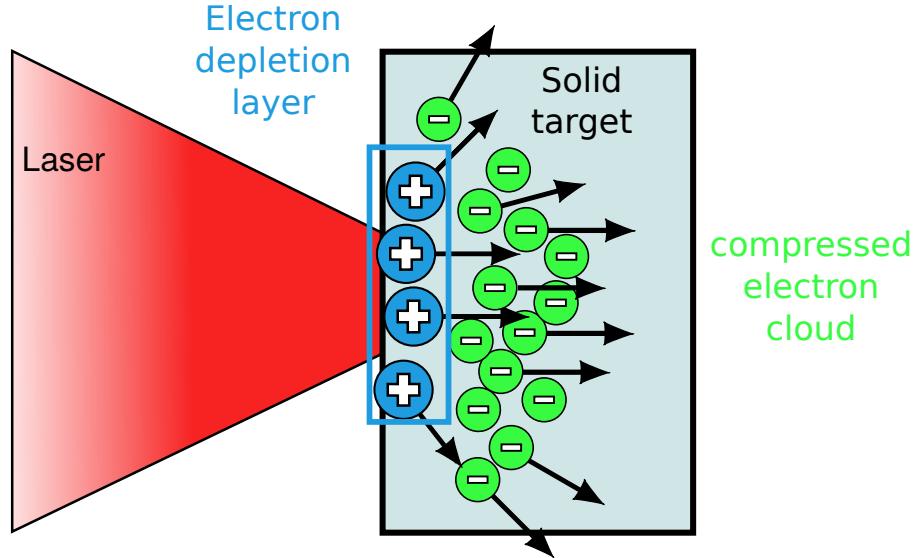The scheme of this behavior of RPA mechanism is sketched in Fig. 2.



**Figure 2:** The scheme of the RPA mechanism. Source: author's master thesis [105].

Note that several acceleration mechanisms (and their mixtures) usually occur together (at the same time or subsequently) during the laser target interaction. Part of the electrons is kept at the front side, participating in the RPA and part propagates through the target and reach the rear side, participating in the TNSA. The dominance of one of these two mechanism in ion acceleration for specific conditions is further investigated in the results part of this dissertation in section 4.2 and in the paper II..

The optimal thickness of the target in the thin foil approximation can be derived by setting $a_0 = \epsilon_0$ in Eq. (8) [32; 43], i.e., preventing a strong effect of relativistic transparency (see section 2.1.2), while keeping the thickness minimal. Note that the same equation can be achieved by assuming all electrons being expelled from the target as is shown in the next section 2.2.3 by Eq. (52) and (53). The optimal target thickness can be expressed in the following form:

$$\frac{l}{\lambda} = \frac{a_0}{\pi} \frac{n_c}{n_e}.$$ (27)

In the next two parts the mechanisms for thin and thick target will be described.

**Thin foil approximation**

The RPA acceleration using a relatively thin target can be described by the model in [32; 119]. Assuming a maximal reflectivity, the radiation pressure is given by

$$P = \frac{E_0'^2}{2\pi} = \left(\frac{\omega'}{\omega}\right)^2 \frac{E_0^2}{2\pi} = \frac{E_0^2}{2\pi}\left(\frac{c-v}{c+v}\right),$$ (28)

which can be also expressed using the irradiance $I_0$ assuming a circular polarization as [2]:

$$P = \frac{2I_0}{c} \left( \frac{c - v}{c + v} \right) \tag{29}$$

The primed quantities refer to the moving reference frame and $v$ is the foil instantaneous velocity:

$$v = \frac{\mathrm{d}x}{\mathrm{d}t} = c\frac{p}{\left(m_{\mathrm{p}}^2 c^2 + p^2\right)^{1/2}}. \tag{30}$$

The laser electric field at the foil location $x(t)$ depends on time as $E_0' = E_0(t - x(t)/c)$, assuming quasi-one-dimensional geometry.

The equation of motion of the foil is then:

$$\frac{\mathrm{d}p}{\mathrm{d}t} = \frac{E_0^2(t - x(t)/c)}{2\pi n_0 l_0} \frac{\left(m_{\mathrm{p}}^2 c^2 + p^2\right)^{1/2} - p}{\left(m_{\mathrm{p}}^2 c^2 + p^2\right)^{1/2} + p}, \tag{31}$$

where $p$ is the momentum of the proton representing the foil, and $l_0$ and $n_0$ are the thickness and initial proton density of the foil.

To derive the maximum proton energy gained during the interaction with a laser pulse of finite duration, the dependence of the laser electromagnetic field on time $t$ and on the coordinate $x$ needs to be assumed, which can be done by using the phase of the wave as a variable

$$\psi = \omega_0(t - x(t)/c), \tag{32}$$

where $\omega_0$ is the incoming laser frequency.

The Eq. (31) can be rewritten using Eq. (30) and (32) into:

$$\frac{\mathrm{d}p}{\mathrm{d}\psi} = \frac{E_0^2(\psi)}{2\pi\omega_0 n_0 l_0} \frac{\left(m_{\mathrm{p}}^2 c^2 + p^2\right)^{1/2}}{\left(m_{\mathrm{p}}^2 c^2 + p^2\right)^{1/2} + p}. \tag{33}$$

The solution (using $w$, which is a function of $\psi$) is [119]:

$$p = m_{\mathrm{p}} c\frac{w(w + 1)}{(w + 1/2)}, \qquad w(\psi) = \int_{-\infty}^{\psi} \frac{E_0^2(s)}{4\pi\omega_0 n_0 l_0 m_{\mathrm{p}} c} \,\mathrm{d}s. \tag{34}$$

The variable $w(\psi)$ is called fluence and represents the integral of the momentum flux through a target unit surface.

The kinetic energy of protons initially at rest can be expressed as:

$$\mathcal{E}_{p,kin} \equiv \left(m_{\mathrm{p}}^2 c^2 + p^2\right)^{1/2} c - m_{\mathrm{p}} c^2 = m_{\mathrm{p}} c^2\frac{w^2}{(w + 1/2)}. \tag{35}$$

The target is also deformed during its interaction with the laser pulse and often forms a cocoon structure or a channel, confining the laser pulse. Therefore, the group velocity of the laser wave is smaller than the speed of light in vacuum (these two being equal was assumed in the model above). This kind of wave is referred to as a slow electromagnetic wave and its interaction with thin target is described in [117].

A model reflecting this behavior is given in [1; 117]: Here a more general case assuming an

imperfect reflection of laser pulse from the thin foil is used, i.e., by introducing the coefficients of reflection $|\rho|^2$, transmission $|\tau|^2$ and absorption $|\alpha|^2$, which are connected by the relation:

$$|\rho|^2 + |\tau|^2 + |\alpha|^2 = 1. \tag{36}$$

Assuming a circularly polarized wave propagating along the $x$-axis with vector potential:

$$\vec{A} = A_0 \left[ \cos(\omega t - kx)\vec{e}_y + \sin(\omega t - kx)\vec{e}_z \right], \tag{37}$$

where $\vec{e}_y$ and $\vec{e}_z$ are the unit vectors along the $y$ - and $z$-axes, and $k$ is the wave number.

The corresponding Poynting vector is

$$\vec{S} = c\vec{E} \times \vec{B}/4\pi = c\omega k A_0^2 \vec{e}_x. \tag{38}$$

In the frame moving with the target (with velocity $v = \beta c$) the $\omega k$ part becomes:

$$\omega' k' = \omega^2 \frac{(\beta_g - \beta)(1 - \beta_g\beta)}{1 - \beta^2}, \tag{39}$$

where $\beta_g = v_g/c$ is the normalized group velocity.

The force acting on the plasma target can be determined by the combination of the values of the Poynting vectors of incident, reflected and transmitted waves:

$$F = \left( 1 + |\rho|^2 - |\tau|^2 \right) S, \tag{40}$$

which can be also expressed using the absorption coefficient instead of the transmission one, using the relation (36), as

$$F = \left( 2|\rho|^2 + |\alpha|^2 \right) S = KS, \qquad K = 2|\rho|^2 + |\alpha|^2 \tag{41}$$

The equation of motion of the surface element of a thin target can be written in the form [117]

$$\frac{1}{\left(1 - \beta_\alpha^2\right)^{3/2}} \frac{\mathrm{d}\beta_\alpha}{\mathrm{d}t} = \frac{KE^2}{4\pi\sigma m_\alpha c} \frac{(\beta_g - \beta_\alpha)(1 - \beta_g\beta_\alpha)}{1 - \beta_\alpha^2}, \tag{42}$$

$\sigma = n_0 l_0$ is equal to the surface density of the target with the thickness $l_0$ and density $n_0$, $\beta_\alpha = p_{\alpha,x}/\left(m_\alpha^2 c^2 + p_{\alpha,x}^2\right)^{1/2}$ is the $x$-component of the normalized velocity of the surface element of the target (of ion type $\alpha$), and $E^2 = (\omega A/c)^2$.

The fluence of this model $w(\psi)$ is a function of the wave phase $\psi = \omega(t - x/c)$, where the coordinate $x(t)$ of the target must be found by solving the equations of motion. It can be expressed in the dimensionless form, assuming $\beta_g = 1$ and taking the value of $w$ in the limit $\psi \to \infty : w = w(\psi)|_{\psi = \infty}$ as [1]:

$$w = \int_{-\infty}^{\psi} \frac{KE_{\mathrm{las}}^2}{4m_\alpha \sigma \omega^2 \lambda} \mathrm{d}\psi, \tag{43}$$

where $\mathcal{E}_{\mathrm{las}} = \int \left(E^2/4\pi\right) \mathrm{d}V$ is the laser pulse energy.

## Hole Boring (HB)

For a relatively thick overdense target a different description needs to be done [2]. The electrons are still pushed by the radiation pressure and the ions followed by the charge

separation field. This process is usually described as the hole boring version of the radiation pressure acceleration. The laser piles up the electrons forming an electron spike, ions are pulled by the arising charge-separation field and form a second spike. In the reference frame moving with the hole boring velocity $v_b$, the unperturbed ions are reflected by the charge separation field between the two spikes into the forward (laser propagation) direction.

In paper II. we compared our simulation results with the relativistic model of the HB regime described in [116]. Its non-relativistic and relativistic description is as follow:

The models assume 1D situation of laser with constant intensity interacting with uniform plasma containing one ion species and perfect reflection (i.e., $|\rho|^2 = 1$). The system is examined via the momentum balance in the instantaneous rest frame (IRF). In the laboratory frame, the plasma surface is moving with the velocity $v_{\mathrm{b}}$ and the bulk of the plasma behind it is at rest. On the contrary, the plasma is moving toward the target surface at $-v_{\mathrm{b}}$ in the IRF, which must be compensated by a beam of plasma propagating at $+v_{\mathrm{b}}$ away from the plasma surface to conserve the particle number. The momentum balance in the IRF is then:

$$\frac{2I}{c} = 2n_{\mathrm{i}}m_{\mathrm{i}}v_{\mathrm{b}}^2, \tag{44}$$

where $n_{\mathrm{i}}$ is the ion density and $m_{\mathrm{i}}$ is the ion mass.

Therefore, $v_b$ can be determined from (44) as:

$$v_{\mathrm{b}} = \sqrt{\frac{I}{n_{\mathrm{i}}m_{\mathrm{i}}c}} = \sqrt{c^2\Xi}. \tag{45}$$

where $\Xi$ is the so-called pistoning parameter [116]

$$\Xi = \frac{I}{m_{\mathrm{i}}n_{\mathrm{i}}c^3} \tag{46}$$

The velocity of the accelerated ions back in the lab frame (using Gallilean transformation) is $v_{\mathrm{i}} = 2v_{\mathrm{b}}$ and their energy in the non-relativistic case is then:

$$\mathcal{E}_{i,NR} = \frac{1}{2}m_i(2v_b)^2 = 2m_ic^2\Xi. \tag{47}$$

In the relativistic case, Eq. (44) in the IRF becomes:

$$\frac{2I}{c}\left(\frac{1 - v_{\mathrm{b}}/c}{1 + v_{\mathrm{b}}/c}\right) = 2\gamma_{\mathrm{b}}^2 m_{\mathrm{i}}n_{\mathrm{i}}v_{\mathrm{b}}^2, \tag{48}$$

which can be rearranged using $\beta_{\mathrm{b}} = v_{\mathrm{b}}/c$ and $\Xi$ into

$$(\Xi - 1)\beta_{\mathrm{b}}^2 - 2\Xi\beta_{\mathrm{b}} + \Xi = 0, \tag{49}$$

giving the hole boring velocity:

$$\frac{v_{\mathrm{b}}}{c} = \beta_{\mathrm{b}} = \frac{\sqrt{\Xi}}{1 + \sqrt{\Xi}}. \tag{50}$$

The ion energy in the lab frame (using appropriate Lorentz transformation) for the relativistic case is then:

$$\mathcal{E}_i = m_{\mathrm{i}}c^2\left[\frac{1 + \beta_{\mathrm{b}}^2}{1 - \beta_{\mathrm{b}}^2} - 1\right] = m_{\mathrm{i}}c^2\left[\frac{2\Xi}{1 + 2\sqrt{\Xi}}\right]. \tag{51}$$

Note that the slow wave approach (similar to the one described above for the thin foil case) can be done also for the Hole Boring regime [117].

### 2.2.3 Coulomb Explosion (CE)

One of the way to produce a mono-energetic ion spectra is to employ a coulomb explosion mechanism in a double-layer target scenario [61]. Here the front layer usually consists of heavy ions and is followed by a relatively thin layer of light ions, e.g., a metal foil with hydrocarbon contaminants. The laser pulse expels electrons from the foil, creating a surplus of positively charged ions. Consequently a strong quasi-static electric field repulsing the ions is generated. Both heavy and light ions are accelerated. However, the efficiency of acceleration is higher for the lighter ions, as the ratio $m_i Z_a/(M_a Z_i)$ can be sufficiently high. Here the mass and charge number for heavy ions are denoted as $m_i$ and $Z_i$ and for light ions as $m_a$ and $Z_a$, i.e., $m_i >> m_a$).

The heavy layer should be thick enough to contain a sufficient number of electrons to be expelled by the laser (to generate strong Coulomb field), but it also needs to be thin enough to generate the electric field at its rear side, to affect the light layer. The light layer should be efficiently thin (so the number of light ion is sufficiently small) to limit effect on the electric field. A scheme of this mechanism is shown in Fig. 3.
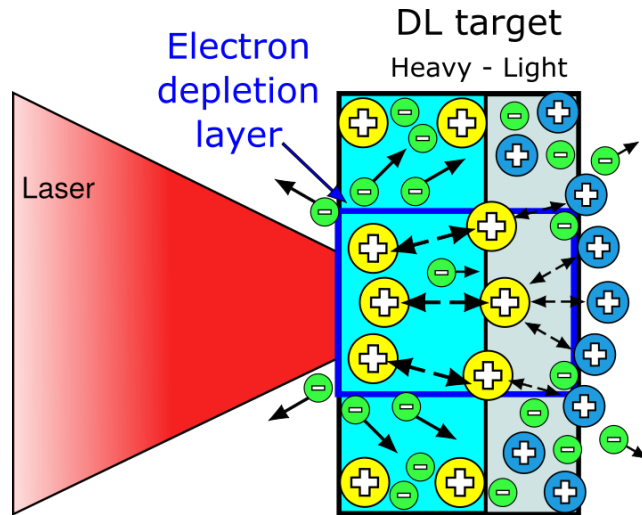


**Figure 3:** The scheme of the (Directed) Coulomb Explosion mechanism.

When all of the electrons are expelled from a plasma region, the maximal Coulomb electric field generated by the remaining ions is

$$E_i = 2\pi e Z_i n_i l = \pi \frac{m_e c \omega}{e} \sigma_0, \qquad \sigma_0 = \frac{n_e l}{n_{cr} \lambda} \tag{52}$$

The parameter $\sigma_0$ represents a dimensionless areal density of the target, which is more relevant to describe the behavior of the interaction than the target thickness only.

Assuming the driving laser electric field to be close to $E_i$ the relation between $a_0$ and $\sigma_0$ (and $\epsilon_0$ (8), which is derived via different approach using the skin depth) is:

$$a_0 = \pi\sigma_0 = \epsilon_0 \tag{53}$$

Assuming the longitudinal (target normal) length of the region with high electric field to be of the order of the laser focal spot radius (i.e. half of the diameter $D/2$), the maximum energy gained by the light ions is:

$$\mathcal{E}_{a,max} = eZ_a E_i D/2 \tag{54}$$

The optimal target areal density for laser absorption and ion energy gain in this regime using a broad range of parameters was discussed in Ref. [120], the empirical formula can be derived from the simulations as

$$\sigma_{0,opt} \approx 3 + 0.4a_0 \approx 0.4a_0. \tag{55}$$

Decreasing $\sigma_0 < \sigma_{0,opt}$ results in higher portion of laser pulse being transmitted through the target. On the other hand, for increasing $\sigma_0 > \sigma_{0,opt}$ the laser pulse reflection from the target is becoming significant.

Using $\sigma_{0,opt}$ and the corresponding electric field $Ei$ given by Eq. 52, the scaling of the maximal energy with the laser power $P$ is:

$$\frac{\mathcal{E}_{a,max}}{Z_a} \sim \sqrt{P} \tag{56}$$

Therefore, the energy scaling does not depend on laser intensity.

The Coulomb explosion can also be realized using a cluster of a small radius $R$ [121–123] which can accelerates ions located initially at the cluster surface to maximal energy of

$$\mathcal{E}_{i,max} = \frac{4}{3}\pi e^2 Z_i n_e R^2 \tag{57}$$

With the increasing laser intensity the Directed Coulomb Explosion (DCE) [42] can be achieved, where the laser pulse not only expels electrons but also accelerates the remaining ion core, which starts to move in the direction of laser propagation. This regime represents an efficient combination of the radiation pressure and Coulomb explosion behavior.

# Chapter 3

# Methods

The plasma can be modeled by several approaches, the main ones are: hydrodynamic (fluid), kinetic, and particle description, which differ in their limitations and applications.

**Hydrodynamic / fluid approach** assumes local thermodynamic equilibrium (LTE) in plasma, have Maxwellian distribution of the velocities of particle species with well-defined temperature. The plasma can be described by its macroscopic variables, which are functions of time and position. This method is very useful to describe the large-scale dynamical behavior of plasmas, e.g., for plasma interaction with low-intensity lasers (lower than $\approx 10^{15}$ W/cm$^2$), where LTE still can be valid. For example the interaction of the laser prepulse with overdense foil was simulated by this approach by our coauthors in paper V.

**Kinetic approach** uses a general distribution function $f_s$ of a particle species $s$, instead of the Maxwellian one. The distribution function represents a statistical description of huge number of interacting particles, where each particle has its own position in the phase space. For the relativistic laser parameters used in this dissertation, the plasma can be assumed to be colissionless. Therefore, the evolution of a single-particle distribution function $f_s(\vec{x}, \vec{v}, t)$ can be described by the Vlasov equation [124]

$$\frac{\partial f_s(\vec{x}, \vec{v}, t)}{\partial t} + \vec{v} \cdot \nabla_{\vec{x}} f_s(\vec{x}, \vec{v}, t) + \frac{q}{m}(\vec{E} + \vec{v} \times \vec{B}) \cdot \nabla_{\vec{v}} f_s = 0 \tag{58}$$

**Particle approach** describes plasma as a system of single particles (i.e., uses equations of motion for each of them), which are moving under the influence of the electric and magnetic fields. Using all plasma particles in the simulation would be very computationally demanding. Therefore, a so-called macro-particles representing a huge number of real particles are used in the simulations. However, the plasma particles needs to be sufficiently sampled, otherwise the noise is increasing, which brings limits to this approach and some specific plasma phenomena need to be investigated by the kinetic approach.

**EPOCH code** [125], which is using the particle approach, was used for the simulations done in this dissertation. The code was created at the University of Warwick and is available as open source at the corresponding Github page [126]. Therefore, it is being continuously developed in collaboration with the scientific community. The code is written in Fortran, parallelized using MPI and well suitable for the use at supercomputer clusters like IT4Innovations. The code exists in three versions for 1D, 2D and 3D simulations. The output data are saved in .sdf (self-describing file) format [127], which is being developed simultaneously with EPOCH. Scripts to load and process .sdf files by Matlab, Python, Visit and other applications are provided together with the EPOCH source code.

## 3.1 Particle-in-cell (PIC)

In this dissertation the particle approach is used via the particle-in cell (PIC) method. Here the distribution function $f_s$ is sampled by so-called macro-particles (or pseudo-particles), which represents a finite phase-fluid elements:

$$f_s\left(\overrightarrow{x}, \overrightarrow{v}, t\right) = \sum_k N_k S_x\left(\overrightarrow{x} - \overrightarrow{x}_k\right) S_v\left(\overrightarrow{v} - \overrightarrow{v}_k\right), \tag{59}$$

where $N_k$ is the number of real physical particles represented by the $k$-th macro-particle of the species $s$, $S_x$ and $S_v$ are shape functions of the particle in the phase space of coordinates $\overrightarrow{x}$ and velocities $\overrightarrow{v}$. $S_v$ is usually set as the Dirac $\delta$-function, keeping the velocity of all real particles represented by a macro-particle the same. On the other hand, $S_x$ is usually set in the form of b-spline. The computation of the motion of macro-particles is equivalent to numerical solving of Vlasov equation (58) [124].

The PIC simulation is usually initialized by dividing the simulation area into cells following the numerical grid, and loading the macro-particles with their predefined properties into their positions inside the cells. The macro-particles can freely move from one cell to another following the influence of electric and magnetic fields calculated on the grid.

The PIC method contains four essential steps which are repeated in a loop: (1) Interpolation of the EM fields from the grid to the particle positions; (2) Integration of the equation of motion of the particles; (3) Computation of the charge and currents densities; (4) Integration of field equations back on the grid. Additionally, modules containing further physical description of the more advanced phenomena can be added in the loop. For example QED module solving nonlinear Compton scattering was used in papers II. and III.. In the Epoch code used for simulations done in this dissertation this module could be inserted between the steps (2) and (3). The cycle of the particle-in-cell method is summed up in the following diagram.
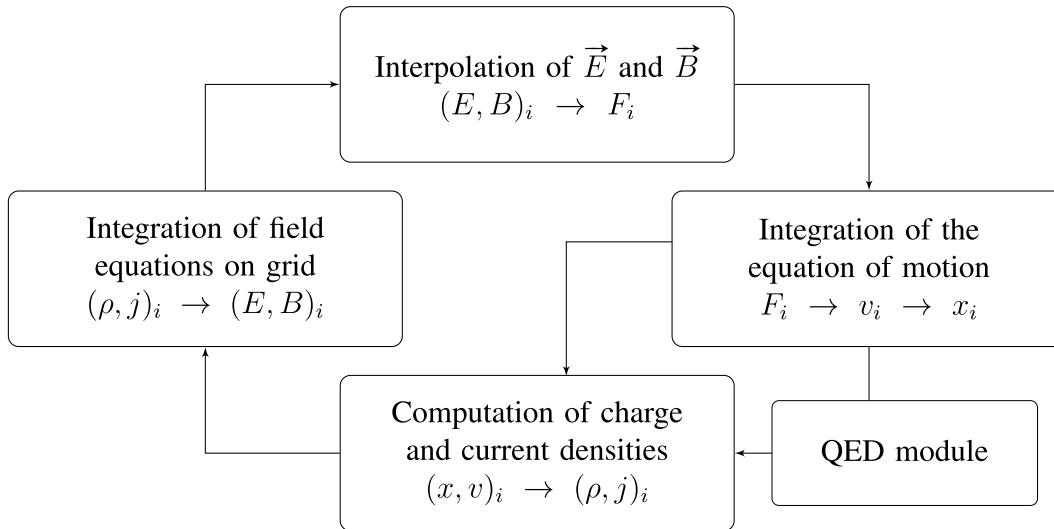


**Figure 4:** Diagram of PIC code computational cycle. If the QED module is not included, the cycle continues from [Integration of equation of motion] directly to [Computation of charge and current densities].

The description of the PIC method in the EPOCH code (used by the author for all of the PIC simulations included in this dissertation) with the employed algorithms are thoroughly described by the author in his master thesis [105]. Here only the final descriptions from [105] are summed up:

**Interpolation of fields:** In the first step, the EM fields are interpolated to the positions of the pseudo-particles. Considering a cell-centered field in 1D geometry with uniformly spaced grid with spacing $\Delta x$ and the shape function in the form of b-spline of the first order, i.e., the shape of the pseudo-particle becomes an isosceles triangle with the peak at a position $X$ and a width of $2\Delta x$, which can be spread over three cells. The field distribution around the mesh point $x_j$ can be assumed as [128; 129]:

$$F(x, t_n) = \begin{cases} F_j, & x_j - \dfrac{\Delta x}{2} \leqslant x \leqslant x_j + \dfrac{\Delta x}{2} \\ 0 & \text{else} \end{cases}. \tag{60}$$

The field acting on the pseudo-particle with the shape peak at $X$ then can be expressed as [128–130]:

$$\begin{aligned} F_X &= \frac{1}{2} F_{j-1} \left( \frac{1}{2} + \frac{x_j - X}{\Delta x} \right)^2 + F_j \left( \frac{3}{4} - \frac{(x_j - X)^2}{\Delta x^2} \right) \\ &+ \frac{1}{2} F_{j+1} \left( \frac{1}{2} - \frac{x_j - X}{\Delta x} \right)^2. \end{aligned} \tag{61}$$

In many codes including the EPOCH, the so-called Yee grid is used. Therefore, fields are in general not cell-centered, but they are placed on the grid by the following rules [130]: The electric field components are moved from the cell centre by half of the grid cell in their own directions and the magnetic field ones are moved from the cell centre by half of the grid cell in all directions except their own direction, if these dimension are available in the simulation. For 1D simulation, $E_x$ is staggered to the grid, but $B_x$ remains cell-centered.

**Integration of the equation of motion**: The macro-particles now can move according to the fields at their positions, which is solved in the discrete time-step by the numerical scheme based on the set of relativistic equations of motion [124]:

$$\frac{\partial \vec{x}_k}{\partial t} = \frac{\vec{p}_k}{\gamma m_k}, \quad \frac{\partial \vec{p}_k}{\partial t} = q_k \left( \vec{E}_k + \frac{\vec{p}_k}{\gamma m_k} \times \vec{B}_k \right), \quad \gamma = \sqrt{1 + \left( \frac{\vec{p}_k}{m_k c} \right)^2} \tag{62}$$

where $\vec{E}_k$ and $\vec{B}_k$ are electric and magnetic fields at the position of $k$-th particle, $m_k$ and $q_k$ are the rest mass and charge of $k$-th particle and $\gamma$ is the relativistic factor. To solve this set of equations, the leap-frog method is used in the majority of the PIC codes, computing coordinates $\vec{x}$ and $\vec{v}$ [131]. The principle of the leap-frog method is that the velocities (or momenta) are computed in the middle of time step, while positions are calculated in the time step edges in the following way:

In the first half of time step ($\Delta t/2$), the macro-particle is moved by its original momentum:

$$x\left( t + \frac{\Delta t}{2} \right) = x(t) + \frac{\Delta t}{2} \frac{p_x}{\gamma m}(t), \qquad \gamma = \sqrt{1 + \frac{p_x^2 + p_y^2 + p_z^2}{m^2 c^2}}. \tag{63}$$

New momentum is evaluated at the position of the moved particle

$$p_x \left( t + \Delta t \right) = p_x(t) + q\Delta t \left[ E_x \left( t + \frac{\Delta t}{2} \right) + v_y \left( t \right) B_z \left( t + \frac{\Delta t}{2} \right) \right.$$
$$\left. - v_z \left( t \right) B_y \left( t + \frac{\Delta t}{2} \right) \right]. \tag{64}$$

In the second half of the time step, newly evaluated momentum is used to move the macro-particle

$$x \left( t + \Delta t \right) = x \left( t + \frac{\Delta t}{2} \right) + \frac{\Delta t}{2} \frac{p_x}{\gamma m} (t + \Delta t). \tag{65}$$

**Computation of charge and current densities:** The properties of the macro-particle need to be interpolated back to the grid in order to affect the EM fields in the next step. It is an analogous operation to the step (1). Assuming the same 1D situation, with triangle shape function of macro-particles, with center at $X$. The part of the macro-particle overlapping the $i$-th cell contributes to the field at the grid point $x_i$ by its property *Data* in the following way:

$$F(i) = Data \cdot \begin{cases} \dfrac{3}{4} - \dfrac{|X - x_i|^2}{\Delta x^2}, & |X - x_i| \leqslant \dfrac{\Delta x}{2} \\ \dfrac{1}{2} \left( \dfrac{3}{2} - \dfrac{|X - x_i|}{\Delta x} \right)^2, & \dfrac{\Delta x}{2} < |X - x_i| \leqslant \dfrac{3\Delta x}{2} \\ 0, & |X - x_i| > \dfrac{3\Delta x}{2} \end{cases}. \tag{66}$$

The general relation for a shape function $S$ can be expressed via the integral for each grid point $x_i$ as:

$$F(i) = Data \int_{x_i - \frac{\Delta x}{2}}^{x_i + \frac{\Delta x}{2}} S \left( X - x \right) dx. \tag{67}$$

The current $\vec{j}$ can be calculated from the charge density $\rho$ using the Villasenor and Buneman scheme [132] solving equation

$$\frac{\partial \rho}{\partial t} = -\nabla \cdot \vec{j} \tag{68}$$

The scheme conserves charge on the grid. Therefore, Poisson's equation remains satisfied for all the simulation time, if it is satisfied initially. The charge density $\rho$ can be obtained from Eq. (66) using the product of the macro-particle charge and numerical weight of the property *Data*.

**Integration of field equations on grid:** Knowing the particles influence at the grid location, the updated electric and magnetic fields can be calculated. In many codes (including EPOCH) the FDTD scheme is applied on the Yee grid, solving the normalized Maxwell equations:

$$\frac{\partial \vec{E}}{\partial t} = \nabla \times \vec{B} - \vec{j}, \tag{69}$$

$$\frac{\partial \vec{B}}{\partial t} = -\nabla \times \vec{E} \tag{70}$$

and Eq. (68):

$$\frac{\partial \rho}{\partial t} = -\nabla \cdot \vec{j}.$$

As described in [105], using the discretization of spatial derivatives [128; 129]

$$\nabla^+ F_{jkl}^n = \left( \frac{F_{j+1kl}^n - F_{jkl}^n}{\Delta x}, \frac{F_{jk+1l}^n - F_{jkl}^n}{\Delta y}, \frac{F_{jkl+1}^n - F_{jkl}^n}{\Delta z} \right),$$
$$\nabla^- F_{jkl}^n = \left( \frac{F_{jkl}^n - F_{j-1kl}^n}{\Delta x}, \frac{F_{jkl}^n - F_{jk-1l}^n}{\Delta y}, \frac{F_{jkl}^n - F_{jkl-1}^n}{\Delta z} \right),$$

(71)

the discrete Maxwell equations become:

$$\frac{\vec{E}_{jkl}^{n+\frac{1}{2}} - \vec{E}_{jkl}^{n-\frac{1}{2}}}{\Delta t} = \vec{\nabla}^- \times \vec{B}_{jkl}^n - \vec{j}_{jkl}^n$$

(72)

$$\frac{\vec{B}_{jkl}^{n+1} - \vec{B}_{jkl}^n}{\Delta t} = -\vec{\nabla}^+ \times \vec{E}_{jkl}^{+\frac{1}{2}}$$

(73)

$$\frac{\vec{\rho}_{jkl}^{n+\frac{3}{2}} - \vec{\rho}_{jkl}^{n+\frac{1}{2}}}{\Delta t} = -\vec{\nabla}^- \cdot \vec{j}_{jkl}^{n+1}$$

(74)

Using the Vlasov solver requires the fields at half time steps. Therefore, the solving of Maxwell's equations is split as follows:

$$\vec{E}_{jkl}^{n+\frac{1}{2}} = \vec{E}_{jkl}^n + \frac{\Delta t}{2} \left( \nabla^- \times \vec{B}_{jkl}^n - j_{jkl}^n \right)$$
$$\vec{B}_{jkl}^{n+\frac{1}{2}} = \vec{B}_{jkl}^n - \frac{\Delta t}{2} \left( \nabla^+ \times \vec{E}_{jkl}^{n+\frac{1}{2}} \right)$$
$$\frac{\vec{\rho}_{jkl}^{n+\frac{3}{2}} \vec{\rho}_{jkl}^{n+\frac{1}{2}}}{\Delta t} = -\vec{\nabla}^- \cdot \vec{j}_{jkl}^{n+1}$$
$$\vec{B}_{jkl}^{n+1} = \vec{B}_{jkl}^{n+\frac{1}{2}} - \frac{\Delta t}{2} \left( \nabla^+ \times \vec{E}_{jkl}^{n+\frac{1}{2}} \right)$$
$$\vec{E}_{jkl}^{n+1} = \vec{E}_{jkl}^{n+\frac{1}{2}} + \frac{\Delta t}{2} \left( \nabla^- \times \vec{B}_{jkl}^{n+1} - j_{jkl}^{n+1} \right)$$

(75)

## 3.2 Evaluation and visualization of large Volumetric data

The 3D simulations can produce a huge amount of data. The amount can be limited by storing only part of the simulation box. Epoch provides techniques to save only every other grid point (user can choose how many points in sequence will be skipped), to save a specific simulation area area and to use a moving window, changing the position of simulation region being calculated. However, for same cases user needs to evaluate the whole simulation area, e.g., for evaluation of energy of both reflected and transmitted laser pulse as done in paper V or for visualization purposes for science popularization. We used another approach interpolating the volumetric data of fields and density distribution to less dense grid. We saved the whole simulation area (and full grid) and performed the interpolation in post-processing, as this function is currently not available directly in the EPOCH code. In our workflow, the simulation data in the .sdf format is firstly loaded into Matlab by the script provided by the EPOCH developers. After processing the data we use the Matlab function *imresize3*, which performs a volumetric 3D interpolation (or extrapolation) to chosen grid. The interpolation method is chosen by the parameter *,'Method'*, in our case the trilinear version is used by setting *'Method'* to *'triangle'*. The interpolated data are then saved using Matlab functions *h5create* and *h5write* into .h5 format, which can be loaded by several visualization tools. In

our case we use the ParaView [133] and the VBL web-browser interactive application [134], which utilizes virtual reality mode. This visualization tools provides a real time viewing of prepared time frames and functions like zoom and rotation. The VBL application is further described in the included papers I. and III.. The use of the ParaView is shown in Fig. 5 and the use of the VBL application in Fig. 6.
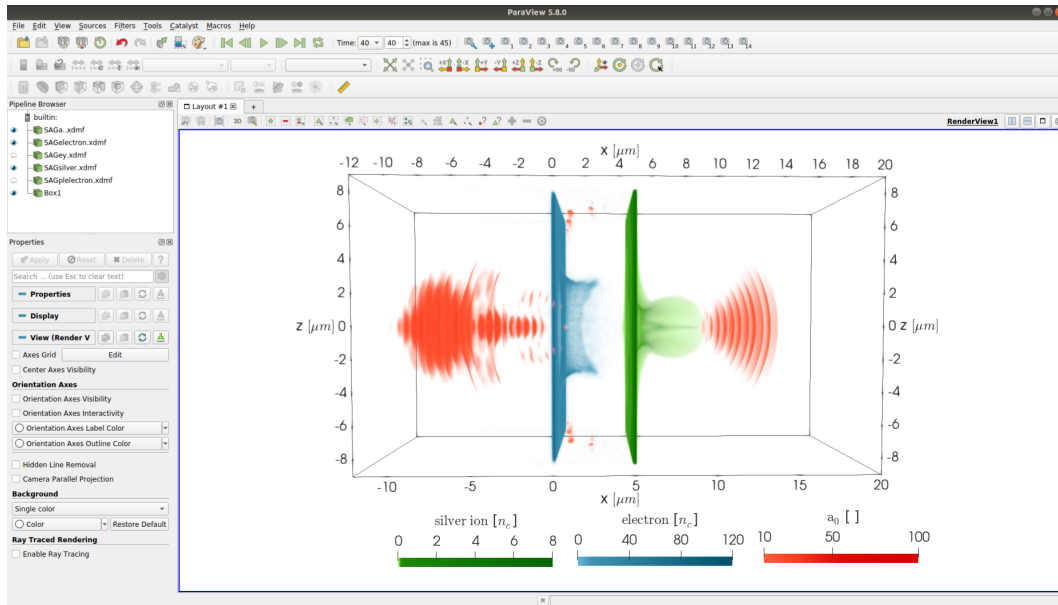


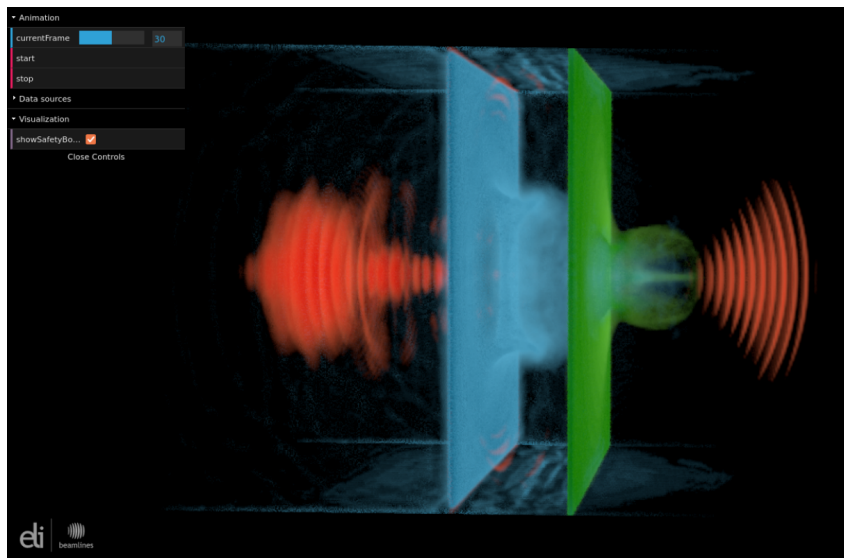**Figure 5:** The visualization of the volumetric data in ParaView



**Figure 6:** The visualization of the volumetric data in the VBL application, available online [135]

# Chapter 4

# Author's original results

## 4.1 Paper 1: High-quality laser-accelerated ion beams from structured targets

**Reference:**

M. Matys, J. Psikal, K. Nishihara, O. Klimo, M. Jirka, P. Valenta and S. V. Bulanov (2023).
High-quality laser-accelerated ion beams from structured targets. *Photonics* **10**, 61.
Attached as Appendix C.1

**Description:**

In this work, our previously published papers are connected together, as they complement each other. The reader can use this paper to see the highlights of the research performed in this dissertation, the connections between them and their common future goal to use the combination of novel schemes to propose a new generation of laser-driven ion accelerators. The details of the particular results can be found in the papers II.-V. described in the chapters 4.2-4.5 . We were invited to submit this paper to the special issue of *Photonics: Progress in Laser Accelerator and Future Prospects* [136] by the special issue editors Prof. Dr. Toshiki Tajima and Prof. Dr. Pisin Chen.

In this paper, we reviewed our results on the prospect of increasing the quality of ion acceleration driven by high-intensity laser pulses using low-$Z$ structured targets. We discussed the dominance of RPA mechanism for laser parameters relevant to research facilities such as ELI Beamlines. We demonstrated that a corrugation fabricated on the interface of double-layer targets leads to the generation of high-density and high-energy ion beams with low divergence. We proposed improvement of the ion acceleration with the laser pulse shaping via the plasma shutter (a thin foil placed in front of the main target), generating a steep-front pulse with locally increased intensity. The paper is supported by several virtual reality visualizations, some of them not published before and made in collaboration with the VBL team of ELI Beamlines (available online [137] and shown in Fig. 7). The paper was selected by the editors as the cover of the January 2023 issue of Photonics [92] (the cover page is included at the beginning of Appendix C.1).

The author wrote the bulk of the manuscript text, carried out the simulations included (with the exception of the 3D simulations in section 3.1, carried out by the author's supervisor), analyzed the results and served the role of the corresponding author.
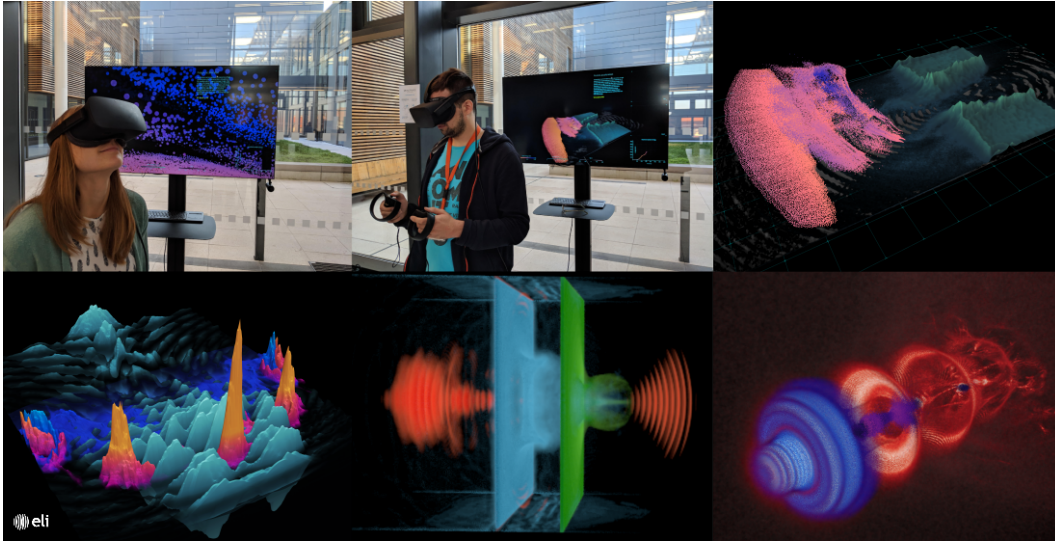
**Figure 7:** Selected Virtual Reality and ParaView visualizations presented in the paper I. Photos demonstrate the use of the Virtual Reality stations at the atrium of ELI Beamlines in Dolní Břežany.

## 4.2   Paper 2: Dominance of hole-boring radiation pressure acceleration regime with thin ribbon of ionized solid hydrogen

**Reference:**

J. Psikal and M. Matys (2018). Dominance of hole-boring radiation pressure acceleration regime with thin ribbon of ionized solid hydrogen. *Plasma Physics and Controlled Fusion* **60**, 044003.
Attached as Appendix C.2

**Description:**

With the current development of multi-PW laser systems (like ELI Beamlines [48–50], APOLLON [53], ELI NP [51; 52], and SEL [54]) and low density targets the ion acceleration can reach other acceleration mechanisms aside the more traditional TNSA. One of the promising mechanism is RPA, as its theoretical models propose higher proton energy and laser absorption into high-energy particles compared to TNSA.

In this paper we investigated with the help of 2D and 3D particle-in-cell simulations the usage of novel cryogenic hydrogen target with thickness down to several tens of micrometers (currently tested in experiments [39; 39; 56; 57; 138]) for ion acceleration driven by multi-PW lasers with parameters relevant to ELI Beamlines [48–50]. Due to its relatively low density, this target is more feasible for RPA acceleration compared to more common targets like thin plastic foil, since hole boring velocity (and therefore the energy in the HB RPA regime) increases with decreasing density and decreasing mass of ion species.

In our simulations we compare two proton populations originated from different mechanisms, as they can be clearly distinguished in space and energy level. We demonstrated that RPA mechanism dominates over TNSA both in numbers and maximum energy. We also

compare this two populations in simulations with lower intensities, as the peak intensity will be a challenge to achieve at experiments. It was shown that the pulse burns through the target for laser intensity equal or larger than $1.5 \times 10^{22}$ W$\cdot$cm$^{-2}$. TNSA started to generate protons with higher energy than RPA for the lowest intensity case of $3.7 \times 10^{21}$ W$\cdot$cm$^{-2}$. Nevertheless, RPA accelerated more particles with energy over 10 MeV than TNSA in all simulated cases.

In real experiments, the target will be partially heated by prepulses before the interaction with the main pulse and low density preplasma will be formed [139]. Therefore, we investigated an influence of exponential density profile of preplasma to ion acceleration. In our case the preplasma effects seems to be minimal, as we observed only slight differences in the final proton energy spectrum, transformation efficiency into high-energy protons and ratio of RPA protons (accelerated in the target interior) to TNSA ones (accelerated from the target rear side). Note that the used target was three orders of magnitude thicker than in the paper V., where the preplasma influence was significant.

The energies of accelerated protons are sometimes overestimated in 2D PIC simulations [47], since transverse particle spread happens only in one dimension. Therefore, we compared our results with computationally demanding 3D simulations. In our case the maximum energy of ions actually increased in 3D simulation compared to its 2D counterpart. This behavior was explained by improved self-focusing of the laser beam in the plasma medium in the 3D geometry, as focusing can occur also in another dimension. This feature is visible in the electric field distribution and is directly connected to the chain of the hole boring RPA relations: higher intensity due to self-focusing $\rightarrow$ higher hole boring velocity $\rightarrow$ higher ion energy. On the other hand, the energy of the ion population accelerated by TNSA mechanism decreased in the 3D compared to 2D, as expected. Therefore, the domination of RPA over TNSA for our cases is even more striking in the 3D geometry.

We also investigated the influence of different polarizations in 3D geometry on the interaction. Circular polarization is usually proposed for the RPA of ultra-thin foils [34; 68; 118; 140], as the oscillatory part of the nonlinear force acting on the electron layer is suppressed in this case. It results in the mitigation of the heating of electrons and consequently of the expansion of the foil. Therefore, the ion acceleration can be significantly prolonged in the case of ultra-thin foils. However, this feature is usually negligible in the case of thick foils undergoing hole boring RPA as the interaction is in principle much longer. Moreover, the foil is bent by the laser beam intensity shape and hot electrons can be generated in the curved surface of the dense target even in the case of circular polarization. Our simulations showed that circular polarization do not improve ion acceleration in our case. On the contrary, the hole boring velocity and energy of ions are even slightly higher in the case of linear polarization.

In addition to Ref. II., the obtained results were also included in conference papers [141; 142], revisited in the review paper I. and presented by the author at conference 44th European Physical Society Conference on Plasma Physics, 2017 Belfast, United Kingdom; and by author's supervisor at conference SPIE Optics&Optoelectronics 2017, Prague, Czech Republic; and by the author at summer school: the 8th Summer School on Atoms and Plasmas in Super-Intense Laser Fields, in Erice Italy 2017. The continuation of this work with particle tracking and virtual reality visualization (available online [143] and shown in Fig. 8 ) is included as a book chapter in Ref. [144].

The author collaborated with his supervisor on each aspect of the manuscript preparation, wrote parts of the manuscript text, carried out the simulations in sections 2 and 3, and the 2D counterparts of the 3D simulations in section 5 and analyzed the corresponding results. The author also helped with the preparation of the revised version of the manuscript

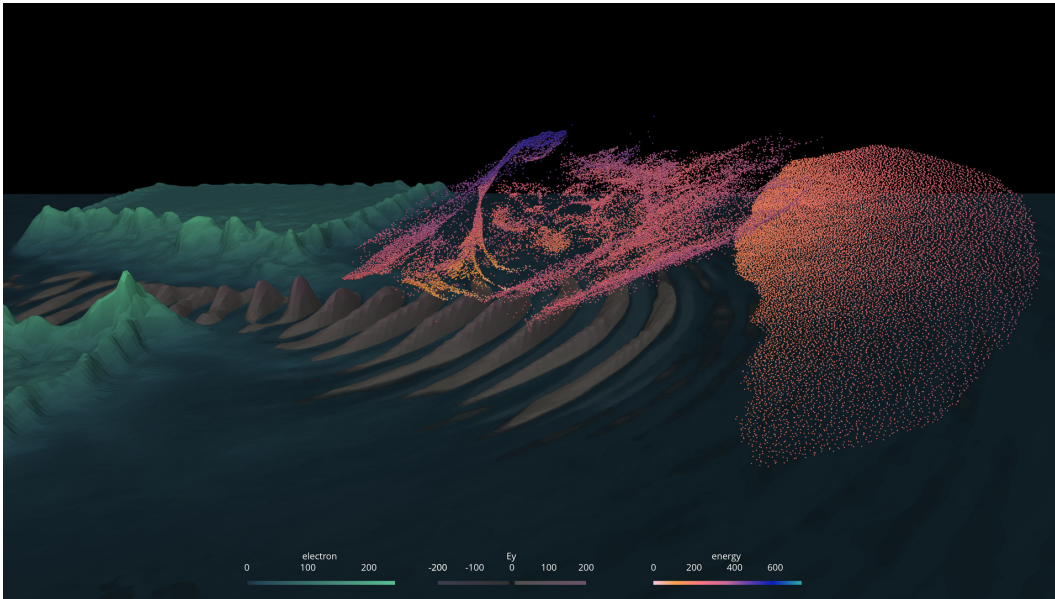(including response to referees) and with the final corrections of the paper.



**Figure 8:** Visualization of tracking particles in the 2D simulation of 10-PW-class laser with cryogenic hydrogen target. Visualized in collaboration with M. Kecová, particle tracker developed in collaboration with V. Horný. Virtual reality application of this simulation is available online [143].

## 4.3 Paper 3: Laser-driven generation of collimated quasi-monoenergetic proton beam using double-layer target with interface modulations

**Reference:**

M. Matys, K. Nishihara, M. Kecova, J. Psikal, G. Korn, S. V. Bulanov (2020). Laser-driven generation of collimated quasi-monoenergetic proton beam using double-layer target with modulated interface. *High Energy Density Physics* **36**, 100844.
Attached as Appendix C.3

The hydrodynamic-like instabilities frequently occur in high-intensity laser-plasma interaction [145; 146]. They are often considered to be detrimental effects, as they negatively affect the stability of a target and are one of the infamous problems in the concept of inertial fusion [147]. On the other hand, if controlled, they can disrupt the foil in a right way to produce quasi-monoenergetic bunches of particles, as shown in several papers with simulations of single-layer targets [73–75].

In this paper we investigated this concept with simulations of double-layer target, namely deuterium and hydrogen layers, with an initial sinusoidal interface corrugation. The interaction is driven by high power (80 PW) laser pulse with a steep front. The steep-front pulse can be generated by techniques like plasma shutter, which we discussed in paper V.

We demonstrated that a corrugation fabricated on the interface of double-layer targets leads to the development of a relativistic instability with Rayleigh-Taylor-like [71; 72] and Richtmyer-Meshkov-like [76; 77] features. The instability development results in the formation

of low-density plasma regions and high-density ion bunches between them at the positions determined by the initial interface corrugation geometry. The bunches are then accelerated by the laser radiation pressure as whole compact structures to energy of several GeV. Moreover, the laser pulse can propagate through the low-density regions, creating an enfolding field around the central bunch, preventing from the perpendicular particle expansion (see the Supplementary Video S1 in the online version of the paper III. or its still image in Fig. 9). These behavior results in the generation of quasi-monoenergetic, well-collimated ion beam. Its transverse emittance is one order of magnitude lower than that in the case of conventional accelerators.
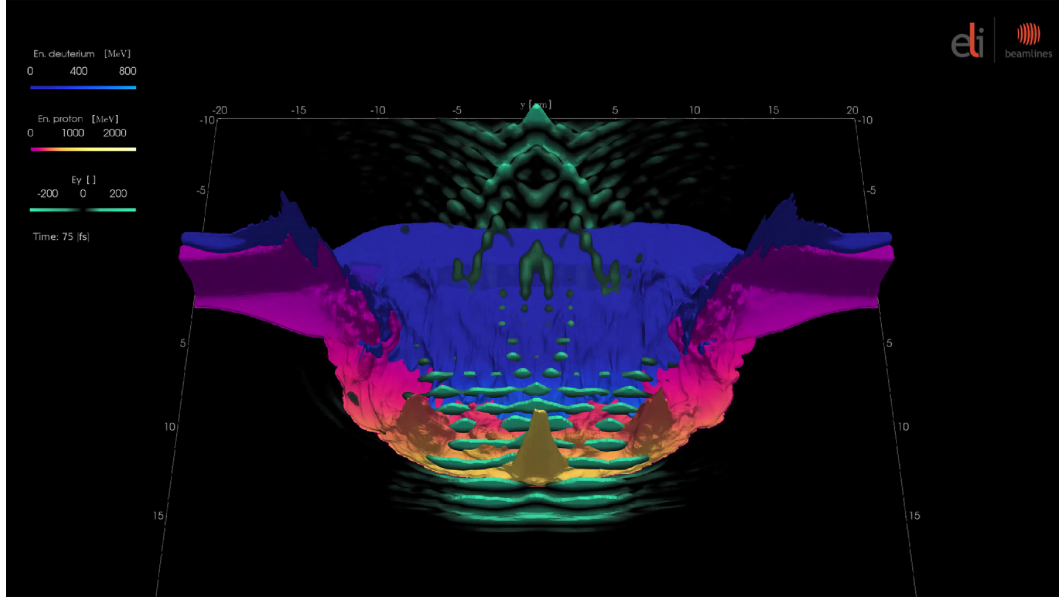


**Figure 9:** Interaction of high-intensity laser pulse with double-layer target with modulated interface (heavy-light case). Visualised in ParaView. This is a still image for the supplementary video S1, which is available in the online version of the paper III..

To show the advantages of such interface corrugation, the target was compared with other simulations of similar configurations – namely, double-layer target without interface corrugation and pure hydrogen single layer target. We demonstrated that bunch structure can be seen in proton energy spectra and density distribution only in the cases with the interface corrugation.

The requirement of a steep-front laser pulse was demonstrated by comparison of our results with a simulation using a full-front laser pulse. In that case the target was disrupted by short-wavelength instabilities [73; 148; 149] driven by a gradually rising beginning of the laser pulse, resulting in lower maximal reached energy and significant reduction of peaks in the proton energy spectrum.

We also thoroughly investigated the influence of different laser polarizations and corrugation wavelengths. The instability leading to the bunch generation developed in both linear polarizations in 2D. However, the central bunch was significantly smaller in the "p" polarization case. This was ascribed to artificially greater electron heating in the simulation plane when using the "p" polarization, while the "s" polarization provides more isochoric heating into all 3 spatial directions. In the case of the circular polarization the instability was

mitigated and the ion bunch was not generated. The laser pulse is confined by the bubble shaped foil and the radiation pressure is properly acting on the whole area of the laser focal spot. The optimal corrugation wavelength for low energy spread is shown to be around the half of the size of the laser focal spot. For substantially smaller corrugation wavelength, more bunches of similar low density are actively developed and for substantially larger one, the enfolding field is too broad and the central bunch spreads.

In addition to Ref. III., the obtained results were also included in conference paper [150], revisited in the review paper I. and is included as a book chapter in Ref. [151]. The results were presented by the author at conferences 46th EPS Conference on Plasma Physics, 2019, Milano, Italy; SPIE Optics&Optoelectronics, 2019, Prague Czech Republic; High-Field Laser Plasma Interaction EPS DPP satellite workshop, 2019, Milano, Italy; Eleventh International Conference of Inertial Fusion Sciences and Applications, 2019, Osaka, Japan; 3rd Users' Conference of IT4Innovations, 2019, Ostrava, Czech Republic; 4th Users' Conference of IT4Innovations, 2020, Ostrava, Czech Republic (online).

The author wrote the bulk of the manuscript text, carried out the simulations included, analyzed the results and served the role of the corresponding author.

## 4.4 Paper 4: Relativistic plasma aperture for laser intensity enhancement

**Reference:**

M. Jirka, O. Klimo, and M. Matys (2021) Relativistic plasma aperture for laser intensity enhancement. *Physical Review Research* **3**, 033175.
Attached as Appendix C.4

The laser pulse parameters can be improved on the target side by the addition of a thin solid density foil in front of the target. This approach provides an on-site pulse modification without the need to change the setup of the laser system. The relativistic laser-plasma interaction provides an onset of relativistic transparency in the interaction of overdense ultra-thin foils [152], affecting the temporal envelope of the laser pulse (and its prepulse) [43; 85]. The interaction with ultra-intense laser pulse results in generation of a relativistic plasma aperture and diffraction of the laser beam [89; 90].

In this paper, we investigated the interaction of a PW-class laser pulse relevant to laser systems like ELI Beamlines [49] with ultra-thin aluminum and silicon nitride foils using 2D and 3D particle-in-cell simulations and analytical model. We have shown that the laser pulse diffraction on the generated aperture leads to its local constructive interference with generated high harmonics, resulting in local intensity increase. We provided theoretical estimates for the maximal field strength and its spatial location as a function of laser pulse and target parameters, for both laser linear polarizations in 2D: "p" (laser electric field is oscillating in the plane of incidence) and "s" (laser electric field is oscillating perpendicularly to the plane of incidence).

The 2D PIC simulations showed the fundamental difference, where for the "s" polarization the electrons from the target are driven toward the laser axis, creating two separated relativistic plasma apertures around it. Therefore the transmitted laser field has a two-lobe structure, resulting in an interference of two transmitted beams, later creating a symmetric field distribution. On the contrary, for the "p" polarization the aperture is firstly created at the laser axis and high-density electron bunches are in turns driven from the opposite aperture edges towards the laser axis [153]. This results in an asymmetric field diffraction

pattern with generated high harmonics propagating at angle towards the laser axis. The estimation of the focal distance observed in the PIC simulations fits well to the theoretical prediction of our model for both "s" and "p" polarizations. The focal distance becomes shorter with increasing target thickness, as predicted by the theory.

The maximal achieved intensity gradually grows with target thickness till reaching the relativistically corrected skin depth (14), where it is saturated as predicted by the theory. The use of thicker targets results in more pronounced absorption of the laser energy into the target (and reflection from it), reducing the maximal achieved intensity in the simulations. This effect is stronger in the "s" polarization, as the energy transmitted through the foil is substantially reduced compared to the "p" polarization.

In the next step we performed a computationally demanding 3D simulation using a silicon nitride foil. The characteristic structures of the diffracted laser field in a plane perpendicular or parallel to the polarization axis (corresponding to the "s" and "p" polarizations in 2D) were also presented in the 3D simulation. The final dimensionless field amplitude can be roughly estimated as the summation of the $a_0^s$ and $a_0^p$ predicted from the "s" and "p" 2D cases, as these two processes can happen independently and simultaneously in 3D and these structures efficiently intersects each other in the 3D simulations. That yields the intensity amplification by a factor $\left[(a_0^s + a_0^p)/a_0\right]^2$, using the initial dimensionless field amplitude $a_0$. In our case the local maximal intensity were amplified by the factor of 7.1 in the 3D simulation, which fits well to the theoretical prediction of factor 7.0. The local intensity increase is shown in Fig. 10.
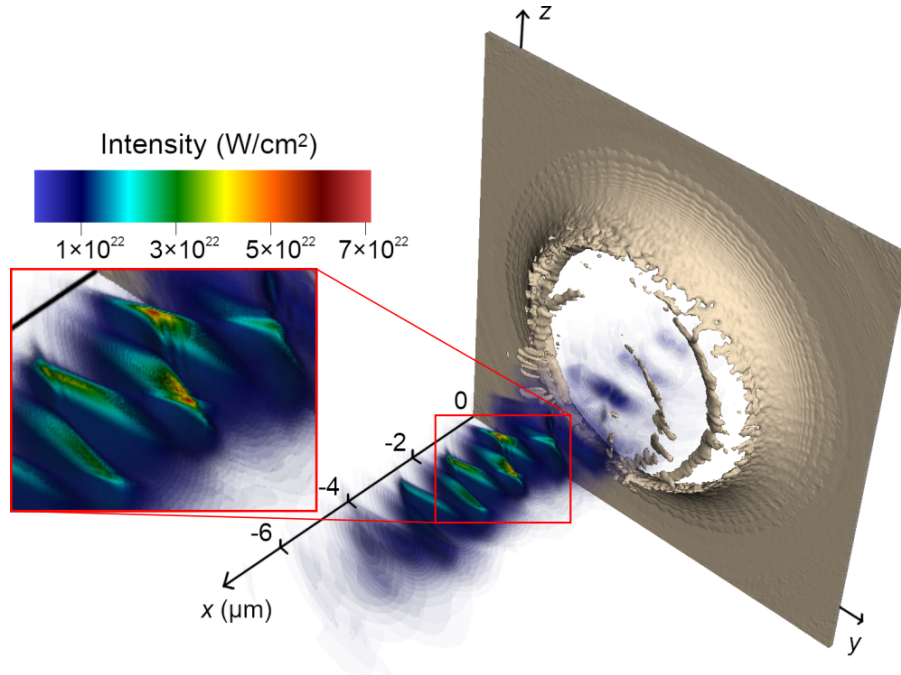


**Figure 10:** The use of the plasma shutter for the local intensity increase in the 3D simulation. Source: paper IV., with highlighting the intensity profile, reused in paper I.

In addition to Ref. IV., the obtained results were revisited in the review paper I., and the continuation of this research, done in combination with hydrodynamic simulations, was

included in conference paper [154]. Part of the results were presented by the author at conferences: 63rd Annual Meeting of the APS Division of Plasma Physics, 2021, Pittsburgh, USA (online); ELI Beamlines User Conference, 2021, Dolní Břežany, Czech Republic.

The author collaborated with his colleagues on the preparation of the manuscript, checked the theoretical model and carried out the 3D simulation and analyzed the intensity increase. The author also helped with the revised version of the manuscript (including response to referees) and with the final corrections of the paper.

## 4.5   Paper 5: Design of plasma shutters for improved heavy ion acceleration by ultra-intense laser pulses

**Reference:**

M. Matys, S. V. Bulanov, M. Kucharik, M. Jirka, J. Nikl, M. Kecova, J. Proska, J. Psikal, G. Korn and O. Klimo (2022). Design of plasma shutters for improved heavy ion acceleration by ultra-intense laser pulses. *New Journal of Physics* **24**, 113046.
Attached as Appendix C.5

In the context of ion acceleration, the plasma shutter is usually a thin solid foil which is attached to the front surface of the target with a gap between them [43; 85–87]. The laser pulse and its prepulse need to burn through this over-dense obstacle before reaching the main target. The shutters were already used in the laser-driven ion acceleration experiments for mitigation of the laser prepulse [86; 87]. They caused the target (which would be otherwise significantly pre-expanded by the prepulse) to remain opaque for the high-intensity part of the laser pulse, improving the subsequent ion acceleration. We continued in this research, focusing not only on the prepulse but also on the shaping of the main pulse itself. As we have shown in the previous paper (Ref IV.) the interaction of a high-intensity laser pulse with ultra-thin foil results in local intensity increase of the transmitted laser pulse. Moreover, a steep front is generated at the beginning of the pulse [43; 87], which stabilizes the laser-target interaction and mitigates the development of the transverse short-wavelength instability as shown in Ref. III. However, a substantial part of the laser pulse energy is inherently lost via the interaction with the overdense plasma shutter (e.g., about 50 % of the laser pulse energy was lost in Ref. IV. for the intensity increase by the factor 7). Therefore, the advantages of the pulse profile modifications need to overcome the laser pulse energy loss for efficient ion acceleration.

In this paper, we investigated the interaction of a PW-class laser pulse relevant to laser systems like ELI Beamlines [49] with ultra-thin silicon nitride plasma shutter and silver targets using 2D and 3D particle-in-cell simulations and also their combination with output from hydrodynamic simulations.

Firstly, we thoroughly investigated the laser pulse interaction with the shutter itself. The transmitted laser pulse gains a steep front and becomes shorter compared to the original pulse, e.g., by 5 laser periods (about 26% of the original pulse) in our reference 3D case. We investigated the effect of varying shutter thickness in 2D and 3D PIC simulations focusing on both the achieved maximal intensity and amount of the transmitted laser pulse energy. We also compared the cycle averaged maximal dimensionless amplitude of the laser field $a_0$ and the focus position with the theoretical model from Ref. IV. As predicted by the theory, the $a_0$ is rising with the thickness and the focal length is decreasing till the thickness around the relativistic skin depth, where the values saturates and starts slowly decreasing. The theoretical model fits well also for the 3D simulations, rising with the thicknesses from 20 nm

to 30 nm. The saturation effect is not observed for thicker shutter and the maximal reached intensity drops to the value of the 20 nm case. This behavior was ascribed to the fact that the 3D case is a combination of "s" and "p" linear polarization, where the effects in the "s" part significantly reduces the energy transmission through the thicker targets as discussed in the previous section. Even though the maximal intensity was increased almost by the factor of 11 in our 3D simulations for the 30 nm case, the amount of transmitted energy dropped from about 50% (in the 20 nm case) to 28%.

Therefore, in the next step we performed a parametric study of ion acceleration from the silver target with and without the shutter in 2D, investigating the influence of shutter and target thicknesses and different distance between them. The dependence on the shutter thickness showed an interesting range between 15 nm and 30 nm, where the maximal ion energy is only slowly decreasing with the shutter thickness for the optimal target thickness of 20 nm. The maximal energy was also significantly higher compared to the simulation without the shutter in the whole range. From this discussion we chose the parameters for the reference 3D simulations using 20 nm silver target and 20 nm shutter, which could be reasonably represented in the 3D simulations having slightly larger cell size due to computational constraints.

For our 3D simulations we compared the laser pulse interaction with the silver target with and without the plasma shutter. The use of the plasma shutter resulted into increase of maximal silver ion energy by 35 %, increase of the total number of high-energy ions in the second half of the energy spectra and into development of a narrow beam-like structure of accelerated ions in the plane perpendicular to the laser polarization (see Fig. 11), significantly reducing the beam divergence.
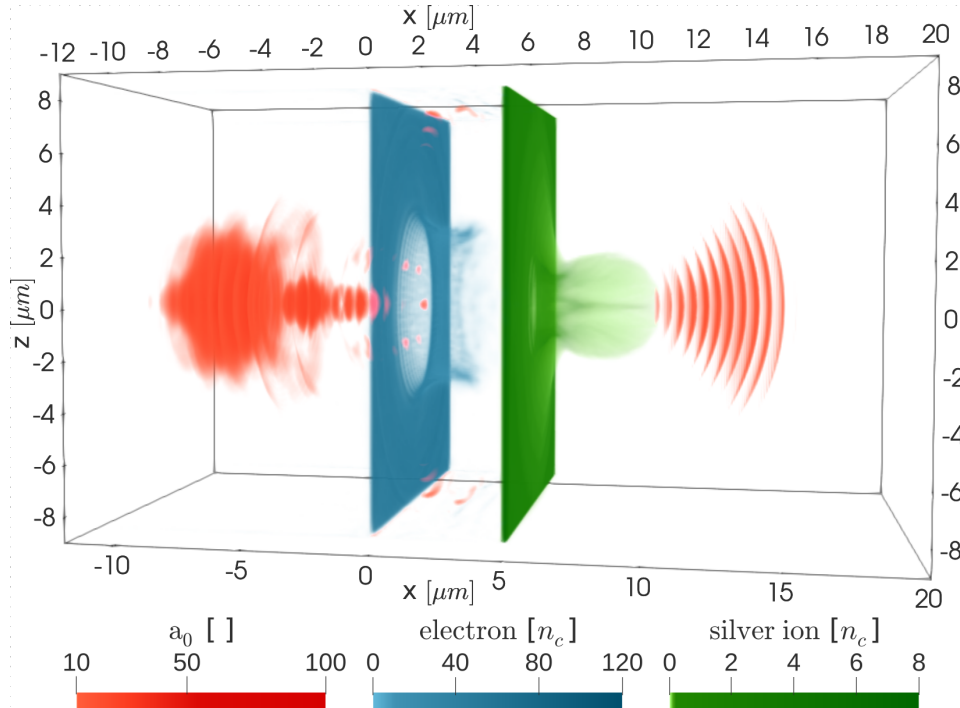


**Figure 11:** Volumetric visualization of the 3D simulation of the plasma shutter (electron density, blue scale), silver target (silver ion density, green scale) and laser pulse ($a_0$, red scale) from paper V.

The effects were ascribed to the generation of the steep-rising front and the intensity increase of the laser pulse transmitted through the plasma shutter. In this configuration, the high intensity part of the laser pulse can interact with a still mostly unperturbed target, resulting in generation of high-density electron bunches. These bunches are responsible for generation of strong electric and magnetic fields inside the target, which in turn affects the electron and ion dynamics. These fields have significantly higher influence in the plane perpendicular to the laser polarization, as the other plane is dominated by the laser pulse itself. The structure of these fields correspond to the structure of the electron bunches, providing conditions to focus ions towards the laser axis.

On the contrary, the target interaction with the original pulse (without the shutter) results in its pre-expansion by the relatively long low-intensity part of the pulse. Therefore the density of electron bunches is significantly reduced and the ion distribution is spread outside the laser axis. Moreover, the transverse short-wavelength instability in the transverse profile of ion density is developed, due to the long low-intensity interaction. This instability is otherwise mitigated by the use of the shutter and the generation of the steep-rising laser front, which corresponds to observations in Ref. III.

The application of the shutter also improved the divergence in the plane of the laser polarization, even though the reduction is significantly lower than in the perpendicular plane. This can be also ascribed to the steep front of the laser pulse. To demonstrate it, a several 2D simulations approximating the generated laser pulse with different steepness of the front were performed. It was shown that till some limit the increase of the front steepness improves the divergence of high energy ions and also their number in the region around the central axis.

Several ion acceleration mechanisms takes place during the laser-target interaction. We have discussed their influence in different interaction phases in 3D using the time evolution of maximal ion energy and electron and ion density profiles (some of them are further discussed in the appendix of the paper). In the first phase, the interaction is dominated by the radiation pressure acceleration mechanism till the time when the target starts becoming partially (relativistically) transparent to the incoming laser pulse. The RPA still significantly contributes to the ion acceleration for some time afterwards. However, its influence is gradually diminishing, as the density of the electron layer is decreasing and other mechanisms like the hybrid RPA-TNSA [45] and Directed coulomb explosion [42] then take over the interaction. However, the rate of increase of the maximal ion energy is then noticeably lower.

We also investigated the effect of circular polarization in the 3D configuration, as it is often proposed for the RPA dominated regimes to increase the maximal ion energy and reduce divergence of the ion beam [34; 68; 118; 140]. For our simulations, we obtained similar ion energy spectra as in the simulations with linear polarization. The increase of the maximal ion energy is slightly higher than in the linear polarization case (about 44% vs. 35%). On the contrary the ion density and field distribution significantly differs for the circular polarization and the effect of the divergence improvement is strongly reduced. The interaction of circularly polarized laser pulse with the ultra-thin shutter also results in generation of a spiral like diffraction structure of the transmitted laser pulse. The mechanism of its development and effects on ion acceleration is currently being investigated by our group.

In the last part of the paper, we proposed the use of a double shutter scenario, where the extra shutter would be used for prepulse filtering. We collaborated with Milan Kuchařík and Jan Nikl from the Czech Technical University in Prague, who performed a 2D hydrodynamic simulations of the prepulse interaction with a thin shutter. The results of these simulations in a form of a density profile of the first shutter expanded after 125 ps of interaction were then imported as initial configuration of a 2D PIC simulations with added the second non-

expanded shutter and the silver foil (each of them separated by 5 μm). We have demonstrated that the double shutter scenario also results in higher maximal ion energy and number of accelerated high-energy ions (with energies above 80 MeV per nucleon, i.e., roughly half of the maximal energy) compared to the case without any shutter. The value is slightly lower than in the case of the idealized single shutter without assuming any prepulse. Nevertheless, most of the ion energy spectra are similar, with only the tail of the spectra affected. One also needs to keep in mind, that the prepulse needs to be assumed in the both cases for a direct comparison. Therefore, we prepared a simulation with the silver target without any shutter but with a prepulse. As expected the maximal silver ion energy decreases with the length of the prepulse, as the target gradually turns from the optimized 20 nm thick target to a few micron thick one with lower density. The direct comparison of the double shutter scenario with the case of no shutter assuming the same prepulse of 125 ps results in the increase of the maximal ion energy by the factor of 2.6 in the 2D simulations. The first shutter was able to withstand the prepulse of this duration in our hydrodynamic simulations, note that a thicker shutter can be used to filter out longer prepulses, if needed. Here we used the same thickness of both shutters for the sake of brevity. The treatment of the ns prepulse by other techniques like (double) plasma mirrors [88] was assumed. A prototype of the double shutter using 30 nm thick silicon nitride membranes separated by 5.88 μm silicon beads was prepared at the Czech Technical University in Prague by our coauthor Jan Proška. We also described the design of the whole double shutter – target scenario with a silver target.

In addition to Ref. V., the obtained results were also included in conference papers [155–157] and revisited in the review paper I.. The results were presented by the author at conferences: 63rd Annual Meeting of the APS Division of Plasma Physics, 2021, Pittsburgh, USA (online); 47th EPS Plasma Physics conference, 2021, Sitges, Spain (online); 48th EPS Plasma Physics conference, 2022, Maastricht, Netherlands (online); SPIE Optics&Optoelectronics, 2021 Prague Czech Republic (online); Flash Radiotherapy & Particle Therapy Conference, 2022, Barcelona, Spain (online); OPTO2021 Symposium on Photon and Beam Science, 2021, Osaka, Japan (online); OPTO2022 Symposium on Photon and Beam Science, 2022, Osaka, Japan (online); 5th Users' Conference of IT4Innovations, 2021, Ostrava, Czech Republic (online); ELI Beamlines User Conference, 2021, Dolní Břežany, Czech Republic. The preliminary results gradually converging to the final results were presented by the author at conferences: 45th European Physical Society Conference, 2018, Prague, Czech Republic; The 35th European Conference on Laser Interaction with Matter, 2018, Rethymno, Greece; and included in the conference paper [158].

The author wrote the bulk of the manuscript text, carried out the PIC simulations included (hydrodynamic simulations were performed by other coauthors), analyzed the results and served the role of the corresponding author.

# Chapter 5

# Conclusion

## 5.1  Summary

The goal of this dissertation was to investigate the novel schemes of ion acceleration using 2D and 3D particle-in-cell simulations of high-intensity laser interaction with solid targets, produced by the EPOCH code. We investigated three different schemes (1) increasing laser pulse intensity, while using low-density (cryogenic) hydrogen target to employ acceleration mechanisms with more efficient energy scaling than the Target Normal Sheath Acceleration (TNSA), mainly the Radiation Pressure Acceleration (RPA); (2) The use of special target geometry and composition, namely double-layer target with interface corrugation; (3) Shaping of the laser pulse profile by employing a plasma shutter (an ultra-thin foil placed in front of the target). We demonstrated improvement of ion beam parameters like maximal ion energy and/or reduction of the beam divergence in all of these cases.

In the first topic, we showed that the RPA mechanism begins to dominate over TNSA (in sense of higher reached ion energies and number of high-energy ions) with increasing laser intensity for the assumed laser-target parameters (cryogenic hydrogen target and multi-PW class laser). This behavior was shown in both 2D and 3D simulations. The hole boring version of RPA was demonstrated to be a robust mechanism with little dependency on laser polarization or development of a reasonably long preplasma.

In the second topic, we achieved significant reduction of the energy spread and divergence of the generated high-energy ion beam using double-layer target with interface corrugation and high-intensity laser pulse with a steep-rising front. This conditions result in development of a relativistic instability, fracturing target into high density ion bunches, located at the positions depending on the initial target geometry. The central bunch is then accelerated as a whole compact structure enfolded by the laser field, preventing from the perpendicular particle expansion. The steep-front of the laser pulse mitigates the development of a transverse short-wavelength instability (shorter than the interface corrugation), disrupting the target in an uncontrolled way otherwise.

In the last topic we investigated the use of an ultra-thin solid foil (plasma shutter) for shaping of the laser pulse. Firstly we demonstrated the local intensity increase and steep-rising front generation of the laser pulse burning through such a shutter. Subsequently we applied this laser pulse shaping for ion acceleration from silver target located behind the shutter. This approach results in significant increase of maximal silver ion energy using both linearly and circularly polarized laser pulse. In the former case, the divergence of the generated ion bunch is also significantly reduced in the plane perpendicular to the laser polarization. In

the later case, the transmitted laser pulse develops a spiral-like structure, its effect on ion acceleration will be further investigated in the future work.

We also studied practical application of such ultra-thin foils, namely use of a double-shutter scenario, where the first shutter filters out the laser prepulse, while the desired shaping of the main part of the pulse occurs by the interaction with the second shutter. We demonstrated the increase of maximal ion energy also in this case using combination of hydrodynamic and 2D PIC simulations. A prototype of this double shutter was prepared at the Czech Technical University in Prague and we discussed the design of the whole shutter-target setup.

Our simulation data were visualized in collaboration with the VBL team at ELI Beamlines in a form of interactive web-based Virtual Reality applications (available online [137]) which are being used for popularization of science at ELI Beamlines and at the Czech Technical University in Prague.

## 5.2    Future research and perspectives

We are currently working on the continuation of several topics investigated in this dissertation.

First one is the finishing of a manuscript for impacted journal based on the conference paper [154], describing the intensity increase using the double-shutter scenario, where the first shutter is expanded by the prepulse into a low density preplasma. With the right choice of parameters, the laser pulse can undergo self-focusing when propagating through the remnants of the first shutter and then further increase its intensity by the effects described in Ref. IV.. We already performed new 3D simulations of this interaction, combining PIC and hydrodynamic approach, with promising results.

The second topic is a further investigation of the principle of generation of spiral-like laser pulse, arising from the interaction of circularly polarized laser pulse with ultra-thin shutter showed in Ref. V. and its effect on ion acceleration from the target located behind. We continue our collaboration with professor Kunioki Mima (Institute of Laser Engineering, Osaka University, Japan) on this topic. Abstracts including the results from this topic were accepted for oral presentations for conferences: Laser and Plasma Accelerators Workshop 2023, Lagos Portugal in March 2023; and SPIE Optics + Optoelectronics 2023, Prague Czech Republic in April 2023.

We also would like to optimize our results using double layer targets with initial corrugation for the 3D configuration, collaborating with professor Katsunobu Nishihara (Institute of Laser Engineering, Osaka University, Japan). This is a challenging topic, where the influence of both "s" and "p" part of the linearly polarized laser pulse needs to be considered in fully 3D configuration, together with quantum electrodynamics effects occurring in the interaction with the high-intensity laser pulse. Some preliminary results are shown in the figure 12.
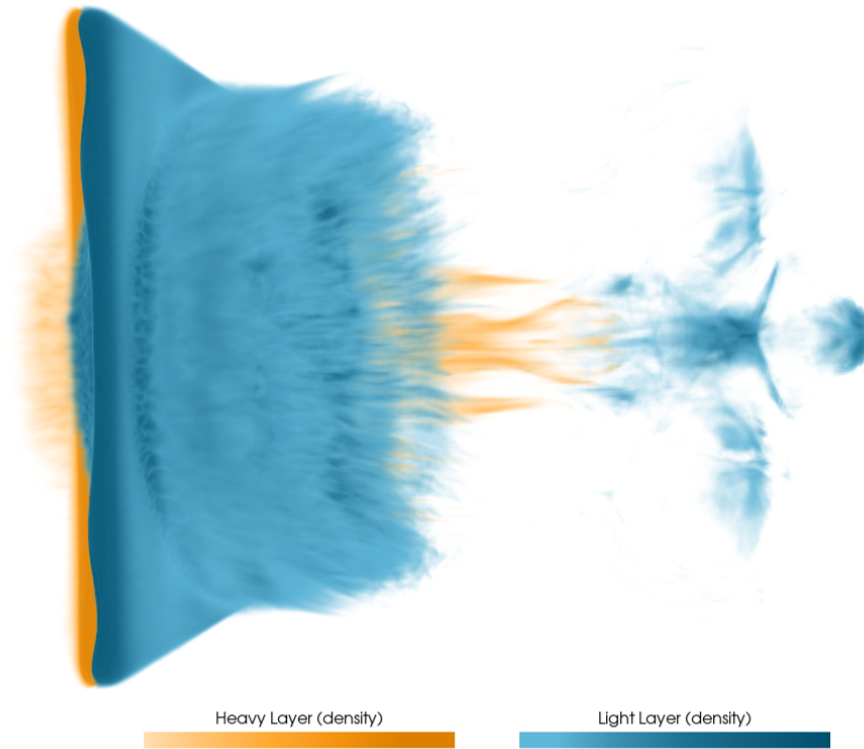
**Figure 12:** Spatial density distributions of the 3D counterpart of simulation from Ref. III. at time $t = 50$ T. The deuterium ion density is represented by the orange scale and proton density by the blue scale.

**Long term prospects** can be subdivided to two directions, which are related to each other in the terms of underlying physics and expected applications: (1) To continue studying the laser-driven ion acceleration and extending my scientific activity to the theory and simulations of various charged particle acceleration and generation of high-energy photons in the regimes closely related to the scientific program of ELI ERIC. (2) To study novel regimes of particle acceleration with ultra-high energy and power. These studies need interpretation of quantum electrodynamics effects to describe laser-matter interaction, which can change currently known scaling of generation of high-energy charged particles and photons.

# Acknowledgments

I would like to express my sincere gratitude to my supervisor Ing. Jan Pšikal, PhD. and to my supervisor specialist Prof. Sergei Bulanov for their guidance, motivation, kind comments, willingness, friendly approach and patience during my PhD. training. I really appreciate that both of them were easy to approach, had open doors for discussions and were always willing to help. I also thank Prof. Bulanov for the opportunity to be part of the HIFI team at ELI Beamlines. I enjoyed the time spent here and the discussions we had.

I also would like to thank to my co-authors Ondřej Klimo, Katsunobu Nishihara, Petr Valenta, Martin Jirka, Jan Nikl, Milan Kuchařík, Jan Proška, Mariana Kecová and Georg Korn for all the hard work done on our publications and for the great time we spent together. Special thanks belong to the VBL team of ELI Beamlines (Mariana Kecová, Pavel Janečka, Jakub Grosz) for all the beautiful visualizations and VR applications they created for us.

At last but not least, I would like to thank to my parents, family, friends and יהוה God for all the support I received during my PhD training, which made finishing this dissertation possible.

# Bibliography

[1] S. V. Bulanov, J. J. Wilkens, T. Z. Esirkepov, G. Korn, G. Kraft, S. D. Kraft, M. Molls, and V. S. Khoroshkov, "Laser ion acceleration for hadron therapy," *Physics-Uspekhi*, vol. 57, no. 12, pp. 1149–1179, 2014. https://doi.org/10.3367/ufne.0184.201412a.1265.

[2] H. Daido, M. Nishiuchi, and A. S. Pirozhkov, "Review of laser-driven ion sources and their applications," *Reports on Progress in Physics*, vol. 75, p. 056401, Apr 2012. https://doi.org/10.1088/0034-4885/75/5/056401.

[3] A. Macchi, M. Borghesi, and M. Passoni, "Ion acceleration by superintense laser-plasma interaction," *Rev. Mod. Phys.*, vol. 85, pp. 751–793, May 2013. https://doi.org/10.1103/RevModPhys.85.751.

[4] M. Passoni, F. M. Arioli, L. Cialfi, D. Dellasega, L. Fedeli, A. Formenti, A. C. Giovannelli, A. Maffini, F. Mirani, A. Pazzaglia, A. Tentori, D. Vavassori, M. Zavelani-Rossi, and V. Russo, "Advanced laser-driven ion sources and their applications in materials and nuclear science," *Plasma Physics and Controlled Fusion*, vol. 62, p. 014022, Dec 2019. https://doi.org/10.1088/1361-6587/ab56c9.

[5] S. V. Bulanov, T. Esirkepov, V. S. Khoroshkov, A. V. Kuznetsov, and F. Pegoraro, "Oncological hadrontherapy with laser ion accelerators," *Physics Letters, Section A: General, Atomic and Solid State Physics*, vol. 299, no. 2-3, pp. 240–247, 2002. https://doi.org/10.1016/S0375-9601(02)00521-2.

[6] T. Tajima, "Prospect for compact medical laser accelerators," *J. Jpn. Soc. Therap. Radiol. Oncol*, vol. 9, no. Suppl. 2), pp. 83–85, 1997.

[7] M. Roth, T. E. Cowan, M. H. Key, S. P. Hatchett, C. Brown, W. Fountain, J. Johnson, D. M. Pennington, R. A. Snavely, S. C. Wilks, K. Yasuike, H. Ruhl, F. Pegoraro, S. V. Bulanov, E. M. Campbell, M. D. Perry, and H. Powell, "Fast ignition by intense laser-accelerated proton beams," *Physical Review Letters*, vol. 86, no. 3, pp. 436–439, 2001. https://doi.org/10.1103/PhysRevLett.86.436.

[8] S. Atzeni, M. Temporal, and J. J. Honrubia, "A first analysis of fast ignition of precompressed ICF fuel by laser-accelerated protons," *Nuclear Fusion*, vol. 42, no. 3, p. L1, 2002. https://doi.org/10.1088/0029-5515/42/3/101.

[9] V. Istokskaia, M. Tosca, L. Giuffrida, J. Psikal, F. Grepl, V. Kantarelou, S. Stancek, S. Di Siena, A. Hadjikyriacou, A. McIlvenny, Y. Levy, J. Huynh, M. Cimrman, P. Pleskunov, D. Nikitin, A. Choukourov, F. Belloni, A. Picciotto, S. Kar, M. Borghesi, A. Lucianetti, T. Mocek, and D. Margarone, "A multi-MeV alpha particle source via proton-boron fusion driven by a 10-GW tabletop laser," *Communications Physics*, vol. 6, p. 27, Feb 2023. https://doi.org/10.1038/s42005-023-01135-x.

[10] M. Nishiuchi, H. Sakaki, T. Z. Esirkepov, K. Nishio, T. A. Pikuz, A. Y. Faenov, I. Y. Skobelev, R. Orlandi, H. Sako, A. S. Pirozhkov, K. Matsukawa, A. Sagisaka, K. Ogura, M. Kanasaki, H. Kiriyama, Y. Fukuda, H. Koura, M. Kando, T. Yamauchi, Y. Watanabe, S. V. Bulanov, K. Kondo, K. Imai, and S. Nagamiya, "Acceleration of highly charged GeV Fe ions from a low-Z substrate by intense femtosecond laser," *Physics of Plasmas*, vol. 22, no. 033107, p. 033107, 2015. https://doi.org/10.1063/1.4913434.

[11] M. Nishiuchi, H. Sakaki, T. Z. Esirkepov, K. Nishio, T. A. Pikuz, A. Y. Faenov, I. Y. Skobelev, R. Orlandi, A. S. Pirozhkov, A. Sagisaka, K. Ogura, M. Kanasaki, H. Kiriyama, Y. Fukuda, H. Koura, M. Kando, T. Yamauchi, Y. Watanabe, S. V. Bulanov, K. Kondo, K. Imai, and S. Nagamiya, "Towards a novel laser-driven method of exotic nuclei extraction-acceleration for fundamental physics and technology," *Plasma Physics Reports*, vol. 42, pp. 327–337, Apr 2016. https://doi.org/10.1134/s1063780x1604005x.

[12] P. Braun-Munzinger, V. Koch, T. Schäfer, and J. Stachel, "Properties of hot and dense matter from relativistic heavy ion collisions," *Physics Reports*, vol. 621, pp. 76–126, 2016. https://doi.org/https://doi.org/10.1016/j.physrep.2015.12.003.

[13] D. Habs, P. G. Thirolf, M. Gross, K. Allinger, J. Bin, A. Henig, D. Kiefer, W. Ma, and J. Schreiber, "Introducing the fission–fusion reaction process: using a laser-accelerated th beam to produce neutron-rich nuclei towards the n=126 waiting point of the r-process," *Applied Physics B*, vol. 103, p. 471–484, Oct 2010. https://doi.org/10.1007/s00340-010-4261-x.

[14] F. H. Lindner, E. G. Fitzpatrick, D. Haffa, L. Ponnath, A.-K. Schmidt, M. Speicher, B. Zielbauer, J. Schreiber, and P. G. Thirolf, "Charge-state resolved laser acceleration of gold ions to beyond 7 mev/u," *Scientific Reports*, vol. 12, p. 4784, Mar 2022. https://doi.org/10.1038/s41598-022-08556-8.

[15] S. Fritzler, V. Malka, G. Grillon, J. P. Rousseau, F. Burgy, E. Lefebvre, E. d'Humières, P. McKenna, and K. W. D. Ledingham, "Proton beams generated with high-intensity lasers: Applications to medical isotope production," *Applied Physics Letters*, vol. 83, no. 15, p. 3039–3041, 2003. https://doi.org/10.1063/1.1616661.

[16] L. Romagnani, J. Fuchs, M. Borghesi, P. Antici, P. Audebert, F. Ceccherini, T. Cowan, T. Grismayer, S. Kar, A. Macchi, P. Mora, G. Pretzler, A. Schiavi, T. Toncian, and O. Willi, "Dynamics of electric fields driving the laser acceleration of multi-mev protons," *Phys. Rev. Lett.*, vol. 95, p. 195001, Oct 2005. https://doi.org/10.1103/PhysRevLett.95.195001.

[17] M. Barberio, S. Veltri, M. Sciscio, and P. Antici, "Laser-accelerated proton beams as diagnostics for cultural heritage," *Scientific Reports*, vol. 7, Mar 2017. https://doi.org/10.1038/srep40415.

[18] F. Mirani, A. Maffini, F. Casamichiela, A. Pazzaglia, A. Formenti, D. Dellasega, V. Russo, D. Vavassori, D. Bortot, M. Huault, G. Zeraouli, V. Ospina, S. Malko, J. I. Apiñaniz, J. A. Pérez-Hernández, D. De Luis, G. Gatti, L. Volpe, A. Pola, and M. Passoni, "Integrated quantitative pixe analysis and edx spectroscopy using a laser-driven particle source," *Science Advances*, vol. 7, Jan 2021. https://doi.org/10.1126/sciadv.abc8660.

[19] P. A. Norreys, A. P. Fews, F. N. Beg, A. R. Bell, A. E. Dangor, P. Lee, M. B. Nelson, H. Schmidt, M. Tatarakis, and M. D. Cable, "Neutron production from picosecond laser irradiation of deuterated targets at intensities of," *Plasma Physics and Controlled Fusion*, vol. 40, p. 175–182, Feb 1998. https://doi.org/10.1088/0741-3335/40/2/001.

[20] A. Yogo, Z. Lan, Y. Arikawa, Y. Abe, S. R. Mirfayzi, T. Wei, T. Mori, D. Golovin, T. Hayakawa, N. Iwata, S. Fujioka, M. Nakai, Y. Sentoku, K. Mima, M. Murakami, M. Koizumi, F. Ito, J. Lee, T. Takahashi, K. Hironaka, S. Kar, H. Nishimura, and R. Kodama, "Laser-driven neutron generation realizing single-shot resonance spectroscopy," *Phys. Rev. X*, vol. 13, p. 011011, Jan 2023. https://doi.org/10.1103/PhysRevX.13.011011.

[21] V. I. Veksler, "The principle of coherent acceleration of charged particles," *The Soviet Journal of Atomic Energy*, vol. 2, p. 525–528, Sep 1957. https://doi.org/10.1007/BF01491001.

[22] B. M. Bolotovskii and A. N. Lebedev, "Academician v i veksler," *Physics-Uspekhi*, vol. 50, p. 847, aug 2007. https://doi.org/10.1070/PU2007v050n08ABEH006356.

[23] T. H. Maiman, "Optical and microwave-optical experiments in ruby," *Physical Review Letters*, vol. 4, no. 11, p. 564–566, 1960. https://doi.org/10.1103/physrevlett.4.564.

[24] F. J. McClung and R. W. Hellwarth, "Giant optical pulsations from ruby," *Journal of Applied Physics*, vol. 33, no. 3, pp. 828–829, 1962. https://doi.org/10.1063/1.1777174.

[25] H. W. Mocker and R. J. Collins, "Mode competition and self-locking effects in a Q-switched ruby laser," *Applied Physics Letters*, vol. 7, no. 10, pp. 270–273, 1965. https://doi.org/10.1063/1.1754253.

[26] W. R. Hook, R. H. Dishington, and R. P. Hilberg, "Laser cavity dumping using time variable reflection," *Applied Physics Letters*, vol. 9, no. 3, pp. 125–127, 1966. https://doi.org/10.1063/1.1754673.

[27] D. Strickland and G. Mourou, "Compression of amplified chirped optical pulses," *Optics Communications*, vol. 56, no. 3, pp. 219–221, 1985. https://doi.org/10.1016/0030-4018(85)90120-8.

[28] S. C. Wilks, A. B. Langdon, T. E. Cowan, M. Roth, M. Singh, S. Hatchett, M. H. Key, D. Pennington, A. MacKinnon, and R. A. Snavely, "Energetic proton generation in ultra-intense laser–solid interactions," *Physics of Plasmas*, vol. 8, no. 2, pp. 542–549, 2001. https://doi.org/10.1063/1.1333697.

[29] R. A. Snavely, M. H. Key, S. P. Hatchett, T. E. Cowan, M. Roth, T. W. Phillips, M. A. Stoyer, E. A. Henry, T. C. Sangster, M. S. Singh, S. C. Wilks, A. MacKinnon, A. Offenberger, D. M. Pennington, K. Yasuike, A. B. Langdon, B. F. Lasinski, J. Johnson, M. D. Perry, and E. M. Campbell, "Intense high-energy proton beams from petawatt-laser irradiation of solids," *Phys. Rev. Lett.*, vol. 85, pp. 2945–2948, Oct 2000. https://doi.org/10.1103/PhysRevLett.85.2945.

[30] S. A. Gaillard, T. Kluge, K. A. Flippo, M. Bussmann, B. Gall, T. Lockard, M. Geissel, D. T. Offermann, M. Schollmeier, Y. Sentoku, and T. E. Cowan, "Increased laser-accelerated proton energies via direct laser-light-pressure acceleration of electrons in microcone targets," *Physics of Plasmas*, vol. 18, no. 5, p. 056710, 2011. https://doi.org/10.1063/1.3575624.

[31] F. Wagner, C. Brabetz, O. Deppert, M. Roth, T. Stöhlker, A. Tauschwitz, A. Tebartz, B. Zielbauer, and V. Bagnoud, "Accelerating ions with high-energy short laser pulses from submicrometer thick targets," *High Power Laser Science and Engineering*, vol. 4, no. e45, 2016. https://doi.org/10.1017/hpl.2016.44.

[32] T. Esirkepov, M. Borghesi, S. V. Bulanov, G. Mourou, and T. Tajima, "Highly efficient relativistic-ion generation in the laser-piston regime," *Physical Review Letters*, vol. 92, apr 2004. https://doi.org/10.1103/PhysRevLett.92.175003.

[33] S. S. Bulanov, E. Esarey, C. B. Schroeder, S. V. Bulanov, T. Z. Esirkepov, M. Kando, F. Pegoraro, and W. P. Leemans, "Radiation pressure acceleration: The factors limiting maximum attainable ion energy," *Physics of Plasmas*, vol. 23, no. 056703, p. ., 2016. https://doi.org/10.1063/1.4946025.

[34] A. Henig, S. Steinke, M. Schnürer, T. Sokollik, R. Hörlein, D. Kiefer, D. Jung, J. Schreiber, B. M. Hegelich, X. Q. Yan, J. Meyer-ter Vehn, T. Tajima, P. V. Nickles, W. Sandner, and D. Habs, "Radiation-pressure acceleration of ion beams driven by circularly polarized laser pulses," *Phys. Rev. Lett.*, vol. 103, p. 245003, Dec 2009. https://doi.org/10.1103/PhysRevLett.103.245003.

[35] S. Kar, M. Borghesi, S. V. Bulanov, M. H. Key, T. V. Liseykina, A. Macchi, A. J. Mackinnon, P. K. Patel, L. Romagnani, A. Schiavi, and O. Willi, "Plasma jets driven by ultraintense-laser interaction with thin foils," *Phys. Rev. Lett.*, vol. 100, p. 225004, Jun 2008. https://doi.org/10.1103/PhysRevLett.100.225004.

[36] C. Scullion, D. Doria, L. Romagnani, A. Sgattoni, K. Naughton, D. R. Symes, P. McKenna, A. Macchi, M. Zepf, S. Kar, and M. Borghesi, "Polarization dependence of bulk ion acceleration from ultrathin foils irradiated by high-intensity ultrashort laser pulses," *Phys. Rev. Lett.*, vol. 119, p. 054801, Aug 2017. https://doi.org/10.1103/PhysRevLett.119.054801.

[37] I. J. Kim, K. H. Pae, I. W. Choi, C.-L. Lee, H. T. Kim, H. Singhal, J. H. Sung, S. K. Lee, H. W. Lee, P. V. Nickles, T. M. Jeong, C. M. Kim, and C. H. Nam, "Radiation pressure acceleration of protons to 93 mev with circularly polarized petawatt laser pulses," *Physics of Plasmas*, vol. 23, no. 7, p. 070701, 2016. https://doi.org/10.1063/1.4958654.

[38] S. S. Bulanov, E. Esarey, C. B. Schroeder, S. V. Bulanov, T. Z. Esirkepov, M. Kando, F. Pegoraro, and W. P. Leemans, "Radiation pressure acceleration: The factors limiting maximum attainable ion energy," *Physics of Plasmas*, vol. 23, no. 5, p. 056703, 2016. https://doi.org/10.1063/1.4946025.

[39] D. Margarone, A. Velyhan, J. Dostal, J. Ullschmied, J. P. Perin, D. Chatain, S. Garcia, P. Bonnay, T. Pisarczyk, R. Dudzak, M. Rosinski, J. Krasa, L. Giuffrida, J. Prokupek, V. Scuderi, J. Psikal, M. Kucharik, M. De Marco, J. Cikhardt, E. Krousky, Z. Kalinowska, T. Chodukowski, G. A. Cirrone, and G. Korn, "Proton acceleration driven by a nanosecond laser from a cryogenic thin solid-hydrogen ribbon," *Physical Review X*, vol. 6, no. 4, p. 041030, 2016. https://doi.org/10.1103/PhysRevX.6.041030.

[40] J. Psikal and M. Matys, "Dominance of hole-boring radiation pressure acceleration regime with thin ribbon of ionized solid hydrogen," *Plasma Physics and Controlled Fusion*, vol. 60, no. 4, p. 044003, 2018. https://doi.org/10.1088/1361-6587/aaa7fa.

[41] A. McIlvenny, D. Doria, L. Romagnani, H. Ahmed, N. Booth, E. J. Ditter, O. C. Ettlinger, G. S. Hicks, P. Martin, G. G. Scott, S. D. R. Williamson, A. Macchi, P. McKenna, Z. Najmudin, D. Neely, S. Kar, and M. Borghesi, "Selective ion acceleration by intense radiation pressure," *Phys. Rev. Lett.*, vol. 127, p. 194801, Nov 2021. https://doi.org/10.1103/PhysRevLett.127.194801.

[42] S. S. Bulanov, A. Brantov, V. Y. Bychenkov, V. Chvykov, G. Kalinchenko, T. Matsuoka, P. Rousseau, S. Reed, V. Yanovsky, D. W. Litzenberg, K. Krushelnick, and A. Maksimchuk, "Accelerating monoenergetic protons from ultrathin foils by flat-top laser pulses in the directed-coulomb-explosion regime," *Physical Review E*, vol. 78, no. 2, p. 026412, 2008. https://doi.org/10.1103/physreve.78.026412.

[43] V. A. Vshivkov, N. M. Naumova, F. Pegoraro, and S. V. Bulanov, "Nonlinear electrodynamics of the interaction of ultra-intense laser pulses with a thin foil," *Physics of Plasmas*, vol. 5, no. 7, pp. 2727–2741, 1998. https://doi.org/10.1063/1.872961.

[44] B. Qiao, S. Kar, M. Geissler, P. Gibbon, M. Zepf, and M. Borghesi, "Dominance of radiation pressure in ion acceleration with linearly polarized pulses at intensities of 10 21 w cm -2," *Physical Review Letters*, vol. 108, no. 11, 2012. https://doi.org/10.1103/physrevlett.108.115002.

[45] A. Higginson, R. J. Gray, M. King, R. J. Dance, S. D. Williamson, N. M. Butler, R. Wilson, R. Capdessus, C. Armstrong, J. S. Green, S. J. Hawkes, P. Martin, W. Q. Wei, S. R. Mirfayzi, X. H. Yuan, S. Kar, M. Borghesi, R. J. Clarke, D. Neely, and P. McKenna, "Near-100 MeV protons via a laser-driven transparency-enhanced hybrid acceleration scheme," *Nature Communications*, vol. 9, p. 724, dec 2018. https://doi.org/10.1038/s41467-018-03063-9.

[46] L. Yin, B. J. Albright, K. J. Bowers, D. Jung, J. C. Fernández, and B. M. Hegelich, "Three-dimensional dynamics of breakout afterburner ion acceleration using high-contrast short-pulse laser and nanoscale targets," *Phys. Rev. Lett.*, vol. 107, p. 045003, Jul 2011. https://doi.org/10.1103/PhysRevLett.107.045003.

[47] J. L. Liu, M. Chen, J. Zheng, Z. M. Sheng, and C. S. Liu, "Three dimensional effects on proton acceleration by intense laser solid target interaction," *Physics of Plasmas*, vol. 20, no. 6, p. 063107, 2013. https://doi.org/10.1063/1.4812458.

[48] S. Weber, S. Bechet, S. Borneis, L. Brabec, M. Bučka, E. Chacon-Golcher, M. Ciappina, M. DeMarco, A. Fajstavr, K. Falk, E.-R. Garcia, J. Grosz, Y.-J. Gu, J.-C. Hernandez, M. Holec, P. Janečka, M. Jantač, M. Jirka, H. Kadlecova, D. Khikhlukha, O. Klimo, G. Korn, D. Kramer, D. Kumar, T. Lastovička, P. Lutoslawski, L. Morejon, V. Olšovcová, M. Rajdl, O. Renner, B. Rus, S. Singh, M. Šmid, M. Sokol, R. Versaci, R. Vrána, M. Vranic, J. Vyskočil, A. Wolf, and Q. Yu, "P3: An installation for high-energy density plasma physics and ultra-high intensity laser–matter interaction at eli-beamlines," *Matter and Radiation at Extremes*, vol. 2, no. 4, pp. 149–176, 2017. https://doi.org/10.1016/j.mre.2017.03.003.

[49] F. P. Condamine, N. Jourdain, J.-C. Hernandez, M. Taylor, H. Bohlin, A. Fajstavr, T. M. Jeong, D. Kumar, T. Laštovička, O. Renner, and S. Weber, "High-repetition rate solid target delivery system for pw-class laser–matter interaction at eli beamlines," *Review of Scientific Instruments*, vol. 92, no. 6, p. 063504, 2021. https://doi.org/10.1063/5.0053281.

[50] N. Jourdain, U. Chaulagain, M. Havlík, D. Kramer, D. Kumar, I. Majerová, V. T. Tikhonchuk, G. Korn, and S. Weber, "The l4n laser beamline of the p3-installation: Towards high-repetition rate high-energy density physics at eli-beamlines," *Matter and Radiation at Extremes*, vol. 6, no. 1, p. 015401, 2021. https://doi.org/10.1063/5.0022120.

[51] N. V. Zamfir, "Nuclear physics with 10 pw laser beams at extreme light infrastructure - nuclear physics (eli-np)," *The European Physical Journal Special Topics*, vol. 223, pp. 1221–1227, MAY 2014. https://doi.org/10.1140/epjst/e2014-02176-0.

[52] K. A. Tanaka, K. M. Spohr, D. L. Balabanski, S. Balascuta, L. Capponi, M. O. Cernaianu, M. Cuciuc, A. Cucoanes, I. Dancus, A. Dhal, B. Diaconescu, D. Doria, P. Ghenuche, D. G. Ghita, S. Kisyov, V. Nastasa, J. F. Ong, F. Rotaru, D. Sangwan, P.-A. Söderström, D. Stutman, G. Suliman, O. Tesileanu, L. Tudor, N. Tsoneva, C. A. Ur, D. Ursescu, and N. V. Zamfir, "Current status and highlights of the eli-np research program," *Matter and Radiation at Extremes*, vol. 5, no. 2, p. 024402, 2020. https://doi.org/10.1063/1.5093535.

[53] D. Papadopoulos, J. Zou, C. Le Blanc, G. Cheriaux, P. Georges, F. Druon, G. Mennerat, L. Martin, A. Fréneaux, A. Beluze, N. Lebas, P. Monot, F. Mathieu, and P. Audebert, "The apollon 10 pw laser: Experimental and theoretical investigation of the temporal characteristics," *High Power Laser Science and Engineering*, vol. 4, 09 2016. https://doi.org/10.1017/hpl.2016.34.

[54] B. Shao, Y. Li, Y. Peng, P. Wang, J. Qian, Y. Leng, and R. Li, "Broad-bandwidth high-temporal-contrast carrier-envelope-phase-stabilized laser seed for 100 pw lasers," *Opt. Lett.*, vol. 45, pp. 2215–2218, Apr 2020. https://doi.org/10.1364/OL.390110.

[55] M. Nishiuchi, N. P. Dover, M. Hata, H. Sakaki, K. Kondo, H. F. Lowe, T. Miyahara, H. Kiriyama, J. K. Koga, N. Iwata, M. A. Alkhimova, A. S. Pirozhkov, A. Y. Faenov, T. A. Pikuz, A. Sagisaka, Y. Watanabe, M. Kando, K. Kondo, E. J. Ditter, O. C. Ettlinger, G. S. Hicks, Z. Najmudin, T. Ziegler, K. Zeil, U. Schramm, and Y. Sentoku, "Dynamics of laser-driven heavy-ion acceleration clarified by ion charge states," *Physical Review Research*, vol. 2, p. 033081, Jul 2020. https://doi.org/10.1103/PhysRevResearch.2.033081.

[56] S. Garcia, D. Chatain, and J. P. Perin, "Continuous production of a thin ribbon of solid hydrogen," *Laser and Particle Beams*, vol. 32, no. 4, p. 569–575, 2014. https://doi.org/10.1017/S0263034614000524.

[57] D. Margarone, G. A. P. Cirrone, G. Cuttone, A. Amico, L. Andò, M. Borghesi, S. S. Bulanov, S. V. Bulanov, D. Chatain, A. Fajstavr, L. Giuffrida, F. Grepl, S. Kar, J. Krasa, D. Kramer, G. Larosa, R. Leanza, T. Levato, M. Maggiore, L. Manti, G. Milluzzo, B. Odlozilik, V. Olsovcova, J.-P. Perin, J. Pipek, J. Psikal, G. Petringa, J. Ridky, F. Romano, B. Rus, A. Russo, F. Schillaci, V. Scuderi, A. Velyhan, R. Versaci, T. Wiste, M. Zakova, and G. Korn, "Elimaia: A laser-driven ion accelerator for multidisciplinary applications," *Quantum Beam Science*, vol. 2, no. 2, 2018. https://doi.org/10.3390/qubs2020008.

[58] T. Chagovets, S. Stanček, L. Giuffrida, A. Velyhan, M. Tryus, F. Grepl, V. Istokskaia, V. Kantarelou, T. Wiste, J. C. Hernandez Martin, F. Schillaci, and D. Margarone, "Automation of target delivery and diagnostic systems for high repetition rate laser-plasma acceleration," *Applied Sciences*, vol. 11, no. 1680, p. 1680, 2021. https://doi.org/10.3390/app11041680.

[59] S. V. Bulanov and V. S. Khoroshkov, "Feasibility of using laser ion accelerators in proton therapy," *Plasma Physics Reports*, vol. 28, no. 5, pp. 453–456, 2002. https://doi.org/10.1134/1.1478534.

[60] S. V. Bulanov, T. Z. Esirkepov, F. F. Kamenets, Y. Kato, A. V. Kuznetsov, K. Nishihara, F. Pegoraro, T. Tajima, and V. S. Khoroshkov, "Generation of high-quality charged particle beams during the acceleration of ions by high-power laser radiation," *Plasma Physics Reports*, vol. 28, no. 12, pp. 975–991, 2002. https://doi.org/10.1134/1.1528239.

[61] T. Esirkepov, S. V. Bulanov, K. Nishihara, T. Tajima, F. Pegoraro, V. S. Khoroshkov, K. Mima, H. Daido, Y. Kato, Y. Kitagawa, K. Nagai, and S. Sakabe, "Proposed double-layer target for the generation of high-quality laser-accelerated ion beams," *Physical Review Letters*, vol. 89, no. 175003, p. 175003, 2002. https://doi.org/10.1103/physrevlett.89.175003.

[62] M. Matys, K. Nishihara, M. Kecova, J. Psikal, G. Korn, and S. V. Bulanov, "Laser-driven generation of collimated quasi-monoenergetic proton beam using double-layer target with modulated interface," *High Energy Density Physics*, vol. 36, p. 100844, 2020. https://doi.org/10.1016/j.hedp.2020.100844.

[63] P. Wang, Z. Gong, S. G. Lee, Y. Shou, Y. Geng, C. Jeon, I. J. Kim, H. W. Lee, J. W. Yoon, J. H. Sung, S. K. Lee, D. Kong, J. Liu, Z. Mei, Z. Cao, Z. Pan, I. W. Choi, X. Yan, C. H. Nam, and W. Ma, "Super-heavy ions acceleration driven by ultrashort laser pulses at ultrahigh intensity," *Phys. Rev. X*, vol. 11, p. 021049, Jun 2021. https://doi.org/10.1103/PhysRevX.11.021049.

[64] A. Alejo, H. Ahmed, A. G. Krygier, R. Clarke, R. R. Freeman, J. Fuchs, A. Green, J. S. Green, D. Jung, A. Kleinschmidt, J. T. Morrison, Z. Najmudin, H. Nakamura, P. Norreys, M. Notley, M. Oliver, M. Roth, L. Vassura, M. Zepf, M. Borghesi, and S. Kar, "Stabilized radiation pressure acceleration and neutron generation in ultrathin deuterated foils," *Phys. Rev. Lett.*, vol. 129, p. 114801, Sep 2022. https://doi.org/10.1103/PhysRevLett.129.114801.

[65] D. Margarone, O. Klimo, I. J. Kim, J. Prokůpek, J. Limpouch, T. M. Jeong, T. Mocek, J. Pšikal, H. T. Kim, J. Proška, K. H. Nam, L. Štolcová, I. W. Choi, S. K. Lee, J. H. Sung, T. J. Yu, and G. Korn, "Laser-driven proton acceleration enhancement by nanostructured foils," *Phys. Rev. Lett.*, vol. 109, p. 234801, Dec 2012. https://doi.org/10.1103/PhysRevLett.109.234801.

[66] J. Psikal, J. Grym, L. Stolcova, and J. Proska, "Hollow target for efficient generation of fast ions by ultrashort laser pulses," *Physics of Plasmas*, vol. 23, no. 12, p. 123121, 2016. https://doi.org/10.1063/1.4972880.

[67] G. Cantono, A. Permogorov, J. Ferri, E. Smetanina, A. Dmitriev, A. Persson, T. Fülöp, and C.-G. Wahlström, "Laser-driven proton acceleration from ultrathin foils with nanoholes," *Scientific Reports*, vol. 11, p. 5006, Mar 2021. https://doi.org/10.1038/s41598-021-84264-z.

[68] M. Chen, A. Pukhov, T. P. Yu, and Z. M. Sheng, "Enhanced collimated GeV monoenergetic ion acceleration from a shaped foil target irradiated by a circularly polarized laser pulse," *Physical Review Letters*, vol. 103, no. 024801, p. 024801, 2009. https://doi.org/10.1103/PhysRevLett.103.024801.

[69] J. L. Liu, M. Chen, Z. M. Sheng, C. S. Liu, W. B. Mori, and J. Zhang, "Stable laser-produced quasimonoenergetic proton beams from interactive laser and target shaping," *Physical Review Special Topics - Accelerators and Beams*, vol. 16, no. 12, p. 121301, 2013. https://doi.org/10.1103/PhysRevSTAB.16.121301.

[70] P. Hadjisolomou, S. V. Bulanov, and G. Korn, "Towards laser ion acceleration with holed targets," *Journal of Plasma Physics*, vol. 86, no. 3, p. 905860304, 2020. https://doi.org/10.1017/S0022377820000379.

[71] Lord Rayleigh, "Investigation of the character of the equilibrium of an incompressible heavy fluid of variable density," *Proceedings of the London Mathematical Society*, vol. 14, pp. 170–177, 1882. https://doi.org/10.1112/plms/s1-14.1.170.

[72] G. Taylor, "The instability of liquid surfaces when accelerated in a direction perpendicular to their planes. I," *Proceedings of the Royal Society of London. Series A. Mathematical and Physical Sciences*, vol. 201, no. 1065, pp. 192–196, 1950. https://doi.org/10.1098/rspa.1950.0052.

[73] F. Pegoraro and S. V. Bulanov, "Photon bubbles and ion acceleration in a plasma dominated by the radiation pressure of an electromagnetic pulse," *Physical Review Letters*, vol. 99, no. 065002, p. 065002, 2007. https://doi.org/10.1103/PhysRevLett.99.065002.

[74] S. V. Bulanov, E. Y. Echkina, T. Z. Esirkepov, I. N. Inovenkov, M. Kando, F. Pegoraro, and G. Korn, "Unlimited energy gain in the laser-driven radiation pressure dominant acceleration of ions," *Physics of Plasmas*, vol. 17, no. 063102, p. 063102, 2010. https://doi.org/10.1063/1.3428741.

[75] E. Y. Echkina, I. N. Inovenkov, T. Z. Esirkepov, F. Pegoraro, M. Borghesi, and S. V. Bulanov, "Dependence of the ion energy on the parameters of the laser pulse and target in the radiation-pressure-dominated regime of acceleration," *Plasma Physics Reports*, vol. 36, no. 1, pp. 15–29, 2010. https://doi.org/10.1134/S1063780X10010022.

[76] R. D. Richtmyer, "Taylor instability in shock acceleration of compressible fluids," *Communications on Pure and Applied Mathematics*, vol. 13, no. 2, pp. 297–319, 1960. https://doi.org/10.1002/cpa.3160130207.

[77] E. E. Meshkov, "Instability of the interface of two gases accelerated by a shock wave," *Fluid Dynamics*, vol. 4, no. 5, pp. 101–104, 1969. https://doi.org/10.1007/BF01015969.

[78] Y. Zhou, "Rayleigh–Taylor and Richtmyer–Meshkov instability induced flow, turbulence, and mixing. I," *Physics Reports*, vol. 720-722, pp. 1–136, 2017. https://doi.org/10.1016/j.physrep.2017.07.005.

[79] M. Jirka, O. Klimo, Y.-J. Gu, and S. Weber, "Enhanced photon emission from a double-layer target at moderate laser intensities.," *Scientific Reports*, vol. 10, no. 8887, p. 8887, 2020. https://doi.org/10.1038/s41598-020-65778-4.

[80] S. V. Bulanov, I. N. Inovenkov, V. I. Kirsanov, N. M. Naumova, and A. S. Sakharov, "Nonlinear depletion of ultrashort and relativistically strong laser pulses in an underdense plasma," *Physics of Fluids B*, vol. 4, no. 7, pp. 1935–1942, 1992. https://doi.org/10.1063/1.860046.

[81] S. V. Bulanov, V. I. Kirsanov, N. M. Naumova, A. S. Sakharov, H. A. Shah, and I. N. Inovenkov, "Stationary shock-front of a relativisticaily strong electromagnetic radiation in an underdense plasma," *Physica Scripta*, vol. 47, no. 2, pp. 209–213, 1993. https://doi.org/10.1088/0031-8949/47/2/014.

[82] C. D. Decker, W. B. Mori, K. C. Tzeng, and T. Katsouleas, "The evolution of ultra-intense, short-pulse lasers in underdense plasmas," *Physics of Plasmas*, vol. 3, no. 5, pp. 2047–2056, 1996. https://doi.org/10.1063/1.872001.

[83] H. Y. Wang, C. Lin, Z. M. Sheng, B. Liu, S. Zhao, Z. Y. Guo, Y. R. Lu, X. T. He, J. E. Chen, and X. Q. Yan, "Laser shaping of a relativistic intense, short gaussian pulse by a plasma lens," *Phys. Rev. Lett.*, vol. 107, p. 265002, Dec 2011. https://doi.org/10.1103/PhysRevLett.107.265002.

[84] J. H. Bin, W. J. Ma, H. Y. Wang, M. J. V. Streeter, C. Kreuzer, D. Kiefer, M. Ye-ung, S. Cousens, P. S. Foster, B. Dromey, X. Q. Yan, R. Ramis, J. Meyer-ter Vehn, M. Zepf, and J. Schreiber, "Ion acceleration using relativistic pulse shaping in near-critical-density plasmas," *Phys. Rev. Lett.*, vol. 115, p. 064801, Aug 2015. https://doi.org/10.1103/PhysRevLett.115.064801.

[85] S. Palaniyappan, B. M. Hegelich, H. C. Wu, D. Jung, D. C. Gautier, L. Yin, B. J. Albright, R. P. Johnson, T. Shimada, S. Letzring, D. T. Offermann, J. Ren, C. Huang, R. Hörlein, B. Dromey, J. C. Fernandez, and R. C. Shah, "Dynamics of relativistic transparency and optical shuttering in expanding overdense plasmas," *Nature Physics*, vol. 8, no. 10, pp. 763–769, 2012. https://doi.org/10.1038/nphys2390.

[86] S. A. Reed, T. Matsuoka, S. Bulanov, M. Tampo, V. Chvykov, G. Kalintchenko, P. Rousseau, V. Yanovsky, R. Kodama, D. W. Litzenberg, K. Krushelnick, and A. Mak-simchuk, "Relativistic plasma shutter for ultraintense laser pulses," *Applied Physics Letters*, vol. 94, no. 20, p. 201117, 2009. https://doi.org/10.1063/1.3139860.

[87] W. Q. Wei, X. H. Yuan, Y. Fang, Z. Y. Ge, X. L. Ge, S. Yang, Y. F. Li, G. Q. Liao, Z. Zhang, F. Liu, M. Chen, L. Zhao, H. B. Zhuo, Y. T. Li, Z. M. Sheng, and J. Zhang, "Plasma optical shutter in ultraintense laser-foil interaction," *Physics of Plasmas*, vol. 24, no. 113111, p. 113111, 2017. https://doi.org/10.1063/1.5008843.

[88] A. Lévy, T. Ceccotti, P. D'Oliveira, F. Réau, M. Perdrix, F. Quéré, P. Monot, M. Bougeard, H. Lagadec, P. Martin, J.-P. Geindre, and P. Audebert, "Double plasma mirror for ultrahigh temporal contrast ultraintense laser pulses," *Opt. Lett.*, vol. 32, pp. 310–312, Feb 2007. https://doi.org/10.1364/OL.32.000310.

[89] B. Gonzalez-Izquierdo, R. Gray, M. King, R. Dance, R. Wilson, J. McCreadie, N. Butler, R. Capdessus, S. Hawkes, J. Green, M. Borghesi, D. Neely, and P. McKenna, "Optically controlled dense current structures driven by relativistic plasma aperture-induced diffrac-tion," *Nature Physics*, vol. 12, p. 505–512, 01 2016. https://doi.org/10.1038/nphys3613.

[90] B. Gonzalez-Izquierdo, M. King, R. Gray, R. Wilson, R. Dance, H. Powell, D. Maclel-lan, J. McCreadie, N. Butler, S. Hawkes, J. Green, C. Murphy, L. Stockhausen, D. Carroll, N. Booth, G. Scott, M. Borghesi, D. Neely, and P. McKenna, "To-wards optical polarization control of laser-driven proton acceleration in foils under-going relativistic transparency," *Nature Communications*, vol. 7, p. 12891, 09 2016. https://doi.org/10.1038/ncomms12891.

[91] "Kansai Photon Science Institute | BLOG: [Event Report] 68th KPSI Seminar (in Japanese)." Available online: https://www.qst.go.jp/site/kansai/31978.html (accessed on 28 February 2023).

[92] "Photonics | january 2023." Available online: https://www.mdpi.com/2304-6732/10/1 (accessed on 28 February 2023).

[93] S. Ter-Avetisyan, P. Varmazyar, P. K. Singh, J.-G. Son, M. Fule, V. Y. Bychenkov, B. Farkas, K. Nelissen, S. Mondal, D. Papp, A. Borzsonyi, J. Csontos, Z. Lecz, T. Somoskoi, L. Toth, S. Toth, V. Andriy, D. Margarone, A. Necas, T. Tajima, G. Mourou, G. Szabo, and K. Osvay, "Ion acceleration with few cycle relativistic laser pulses from foil targets," *arXiv:2212.00817*, 2022. https://doi.org/10.48550/ARXIV.2212.00817.

[94] K. Osvay, "Proton and deuteron acceleration with few-cycle, relativistic intensity laser pulses." presentation at EuroNNAc Special Topics Workshop, 2022. Available online: https://agenda.infn.it/event/28376/contributions/179357/ (accessed on 28 February 2023).

[95] P. Kulhánek, *Úvod do teorie plazmatu.* AGA, 2017. ISBN: 978-80904582-2-2. Available online: https://www.aldebaran.cz/studium/fpla.pdf (accessed on 28 February 2023).

[96] G. A. Mourou, T. Tajima, and S. V. Bulanov, "Optics in the relativistic regime," *Reviews of Modern Physics*, vol. 78, no. 2, pp. 309–371, 2006. https://doi.org/10.1103/RevModPhys.78.309.

[97] P. Gibbon, *Short pulse laser interactions with matter.* Imperial College Press London, 2005. https://doi.org/10.1142/p116.

[98] J. W. Yoon, Y. G. Kim, I. W. Choi, J. H. Sung, H. W. Lee, S. K. Lee, and C. H. Nam, "Realization of laser intensity over $10^{23}$ W/cm$^2$," *Optica*, vol. 8, pp. 630–635, May 2021. https://doi.org/10.1364/OPTICA.420520.

[99] T. Nakamura, S. V. Bulanov, T. Z. Esirkepov, and M. Kando, "High-energy ions from near-critical density plasmas via magnetic vortex acceleration," *Phys. Rev. Lett.*, vol. 105, p. 135002, Sep 2010.

[100] Y. Sentoku, K. Mima, Z. M. Sheng, P. Kaw, K. Nishihara, and K. Nishikawa, "Three-dimensional particle-in-cell simulations of energetic electron generation and transport with relativistic laser pulses in overdense plasmas," *Phys. Rev. E*, vol. 65, p. 046408, Mar 2002. https://doi.org/10.1103/PhysRevE.65.046408.

[101] L. Gremillet, G. Bonnaud, and F. Amiranoff, "Filamented transport of laser-generated relativistic electrons penetrating a solid target," *Physics of Plasmas*, vol. 9, no. 3, pp. 941–948, 2002. https://doi.org/10.1063/1.1432994.

[102] Y. Sentoku, T. E. Cowan, A. Kemp, and H. Ruhl, "High energy proton acceleration in interaction of short laser pulse with dense plasma target," *Physics of Plasmas*, vol. 10, no. 5, pp. 2009–2015, 2003. https://doi.org/10.1063/1.1556298.

[103] B. M. Hegelich, B. J. Albright, J. Cobble, K. Flippo, S. Letzring, M. Paffett, H. Ruhl, J. Schreiber, R. K. Schulze, and J. C. Fernández, "Laser acceleration of quasi-monoenergetic mev ion beams," *Nature*, vol. 439, p. 441–444, Jan 2006. https://doi.org/10.1038/nature04400.

[104] K. Flippo, B. Hegelich, B. Albright, L. Yin, D. Gautier, S. Letzring, M. Schollmeier, J. Schreiber, R. Schulze, J. Fernández, and et al., "Laser-driven ion accelerators: Spectral control, monoenergetic ions and new acceleration mechanisms," *Laser and Particle Beams*, vol. 25, no. 1, p. 3–8, 2007. https://doi.org/10.1017/S0263034607070012.

[105] M. Matys, "Ion acceleration driven by 10 pw laser," Master's thesis, Czech Technical University in Prague, Faculty of Nuclear Sciences and Physical Engineering, 2017. https://dspace.cvut.cz/handle/10467/75887.

[106] P. Mora, "Plasma expansion into a vacuum," *Phys. Rev. Lett.*, vol. 90, p. 185002, May 2003. https://doi.org/10.1103/PhysRevLett.90.185002.

[107] M. PASSONI and M. LONTANO, "One-dimensional model of the electrostatic ion acceleration in the ultraintense laser–solid interaction," *Laser and Particle Beams*, vol. 22, no. 2, p. 163–169, 2004. https://doi.org/10.1017/S026303460422211X.

[108] M. Passoni, V. T. Tikhonchuk, M. Lontano, and V. Y. Bychenkov, "Charge separation effects in solid targets and ion acceleration with a two-temperature electron distribution," *Phys. Rev. E*, vol. 69, p. 026411, Feb 2004. https://doi.org/10.1103/PhysRevE.69.026411.

[109] M. Nishiuchi, A. Fukumi, H. Daido, Z. Li, A. Sagisaka, K. Ogura, S. Orimo, M. Kado, Y. Hayashi, M. Mori, S. Bulanov, T. Esirkepov, K. Nemoto, Y. Oishi, T. Nayuki, T. Fujii, A. Noda, Y. Iwashita, T. Shirai, and S. Nakamura, "The laser proton acceleration in the strong charge separation regime," *Physics Letters A*, vol. 357, no. 4, pp. 339–344, 2006. https://doi.org/10.1016/j.physleta.2006.04.053.

[110] J. Fuchs, P. Antici, E. d'Humières, E. Lefebvre, M. Borghesi, E. Brambrink, C. A. Cecchetti, M. Kaluza, V. Malka, M. Manclossi, S. Meyroneinc, P. Mora, J. Schreiber, T. Toncian, H. Pépin, and P. Audebert, "Laser-driven proton scaling laws and new paths towards energy increase," *Nature Physics*, vol. 2, p. 48–54, Dec 2005. https://doi.org/10.1038/nphys199.

[111] M. Passoni and M. Lontano, "Theory of light-ion acceleration driven by a strong charge separation," *Phys. Rev. Lett.*, vol. 101, p. 115001, Sep 2008. https://doi.org/10.1103/PhysRevLett.101.115001.

[112] M. Passoni, L. Bertagna, and A. Zani, "Energetic ions from next generation ultraintense ultrashort lasers: Scaling laws for target normal sheath acceleration," *Nuclear Instruments and Methods in Physics Research Section A: Accelerators, Spectrometers, Detectors and Associated Equipment*, vol. 620, no. 1, pp. 46–50, 2010. https://doi.org/10.1016/j.nima.2010.01.058.

[113] S. C. Wilks, W. L. Kruer, M. Tabak, and A. B. Langdon, "Absorption of ultra-intense laser pulses," *Phys. Rev. Lett.*, vol. 69, pp. 1383–1386, Aug 1992. https://doi.org/10.1103/PhysRevLett.69.1383.

[114] G. Malka and J. L. Miquel, "Experimental confirmation of ponderomotive-force electrons produced by an ultrarelativistic laser pulse on a solid target," *Phys. Rev. Lett.*, vol. 77, pp. 75–78, Jul 1996. https://doi.org/10.1103/PhysRevLett.77.75.

[115] N. Naumova, T. Schlegel, V. T. Tikhonchuk, C. Labaune, I. V. Sokolov, and G. Mourou, "Hole boring in a dt pellet and fast-ion ignition with ultraintense laser pulses," *Phys. Rev. Lett.*, vol. 102, p. 025002, Jan 2009. https://doi.org/10.1103/PhysRevLett.102.025002.

[116] A. P. L. Robinson, P. Gibbon, M. Zepf, S. Kar, R. G. Evans, and C. Bellei, "Relativistically correct hole-boring and ion acceleration by circularly polarized laser pulses," *Plasma Physics and Controlled Fusion*, vol. 51, p. 024004, jan 2009. https://doi.org/10.1088/0741-3335/51/2/024004.

[117] S. V. Bulanov, T. Z. Esirkepov, M. Kando, F. Pegoraro, S. S. Bulanov, C. G. R. Geddes, C. B. Schroeder, E. Esarey, and W. P. Leemans, "Ion acceleration from thin foil and extended plasma targets by slow electromagnetic wave and related ion-ion beam instability," *Physics of Plasmas*, vol. 19, no. 10, p. 103105, 2012. https://doi.org/10.1063/1.4757981.

[118] O. Klimo, J. Psikal, J. Limpouch, and V. T. Tikhonchuk, "Monoenergetic ion beams from ultrathin foils irradiated by ultrahigh-contrast circularly polarized laser pulses," *Physical Review Special Topics - Accelerators and Beams*, vol. 11, no. 3, p. 031301, 2008. https://doi.org/10.1103/PhysRevSTAB.11.031301.

[119] S. Bulanov, T. Esirkepov, P. Migliozzi, F. Pegoraro, T. Tajima, and F. Terranova, "Neutrino oscillation studies with laser-driven beam dump facilities," *Nuclear Instruments and Methods in Physics Research Section A: Accelerators, Spectrometers, Detectors and Associated Equipment*, vol. 540, no. 1, pp. 25–41, 2005. https://doi.org/10.1016/j.nima.2004.11.013.

[120] T. Esirkepov, M. Yamagiwa, and T. Tajima, "Laser ion-acceleration scaling laws seen in multiparametric particle-in-cell simulations," *Phys. Rev. Lett.*, vol. 96, p. 105001, Mar 2006. https://doi.org/10.1103/PhysRevLett.96.105001.

[121] T. Esirkepov, R. Bingham, S. Bulanov, T. Honda, K. Nishihara, and F. Pegoraro, "Coulomb explosion of a cluster irradiated by a high intensity laser pulse," *Laser and Particle Beams*, vol. 18, p. 503–506, Jul 2000. https://doi.org/10.1017/s0263034600183211.

[122] K. Nishihara, H. Amitani, M. Murakami, S. Bulanov, and T. Esirkepov, "High energy ions generated by laser driven coulomb explosion of cluster," *Nuclear Instruments and Methods in Physics Research Section A: Accelerators, Spectrometers, Detectors and Associated Equipment*, vol. 464, no. 1, pp. 98–102, 2001. https://doi.org/10.1016/S0168-9002(01)00014-6.

[123] V. Y. Bychenkov and V. F. Kovalev, "Coulomb explosion in a cluster plasma," *Plasma Physics Reports*, vol. 31, p. 178–183, Feb 2005. https://doi.org/10.1134/1.1866599.

[124] J. Pšikal, *Ion Acceleration in Small-size Targets by Ultra-intense Short Laser Pulses*. Prague: CTU, 2009. Ph.D. Thesis. Czech Technical University in Prague, Faculty of Nuclear Sciences and Physical Engineering, Department of Physical Electronics.

[125] T. D. Arber, K. Bennett, C. S. Brady, A. Lawrence-Douglas, M. G. Ramsay, N. J. Sircombe, P. Gillies, R. G. Evans, H. Schmitz, A. R. Bell, and C. P. Ridgers, "Contemporary particle-in-cell approach to laser-plasma modelling," *Plasma Physics and Controlled Fusion*, vol. 57, no. 113001, p. 113001, 2015. https://doi.org/10.1088/0741-3335/57/11/113001.

[126] "Github - warwick-plasma/epoch: Particle-in-cell code for plasma physics simulations." Available online: https://github.com/Warwick-Plasma/epoch (accessed on 28 February 2023).

[127] "Github - warwick-plasma/sdf." Available online: https://github.com/Warwick-Plasma/SDF (accessed on 28 February 2023).

[128] H. Ruhl, *Classical Particle Simulations with the PSC code.* Ruhrstadt Universität Bochum, 2005. Available online: https://www.plasma-simulation-code.net/documentation/ (accessed on 28 February 2023).

[129] K. Germaschewski, W. Fox, S. Abbott, N. Ahmadi, K. Maynard, L. Wang, H. Ruhl, and A. Bhattacharjee, "The plasma simulation code: A modern particle-in-cell code with patch-based load-balancing," *Journal of Computational Physics*, vol. 318, pp. 305–326, 2016. https://doi.org/10.1016/j.jcp.2016.05.013.

[130] K. Bennett, *Developers Manual for the EPOCH PIC codes*, 2013.

[131] C. K. Birdsall and A. B. Langdon, *Plasma physics via computer simulation.* New York: Taylor and Francis, first ed., 2005. http://www.bibsonomy.org/bibtex/2bb3c422944f49d120b48bdad3192766c/pkilian.

[132] J. Villasenor and O. Buneman, "Rigorous charge conservation for local electromagnetic field solvers," *Computer Physics Communications*, vol. 69, no. 2, pp. 306 – 316, 1992. https://doi.org/10.1016/0010-4655(92)90169-Y.

[133] J. Ahrens, B. Geveci, and C. Law, "ParaView: An end-user tool for large-data visualization," in *Visualization Handbook*, pp. 717–731, Elsevier Inc., 2005. https://doi.org/10.1016/B978-012387582-2/50038-1.

[134] M. Danielova, P. Janecka, J. Grosz, and A. Holy, "Interactive 3D Visualizations of Laser Plasma Experiments on the Web and in VR," in *EuroVis 2019 - Posters* (J. Madeiras Pereira and R. G. Raidou, eds.), The Eurographics Association, 2019. https://doi.org/10.2312/eurp.20191145.

[135] "Plasma shutter for heavy ion acceleration enhancement." Available online: https://vbl.eli-beams.eu/mm-shutter/ (accessed on 28 February 2023).

[136] "Photonics | special issue : Progress in laser accelerator and future prospects." Available online: https://www.mdpi.com/journal/photonics/special_issues/Laser_Accelerator (accessed on 28 February 2023).

[137] "Virtual beamline." Available online: https://vbl.eli-beams.eu/ (accessed on 28 February 2023).

[138] T. Chagovets, J. Viswanathan, M. Tryus, F. Grepl, A. Velyhan, S. Stancek, L. Giuffrida, F. Schillaci, J. Cupal, L. Koubikova, D. Garcia, J. Manzagol, P. Bonnay, F. Souris, D. Chatain, A. Girard, and D. Margarone, "A cryogenic hydrogen ribbon for laser driven proton acceleration at hz-level repetition rate," *Frontiers in Physics*, vol. 9, Jan 2022. https://doi.org/10.3389/fphy.2021.754423.

[139] F. Wagner, S. Bedacht, A. Ortner, M. Roth, A. Tauschwitz, B. Zielbauer, and V. Bagnoud, "Pre-plasma formation in experiments using petawatt lasers," *Optics Express*, vol. 22, no. 24, p. 29505, 2014. https://doi.org/10.1364/oe.22.029505.

[140] A. P. Robinson, M. Zepf, S. Kar, R. G. Evans, and C. Bellei, "Radiation pressure acceleration of thin foils with circularly polarized laser pulses," *New Journal of Physics*, vol. 10, no. 013021, p. 013021, 2008. https://doi.org/10.1088/1367-2630/10/1/013021.

[141] M. Matys, J. Psikal, and D. Margarone, "Simulation studies on ion acceleration driven by 10 PW laser," in *44th EPS Conference on Plasma Physics, EPS 2017* (M. Fajardo, E. Westerhof, C. Riconda, A. Melzer, A. Bret, and B. Dromey, eds.), vol. Vol. 41F, p. P1.204, 2017. http://ocs.ciemat.es/EPS2017PAP/pdf/P1.204.pdf.

[142] J. Psikal and M. Matys, "Ultra-intense laser interaction with specially-designed targets as a source of energetic protons," in *Research Using Extreme Light: Entering New Frontiers with Petawatt-Class Lasers III* (E. Esarey, C. Schroeder, and J. Schreiber, eds.), vol. 10241 of *Proc. of SPIE*, p. 102411K, 2017. https://doi.org/10.1117/12.2271026.

[143] "Laser-driven proton acceleration from cryogenic hydrogen target." Available online: https://vbl.eli-beams.eu/mm-track/ (accessed on 28 February 2023).

[144] M. Matys, J. Psikal, M. Danielova, P. Valenta, and S. V. Bulanov, "Laser-driven ion acceleration using cryogenic hydrogen targets," in *Supercomputing in Science and Engineering 2017-18* (K. Pešatová, B. Poláková, J. Cawley, and Z. Červenková, eds.), pp. 149–151, ISBN 978–80–248–4289–9, VSB – Technical University of Ostrava, 2019. Available online: https://www.it4i.cz/en/about/publications (accessed on 28 February 2023).

[145] Y. Zhou, T. T. Clark, D. S. Clark, S. Gail Glendinning, M. Aaron Skinner, C. M. Huntington, O. A. Hurricane, A. M. Dimits, and B. A. Remington, "Turbulent mixing and transition criteria of flows induced by hydrodynamic instabilities," *Physics of Plasmas*, vol. 26, no. 080901, p. 080901, 2019. https://doi.org/10.1063/1.5088745.

[146] Y. Zhou, R. J. Williams, P. Ramaprabhu, M. Groom, B. Thornber, A. Hillier, W. Mostert, B. Rollin, S. Balachandar, P. D. Powell, A. Mahalov, and N. Attal, "Rayleigh–taylor and richtmyer–meshkov instabilities: A journey through scales," *Physica D: Nonlinear Phenomena*, vol. 423, p. 132838, 2021. https://doi.org/10.1016/j.physd.2020.132838.

[147] J. D. Lindl, R. L. Mccrory, and E. M. Campbell, "Progress toward Ignition and Burn Propagation in Inertial Confinement Fusion," *Physics Today*, vol. 45, no. 9, pp. 32–40, 1992. https://doi.org/10.1063/1.881318.

[148] Y. Wan, C. H. Pai, C. J. Zhang, F. Li, Y. P. Wu, J. F. Hua, W. Lu, Y. Q. Gu, L. O. Silva, C. Joshi, and W. B. Mori, "Physical Mechanism of the Transverse Instability in Radiation Pressure Ion Acceleration," *Physical Review Letters*, vol. 117, no. 234801, p. 234801, 2016. https://doi.org/10.1103/PhysRevLett.117.234801.

[149] Y. Wan, C. H. Pai, C. J. Zhang, F. Li, Y. P. Wu, J. F. Hua, W. Lu, C. Joshi, W. B. Mori, and V. Malka, "Physical mechanism of the electron-ion coupled transverse instability in laser pressure ion acceleration for different regimes," *Physical Review E*, vol. 98, no. 013202, p. 013202, 2018. https://doi.org/10.1103/PhysRevE.98.013202.

[150] M. Matys, K. Nishihara, M. Danielova, J. Psikal, G. Korn, and S. Bulanov, V, "Generation of collimated quasi-mono-energetic ion beams using a double layer target with interface modulations," in *Laser Acceleration of Electrons, Protons, and Ions V* (E. Esarey, C. Schroeder, and J. Schreiber, eds.), vol. 11037 of *Proc. of SPIE*, p. 110370Z, 2019. https://doi.org/10.1117/12.2520951.

[151] M. Matys, P. Valenta, M. Kecova, K. Nishihara, J. Psikal, T. Z. Esirkepov, J. K. Koga, A. Necas, G. M. Grittani, C. M. Lazzarini, O. Klimo, G. Korn, and S. V. Bulanov,

"Laser-driven acceleration of charged particles," in *Supercomputing in Science and Engineering 2019-20* (B. J. Vit Vondrak, Tomas Kozubek, ed.), pp. 86–88, ISBN 978–80–248–4567–8, VSB – Technical University of Ostrava, 2021. Available online: https://www.it4i.cz/en/about/publications (accessed on 28 February 2023).

[152] J. C. Fernández, D. Cort Gautier, C. Huang, S. Palaniyappan, B. J. Albright, W. Bang, G. Dyer, A. Favalli, J. F. Hunter, J. Mendez, M. Roth, M. Swinhoe, P. A. Bradley, O. Deppert, M. Espy, K. Falk, N. Guler, C. Hamilton, B. M. Hegelich, D. Henzlova, K. D. Ianakiev, M. Iliev, R. P. Johnson, A. Kleinschmidt, A. S. Losko, E. McCary, M. Mocko, R. O. Nelson, R. Roycroft, M. A. Santiago Cordoba, V. A. Schanz, G. Schaumann, D. W. Schmidt, A. Sefkow, T. Shimada, T. N. Taddeucci, A. Tebartz, S. C. Vogel, E. Vold, G. A. Wurden, and L. Yin, "Laser-plasmas in the relativistic-transparency regime: Science and applications," *Physics of Plasmas*, vol. 24, no. 5, p. 056702, 2017. https://doi.org/10.1063/1.4983991.

[153] M. J. Duff, R. Wilson, M. King, B. Gonzalez-Izquierdo, A. Higginson, S. D. R. Williamson, Z. E. Davidson, R. Capdessus, N. Booth, S. Hawkes, D. Neely, R. J. Gray, and P. McKenna, "High order mode structure of intense light fields generated via a laser-driven relativistic plasma aperture," *Scientific Reports*, vol. 10, p. 105, Jan 2020. https://doi.org/10.1038/s41598-019-57119-x.

[154] J. Nikl, M. Jirka, M. Matys, M. Kuchařík, and O. Klimo, "Contrast enhancement of ultra-intense laser pulses by relativistic plasma shutter," in *High Power Lasers and Applications* (J. Hein, T. J. Butcher, P. Bakule, C. L. Haefner, G. Korn, and L. O. Silva, eds.), vol. 11777 of *Proc. of SPIE*, p. 117770X, 2021. https://doi.org/10.1117/12.2589245.

[155] M. Matys, S. Bulanov, M. Kecova, M. Kucharik, M. Jirka, P. Janecka, J. Psikal, J. Nikl, J. Grosz, G. Korn, and O. Klimo, "Ion acceleration enhancement by laser-pulse shaping via plasma shutter," in *Laser Acceleration of Electrons, Protons, and Ions VI* (S. S. Bulanov, J. Schreiber, and C. B. Schroeder, eds.), vol. 11779 of *Proc. of SPIE*, p. 117790Q, 2021. https://doi.org/10.1117/12.2589096.

[156] M. Matys, M. Kecova, M. Kucharik, J. Nikl, S. V. Bulanov, M. Jirka, P. Janecka, J. Psikal, G. Korn, G. J., and O. Klimo, "Laser-driven ion acceleration enhancement using silicon nitride plasma shutter," in *47th EPS Conference on Plasma Physics, EPS 2021* (G. Giruzzi, C. Arnas, D. Borba, A. Gopal, S. Lebedev, and M. Mantsinen, eds.), vol. 45A, p. P3.2026, European Physical Society, 2021. http://ocs.ciemat.es/EPS2021PAP/pdf/P3.2026.pdf.

[157] M. Matys, S. V. Bulanov, M. Kucharik, M. Jirka, J. Nikl, M. Kecova, J. Proska, J. Psikal, G. Korn, and O. Klimo, "Influence of the laser pulse steep rising front on ion acceleration," in *48th EPS Conference on Plasma Physics, EPS 2022* (T. Klinger, J. Hobirk, S. Orlando, L. Lancia, D. Maric, and E. Westerhof, eds.), vol. 46A, p. P2b.202, European Physical Society, 2022. http://ocs.ciemat.es/EPS2022PAP/pdf/P2b.202.pdf.

[158] M. Matys, O. Klimo, J. Psikal, and S. V. Bulanov, "Simulation studies on transmissivity of silicon nitride plasma shutter for laser pulse contrast enhancement," in *45th EPS Conference on Plasma Physics, EPS 2018* (S. Coda, J. Berndt, G. Lapenta, M. Mantsinen, C. Michaut, and S. Weber, eds.), vol. 42A, p. P4.2031, 2018. http://ocs.ciemat.es/EPS2018PAP/pdf/P4.2031.pdf.

# Appendices

# Appendix A

# List of author's publications

*Below, the reader can find the full list of publications (as of the day of submission of this dissertation) in peer-reviewed journals, conference proceedings, and as book chapters authored or co-authored by the author of this dissertation during the author's postgraduate studies. The publications are listed in chronological order.*

## A.1 Publications in peer-reviewed journals

- J. Psikal and M. Matys (2018). Dominance of hole-boring radiation pressure acceleration regime with thin ribbon of ionized solid hydrogen. *Plasma Physics and Controlled Fusion* **60**, 044003.

- M. Matys, K. Nishihara, M. Kecova, J. Psikal, G. Korn, S. V. Bulanov (2020). Laser-driven generation of collimated quasi-monoenergetic proton beam using double-layer target with modulated interface. *High Energy Density Physics* **36**, 100844.

- M. Jirka, O. Klimo, and M. Matys (2021) Relativistic plasma aperture for laser intensity enhancement. *Physical Review Research* **3**, 033175.

- M. Matys, S. V. Bulanov, M. Kucharik, M. Jirka, J. Nikl, M. Kecova, J. Proska, J. Psikal, G. Korn and O. Klimo (2022). Design of plasma shutters for improved heavy ion acceleration by ultra-intense laser pulses. *New Journal of Physics* **24**, 113046.

- M. Matys, J. Psikal, K. Nishihara, O. Klimo, M. Jirka, P. Valenta and S. V. Bulanov (2023). High-quality laser-accelerated ion beams from structured targets. *Photonics* **10**, 61.

## A.2 Publications in conference proceedings

- M. Matys, J. Psikal and D. Margarone (2017). Simulation studies on ion acceleration driven by 10 PW laser. In M. Fajardo, E. Westerhof, C. Riconda, A. Melzer, A. Bret, B. Dromey, editors, *44th EPS Conference on Plasma Physics*, page P1.204, Vol. 41F, ISBN: 979-10-96389-07, European Physical Society.

- J. Psikal and M. Matys (2017). Ultra-intense laser interaction with specially-designed targets as a source of energetic protons. *Proc. SPIE 10241, Research Using Extreme Light: Entering New Frontiers with Petawatt-Class Lasers III*, 102411K

- M. Matys, O. Klimo, J. Psikal, S.V. Bulanov (2018). Simulation studies on transmissivity of silicon nitride plasma shutter for laser pulse contrast enhancement. In S. Coda, J. Berndt, G. Lapenta, M. Mantsinen, C. Michaut, S. Weber, editors, *45th EPS Conference on Plasma Physics*, page P4.2031, Vol. 42A, ISBN: 979-10-96389-08-7, European Physical Society.

- M. Matys, K. Nishihara, M. Danielova, J. Psikal, G. Korn, S. V. Bulanov (2019). Generation of collimated quasi-mono-energetic ion beams using a double layer target with interface modulations *Proc. SPIE 11037, Laser Acceleration of Electrons, Protons, and Ions V*, 110370Z.

- J. Psikal, V. Horny, M. Zakova, M. Matys (2019). Comparison of ion acceleration from nonexpanded and expanded thin foils irradiated by ultrashort petawatt laser pulse *Proc. SPIE 11037, Laser Acceleration of Electrons, Protons, and Ions V*, 1103708.

- M. Matys, S. V. Bulanov, M. Kecova, M. Kucharik, M. Jirka, P. Janecka, J. Psikal, J. Nikl, J. Grosz, G. Korn, and O. Klimo (2021). Ion acceleration enhancement by laser-pulse shaping via plasma shutter Proc. SPIE 11779, Laser Acceleration of Electrons, Protons, and Ions VI, 117790Q ;

- Nikl, M. Jirka, M. Matys, M. Kuchařík, and O. Klimo (2021) .Contrast enhancement of ultra-intense laser pulses by relativistic plasma shutter. Proc. SPIE 11777, High Power Lasers and Applications, 117770X;

- M. Matys, M. Kecova, M. Kucharik, J. Nikl, S. V. Bulanov, M. Jirka, P. Janecka, J. Psikal, G. Korn, J. Grosz and O. Klimo (2021). Laser-driven ion acceleration enhancement using silicon nitride plasma shutter. In G. Giruzzi, C. Arnas, D. Borba, A. Gopal, S. Lebedev, M. Mantsinen, editors, *47th EPS Conference on Plasma Physics*, page P3.2026, Vol. 45A, ISBN: 979-10-96389-13-1, European Physical Society.

- M. Matys, S. V. Bulanov, M. Kucharik, M. Jirka, J. Nikl, M. Kecova, J. Proska, J. Psikal, G. Korn and O. Klimo (2022). Influence of the laser pulse steep rising front on ion acceleration. In T. Klinger, J. Hobirk, S. Orlando, L. Lancia, D. Maric, E. Westerhof. editors, *48th EPS Conference on Plasma Physics*, page P2b.202, Vol. 46A, ISBN: 979-10-96389-16-2, European Physical Society.

## A.3 Book chapters

- M. Matys, J. Psikal, M. Danielova, P. Valenta, S. V. Bulanov. (2019). Laser-driven ion acceleration using cryogenic hydrogen targets. In K. Pešatová, B. Poláková, J. Cawley and Z. Červenková, editors, *Supercomputing in Science and Engineering 2017-18*, pages 149–151, ISBN 978-80-248-4289-9. VSB - Technical University of Ostrava.

- M. Matys, P. Valenta, M. Kecova, K. Nishihara, J. Psikal, T. Zh. Esirkepov, J. K. Koga, A. Necas, G., M. Grittani, C. M. Lazzarini, O. Klimo, G. Korn, S. V. Bulanov. (2021). Laser-driven acceleration of charged particles. In V. Vondrák, T. Kozubek and B. Jansík, editors, *Supercomputing in Science and Engineering 2019-20*, pages 86–88, ISBN 978-80-248-4567-8. VSB - Technical University of Ostrava.

# Appendix B

# List of author's conference presentations

*Below, the reader can find the full list of oral and poster conference presentations (as of the day of submission of this dissertation) given by the author of this dissertation during the author's postgraduate studies. The presentations are listed in chronological order.*

## B.1 Oral presentations

- EPS DPP satellite workshop on High-Field Laser Plasma Interaction, Milano: *Double layer target with interface modulations for laser acceleration of collimated ion beams*, 13. July 2019, Milano, Italy

- 3rd Users' Conference of IT4Innovations: *Double layer target with interface modulations for laser acceleration of collimated ion beams*, 5. - 6. November 2019, Ostrava, Czech Republic

- SPIE Optics&Optoelectronics 2021: *Ion acceleration enhancement by laser-pulse shaping via plasma shutter*, 19. - 22. April 2021, Prague, Czech Republic (online)

- ELI Beamlines USER CONFERENCE 2021: *Enhancement of Ion Acceleration by Laser-Pulse Shaping via Plasma Shutter*, 20-21 October 2021, Dolní Břežany

- 63rd Annual Meeting of the APS Division of Plasma Physics: *Enhancement of laser-driven ion acceleration by laser pulse shaping via plasma shutter*, 8.-12. November 2021, Pittsburgh, USA (online)

## B.2 Poster presentations

- 44th European Physical Society Conference on Plasma Physics: *Simulation studies on ion acceleration driven by 10 PW laser*, 26th–30th June 2017, Belfast, United Kingdom.

- 45th European Physical Society Conference: *Simulation studies on transmissivity of silicon nitride plasma shutter for laser pulse contrast enhancement*, 2-6 July 2018, Prague, Czech Republic

- 35th European Conference on Laser Interaction with Matter: *Laser pulse contrast and ion acceleration enhancement using a plasma shutter*, 22-26 October 2018, Rethymno, Greece.

- 2nd Users' Conference of IT4Innovations 2018: *Laser pulse contrast and laser-driven ion acceleration enhancement using a plasma shutter*, 7 November 2018, Ostrava, Czech Republic

- SPIE Optics&Optoelectronics 2019: *Generation of collimated quasi-mono-energetic ion beams using a double layer target with interface modulations*, 1 - 4 April 2019 , Prague, Czech Republic

- 46th EPS Conference on Plasma Physics: *Double layer target with interface modulations for laser acceleration of collimated ion beams*, 8.- 12. July 2019, Milano, Italy,

- Eleventh International Conference of Inertial Fusion Sciences and Applications: *Laser-driven acceleration of collimated ion beams via double layer target with interface modulations*, 22. - 27. September 2019, Osaka, Japan.

- 4th Users' Conference of IT4Innovations: *Generation of collimated quasi-monoenergetic proton beam using double-layer target with modulated interface*, 5. November 2020, Ostrava, Czech Republic (online)

- OPTO2021 Symposium on Photon and Beam Science: *Plasma shutter for improved ion acceleration driven by ultraintense laser pulses*, 22. June 2021, Osaka, Japan (online)

- 47th EPS Plasma Physics conference: *Laser-driven ion acceleration enhancement using silicon nitride plasma shutter*, 21. - 25. June. 2021, Sitges, Spain (online)

- 47th Conference on Plasma Physics - Satellite Meeting: High Field laser-plasma interaction (HIFI) & Laser-driven particle and radiation sources for application (LASA): *Plasma shutter for improved ion acceleration by ultraintense laser pulses* 28. - 29. June 2021, Sitges, Spain (online)

- 5th Users' Conference of IT4Innovations: *Enhancement of ion acceleration by laser-pulse shaping via plasma shutter*, 9. November 2021, Ostrava, Czech Republic (online)

- 48th EPS Plasma Physics conference: *Influence of the laser pulse steep rising front on ion acceleration*, 27 June - 1 July 2022, Maastricht, Netherlands (online)

- OPTO2022 Symposium on Photon and Beam Science: *Optimization of ion beam parameters using steep-front laser pulse*, 28-29th June, 2022, Osaka, Japan (online)

- Flash Radiotherapy & Particle Therapy Conference (FRPT 2022): *Laser-driven ion acceleration using multi-layer target with plasma shutter*, 30 November - 2 December 2022, Barcelona, Spain (online)

# Appendix C

# Selected publications

## C.1 High-quality laser-accelerated ion beams from structured targets

The following article is reproduced from M. Matys, J. Psikal, K. Nishihara, O. Klimo, M. Jirka, P. Valenta and S. V. Bulanov (2023). High-quality laser-accelerated ion beams from structured targets. *Photonics* **10**, 61.
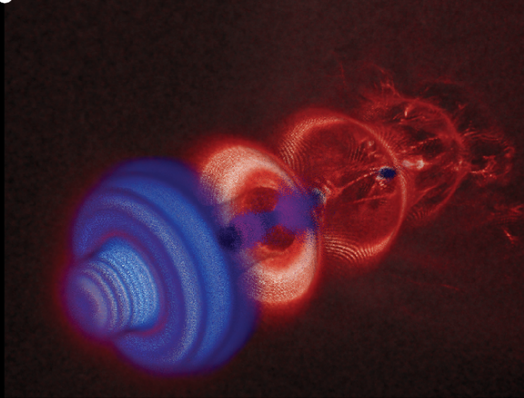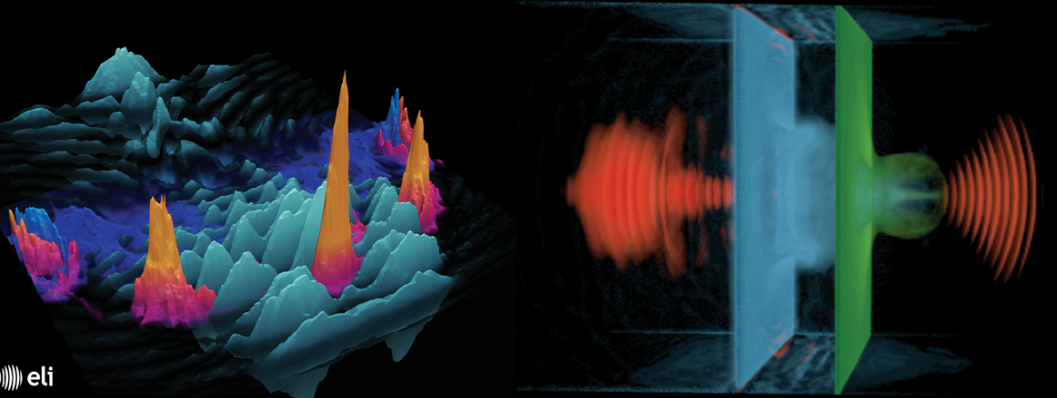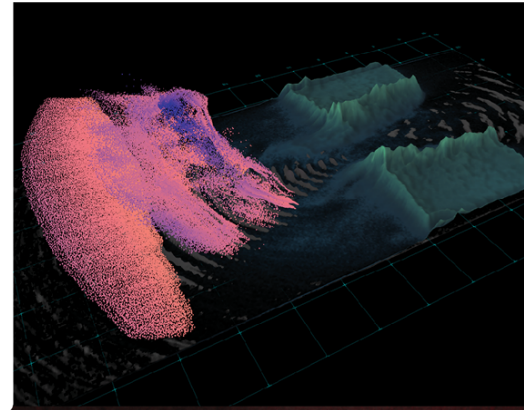
# High-Quality Laser-Accelerated Ion Beams from Structured Targets

# High-Quality Laser-Accelerated Ion Beams from Structured Targets

**Martin Matys** [1,2,*] [ID], **Jan Psikal** [1,2] [ID], **Katsunobu Nishihara** [3] [ID], **Ondrej Klimo** [1,2] [ID], **Martin Jirka** [1,2] [ID], **Petr Valenta** [1,2] [ID] **and Sergei V. Bulanov** [1,4] [ID]

[1] Extreme Light Infrastructure ERIC, ELI Beamlines Facility, Za Radnici 835, 252 41 Dolni Brezany, Czech Republic

[2] Faculty of Nuclear Sciences and Physical Engineering, Czech Technical University in Prague, Brehova 7, 11519 Prague, Czech Republic

[3] Institute of Laser Engineering, Osaka University, Suita 565-0871, Osaka, Japan

[4] Kansai Photon Science Institute, National Institutes for Quantum Science and Technology, 8-1-7 Umemidai, Kizugawa-shi 619-0215, Kyoto, Japan

[*] Correspondence: Martin.Matys@eli-beams.eu

**Abstract:** In this work, we reviewed our results on the prospect of increasing the quality of ion acceleration driven by high-intensity laser pulses using low-Z structured targets. It is shown that the radiation pressure acceleration mechanism dominates over target normal sheath acceleration for assumed laser target parameters when the laser intensity is high enough. The target thickness is optimized for this regime and double-layer structure is investigated. When a corrugation is fabricated on the interface of such a target, a relativistic instability with Rayleigh–Taylor and Richtmyer–Meshkov like features can be driven by the target interaction with a high intensity laser pulse. The proper development of this instability leads to the generation of a collimated quasi-monoenergetic ion beam with lower emittance, divergence, and energy spread compared to a single and double-layer target with planar interface. A steep-front laser pulse is used in our simulations to mitigate other type of instabilities arising at the target surface from the laser–target interaction. We discuss the use of a plasma shutter to generate the required pulse profile, which also locally increases intensity. The obtained shape improves the ion acceleration, including higher maximal energy and lower beam divergence, in our simulation of a high-Z target.

**Keywords:** high quality; monoenergetic; ion acceleration; laser-driven; plasma; low divergence; particle-in-cell; instability; steep front; plasma shutter

## 1. Introduction

Laser driven ion acceleration is currently receiving particular scientific attention for its impressive applications, such as hadron therapy [1–3], nuclear fusion [4,5], use in material sciences and nuclear physics research [6], and other areas [7–9]. Cryogenic (solid) hydrogen targets provide an interesting medium for ion acceleration as they can be made relatively thin, with low density, lacking contaminants, debris-free, and can be used in high-repetition laser–target experiments [10–13].

In this work, we review our results on the prospect of increasing the quality of future ion acceleration driven by the current and forthcoming multi-(tens) PW laser systems (such as ELI Beamlines [14–16], APOLLON [17], ELI NP [18], and SEL [19]) using structured cryogenic targets. It is shown that, with the use of a 10 PW-class laser system with pulse duration over 100 fs and cryogenic targets of current thickness [11], the radiation pressure acceleration (RPA) [20] mechanism dominates over the target normal sheath acceleration (TNSA) [21,22] in both the number of accelerated protons (with energy > 10 MeV) and the maximal reached energies [23]. The laser–target conditions relevant for RPA has been

thoroughly investigated in this millennia, e.g., in Refs. [24–26], and the experimental indications of the RPA regime have already been observed [27–30]. Note that the laser–target condition optimal for RPA overlaps with other mechanisms investigated at moderately relativistic intensities [31], such as phase stable acceleration (PSA) [32,33], which is also referred to as coherent acceleration of ions by laser (CAIL) [34]. Usually, two subregimes of RPA are distinguished, the hole boring [35–37] for a relatively thick target and light sail [38,39] for ultrathin targets; the transitions between them can occur by decreasing the target areal density and/or increasing the laser pulse intensity [40]. Therefore, the thickness of the cryogenic target for the use of a 100 PW class laser system was reduced in our simulations [41] to be optimized for the RPA mechanism [20]. The properties of the generated particles can be improved using structured targets made of heavy and light ion layers [1,42–44] and by properly introducing instability, transforming the target into compact ion bunches either from the planar target [45] or the target with a modulated surface [46]. We investigate the introduction of the initial corrugation on the interface between the double-layer target [41] with a high intensity laser pulse. In these conditions a relativistic instability arises, which is determined by the target geometry, having features of the Rayleigh–Taylor (RTI) [47,48] and Richtmyer–Meshkov (RMI) [49,50] instabilities. Both of them are currently being thoroughly investigated [51–59]. They can be found on different space scales ranging from the parsec-size in astrophysics (e.g., the development of the filament structure of the Crab Nebula [60]) to a μm-size in laser-plasma, e.g., affecting the creation of the hot spot in the inertial fusion [61]. The main differences between RTI and RMI are shown via the experimental results [62,63] in Figure 1. The driving force is in principle continuous for RTI, resulting in exponential growth, therefore experiencing slower growth in early time in Figure 1 (left). RTI can occur only when the acceleration is being driven from lighter to heavier media [51]. In contrast, the RMI behavior is rather impulsive and a perturbation grows linearly in time, as shown in Figure 1 (right), and it can occur for shocks directed toward either side of the interface. In the case of heavy-light direction of acceleration, RMI exhibits a characteristic phase inversion of the corrugated interface, as was predicted in theory [53,64,65] and shown via experiment [63]. The inversion (switch of corrugation maxima and minima) is visible in Figure 1 (right), e.g., compare the position of maxima and minima in sub-figures (a) and (d). In contrast, the maxima and minima stay at the same position for RTI in Figure 1 (left).

The instability can be influenced by the fabricated interface corrugation to generate a high-density proton bunch, which can be accelerated by the radiation pressure as a compact structure. Therefore, the generated proton beam has good quality and properties such as low energy spread, divergence, and emittance [41].

In our simulations, we use a steep-front laser pulse to mitigate the development of other transverse instabilities (with relatively short wavelength) arising from laser–target interaction on the target surface, usually ascribed to Rayleigh–Taylor [45,66,67] or electron-ion coupled instability [68,69], as was proposed by theory [45] to increase the target stability. Without this treatment, the target can be shattered into many small bunches, ignoring the target geometry. We discuss the use of the plasma shutter (usually a thin solid foil attached to the front surface of the target with a gap between them) [70–79] to obtain the required pulse profile. In addition to the steep-rising front, the shutter can also locally increase the peak intensity of the laser pulse [78]. The obtained shape can improve the ion acceleration from the target located behind the plasma shutter, including higher maximal energy and lower divergence [79].

The paper is organized as follows. The simulation method and parameters of the simulations used in the particular subsections of results are described in Section 2. Section 3, which contains the results, is divided into three sections. First, the dominance of the RPA mechanism for the assumed parameters is shown in Section 3.1. The target thickness is then reduced, and the influence of the corrugated interface of the double-layer target, including the bunch generation with low emittance, divergence, and energy spread, is investigated and compared to similar targets in Section 3.2. Finally, the foil stability is discussed in

Section 3.3, comparing the results using steep-front and full-front laser pulses. The use of the plasma shutter for our concept and for heavy ion acceleration from different targets is also discussed in this section. Appendix A contains the description of the virtual reality application (called VBL-Virtual BeamLine) used for visualization of our results.
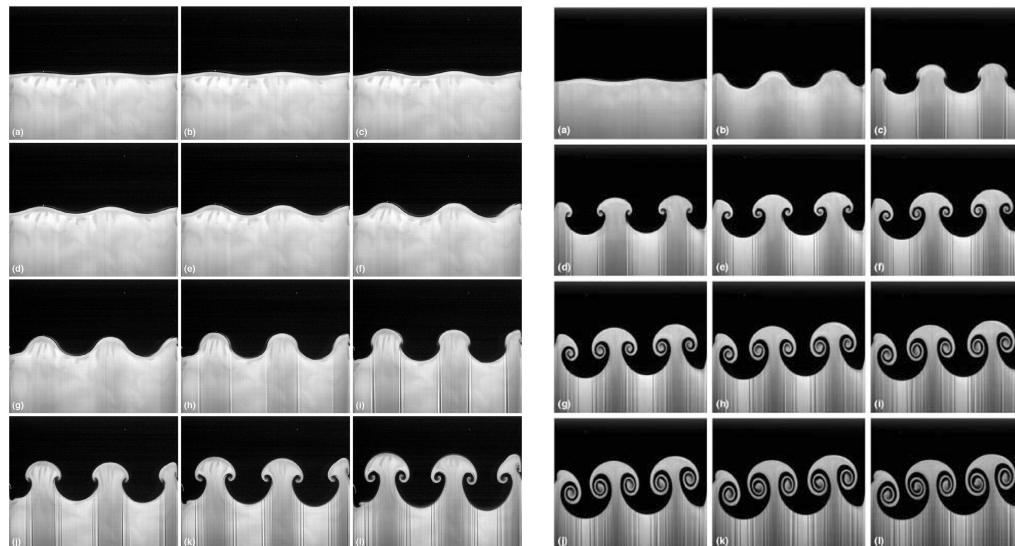


**Figure 1.** Difference between RTI and RMI in a sled experimental setup. (**left**) RTI, the time increment between each subsequent image is 33 ms. Reprinted from [62], with the permission of AIP Publishing. (**right**) RMI, the first image is at time before the shock is delivered, the time increment between each other subsequent image is about 83.5 ms (66 ms between the last two ones). Source [63], reproduced with permission.

## 2. Methods

We performed 2D and 3D particle-in-cell simulations using the code EPOCH [80]. In Sections 3.1 and 3.2, the quantum electrodynamics (QED) module [81] resolving non-linear Compton scattering is included in the simulations, assuming high intensity interaction. The EPOCH default Yee solver was used, and current smoothing option was applied. In Section 3.1, the triangular shape of particles was used, whereas the preprocessor directive for 3rd order b-spline shape function of the quasi-particles (PARTICLE_SHAPE_BSPLINE3) was used in Sections 3.2 and 3.3. The main laser–target simulation parameters are shown in Table 1, and further simulation details are described in the following paragraphs of this section.

**Table 1.** The main laser–target simulation parameters. In order: Intensity $I$, polarization, wavelength $\lambda$, width of Gaussian space profile at FWHM, temporal shape-duration for $\sin^2(t)$ and FWHM for Gaussian, target material, thickness, and electron density $n_e$ in the corresponding critical density $n_c$.

| Section | $I$ [W/cm²] | Pol. | $\lambda$ [µm] | Width [µm] | $t$-Shape | Target | Thickness | $n_e$ [$n_c$] |
|---|---|---|---|---|---|---|---|---|
| 3.1-2D | $3 \times 10^{22}$ | p | 1.1 | 5 | $\sin^2(t)$ 320 fs | H | 25 µm | 56 |
| 3.1-3D | $1.5 \times 10^{22}$ | p | 1.1 | 5 | $\sin^2(t)$ 200 fs | H | 15 µm | 56 |
| 3.1-VR | $3 \times 10^{22}$ | p | 1.1 | 5 | $\sin^2(t)$ 200 fs | H | 15 µm | 56 |
| 3.2-2D | $1.37 \times 10^{23}$ | s | 1.0 | 10 | Gauss 26.7 fs | $^2$H-H | (1 + 1) µm | 48 |
| 3.3-3D | $1 \times 10^{22}$ | p | 1.0 | 3 | $\sin^2(t)$ 64 fs | Shutter Si₃N₄ | 20 nm | 835 |
| | | | | | | Target Ag | 20 nm | 2100 |

In Section 3.1, the laser pulse parameters of the reference 2D case are as follows: p-polarization, peak intensity $I = 3 \times 10^{22}$ W/cm², wavelength $\lambda = 1.1$ µm, beam width is 5 µm, and full pulse duration is 320 fs for $\sin^2(t)$ shape in intensity. Its energy corresponds

to a Gaussian temporal profile with 150 fs FWHM. The peak power is about 9 PW and energy is 1.35 kJ. Dependence on intensity ranging between $I = 0.375 \times 10^{22}$ W/cm$^2$ and $I = 3 \times 10^{22}$ W/cm$^2$ is also discussed while keeping the other parameters same (i.e., changing pulse energy and power). The intensity of $I = 1.5 \times 10^{22}$ W/cm$^2$ was used for 3D simulation. The target is made by 25 μm thick fully ionized hydrogen target with electron density of 56 $n_{c1.1}$, where $n_{c1.1}$ is the non-relativistic critical density for $\lambda = 1.1$ μm. For the 3D simulations and virtual reality visualization, the laser and target parameters were reduced by a factor of 5/3 to 200 fs and 15 μm. For 2D simulations, square cells with the size of 20 nm are used. Each cell occupied by plasma contains 56 electrons and 56 protons. For the 3D simulation, the cell size is 20 nm in the longitudinal direction and 30 nm in the transverse direction. The number of particles per cell was reduced to 10 electrons and 10 protons. More information about simulation parameters can be found in [23].

In Section 3.2 (and the first part of Section 3.3), the laser pulse parameters are as follows: s-polarization (electric field is perpendicular to the plane of incidence), peak intensity $I = 1.37 \times 10^{23}$ W/cm$^2$, wavelength $\lambda = 1$ μm, beam width is 10 μm, beam duration at FWHM is equal to 8 laser periods $T$. The steep front is realized by filtering out the low-intensity part at the front of the laser pulse until 2.4 $T$ (i.e., 30% of FWHM) before the peak of the temporal Gaussian profile. The double-layer target consists of light (solid hydrogen) and heavy (deuterium) ion layers. The electron density is same in both layers $n_e = 48\, n_c$, where $n_c$ is the non-relativistic critical density for $\lambda = 1$ μm. The deuterium layer has the same electron and ion number density as the proton layer, but two times heavier ion mass. Square cells with the size of 10 nm are used. Each cell occupied by plasma contains 48 electrons and 48 protons/deuterium ions. More information about simulation parameters can be found in [41].

In the rest of Section 3.3 (results with the plasma shutter), the laser pulse parameters are as follows: p-polarization, peak intensity $I = 1 \times 10^{22}$ W/cm$^2$, wavelength $\lambda = 1$ μm, beam width is 3 μm, and full pulse duration is 64 fs for $\sin^2(t)$ shape in intensity. Its energy corresponds to Gaussian temporal profile with 30 fs FWHM of 1 PW laser pulse. The plasma shutter is made of silicon nitride (Si$_3$N$_4$) solid foil. Full ionization of the foil is assumed with electron density $n_e = 835\, n_c$, where $n_c$ is the non-relativistic critical density for $\lambda = 1$ μm . The thickness of the plasma shutter is set to 20 nm. The target, located behind the plasma shutter, corresponds to a silver solid foil with thickness of 20 nm. Partial ionization of the target is assumed (charge number $Z = 40$), electron density is $n_e = 2100\, n_c$. The mesh has square cells of the size 3 nm in 2D simulations and cuboid cells of the size 5 nm in the laser propagation direction and 25 nm in the transverse ones in 3D. The number of electrons in 2D is 835 particles per cell inside the plasma shutter (400 in 3D) and 1050 inside the target (1000 in 3D), respectively. The numbers of ions correspond to their charge ratios. More information about simulation parameters can be found in [78,79].

## 3. Results

### 3.1. The Prominence of Different Acceleration Mechanisms Using Cryogenic Targets

In order to properly optimize the target thickness and structure, one first needs to know which acceleration mechanism to focus on. More mechanisms usually occur during the laser–target interaction, and their interplay depends on the target and laser parameters [82]. Currently, the most employed acceleration mechanism is the target normal sheath acceleration (TNSA) [21,22]. In this section, we examine the shift from the TNSA dominated regime with the increasing laser pulse intensity for low density cryogenic targets of current thicknesses [11] and 10 PW class laser systems with pulse duration over 100 fs. Understanding of this topic then helps with choosing the parameters used for the structured cryogenic target in Section 3.2.

In our simulations [23], the assumed intensity ranges between $I = 0.375 \times 10^{22}$ W/cm$^2$ and $I = 3 \times 10^{22}$ W/cm$^2$; the thickness of the fully ionized hydrogen target is 25 μm. We focuses on the difference of the well established TNSA mechanism and the emerging

mechanisms that differ from it, mainly radiation pressure acceleration (RPA). These two mechanisms can be clearly distinguished from each other at the early and middle stages as they act at different positions of the target. The TNSA gets involved on the rear side of the target, whereas the RPA is acting on the front side and interior of the target. This behavior is shown in Figure 2 using the proton energy layers (i.e., protons at various energy intervals in the 2D simulation area) for the peak laser intensity $I = 3 \times 10^{22}$ W/cm$^2$. The conversion efficiency of the laser pulse energy to the high-energy protons (exceeding 10 MeV) in this case is about 27%.
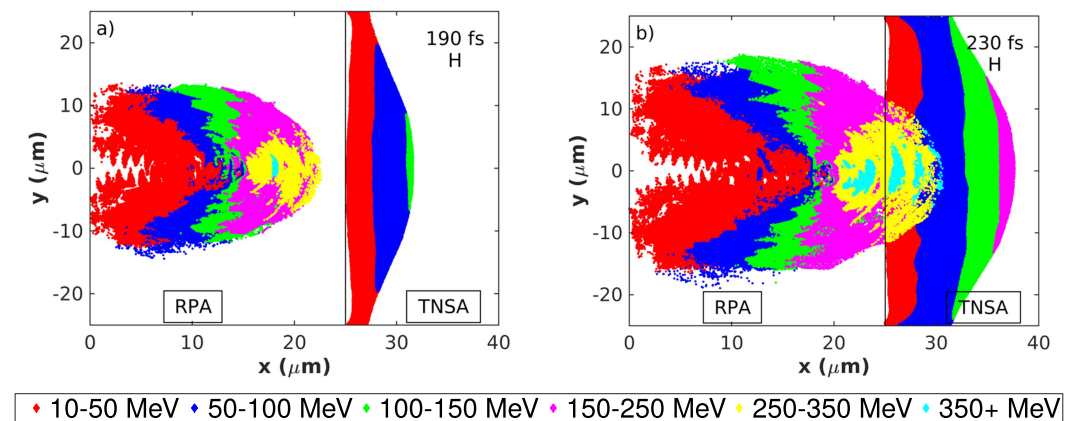


**Figure 2.** Proton energy layers for hydrogen target: (**a**) at 190 fs (**b**) at 230 fs from the beginning of laser–target interaction. The initial position of the target is between 0 μm and 25 μm (denoted by the black line). Republished with permission of IOP Publishing, Ltd., from [23], permission conveyed through Copyright Clearance Center, Inc.

The highest energies in the first stage (Figure 2a) are achieved by the RPA regime in the target interior. Here, the low density of the target provides good conditions for the hole boring phase of the RPA mechanism. The hole boring velocity inferred from our simulation is $u_{hb} = 0.31\ c$, which is slightly higher than the theoretical value of $u_{hb} = 0.26\ c$ calculated using the analytical model [36]. The character $c$ denotes speed of light in vacuum. In the second stage (Figure 2b), the target is still not transparent for the laser pulse, and the most energetic protons from the inside of the target (accelerated to velocities higher than $u_{hb}$) enter into the TNSA field behind the initial position of the target rear side (denoted by the black line). Although the ions from both populations are now located in the same area, they can still be distinguished from one another by the combination of their energy and position. The energy of protons accelerated by the TNSA mechanism strongly depends on their distance from the target rear side, with the most energetic protons located on top of the proton cloud, as can be seen in Figure 2a. Therefore, the entering RPA protons can be distinguished by their significantly higher energy, which does not fit the energy layer of the surrounding TNSA protons. Thus, RPA results in higher proton energy than TNSA also in this stage. The separation of the two populations is more visible in the pseudo-3D visualization, with the proton energy represented also by the vertical height (Figure 3). Here, the laser pulse (incoming from left) is represented in the gray scale, the electron density by the turquoise scale, and the scale for proton energy is ranging from white (zero energy) to purple (about 400 MeV) to light blue (over 600 MeV). Note that for this visualization, the laser and target parameters were reduced in the similar way as for the 3D simulations (factor of 5/3) discussed below, and only the protons reaching the highest energy at the end of the simulation (above 300 MeV) are being tracked (see more information in [83] and in Appendix A). The interactive visualization (available online [84]) is made in the virtual reality web-based application [85], discussed in Appendix A.
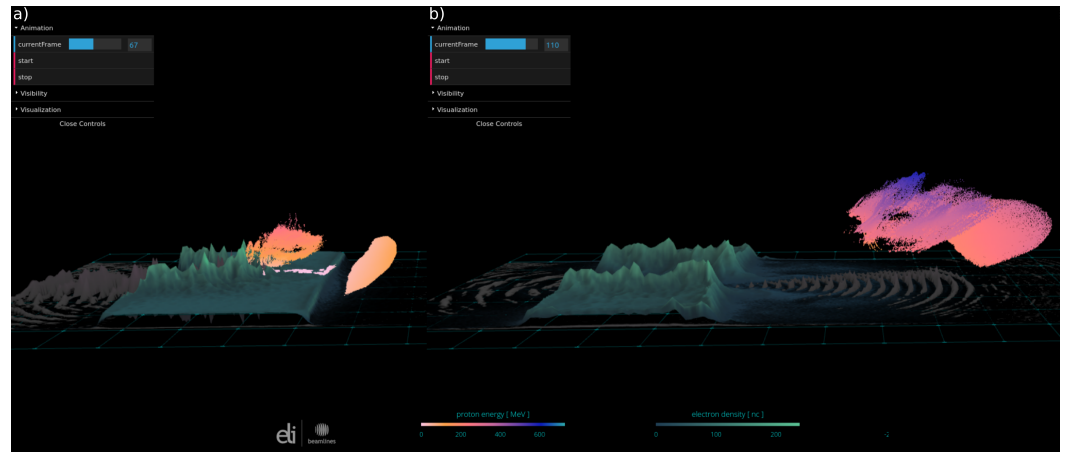
**Figure 3.** VBL visualization of different proton populations using the hydrogen target: (**a**) at time frame 67, (**b**) at time frame 110. The dots represent the simulated protons (only protons that exceed 300 MeV at the end of the simulations are included); the vertical height and color denote their energy using the white–red–blue scale. Laser pulse intensity is represented by the gray scale, electron density by the turquoise scale, and both values are also visualized using the vertical height. The interactive VBL application of the full time evolution is accessible online [84].

The third stage may occur if the laser pulses reach the rear side of the target and eventually punch through it, which happens around time $t = 270$ fs in the simulation with maximal intensity shown in Figure 2. The protons can be further accelerated to very high energies around the onset of the relativistic transparency by regimes such as the hybrid RPA-TNSA mechanism [86,87], break-out afterburner [88,89] and directed Coulomb explosion [90]. To see the dependence of the mechanisms interplay on intensity, other simulations were performed with the same parameters but with lower pulse intensities (and thus lower pulse power). Figure 4a shows the time evolution of the maximal reached proton energy by RPA (solid lines) and TNSA (dashed lines) in these simulations. Note that, for the times after the laser pulse burns through the target, all the ions originated from the target interior are labeled as RPA in Figure 4a for the sake of brevity.
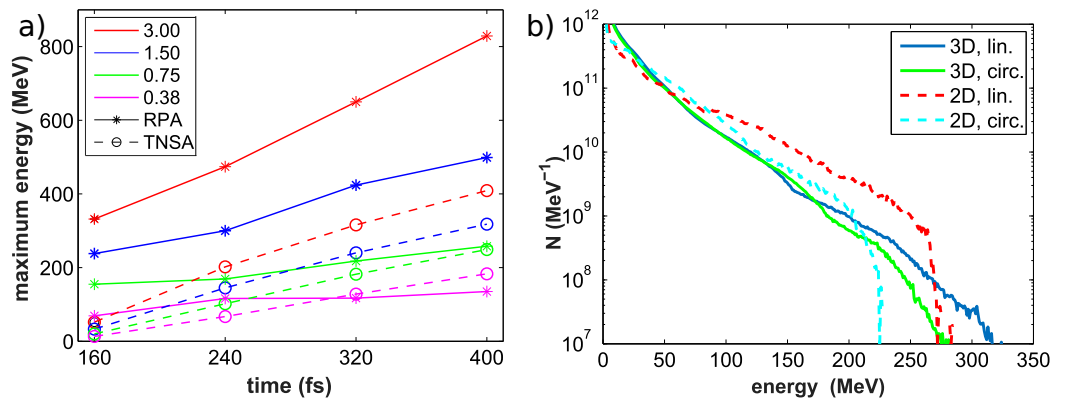


**Figure 4.** Maximal proton energy and ion spectra from hydrogen target. (**a**) Temporal evolution of maximum energies of protons accelerated by the RPA and TNSA mechanisms for various laser intensities. (**b**) Proton energy spectra for linearly and circularly polarized laser beams in 2D and 3D simulations at 260 fs from the beginning of the laser pulse interaction. Target thickness is reduced to 15 μm and pulse duration to 200 fs. Peak intensity $I = 1.5 \times 10^{22} \text{W/cm}^2$. Republished with permission of IOP Publishing, Ltd., from [23], permission conveyed through Copyright Clearance Center, Inc.

The RPA mechanism accelerates protons to higher energies than the TNSA in our simulations with intensities above $0.75 \times 10^{22} \text{ W/cm}^2$. Note that, for these simulations, the

laser pulse reached the rear side of the target, as further discussed in reference [23]. For the lowest intensity case, the target is too thick for an efficient RPA acceleration, and the TNSA plays the role of the dominating mechanism in the sense of proton energy.

Two-dimensional simulations are known to usually overestimate the maximal reached energy and heating of electrons (especially in the linear p-polarization) [89,91]. Therefore, our findings are also verified via 3D simulations. Intensity $I = 1.5 \times 10^{22}$ W/cm$^2$ is chosen for the demonstration. Both the laser pulse duration and target thickness are reduced by a factor of 5/3 to 200 fs and 15 μm due to computational constraints. Corresponding 2D simulations with the same reductions and simulations with the circular polarization were also performed for comparison. The proton energy spectra at the time 260 fs are shown in Figure 4b. Unexpectedly, the 3D simulations resulted in higher maximal energy than their 2D counterparts for our parameters with a relatively thick target. Further examination by separation of TNSA and RPA protons shows that only the energy of ions accelerated by RPA is higher in the 3D simulations. For example, before mixing these two populations at time 180 fs, the maximal energy of RPA protons increases from 180 MeV to 255 MeV when the third dimension is included. In this stage, the RPA mechanism represents a clear hole boring phase. This increase can be explained with the effect of the self-focusing of the laser beam propagating in the plasma. The laser pulse intensity is thus higher in 3D, as the self-focusing is not limited into just one plane as it is in 2D (see the comparison of electron density and electric field in Figure 6 in [23]). Consequently, the hole boring velocity (and thus the proton energy) is higher in 3D.

In contrast, at the same time instant, the energy of protons accelerated by pure TNSA decreases from 155 MeV to 80 MeV, which corresponds to the previous observations related to higher electron heating in 2D [91].

Circular polarization is often proposed for the laser pulse interaction with ultra-thin targets as it can improve the foil stability and reduce the electron heating and consequently results in higher ion energy [28,66,67,92]. In our simulations, these advantages diminish as the larger thickness of the target prevents it from immediately breaking. The electron heating at later stages is also similar in the linear and circular polarization due to the bending of the target surface (see the discussion in [23]). Therefore, the proton energy spectra of 3D simulations are similar until the energy is approximately 185 MeV. The linear polarization enhances the tail of the proton spectrum, resulting in higher maximal energy than the circular one in our simulations. This behavior can be ascribed to the presence of the oscillatory component of the ponderomotive force.

### 3.2. Improving Ion Properties Using Double-Layer Targets with Interface Corrugation

On the basis of our findings in the previous section, we choose the cryogenic target optimized for the RPA mechanism in our next study involving future 100 PW class laser systems. The optimal thickness $l$ [20] of such a target can be expressed as:

$$\frac{l}{\lambda} = \frac{a_0}{\pi} \frac{n_c}{n_e},$$

(1)

yielding the thickness of 2 μm for our laser and target parameters (see Section 2). Here, $a_0$ is the dimensionless amplitude of the laser electric field.

The properties of the ions accelerated from the solid target can be improved by its proper structuring. In our preliminary results in [93], we briefly compared the sinusoidal corrugation on the interface of a double-layer target with the one on the surface of single-layer-target and with the target without a corrugation (see Figure 5a–c).
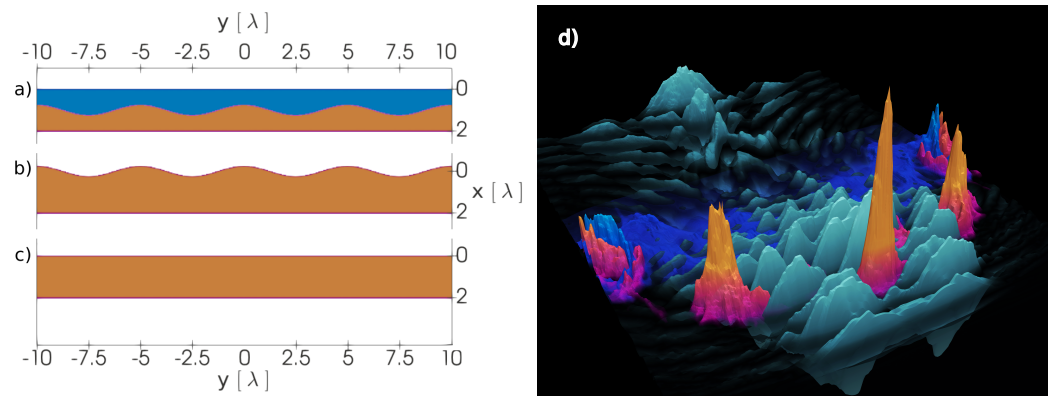
**Figure 5.** Structured targets and generation of proton bunch, source of the left part (**a**–**c**) [76]. Initial configuration of deuterium layer (blue) and proton layer (orange) in the cases: (**a**) double–layer target with the modulation on the interface, (**b**) single–layer target with the modulation on the front surface, (**c**) without the modulation. (**d**) Visualization of case (**a**) during the laser–target interaction. Coloring: electric field (gray), density of deuterium (blue) and hydrogen (orange). Colors saturated with maximum value set to the initial density. Values are also represented by the vertical height. The distinguished high density proton bunch enfolded by the laser pulse is developed. Source of (**d**): [94].

The corrugation located at the interface of a double-layer target is especially interesting as it resulted in a significant peak in ion spectra (more significant than in the reference case of surface modulation as is briefly discussed in Section 3.3). The interface corrugation was then thoroughly investigated in [41]. Figure 5d contains the visualization of the target density (deuterium: blue, proton: orange) and laser pulse electric field (gray). The values are also represented by the vertical height. The interaction of the laser pulse with the target results in the rise of the relativistic instability, with RTI and RMI features depending on the target geometry. The target is fractured into high density regions (located around the initial corrugation maxima at positions $-5$ μm, 0 μm, and 5 μm) and low density regions between them (around the initial minima). Moreover, as can be seen in Figure 5d, the laser pulse enfolds the central proton bunch, limiting the bunch broadening in space. Therefore, the ions are accelerated by the radiation pressure as a compact structure, having a low energy spread. The quality and properties of these protons are summarized in Figure 6a–c.
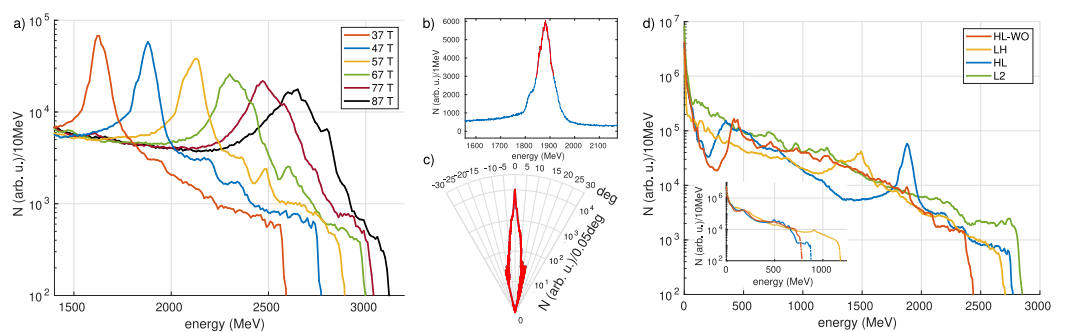


**Figure 6.** Properties of the ion beam. (**a**) Time evolution of the tail of the proton energy spectra in the HL case, (**b**) proton energy spectra of the HL case at time t = 47 T, with highlighted FWHM section used for (**c**) angular distribution, (**d**) proton energy spectra (corresponding deuteron energy spectra in inset) for various targets (see details in the text) at time t = 47 T. Reprinted from [41], with permission from Elsevier.

Figure 6a shows the time evolution of the tail of the proton energy spectra. Although the bunch structure is spreading in the later stages, the bunch structure is presented until the end of the simulation. Moreover, the structure is gradually shifting towards the end of the energy spectra with time. The time at 47 T (blue line) is further examined in Figure 6b,c. The average energy of the bunch is 1882 MeV, its bandwidth at FWHM is 67 MeV, and

energy spread is about 3.7%. The energy conversion of the laser pulse into the protons inside the bunch is around 3.4%. The conversion into all protons propagating in the forward direction is around 28.7%. The red part of Figure 6b denotes the part of the beam above its FWHM. The angular spectrum of this red part is shown in Figure 6c using the logarithmic scale. The beam is well collimated, with the angular spread $2\theta = 0.65°$ (at FWHM), the solid angle $\Omega = 2\pi(1 - \cos(\theta)) = 0.1$ mrad, the normalized rms transverse emittance [95] $\epsilon_{rms} = \sqrt{\langle y^2 \rangle \langle p_y^2 \rangle - \langle y p_y \rangle^2}/m_p c = 0.046$ mm · mrad, where $m_p$ and $p_y$ are proton mass and momentum in the $y$-direction. This emittance is one order of magnitude lower than in the case of conventional proton accelerators [96], but still one order of magnitude higher than the emittance reported in [97] (where the energy range of protons was lower than in our case, up to 10 MeV). The transverse emittance can be also defined in real space via the beam divergence as in [98], yielding emittance $\epsilon_y = 0.218$ mm · mrad and divergence $\Theta_{div} = 0.038$ rad.

To show the effect of the corrugation, this simulation of the deuterium-proton layer (configuration shown in Figure 5a), denoted as HL (heavy-light), is compared with other simulations. Specifically, simulations of a double-layer target without corrugation (HL-WO), the double-layer target with corrugation, but with opposite order of layers (LH, light-heavy), and the single-layer hydrogen target (L2), (see the details in [41]). Both cases without the corrugation (HL-WO and L2) do not provide a significant peak in the energy spectrum (Figure 6d). The LH case provides a peak but with lower energy and higher energy spread. This behaviors correspond to the proton density shown in Figure 7.

Here, the density is denoted by the vertical height, and the color represents the proton energy at that position. Both simulations with corrugations (Figure 7a,b) generate and maintain the high density bunches influenced by the target geometry as described above. In contrast, the non-corrugated cases (Figure 7c,d) generate a bubble structure typical for RPA acceleration of a planar target [45]. The RPA mechanism then can accelerate a smaller part of the particles at the bubble front to very high energies, but without the desired peak in the proton energy spectra, which is provided by the corrugation.

The influence of different laser polarization and corrugation wavelengths in the HL case is also thoroughly investigated in [41]. The instability leading to bunch generation (and peak in the ion energy spectra) also developed in the case of p-polarization. However, the central bunch was significantly smaller compared to the s-polarization case (shown in this section). This behavior was explained by artificially greater electron heating in the simulation plane in the p-polarization, as previously demonstrated in [89,91]. In contrast, the instability was mitigated in the case of circular polarization, and the ion bunch was not generated. The optimal corrugation wavelength was shown to be around the half of the size of the focal spot, which is used in the simulations in this section.
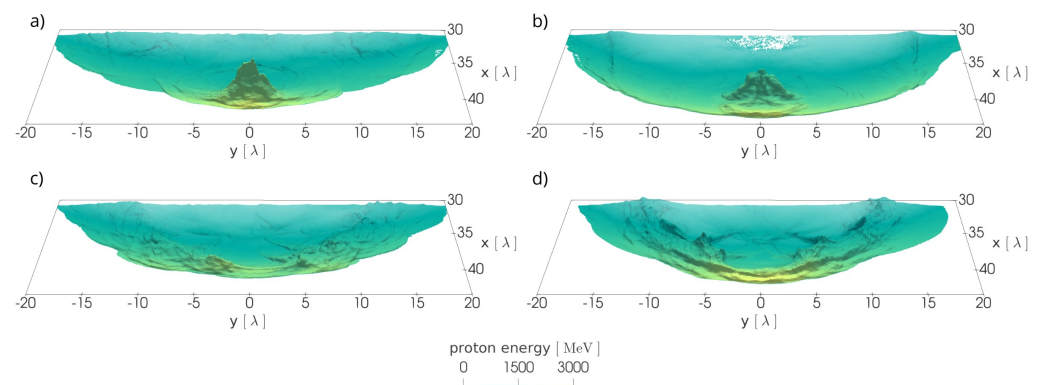


**Figure 7.** Spatial density distributions at time t = 47 T. The proton density is represented by the vertical height, and proton energy is represented by the blue to yellow scale. The simulated cases are: (**a**) HL, (**b**) LH, (**c**) HL–WO, (**d**) L2 (see parameters of all the targets in the text). Reprinted from [41], with permission from Elsevier.

### 3.3. Target Stability and Generation of the Steep-Front Laser Pulse

The foil stability is often worsened by the onset of unwanted kinds of instabilities. Especially with the treatment of a relatively short wavelength (independent on the target geometry), transverse instability arising from the laser–target interaction needs to be assumed. This instability is usually ascribed to Rayleigh–Taylor [45,66,67] or electron–ion coupled instability [68,69]. For the sake of brevity and its shorter wavelength compared to the desired instability driving the bunch generation discussed in Section 3.2, this instability will be referred to as short-wavelength instability regardless of its origin hereinafter. Its uncontrolled development results in the lower efficiency of ion acceleration in our case, as the target is shattered into many small bunches, as can be seen in Figure 8a.
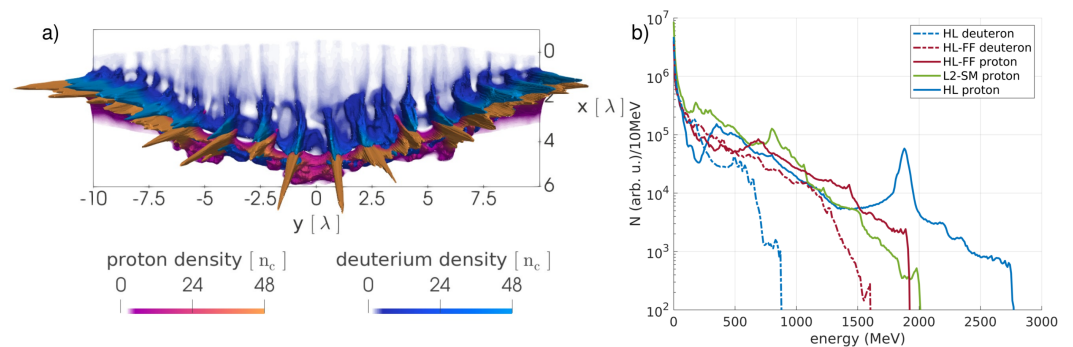


**Figure 8.** Short-wavelength instability. (**a**) Spatial distributions in the HL-FF (with full-front laser pulse) case at time t = 14 T. Blue and red scales represent deuterium and proton densities, with maximum value set to the initial density. Full density is indicated by the vertical height. (**b**) Proton and deuteron energy spectra for HL (steep-front, interface corrugation), HL-FF (full-front, interface corrugation), and L2-SM (steep-front, surface corrugation) cases at time t = 47 T. Reprinted from [41], with permission from Elsevier.

As noted in Section 3.1, circular polarization is often used for improving foil stability by mitigation of instabilities. However, circular polarization cannot be applied to our scheme, as it would weaken both the desired and unwanted instabilities, lowering the energy and quality of the proton beam in our simulations (see details about polarization dependence in [41]).

In our simulations, we use a steep-front laser pulse as proposed by theory [45]. Under this condition, the unwanted short-wavelength (RTI-like) instability does not have enough time to significantly develop. On the contrary, the wanted relatively long-wavelength instability induced by the target geometry (with RMI features) can immediately respond to the high radiation pressure and develop properly. This approached was used in all simulations presented in Section 3.2, where the steep-front was simulated by filtering out the beginning of the laser pulse until 2.4 *T* before the peak of the laser pulse. The simulation shown in Figure 8a represents the uncut full front, being 8 *T* longer. The effect of the laser front steepness on ion acceleration is shown in the ion energy spectra in Figure 8b. With the use of the full-front laser pulse (HL-FF), the distinctive good-quality peak in the proton spectrum is not developed. A less distinctive, relative broad peak is present, but at significantly lower energy compared to the steep-front case. The proton spectrum is somehow similar to the one of a single-layer hydrogen target with corrugation on its surface (L2-SM, configuration shown in Figure 5b), where the driving instability also originated from the surface. The foil disruption in the HL-FF case also reduces the maximal proton energy. In contrast, the energy of deuterons from the first layer is enhanced compared to the steep-front case, as they are more mixed with the protons.

The required steep-front laser pulse can be generated by several phenomena. If the laser pulse propagates through an underdense plasma [99–101] or a near critical density plasma [102–108], the desired shape can develop through the nonlinear evolution of the laser pulse. Another method is to use a thin overdense plasma foil (usually referred to as

a plasma shutter [70–79]). The front of the laser pulse (with low intensity) is filtered out and the desired (high intensity) part propagates through the foil undergoing relativistic transparency, gaining the steep-front profile. In our further research, we focuses on the plasma shutter technique, first with a PW-class laser pulse utilizing a silicon nitride ($Si_3N_4$) plasma shutter. The plasma shutter made of this material has several advantages, such as a well defined surface, commercial availability in various thicknesses, and high quality of mechanical and optical properties [109,110]. A visualization of our 3D simulation [78] is shown in Figure 9a.
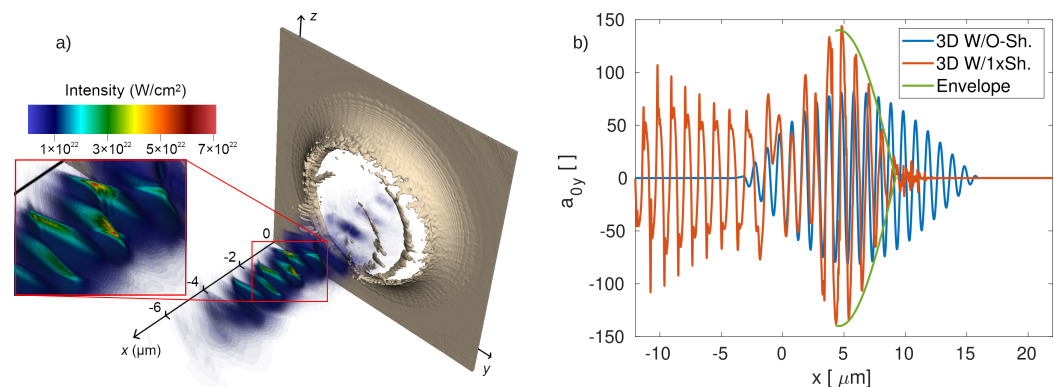


**Figure 9.** Plasma shutter. (**a**) The distribution of the laser intensity in the horizontal slice of the laser pulse from 3D simulation with the plasma shutter when the maximum intensity value is reached, source [78]. (**b**) The 1D profile (at $y = 0$ and $z = 0$) of dimensionless amplitude of the electric field in the $y$-direction ($a_{0y}$) after the laser pulse propagates through the plasma shutter in the 3D simulation. Comparison of the transmitted laser pulse (W/1xSh) with the original one (W/O–Sh). Steep front is generated, its envelope is approximated using the equation $y = 140 \cdot \sin(\pi \cdot x/9.2)$. Source [79]. Figures reprinted under the terms of the Creative Commons Attribution 4.0.

The laser pulse burns through the plasma shutter, shaping its profile and creating the so-called relativistic plasma aperture [111]. Consequently, the laser pulse is diffracted on such an aperture and, due to its constructive interference with generated high harmonics, the local intensity is amplified [78]. Local amplification by a factor of 7 (from the initial intensity of $1 \times 10^{22}$ W/cm$^2$) can be seen in the highlighted area of Figure 9a, where the 2D profile of the laser pulse intensity in the polarization plane (*x-y*) is shown. Figure 9b shows the 1D profile (at the center of the pulse) at a later time, when the envelope stabilizes [76]. The blue line represents the original pulse in the simulation without the plasma shutter (W/O-Sh), and the red line is from the simulation with the plasma shutter (W/1xSh). The pulse front is about five periods shorter and significantly steeper compared to the original pulse. The maximal amplitude of this central (1D) profile is also enhanced, although the main intensity amplification occurs off-axis, as shown in Figure 9a. The application of the produced laser pulse for ion acceleration from a silver target was briefly investigated, with the preliminary results in [76], and then thoroughly discussed in [79], where the position of the target was also optimized. The setup of this 3D simulation is shown in our VR application in Figure 10, where the laser pulse (incoming from the left) is represented by the red color scale, electron density of the shutter is represented by the blue scale, and the density of silver ions from the target are represented by the green scale.
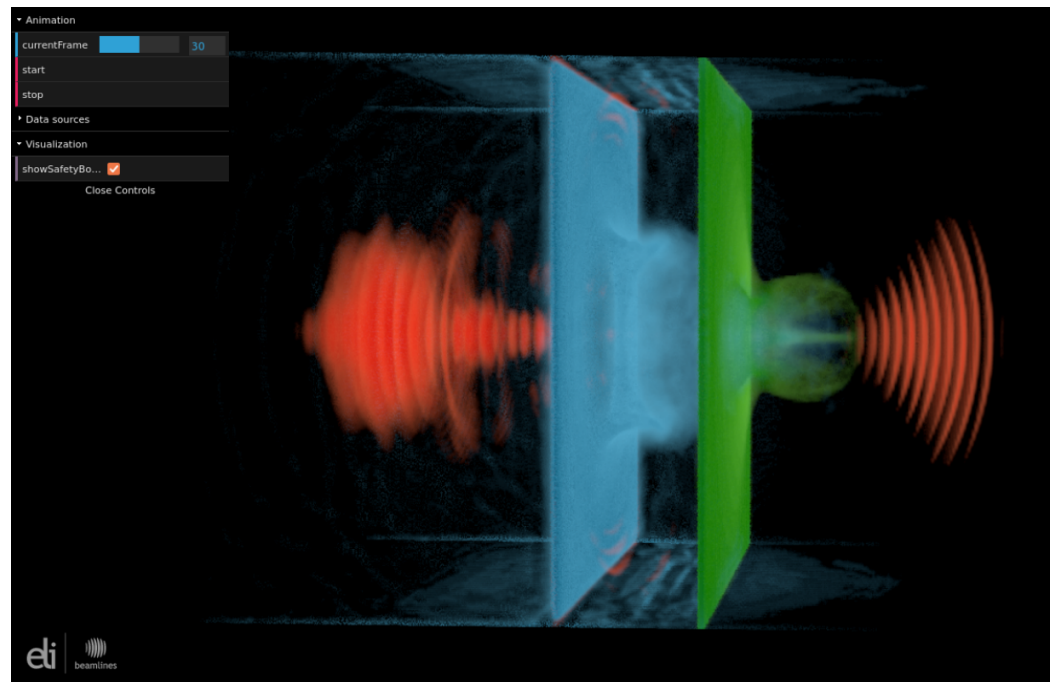
**Figure 10.** Application of the plasma shutter with a silver target: VBL visualization of our simulation of 1 PW laser (electric field: red color) interacting with the plasma shutter (blue: electron density) and the silver target (green: ion density). Laser pulse is shaped by the plasma shutter (resulting in the aperture) and accelerates ions from the silver target. A high energy ion beam with low divergence is generated. Data used for this visualization come from [79]. The interactive VBL application of the full time evolution is accesible online [112].

The use of the plasma shutter can result in an increase in maximal energy of heavy ions, as shown in Figure 11a, although a part of the laser pulse energy is lost during the development of the aperture [79]. For the linear polarization, the maximal energy of silver ions at the end of the simulation increases from 115 to 155 MeV per nucleon (about 35%) when the plasma shutter is included in the simulation. The same effect is also observed for the circular polarization, where the maximal energy increase is even slightly higher (about 44%). Moreover, in the case of linear polarization, the divergence of the accelerated ion beam in the $x$-$z$ plane (Figure 11c) significantly decreases as the ions are focused towards the laser axis in the plane perpendicular to the laser polarization. This beam-like structure is visible in Figure 10 behind the silver target (green color) around the laser axis. The shutter also has a positive effect on the beam divergence in the $x$–$y$ plane, as shown in Figure 11d; this effect was ascribed to the steep-front generation. The transverse instability in ion density (similar to the instability in Figure 8a) is also reduced when the shutter is included (and the steep-front is generated); see the full discussion in [79]. This finding corresponds to the results discussed above. In addition, two (or a series of) plasma shutters can be used to mitigate the prepulses accompanying the main pulse, thus also improving the laser contrast. The double-shutter scenario was investigated using a combination of 2D PIC and hydrodynamic simulations in [79]. The first shutter can withstand the assumed sub-ns prepulse (treatment of ns and ps prepulses by other techniques is assumed; alternatively increasing the thickness of the first shutter may filter out longer prepulses), whereas the steep front generation and the local intensity increase occurred via interaction with the second non-expanded shutter. The increase in the maximal ion energy compared to the 2D simulation without any shutter is also demonstrated in this case. A prototype of such a double shutter is presented and the design of the whole shutter-target setup is discussed in [79].
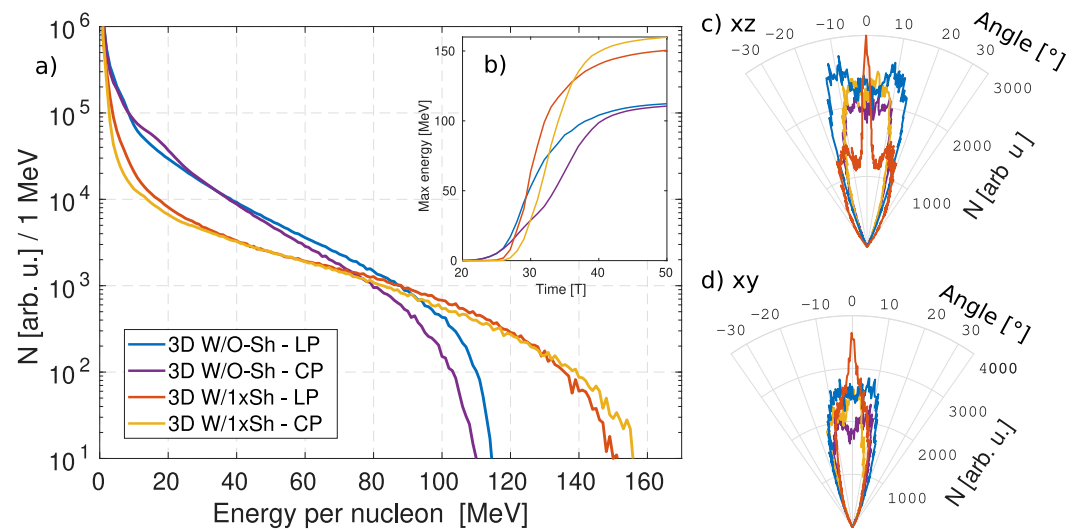
**Figure 11.** Properties of silver ions from the 3D simulations with the plasma shutter (W/1xSh) and without (W/O-sh) for linear (LP) and circular (CP) polarization. (**a**) Energy spectra at the end of the simulation ($t = 70\ T$), (**b**) time evolution of the maximal energy. Angular distributions of ions with energy over 55 MeV per nucleon in the *x-z* plane (**c**) and *x-y* plane (**d**). Source: [79]. Figures reprinted under the terms of the Creative Commons Attribution 4.0.

According to our findings, the plasma shutter provides a promising possible solution to the question of target stability via steep-front laser pulse generation. However, further research and optimization is required for its application for the interaction of 100 PW class lasers with double-layer targets.

## 4. Discussion

In this work, we review our results on the prospect of improving the quality and properties of protons accelerated by future laser systems using cryogenic targets. It is shown that, for these low density targets, the RPA mechanism can become the dominant acceleration regime. The domination is stronger with increasing laser intensity. The use of structured double-layered targets with interface corrugation in our simulations results in the occurrence of a relativistic instability influenced by the target geometry. Its development leads to the generation of a high-density and high-energy proton bunch. This bunch is accelerated by the dominant RPA mechanism as a compact structure, resulting in a proton beam of high quality. It includes low divergence, transverse emittance, and energy spread of accelerated protons. This beam is not developed in the reference cases without the corrugation on the target interface.

We further discuss the stability of this laser–target interaction. Another instability arising rather from the laser interaction with the target surface (with shorter wavelength compared to the interface corrugation assumed) needs to be reduced in order to generate the high-quality proton bunch. It is shown that the development of this short-wavelength instability is mitigated using a steep-front laser pulse. We propose the use of the plasma shutter to obtain the required laser pulse shape. Although a part of the laser pulse energy would be lost, the transmitted laser pulse will gain the steep-front time profile and locally increase the peak pulse intensity. This concept has been shown advantageous for ion acceleration using a PW-class laser pulse, improving both the maximal ion energy and beam properties [79].

The optimization of shutter parameters for use with the structured targets and laser systems with higher power assumed in this work will require additional research. The fully 3D simulation of this concept will be performed in the future.

## Abbreviations

The following abbreviations are used in this manuscript:

| | |
|---|---|
| RPA | Radiation Pressure Acceleration |
| TNSA | Target Normal Sheath Acceleration |
| RTI | Rayleigh–Taylor Instability |
| RMI | Richtmyer–Meshkov Instability |
| HL | Heavy-Light |
| LH | Light-Heavy |
| HL-WO | HL without Modulation |
| L2 | Light Single-Layer with the Same Thickness as HL |
| HL-FF | HL with Full-Front Laser Pulse |
| L2-SM | L2 with Surface Modulation |
| W/O-Sh | Without Plasma Shutter |
| W/1xSh | With Plasma Shutter |
| VBL | Virtual BeamLine |
| VR | Virtual Reality |

## Appendix A. Virtual Reality Visualization

Virtual reality (VR) technology is receiving more and more attention in the field of scientific visualization. It utilizes computational power and human–machine interaction concepts to emulate the effect of a 3D world. The audience uses a VR headset (i.e., a device worn on the head having small display(s), with embedded lenses and semi-transparent mirrors) and VR controllers to interact with the objects representing the scientific datasets and explore their complicated spatial and temporal structures in a way that makes them easy to understand.

At ELI Beamlines, we use a custom WebGL [113] render solution in the form of a complex web client–server application running inside a regular web browser. The application, called Virtual Beamline—VBL [114], renders the output of interactive visualization in real time (i.e., at sufficiently high frame rates) to user's regular and VR displays. The VBL application has been used not only for research itself, but also for educational purposes and science popularization. The use of the VR stations located at the atrium of ELI Beamlines is shown in the upper part of Figure A1, running the visualization discussed in Section 3.1.

**Figure A1.** VBL application. (**top**) The use of the VBL application on the VR stations at ELI Beamlines (photo from [83]). (**bottom**) Example of a visualization based on the 3D PIC simulation data [116] using the VBL application.

The VBL application can visualize multi-dimensional mesh- and particle-based data that may be obtained from computer simulations or experimental measurements. The raw data must be preprocessed and converted to binary buffers that the application can read. At this point, one should also ensure that the size of the processed data complies with the capabilities of the machine used for the visualization. Finally, the resulting buffers together with a scene description in a form of a JSON [115] file are stored on a web server acting as a data input for the visualization engine of the VBL application. More details about the VBL application can be found in [85].

As can be seen in Figure A1, the application window contains multiple viewports that may show, apart from the full 3D view, the data projections along a certain plane or axis, time-dependent plots of a selected parameter, textual and numerical data, etc. On top of that, there is an additional layer containing a description of displayed dataset as well as a graphical user interface (GUI). It utilizes d3.js library for graphical elements and dat.GUI library for the interface providing animation control and layer visibility management. GUI controls together with VR controllers enable users to interact with a displayed scene by moving and scaling it in the 3D space, filtering its content, and navigating in the animation timeline.

The bottom part of Figure A1 shows an example of a visualization based on the 3D PIC simulation data. The simulation investigates evolution of the radial profile of a high-power laser pulse in a low-density plasma [116]. The VBL application helped considerably to reveal the mechanisms of coupled electromagnetic and electron rings formation during the interaction and to understand how these structures can be controlled. The simulation was

calculated by the EPOCH code [80]; it took $\approx 2 \times 10^5$ core-hours, producing $\approx 2$ TB of raw data. The final size of the data processed for the purpose of the visualization in the VBL application is $\approx 10$ GB. The interactive visualization is available online [117] (note that the client device is required to have at least 16 GB of free memory and the VR mode has been tested for Oculus Rift in Firefox). The visualization shown in Figure 3 and the upper part of Figure A1 has lower size (as it is based on 2D simulation) and is available online [84]. Other visualizations made at ELI Beamlines can be viewed online [114], including the shutter visualization [112] from Figure 10.

## References

1. Bulanov, S.V.; Esirkepov, T.; Khoroshkov, V.S.; Kuznetsov, A.V.; Pegoraro, F. Oncological hadrontherapy with laser ion accelerators. *Phys. Lett. A* **2002**, *299*, 240–247. [CrossRef]
2. Bulanov, S.V.; Wilkens, J.J.; Esirkepov, T.Z.; Korn, G.; Kraft, G.; Kraft, S.D.; Molls, M.; Khoroshkov, V.S. Laser ion acceleration for hadron therapy. *Physics-Uspekhi* **2014**, *57*, 1149–1179. [CrossRef]
3. Tajima, T. Prospect for compact medical laser accelerators. *J. Jpn. Soc. Therap. Radiol. Oncol.* **1997**, *9*, 83–85.
4. Roth, M.; Cowan, T.E.; Key, M.H.; Hatchett, S.P.; Brown, C.; Fountain, W.; Johnson, J.; Pennington, D.M.; Snavely, R.A.; Wilks, S.C.; et al. Fast ignition by intense laser-accelerated proton beams. *Phys. Rev. Lett.* **2001**, *86*, 436–439. [CrossRef] [PubMed]
5. Atzeni, S.; Temporal, M.; Honrubia, J.J. A first analysis of fast ignition of precompressed ICF fuel by laser-accelerated protons. *Nucl. Fusion* **2002**, *42*, L1. [CrossRef]
6. Nishiuchi, M.; Sakaki, H.; Esirkepov, T.Z.; Nishio, K.; Pikuz, T.A.; Faenov, A.Y.; Skobelev, I.Y.; Orlandi, R.; Sako, H.; Pirozhkov, A.S.; et al. Acceleration of highly charged GeV Fe ions from a low-Z substrate by intense femtosecond laser. *Phys. Plasmas* **2015**, *22*, 033107. [CrossRef]
7. Daido, H.; Nishiuchi, M.; Pirozhkov, A.S. Review of laser-driven ion sources and their applications. *Rep. Prog. Phys.* **2012**, *75*, 056401. [CrossRef]
8. Macchi, A.; Borghesi, M.; Passoni, M. Ion acceleration by superintense laser-plasma interaction. *Rev. Mod. Phys.* **2013**, *85*, 751–793. [CrossRef]
9. Passoni, M.; Arioli, F.M.; Cialfi, L.; Dellasega, D.; Fedeli, L.; Formenti, A.; Giovannelli, A.C.; Maffini, A.; Mirani, F.; Pazzaglia, A.; et al. Advanced laser-driven ion sources and their applications in materials and nuclear science. *Plasma Phys. Control. Fusion* **2019**, *62*, 014022. [CrossRef]
10. Garcia, S.; Chatain, D.; Perin, J.P. Continuous production of a thin ribbon of solid hydrogen. *Laser Part. Beams* **2014**, *32*, 569–575. [CrossRef]
11. Margarone, D.; Velyhan, A.; Dostal, J.; Ullschmied, J.; Perin, J.P.; Chatain, D.; Garcia, S.; Bonnay, P.; Pisarczyk, T.; Dudzak, R.; et al. Proton acceleration driven by a nanosecond laser from a cryogenic thin solid-hydrogen ribbon. *Phys. Rev. X* **2016**, *6*, 041030. [CrossRef]
12. Margarone, D.; Cirrone, G.A.P.; Cuttone, G.; Amico, A.; Andò, L.; Borghesi, M.; Bulanov, S.S.; Bulanov, S.V.; Chatain, D.; Fajstavr, A.; et al. ELIMAIA: A Laser-Driven Ion Accelerator for Multidisciplinary Applications. *Quantum Beam Sci.* **2018**, *2*, 8. [CrossRef]
13. Chagovets, T.; Stanček, S.; Giuffrida, L.; Velyhan, A.; Tryus, M.; Grepl, F.; Istokskaia, V.; Kantarelou, V.; Wiste, T.; Hernandez Martin, J.; et al. Automation of Target Delivery and Diagnostic Systems for High Repetition Rate Laser-Plasma Acceleration. *Appl. Sci.* **2021**, *11*, 1680. [CrossRef]
14. Weber, S.; Bechet, S.; Borneis, S.; Brabec, L.; Bučka, M.; Chacon-Golcher, E.; Ciappina, M.; DeMarco, M.; Fajstavr, A.; Falk, K.; et al. P3: An installation for high-energy density plasma physics and ultra-high intensity laser–matter interaction at ELI-Beamlines. *Matter Radiat. Extrem.* **2017**, *2*, 149–176. [CrossRef]
15. Condamine, F.P.; Jourdain, N.; Hernandez, J.C.; Taylor, M.; Bohlin, H.; Fajstavr, A.; Jeong, T.M.; Kumar, D.; Laštovička, T.; Renner, O.; et al. High-repetition rate solid target delivery system for PW-class laser–matter interaction at ELI Beamlines. *Rev. Sci. Instrum.* **2021**, *92*, 063504. [CrossRef]
16. Jourdain, N.; Chaulagain, U.; Havlík, M.; Kramer, D.; Kumar, D.; Majerová, I.; Tikhonchuk, V.T.; Korn, G.; Weber, S. The L4n laser beamline of the P3-installation: Towards high-repetition rate high-energy density physics at ELI-Beamlines. *Matter Radiat. Extrem.* **2021**, *6*, 015401. [CrossRef]
17. Papadopoulos, D.; Zou, J.; Le Blanc, C.; Cheriaux, G.; Georges, P.; Druon, F.; Mennerat, G.; Martin, L.; Fréneaux, A.; Beluze, A.; et al. The Apollon 10 PW laser: Experimental and theoretical investigation of the temporal characteristics. *High Power Laser Sci. Eng.* **2016**, *4*, E34. [CrossRef]
18. Zamfir, N.V. Nuclear Physics with 10 PW laser beams at Extreme Light Infrastructure-Nuclear Physics (ELI-NP). *Eur. Phys. J. Spec. Top.* **2014**, *223*, 1221–1227. [CrossRef]
19. Shao, B.; Li, Y.; Peng, Y.; Wang, P.; Qian, J.; Leng, Y.; Li, R. Broad-bandwidth high-temporal-contrast carrier-envelope-phase-stabilized laser seed for 100 PW lasers. *Opt. Lett.* **2020**, *45*, 2215–2218. [CrossRef]
20. Esirkepov, T.; Borghesi, M.; Bulanov, S.V.; Mourou, G.; Tajima, T. Highly efficient relativistic-ion generation in the laser-piston regime. *Phys. Rev. Lett.* **2004**, *92*, 175003. [CrossRef]

21. Wilks, S.C.; Langdon, A.B.; Cowan, T.E.; Roth, M.; Singh, M.; Hatchett, S.; Key, M.H.; Pennington, D.; MacKinnon, A.; Snavely, R.A. Energetic proton generation in ultra-intense laser–solid interactions. *Phys. Plasmas* **2001**, *8*, 542–549. [CrossRef]

22. Snavely, R.A.; Key, M.H.; Hatchett, S.P.; Cowan, T.E.; Roth, M.; Phillips, T.W.; Stoyer, M.A.; Henry, E.A.; Sangster, T.C.; Singh, M.S.; et al. Intense High-Energy Proton Beams from Petawatt-Laser Irradiation of Solids. *Phys. Rev. Lett.* **2000**, *85*, 2945–2948. [CrossRef] [PubMed]

23. Psikal, J.; Matys, M. Dominance of hole-boring radiation pressure acceleration regime with thin ribbon of ionized solid hydrogen. *Plasma Phys. Control. Fusion* **2018**, *60*, 044003. [CrossRef]

24. Macchi, A.; Cattani, F.; Liseykina, T.V.; Cornolti, F. Laser Acceleration of Ion Bunches at the Front Surface of Overdense Plasmas. *Phys. Rev. Lett.* **2005**, *94*, 165003. [CrossRef]

25. Schwoerer, H.; Pfotenhauer, S.; Jäckel, O.; Amthor, K.U.; Liesfeld, B.; Ziegler, W.; Sauerbrey, R.; Ledingham, K.W.D.; Esirkepov, T. Laser-plasma acceleration of quasi-monoenergetic protons from microstructured targets. *Nature* **2006**, *439*, 445–448. [CrossRef] [PubMed]

26. Hegelich, B.M.; Albright, B.J.; Cobble, J.; Flippo, K.; Letzring, S.; Paffett, M.; Ruhl, H.; Schreiber, J.; Schulze, R.K.; Fernández, J.C. Laser acceleration of quasi-monoenergetic MeV ion beams. *Nature* **2006**, *439*, 441–444. [CrossRef]

27. Kar, S.; Borghesi, M.; Bulanov, S.V.; Key, M.H.; Liseykina, T.V.; Macchi, A.; Mackinnon, A.J.; Patel, P.K.; Romagnani, L.; Schiavi, A.; et al. Plasma Jets Driven by Ultraintense-Laser Interaction with Thin Foils. *Phys. Rev. Lett.* **2008**, *100*, 225004. [CrossRef]

28. Henig, A.; Steinke, S.; Schnürer, M.; Sokollik, T.; Hörlein, R.; Kiefer, D.; Jung, D.; Schreiber, J.; Hegelich, B.M.; Yan, X.Q.; et al. Radiation-Pressure Acceleration of Ion Beams Driven by Circularly Polarized Laser Pulses. *Phys. Rev. Lett.* **2009**, *103*, 245003. [CrossRef]

29. Kar, S.; Kakolee, K.F.; Qiao, B.; Macchi, A.; Cerchez, M.; Doria, D.; Geissler, M.; McKenna, P.; Neely, D.; Osterholz, J.; et al. Ion Acceleration in Multispecies Targets Driven by Intense Laser Radiation Pressure. *Phys. Rev. Lett.* **2012**, *109*, 185006. [CrossRef]

30. Kim, I.J.; Pae, K.H.; Choi, I.W.; Lee, C.L.; Kim, H.T.; Singhal, H.; Sung, J.H.; Lee, S.K.; Lee, H.W.; Nickles, P.V.; et al. Radiation pressure acceleration of protons to 93 MeV with circularly polarized petawatt laser pulses. *Phys. Plasmas* **2016**, *23*, 070701. [CrossRef]

31. Henig, A.; Kiefer, D.; Markey, K.; Gautier, D.C.; Flippo, K.A.; Letzring, S.; Johnson, R.P.; Shimada, T.; Yin, L.; Albright, B.J.; et al. Enhanced Laser-Driven Ion Acceleration in the Relativistic Transparency Regime. *Phys. Rev. Lett.* **2009**, *103*, 045002. [CrossRef] [PubMed]

32. Yan, X.Q.; Lin, C.; Sheng, Z.M.; Guo, Z.Y.; Liu, B.C.; Lu, Y.R.; Fang, J.X.; Chen, J.E. Generating High-Current Monoenergetic Proton Beams by a CircularlyPolarized Laser Pulse in the Phase-StableAcceleration Regime. *Phys. Rev. Lett.* **2008**, *100*, 135003. [CrossRef] [PubMed]

33. Yan, X.Q.; Tajima, T.; Hegelich, M.; Yin, L.; Habs, D. Theory of laser ion acceleration from a foil target of nanometer thickness. *Appl. Phys. B* **2009**, *98*, 711–721. [CrossRef]

34. Tajima, T.; Habs, D.; Yan, X. *Laser Acceleration of Ions for Radiation Therapy*; World Scientific: Singapore, 2009; pp. 201–228. [CrossRef]

35. Naumova, N.; Schlegel, T.; Tikhonchuk, V.T.; Labaune, C.; Sokolov, I.V.; Mourou, G. Hole Boring in a DT Pellet and Fast-Ion Ignition with Ultraintense Laser Pulses. *Phys. Rev. Lett.* **2009**, *102*, 025002. [CrossRef] [PubMed]

36. Robinson, A.P.L.; Gibbon, P.; Zepf, M.; Kar, S.; Evans, R.G.; Bellei, C. Relativistically correct hole-boring and ion acceleration by circularly polarized laser pulses. *Plasma Phys. Control. Fusion* **2009**, *51*, 024004. [CrossRef]

37. Bulanov, S.V.; Esirkepov, T.Z.; Kando, M.; Pegoraro, F.; Bulanov, S.S.; Geddes, C.G.R.; Schroeder, C.B.; Esarey, E.; Leemans, W.P. Ion acceleration from thin foil and extended plasma targets by slow electromagnetic wave and related ion-ion beam instability. *Phys. Plasmas* **2012**, *19*, 103105. [CrossRef]

38. Macchi, A.; Veghini, S.; Pegoraro, F. "Light Sail" Acceleration Reexamined. *Phys. Rev. Lett.* **2009**, *103*, 085003. [CrossRef]

39. Mackenroth, F.; Bulanov, S.S. Tailored laser pulse chirp to maintain optimum radiation pressure acceleration of ions. *Phys. Plasmas* **2019**, *26*, 023103. [CrossRef]

40. Kar, S.; Kakolee, K.F.; Cerchez, M.; Doria, D.; Macchi, A.; McKenna, P.; Neely, D.; Osterholz, J.; Quinn, K.; Ramakrishna, B.; et al. Experimental investigation of hole boring and light sail regimes of RPA by varying laser and target parameters. *Plasma Phys. Control. Fusion* **2013**, *55*, 124030. [CrossRef]

41. Matys, M.; Nishihara, K.; Kecova, M.; Psikal, J.; Korn, G.; Bulanov, S.V. Laser-driven generation of collimated quasi-monoenergetic proton beam using double-layer target with modulated interface. *High Energy Density Phys.* **2020**, *36*, 100844. [CrossRef]

42. Bulanov, S.V.; Khoroshkov, V.S. Feasibility of using laser ion accelerators in proton therapy. *Plasma Phys. Rep.* **2002**, *28*, 453–456. [CrossRef]

43. Bulanov, S.V.; Esirkepov, T.Z.; Kamenets, F.F.; Kato, Y.; Kuznetsov, A.V.; Nishihara, K.; Pegoraro, F.; Tajima, T.; Khoroshkov, V.S. Generation of high-quality charged particle beams during the acceleration of ions by high-power laser radiation. *Plasma Phys. Rep.* **2002**, *28*, 975–991. [CrossRef]

44. Esirkepov, T.; Bulanov, S.V.; Nishihara, K.; Tajima, T.; Pegoraro, F.; Khoroshkov, V.S.; Mima, K.; Daido, H.; Kato, Y.; Kitagawa, Y.; et al. Proposed double-layer target for the generation of high-quality laser-accelerated ion beams. *Phys. Rev. Lett.* **2002**, *89*, 175003. [CrossRef] [PubMed]

45. Pegoraro, F.; Bulanov, S.V. Photon bubbles and ion acceleration in a plasma dominated by the radiation pressure of an electromagnetic pulse. *Phys. Rev. Lett.* **2007**, *99*, 065002. [CrossRef]

46. Echkina, E.Y.; Inovenkov, I.N.; Esirkepov, T.Z.; Pegoraro, F.; Borghesi, M.; Bulanov, S.V. Dependence of the ion energy on the parameters of the laser pulse and target in the radiation-pressure-dominated regime of acceleration. *Plasma Phys. Rep.* **2010**, *36*, 15–29. [CrossRef]

47. Lord Rayleigh. Investigation of the character of the equilibrium of an incompressible heavy fluid of variable density. *Proc. Lond. Math. Soc.* **1882**, *14*, 170–177. [CrossRef]

48. Taylor, G. The instability of liquid surfaces when accelerated in a direction perpendicular to their planes. I. *Proc. R. Soc. Lond. Ser. A Math. Phys. Sci.* **1950**, *201*, 192–196. [CrossRef]

49. Richtmyer, R.D. Taylor instability in shock acceleration of compressible fluids. *Commun. Pure Appl. Math.* **1960**, *13*, 297–319. [CrossRef]

50. Meshkov, E.E. Instability of the interface of two gases accelerated by a shock wave. *Fluid Dyn.* **1969**, *4*, 101–104. [CrossRef]

51. Zhou, Y. Rayleigh–Taylor and Richtmyer–Meshkov instability induced flow, turbulence, and mixing. I. *Phys. Rep.* **2017**, *720-722*, 1–136. [CrossRef]

52. Palmer, C.A.; Schreiber, J.; Nagel, S.R.; Dover, N.P.; Bellei, C.; Beg, F.N.; Bott, S.; Clarke, R.J.; Dangor, A.E.; Hassan, S.M.; et al. Rayleigh-Taylor instability of an ultrathin foil accelerated by the radiation pressure of an intense laser. *Phys. Rev. Lett.* **2012**, *108*, 225002. [CrossRef] [PubMed]

53. Yang, Y.; Zhang, Q.; Sharp, D.H. Small amplitude theory of Richtmyer-Meshkov instability. *Phys. Fluids* **1994**, *6*, 1856–1873. [CrossRef]

54. Wouchuk, J.G.; Nishihara, K. Asymptotic growth in the linear Richtmyer-Meshkov instability. *Phys. Plasmas* **1997**, *4*, 1028–1038. [CrossRef]

55. Nishihara, K.; Wouchuk, J.G.; Matsuoka, C.; Ishizaki, R.; Zhakhovsky, V.V. Richtmyer-Meshkov instability: Theory of linear and nonlinear evolution. *Philos. Trans. R. Soc. A Math. Phys. Eng. Sci.* **2010**, *368*, 1769–1807. [CrossRef] [PubMed]

56. Mohseni, F.; Mendoza, M.; Succi, S.; Herrmann, H.J. Relativistic effects on the Richtmyer-Meshkov instability. *Phys. Rev. D Part. Fields Gravit. Cosmol.* **2014**, *90*, 125028. [CrossRef]

57. Matsuoka, C.; Nishihara, K.; Sano, T. Nonlinear Dynamics of Non-uniform Current-Vortex Sheets in Magnetohydrodynamic Flows. *J. Nonlinear Sci.* **2017**, *27*, 531–572. [CrossRef]

58. Zhou, Y.; Clark, T.T.; Clark, D.S.; Gail Glendinning, S.; Aaron Skinner, M.; Huntington, C.M.; Hurricane, O.A.; Dimits, A.M.; Remington, B.A. Turbulent mixing and transition criteria of flows induced by hydrodynamic instabilities. *Phys. Plasmas* **2019**, *26*, 080901. [CrossRef]

59. Zhou, Y.; Williams, R.J.; Ramaprabhu, P.; Groom, M.; Thornber, B.; Hillier, A.; Mostert, W.; Rollin, B.; Balachandar, S.; Powell, P.D.; et al. Rayleigh–Taylor and Richtmyer–Meshkov instabilities: A journey through scales. *Phys. D Nonlinear Phenom.* **2021**, *423*, 132838. [CrossRef]

60. Hester, J.J. The Crab Nebula: An Astrophysical Chimera. *Annu. Rev. Astron. Astrophys.* **2008**, *46*, 127–155. [CrossRef]

61. Lindl, J.D.; Mccrory, R.L.; Campbell, E.M. Progress toward Ignition and Burn Propagation in Inertial Confinement Fusion. *Phys. Today* **1992**, *45*, 32–40. [CrossRef]

62. Waddell, J.T.; Niederhaus, C.E.; Jacobs, J.W. Experimental study of Rayleigh–Taylor instability: Low Atwood number liquid systems with single-mode initial perturbations. *Phys. Fluids* **2001**, *13*, 1263–1273. [CrossRef]

63. Niederhaus, C.E.; Jacobs, J.W. Experimental study of the Richtmyer-Meshkov instability of incompressible fluids. *J. Fluid Mech.* **2003**, *485*, 243–277. [CrossRef]

64. Velikovich, A.L. Analytic theory of Richtmyer-Meshkov instability for the case of reflected rarefaction wave. *Phys. Fluids* **1996**, *8*, 1666–1679. [CrossRef]

65. Wouchuk, J.G.; Nishihara, K. Linear perturbation growth at a shocked interface. *Phys. Plasmas* **1996**, *3*, 3761–3776. [CrossRef]

66. Klimo, O.; Psikal, J.; Limpouch, J.; Tikhonchuk, V.T. Monoenergetic ion beams from ultrathin foils irradiated by ultrahigh-contrast circularly polarized laser pulses. *Phys. Rev. Spec. Top. Accel. Beams* **2008**, *11*, 031301. [CrossRef]

67. Robinson, A.P.; Zepf, M.; Kar, S.; Evans, R.G.; Bellei, C. Radiation pressure acceleration of thin foils with circularly polarized laser pulses. *New J. Phys.* **2008**, *10*, 013021. [CrossRef]

68. Wan, Y.; Pai, C.H.; Zhang, C.J.; Li, F.; Wu, Y.P.; Hua, J.F.; Lu, W.; Gu, Y.Q.; Silva, L.O.; Joshi, C.; et al. Physical Mechanism of the Transverse Instability in Radiation Pressure Ion Acceleration. *Phys. Rev. Lett.* **2016**, *117*, 234801. [CrossRef]

69. Wan, Y.; Pai, C.H.; Zhang, C.J.; Li, F.; Wu, Y.P.; Hua, J.F.; Lu, W.; Joshi, C.; Mori, W.B.; Malka, V. Physical mechanism of the electron-ion coupled transverse instability in laser pressure ion acceleration for different regimes. *Phys. Rev. E* **2018**, *98*, 013202. [CrossRef]

70. Vshivkov, V.A.; Naumova, N.M.; Pegoraro, F.; Bulanov, S.V. Nonlinear electrodynamics of the interaction of ultra-intense laser pulses with a thin foil. *Phys. Plasmas* **1998**, *5*, 2727–2741. [CrossRef]

71. Reed, S.A.; Matsuoka, T.; Bulanov, S.; Tampo, M.; Chvykov, V.; Kalintchenko, G.; Rousseau, P.; Yanovsky, V.; Kodama, R.; Litzenberg, D.W.; et al. Relativistic plasma shutter for ultraintense laser pulses. *Appl. Phys. Lett.* **2009**, *94*, 201117. [CrossRef]

72. Palaniyappan, S.; Hegelich, B.M.; Wu, H.C.; Jung, D.; Gautier, D.C.; Yin, L.; Albright, B.J.; Johnson, R.P.; Shimada, T.; Letzring, S.; et al. Dynamics of relativistic transparency and optical shuttering in expanding overdense plasmas. *Nat. Phys.* **2012**, *8*, 763–769. [CrossRef]

73. Wei, W.Q.; Yuan, X.H.; Fang, Y.; Ge, Z.Y.; Ge, X.L.; Yang, S.; Li, Y.F.; Liao, G.Q.; Zhang, Z.; Liu, F.; et al. Plasma optical shutter in ultraintense laser-foil interaction. *Phys. Plasmas* **2017**, *24*, 113111. [CrossRef]

74. Matys, M.; Klimo, O.; Psikal, J.; Bulanov, S.V. Simulation studies on transmissivity of silicon nitride plasma shutter for laser pulse contrast enhancement. In Proceedings of the 45th EPS Conference on Plasma Physics, EPS, Prague, Czech Republic, 2–6 July 2018; Coda, S., Berndt, J., Lapenta, G., Mantsinen, M., Michaut, C., Weber, S., Eds.; 2018; pp. 1332–1335.

75. Jirka, M.; Klimo, O.; Gu, Y.J.; Weber, S. Enhanced photon emission from a double-layer target at moderate laser intensities. *Sci. Rep.* **2020**, *10*, 8887. [CrossRef] [PubMed]

76. Matys, M.; Bulanov, S.; Kecova, M.; Kucharik, M.; Jirka, M.; Janecka, P.; Psikal, J.; Nikl, J.; Grosz, J.; Korn, G.; et al. Ion acceleration enhancement by laser-pulse shaping via plasma shutter. In Proceedings of the Laser Acceleration of Electrons, Protons, and Ions VI, Online, 19–23 April 2021; Bulanov, S.S., Schreiber, J., Schroeder, C.B., Eds.; SPIE: Bellingham, WA, USA, 2021; Volume 11779. [CrossRef]

77. Nikl, J.; Jirka, M.; Matys, M.; Kuchařík, M.; Klimo, O. Contrast enhancement of ultra-intense laser pulses by relativistic plasma shutter. In Proceedings of the High Power Lasers and Applications, Online, 19–29 April 2021; Hein, J., Butcher, T.J., Bakule, P., Haefner, C.L., Korn, G., Silva, L.O., Eds.; SPIE: Bellingham, WA, USA, 2021; Volume 11777, p. 117770X. [CrossRef]

78. Jirka, M.; Klimo, O.; Matys, M. Relativistic plasma aperture for laser intensity enhancement. *Phys. Rev. Res.* **2021**, *3*, 033175. [CrossRef]

79. Matys, M.; Bulanov, S.V.; Kucharik, M.; Jirka, M.; Nikl, J.; Kecova, M.; Proska, J.; Psikal, J.; Korn, G.; Klimo, O. Design of plasma shutters for improved heavy ion acceleration by ultra-intense laser pulses. *New J. Phys.* **2022**, *24*, 113046. [CrossRef]

80. Arber, T.D.; Bennett, K.; Brady, C.S.; Lawrence-Douglas, A.; Ramsay, M.G.; Sircombe, N.J.; Gillies, P.; Evans, R.G.; Schmitz, H.; Bell, A.R.; et al. Contemporary particle-in-cell approach to laser-plasma modelling. *Plasma Phys. Control. Fusion* **2015**, *57*, 113001. [CrossRef]

81. Ridgers, C.P.; Kirk, J.G.; Duclous, R.; Blackburn, T.G.; Brady, C.S.; Bennett, K.; Arber, T.D.; Bell, A.R. Modelling gamma-ray photon emission and pair production in high-intensity laser-matter interactions. *J. Comput. Phys.* **2014**, *260*, 273–285. [CrossRef]

82. Bulanov, S.S.; Esarey, E.; Schroeder, C.B.; Bulanov, S.V.; Esirkepov, T.Z.; Kando, M.; Pegoraro, F.; Leemans, W.P. Radiation pressure acceleration: The factors limiting maximum attainable ion energy. *Phys. Plasmas* **2016**, *23*, 056703. [CrossRef]

83. Matys, M.; Psikal, J.; Danielova, M.; Valenta, P.; Bulanov, S.V. Laser-driven Ion Acceleration Using Cryogenic Hydrogen Targets. In Proceedings of the Supercomputing in Science and Engineering 2017–2018, Ostrava, Czechia, 21–25 January 2019; Pešatová, K., Poláková, B., Cawley, J., Červenková, Z., Eds.; VSB–Technical University of Ostrava: Ostrava, Czechia, 2019; pp. 149–151. ISBN 978–80–248–4289–9.

84. Laser-Driven Proton Acceleration from Cryogenic Hydrogen Target. Available online: https://vbl.eli-beams.eu/mm-track/ (accessed on 2 June 2022).

85. Danielova, M.; Janecka, P.; Grosz, J.; Holy, A. Interactive 3D Visualizations of Laser Plasma Experiments on the Web and in VR. In Proceedings of the EuroVis 2019-Posters, Porto, Portugal, 3–7 June 2019; Madeiras Pereira, J., Raidou, R.G., Eds.; The Eurographics Association: Porto, Portugal, 2019. [CrossRef]

86. Higginson, A.; Gray, R.J.; King, M.; Dance, R.J.; Williamson, S.D.; Butler, N.M.; Wilson, R.; Capdessus, R.; Armstrong, C.; Green, J.S.; et al. Near-100 MeV protons via a laser-driven transparency-enhanced hybrid acceleration scheme. *Nat. Commun.* **2018**, *9*, 724. [CrossRef]

87. Qiao, B.; Kar, S.; Geissler, M.; Gibbon, P.; Zepf, M.; Borghesi, M. Dominance of Radiation Pressure in Ion Acceleration with Linearly Polarized Pulses at Intensities of 10(21) W cm(-2). *Phys. Rev. Lett.* **2012**, *108*, 115002. [CrossRef]

88. Yin, L.; Albright, B.J.; Bowers, K.J.; Jung, D.; Fernández, J.C.; Hegelich, B.M. Three-Dimensional Dynamics of Breakout Afterburner Ion Acceleration Using High-Contrast Short-Pulse Laser and Nanoscale Targets. *Phys. Rev. Lett.* **2011**, *107*, 045003. [CrossRef] [PubMed]

89. Liu, J.L.; Chen, M.; Zheng, J.; Sheng, Z.M.; Liu, C.S. Three dimensional effects on proton acceleration by intense laser solid target interaction. *Phys. Plasmas* **2013**, *20*, 063107. [CrossRef]

90. Bulanov, S.S.; Brantov, A.; Bychenkov, V.Y.; Chvykov, V.; Kalinchenko, G.; Matsuoka, T.; Rousseau, P.; Reed, S.; Yanovsky, V.; Litzenberg, D.W.; et al. Accelerating monoenergetic protons from ultrathin foils by flat-top laser pulses in the directed-Coulomb-explosion regime. *Phys. Rev. E* **2008**, *78*, 026412. [CrossRef] [PubMed]

91. Stark, D.J.; Yin, L.; Albright, B.J.; Guo, F. Effects of dimensionality on kinetic simulations of laser-ion acceleration in the transparency regime. *Phys. Plasmas* **2017**, *24*, 053103. [CrossRef]

92. Chen, M.; Pukhov, A.; Yu, T.P.; Sheng, Z.M. Enhanced collimated GeV monoenergetic ion acceleration from a shaped foil target irradiated by a circularly polarized laser pulse. *Phys. Rev. Lett.* **2009**, *103*, 024801. [CrossRef]

93. Matys, M.; Nishihara, K.; Danielova, M.; Psikal, J.; Korn, G.; Bulanov, V.S. Generation of collimated quasi-mono-energetic ion beams using a double layer target with interface modulations. In Proceedings of the Laser Acceleration of Electrons, Protons, and Ions V, Prague, Czech Republic, 1–3 April 2019; Esarey, E., Schroeder, C., Schreiber, J., Eds.; SPIE: Bellingham, WA, USA, 2019; Volume 11037, p. 110370Z. [CrossRef]

94. Matys, M.; Valenta, P.; Kecova, M.; Nishihara, K.; Psikal, J.; Esirkepov, T.Z.; Koga, J.K.; Necas, A.; Grittani, G.M.; Lazzarini, C.M.; et al. Laser-Driven Acceleration of Charged Particles. In *Supercomputing in Science and Engineering 2019–2020*; Vondrak, V., Tomas Kozubek, B.J., Eds.; VSB–Technical University of Ostrava: Ostrava, Czechia, 2021; pp. 86–88. ISBN 978–80–248–4567–8.

95. Floettmann, K. Some basic features of the beam emittance. *Phys. Rev. Spec. Top. Accel. Beams* **2003**, *6*, 80–86. [CrossRef]

96. Zhang, T.; Peng, S.X.; Wu, W.B.; Ren, H.T.; Zhang, J.F.; Wen, J.M.; Ma, T.H.; Jiang, Y.X.; Sun, J.; Guo, Z.Y.; et al. Practical 2.45-GHz microwave-driven Cs-free H- ion source developed at Peking University. *Chin. Phys. B* **2018**, *27*, 105208. [CrossRef]

97. Cowan, T.E.; Fuchs, J.; Ruhl, H.; Kemp, A.; Audebert, P.; Roth, M.; Stephens, R.; Barton, I.; Blazevic, A.; Brambrink, E.; et al. Ultralow emittance, multi-MeV proton beams from a laser virtual-cathode plasma accelerator. *Phys. Rev. Lett.* **2004**, *92*, 204801. [CrossRef]

98. Gu, Y.J.; Zhu, Z.; Li, X.F.; Yu, Q.; Huang, S.; Zhang, F.; Kong, Q.; Kawata, S. Stable long range proton acceleration driven by intense laser pulse with underdense plasmas. *Phys. Plasmas* **2014**, *21*, 063104. [CrossRef]

99. Bulanov, S.V.; Inovenkov, I.N.; Kirsanov, V.I.; Naumova, N.M.; Sakharov, A.S. Nonlinear depletion of ultrashort and relativistically strong laser pulses in an underdense plasma. *Phys. Fluids B* **1992**, *4*, 1935–1942. [CrossRef]

100. Bulanov, S.V.; Kirsanov, V.I.; Naumova, N.M.; Sakharov, A.S.; Shah, H.A.; Inovenkov, I.N. Stationary shock-front of a relativisticaily strong electromagnetic radiation in an underdense plasma. *Phys. Scr.* **1993**, *47*, 209–213. [CrossRef]

101. Decker, C.D.; Mori, W.B.; Tzeng, K.C.; Katsouleas, T. The evolution of ultra-intense, short-pulse lasers in underdense plasmas. *Phys. Plasmas* **1996**, *3*, 2047–2056. [CrossRef]

102. Wang, H.; Lin, C.; Sheng, Z.; Liu, B.; Zhao, S.; Guo, Z.; Lu, Y.; He, X.; Chen, J.; Yan, X. Laser Shaping of a Relativistic Intense, Short Gaussian Pulse by a Plasma Lens. *Phys. Rev. Lett.* **1996**, *107*, 265002. [CrossRef] [PubMed]

103. Bin, J.; Ma, W.; Wang, H.; Streeter, M.; Kreuzer, C.; Kiefer, D.; Yeung, M.; Cousens, S.; Foster, P.; Dromey, B.; et al. Ion Acceleration Using Relativistic Pulse Shaping in Near-Critical-Density Plasmas. *Phys. Rev. Lett.* **2015**, *115*, 064801. [CrossRef] [PubMed]

104. Fedeli, L.; Formenti, A.; Cialfi, L.; Pazzaglia, A.; Passoni, M. Ultra-intense laser interaction with nanostructured near-critical plasmas. *Sci. Rep.* **2018**, *8*, 3834. [CrossRef]

105. Horný, V.; Chen, S.; Davoine, X.; Lelasseux, V.; Gremillet, L.; Fuchs, J. High-flux neutron generation by laser-accelerated ions from single- and double-layer targets. *Sci. Rep.* **2022**, *12*, 19767. [CrossRef]

106. Park, J.; Bulanov, S.; Bin, J.; Ji, Q.; Steinke, S.; Vay, J.; Geddes, C.; Schroeder, C.; Leemans, W.; Schenkel, T.; et al. Ion acceleration in laser generated megatesla magnetic vortex. *Phys. Plasmas* **2019**, *26*, 103108. [CrossRef]

107. Hakimi, S.; Obst-Huebl, L.; Huebl, A.; Nakamura, K.; Bulanov, S.; Steinke, S.; Leemans, W.; Kober, Z.; Ostermayr, T.; Schenkel, T.; et al. Laser–solid interaction studies enabled by the new capabilities of the iP2 BELLA PW beamline. *Phys. Plasmas* **2022**, *29*, 083102. [CrossRef]

108. Yogo, A.; Daido, H.; Bulanov, S.; Nemoto, K.; Oishi, Y.; Nayuki, T.; Fujii, T.; Ogura, K.; Orimo, S.; Sagisaka, A.; et al. Laser ion acceleration via control of the near-critical density target. *Phys. Rev. E* **2008**, *77*, 016401. [CrossRef]

109. Zwickl, B.M.; Shanks, W.E.; Jayich, A.M.; Yang, C.; Bleszynski Jayich, A.C.; Thompson, J.D.; Harris, J.G.E. High quality mechanical and optical properties of commercial silicon nitride membranes. *Appl. Phys. Lett.* **2008**, *92*, 103125. [CrossRef]

110. Kaloyeros, A.E.; Jové, F.A.; Goff, J.; Arkles, B. Review—Silicon Nitride and Silicon Nitride-Rich Thin Film Technologies: Trends in Deposition Techniques and Related Applications. *ECS J. Solid State Sci. Technol.* **2017**, *6*, P691–P714. [CrossRef]

111. Gonzalez-Izquierdo, B.; Gray, R.; King, M.; Dance, R.; Wilson, R.; McCreadie, J.; Butler, N.; Capdessus, R.; Hawkes, S.; Green, J.; et al. Optically controlled dense current structures driven by relativistic plasma aperture-induced diffraction. *Nat. Phys.* **2016**, *12*, 505–512. [CrossRef]

112. Plasma Shutter for Heavy ION Acceleration Enhancement. Available online: https://vbl.eli-beams.eu/mm-shutter/ (accessed on 7 December 2022).

113. Parisi, T. *WebGL: Up and Running*, 1st ed.; O'Reilly Media, Inc.: Sebastopol, CA, USA, 2012; ISBN 144932357X.

114. Virtual BeamLine. Available online: https://vbl.eli-beams.eu/ (accessed on 2 June 2022).

115. Pezoa, F.; Reutter, J.L.; Suarez, F.; Ugarte, M.; Vrgoč, D. Foundations of JSON schema. In Proceedings of the 25th International Conference on World Wide Web. International World Wide Web Conferences Steering Committee, Montreal, QC, Canada, 11–15 May 2016; pp. 263–273. [CrossRef]

116. Valenta, P.; Grittani, G.M.; Lazzarini, C.M.; Klimo, O.; Bulanov, S.V. On the electromagnetic-electron rings originating from the interaction of high-power short-pulse laser and underdense plasma. *Phys. Plasmas* **2021**, *28*, 122104. [CrossRef]

117. Electromagnetic-Electron Rings. Available online: https://valenpe7.github.io/on_the_electromagnetic-electron_rings/ (accessed on 2 June 2022).

## C.2 Dominance of hole-boring radiation pressure acceleration regime with thin ribbon of ionized solid hydrogen

The following article is reproduced from J. Psikal and M. Matys (2018). Dominance of hole-boring radiation pressure acceleration regime with thin ribbon of ionized solid hydrogen. *Plasma Physics and Controlled Fusion* **60**, 044003.
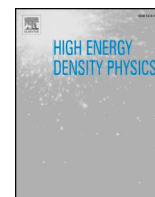
## C.3 Laser-driven generation of collimated quasi-monoenergetic proton beam using double-layer target with modulated interface

The following article is reproduced with permission from M. Matys, K. Nishihara, M. Kecova, J. Psikal, G. Korn, S. V. Bulanov (2020). Laser-driven generation of collimated quasi-monoenergetic proton beam using double-layer target with modulated interface. *High Energy Density Physics* **36**, 100844.

# Laser-driven generation of collimated quasi-monoenergetic proton beam using double-layer target with modulated interface

Martin Matys[*,a,b], Katsunobu Nishihara[a,c,d], Mariana Kecova[a], Jan Psikal[a,b], Georg Korn[a], Sergei V. Bulanov[a,e,f]

[a] FZU - Institute of Physics of the Czech Academy of Sciences, ELI Beamlines, Na Slovance 2, Prague 18221, Czech Republic
[b] Faculty of Nuclear Sciences and Physical Engineering, Czech Technical University in Prague, Brehova 7, Prague, 115 19, Czech Republic
[c] Graduate School of Engineering, Osaka City University, Sugimoto-cho, Sumiyoshi, Osaka 558-8585, Japan
[d] Institute of Laser Engineering, Osaka University, Suita, Osaka 565-0871, Japan
[e] Kansai Photon Science Institute, National Institutes for Quantum and Radiological Science and Technology, 8-1-7 Umemidai, Kizugawa-shi, Kyoto 619-0215, Japan
[f] Prokhorov Institute of General Physics of the Russian Academy of Sciences, Vavilova 38, Moscow, 119991, Russia

## ARTICLE INFO

## ABSTRACT

Usage of double-layer targets consisting of heavy and light material with modulated interface between them provides a way for laser-driven generation of collimated ion beams. With extensive 2D3V PIC simulations we show that this configuration may result in a development of a relativistic instability with Rayleigh-Taylor and Richtmyer-Meshkov like features. Initially small perturbations are amplified during the laser-target interaction leading to the formation of low-density plasma regions and high-density bunches between them, which are accelerated by the laser radiation pressure as whole compact structures. That results in collimated quasi-monoenergetic proton beam with high average energy. The properties of this proton beam such as its low emittance (one order of magnitude lower compared to that of conventional accelerators) and divergence are discussed. Results are compared with similar acceleration schemes such as double-layer target without corrugation and single-layer target.

## 1. Introduction

Laser-driven ion accelerators has received a great deal of interest in last several decades as they are capable of sustaining relatively higher accelerating gradients than their conventional counterparts, and are currently able to accelerate protons to energies of 100 MeV [1]. With the advent of multi-petawatt laser systems like ELI Beamlines (Czech Republic), APOLLON (France) or SEL (China) the laser pulses will soon reach intensities over $10^{23}$ W/cm$^2$ entering the acceleration regimes dominated by radiation pressure [2,3], which promises proton/ion acceleration above energy of several GeV.

Studies of the high-intensity laser interaction with single-layer planar targets [4] shows the development of relativistic Rayleigh-Taylor [5,6] like instability (RTI) leading to the formation of low-density regions and high-density ion bunches between them. The bunches exhibit quasi-monoenergetic behavior [4,7]. The instability can develop in a controlled way, when a corrugation is imprinted on the

front surface of the target [8]. Bunches are then generated at the positions determined by the corrugation geometry.

The composite targets, consisting of planar heavy and light ion layers, have also been considered for generation of high quality ion beams [9–12] required for various applications as hadron therapy [13] and nuclear fusion [14,15]. When the corrugation is tailored on the interface between two different layers, rather impulsive Richtmyer-Meshkov [16,17] like instability (RMI) can develop.

These two instabilities belong to the same family group and are being thoroughly investigated [18–23], as they play important roles in various fields as the astrophysics (e.g., in the development of the filament structure of the Crab Nebula [24]) and are affecting the creation of the hot spot in the inertial fusion [25]. The main differences between them are the dependence of the instability appearance on the duration of the driving force and the direction of the acceleration toward the interface [18]. The driving force of RTI is in principle continuous, while RMI is impulsive. RMI can occur when the acceleration is directed toward either side of the

interface, whereas RTI can occur only for the direction from lighter to heavier media [18]. Moreover, in the case of heavy-light direction of acceleration, RMI exhibits characteristic phase inversion of the corrugated interface as was shown theoretically [20,26,27] and in the experiments [28]. Several theoretical models of RMI are known, including the exact linear solution [27], asymptotic solution [29,30] and relativistic solution [31]. Behavior of RMI can be also explained by the description of velocity shear induced at the corrugated interface [21,22].

In this paper we present a positive effect of a controlled development of collisionless relativistic instability with RMI-like features on ion acceleration. The instability originates from the interaction of steep-front high-intensity, high-power laser pulse (with intensity of $10^{23}$ W/cm$^2$ and power of 80 PW) with a double-layer target having interface modulation. The assumed laser pulse is linearly polarized. This is in a direct contrast to several schemes for monoenergetic bunch generation, which have some similar features, but require circular polarisation. This includes, e.g., using of single-cycle laser pulses [32]; generation of self-organizing proton beam by stabilizing the central part of the foil, while letting the laser pulse propagate around it through unstable transparent wing regions [33]; using of dual parabola target [34] or shaping the target in the transverse direction to match the laser intensity profile [35]. The laser pulses assumed in these schemes (single-cycle and trapezoid) also inherently provide some sort of steep-front, required in our case, as the intensity rises from minimum to maximum in less (equal) than one laser period (trapezoid pulse profiles with rising ramps with the length of one and ten periods were compared in Ref. [33], longer ramp resulted in lower ion energy; ramp with the length of five laser periods was used in Ref. [34]). The circular polarisation is often proposed for the stabilisation of the foil by suppressing the instabilities [36,37]. Therefore, the linear polarisation is needed in our case to embrace the instability development.

Initially small perturbations at the interface are then amplified during the laser-target interaction, leading to the formation of low-density regions at the positions determined by the initial perturbation geometry and high-density plasma bunches between them. The bunches, with higher density than the density of the initial foil are then accelerated by the laser radiation pressure as whole compact structures. Moreover, the laser field propagating through the low-density regions enfolds the central plasma bunch, preventing from the perpendicular particle expansion. These behaviors result in the generation of quasi-monoenergetic, well-collimated ion beam with the average energy in the multi-GeV range and transverse emittance of one order of magnitude lower than that in the case of conventional accelerators. The laser accelerated high-energy ion beams from composite targets may also find applications in material sciences and nuclear physics research [38].

The paper is organized as follows. The simulation method and parameters are described in Section 2. Section 3, containing results, is divided into four subsections. Firstly, the mechanisms of the development of the instability with RMI-like features and beam generation are described in Section 3.1. Then the properties of the collimated quasi-monoenergetic proton beam such as its low emittance and divergence are discussed in Section 3.2. The effects of different laser pulse polarisation and corrugation wavelength are studied in Section 3.3. Lastly, our acceleration scheme is compared with schemes with different configurations such as using double-layer target without interface modulation, single-layer target and a case where full-front laser pulse is used instead of the steep-front pulse in Section 3.4. After the Conclusions Section 4, the Appendix A follows, describing visualisation of our data in the form of figures, videos and a web-based application with virtual reality mode [39]. The supplementary videos of time evolution of a selected simulation case are also included there.

## 2. Simulation method and parameters

To demonstrate the ion acceleration scheme based on double-layer target with corrugated interface between two ion species and its advantages compared to targets without corrugations we performed 2D particle-in-cell simulations using the code EPOCH [40]. The QED (quantum electrodynamics) module [41] resolving non-linear Compton scattering is included in the simulations, since this phenomenon occurs in the assumed laser intensity range.

In our case, linearly s-polarized (electric field is perpendicular to the plane of incidence) Gaussian laser pulse with a steep front incidents normally on the target. The radiation wavelength is $\lambda = 1$ $\mu$m and the peak intensity is $I_{\max} = 1.37 \times 10^{23}$ W/cm$^2$, thus yielding dimensionless amplitude $a_0 = eE_0/m_e\omega c \approx 0.85\sqrt{I[10^{18}\text{W cm}^2]\lambda^2[\mu\text{m}]} \approx 315$. The critical plasma density is equal to $n_c = \epsilon_0 m_e \omega^2/e^2 \approx 1.115 \times 10^{21}$ cm$^{-3}$. Here, $E_0$ is the electric field amplitude, $\epsilon_0$ is permittivity of vacuum, $\omega$ is laser angular frequency, $m_e$ and $e$ are electron mass and charge, respectively, and $c$ is speed of light in vacuum. The amplitude $a_0$ can locally exceeds value of 500 in our simulations, due to the self-focusing. Therefore, implementing of radiation friction in QED regime [42] is required in our case. The laser beam width at the full width at half maximum (FWHM) is 10 $\lambda$ and beam duration at FWHM equals to 8 laser periods $T$. The steep front is realized by filtering out the low-intensity part at the front of the laser pulse till 2.4 $T$ (i.e., 30% of FWHM) before the peak of the temporal Gaussian profile.

The laser profile can be produced by several methods, e.g., by using a thin overdense foil, so-called plasma-shutter [43–48] or it may occur due to the nonlinear evolution of the laser pulse propagating through an underdense plasma [49–51]. This approach may also improve spatio-temporal contrast of intense laser beam in possible future experiments by filtering a prepulse that accompanies the main pulse [52]. The generated steep front of the laser pulse can reduce the development of transverse short-wavelength instabilities (hereinafter referred as SWI), as proposed in theory [4]. These instabilities cause the disruption of even initially planar foils during radiation pressure acceleration and are usually ascribed to RTI [4,36,37] or electron-ion coupled instability [53,54]. Reduction of SWI then enables the development of long-wavelength instabilities induced by the target geometry.

The double-layer target consists of light and heavy ion layers. The light layer is made of solid hydrogen with electron density $n_e = 5.36 \times 10^{22}$ cm$^{-3}$, i.e., 48 $n_c$. It corresponds to targets already demonstrated in experiments [55] (with thickness down to 20 $\mu$m). The heavy layer consists of corresponding cryogenic deuterium with the same electron and ion number density, but with two times heavier ion mass than in the case of the light layer. Therefore, the Atwood number $A = (m_2\rho_2 - m_1\rho_1)/(m_2\rho_2 + m_1\rho_1) = \pm 0.33$, where $m_{1,2}, \rho_{1,2}$ are the ion masses and densities at the front (1) and rear (2) layers. The sign depends on the direction of the acceleration, i.e., plus for the light-heavy (LH) case and minus for the heavy-light (HL) case.

The wavelength of the initial sinusoidal interface perturbation is 5 $\lambda$ and its amplitude is set to 0.25 $\lambda$. The phase of the modulation is shifted by $\pi$ between HL and LH cases in order to ensure the maximum number of proton particles around the y-axis. Target thickness is set to 2 $\lambda$ (1 $\lambda$ per each layer), corresponding to the optimal thickness $l$ for radiation pressure acceleration mechanism

$$\frac{l}{\lambda} = \frac{a_0 n_c}{\pi n_e}. \tag{1}$$

The radiation pressure acceleration mechanism starts to dominate over more traditional target normal sheath acceleration mechanism for these relatively low-density (but still overdense) targets, like cryogenic hydrogen, at even lower intensities [36,56,57].

The laser plasma interaction occurs in the simulation box with the size of 80 $\lambda$ × 40 $\lambda$. The mesh has square cells. The size of the cells is set to 0.01 $\lambda$ to be shorter than the plasma skin depth $c/\omega_{pe} \approx 0.02\lambda$, where $\omega_{pe}$ is electron plasma frequency. Since the 3rd order b-spline shape of the quasi-particles and current smoothing are used in our simulations, it is ensured that numerical heating is strongly reduced even for the cells larger than the plasma Debye length [40]. The simulation time step has been set by EPOCH code in order to satisfy CFL (Courant-

Friedrichs-Lewy) condition [58] to $6.7 \times 10^{-3}\, T$. Each cell inside the plasma slab initially contains 48 quasi-particle electrons and the same number of protons or deuterium ions, respectively. Temperatures of all particles are initialized to 5 keV to further reduce numerical heating. The particle solver begins to move the particles just a few time steps before the arrival of the laser pulse front to the target. Target is placed at the position $x = 0$, situated $10\,\lambda$ from the simulation box boundary in the direction of the laser propagation. The time instant, when the laser pulse front reaches the edge of the plasma is referred as $t = 0$. The transverse size of the target is $40\,\lambda$, i.e., the target is reaching the simulation box boundaries at positions $y = \pm 20\,\lambda$ where thermal boundary conditions for particles are applied.

## 3. Results

### 3.1. Mechanisms of the beam generation

Despite its relatively low density, the target does not become fully relativistically transparent, as would be suggested by linear analysis $n_e < \gamma n_{ec}$ [59] (where $\gamma = \sqrt{1 + a_0^2/2}$ for linear polarisation), since electrons from the front layer are being pushed into the target by the ponderomotive force, piling up the initial electron density. Therefore, the radiation pressure can still be efficiently acting on the target [56], driving a collisionless compression wave propagating toward the corrugated interface in the middle of the target (see Fig. 1-a and -e). For the sake of brevity and continuity with the currently established fluid RMI theory [18], this shock-like jump discontinuity will be hereinafter referred as shock and its reflection in the HL case as rarefaction [20].

In the case of HL interaction, the shock reaches the interface at time $t = 1.25\, T$ (see Fig. 1-a). Therefore, the average shock speed is above $0.6\, c$. The incident shock interacts with the corrugated interface (Fig. 1-b). The reflected rarefaction wave is observed in Fig. 1-c. Time evolution of phase inversion of the corrugated interface (i.e., switching the positions of corrugation maxima and minima), characteristic for RMI in the HL case, can be observed comparing the areas at the left hand side of Fig. 1. Particularly, at the $y$-positions $\pm 2.5\,\lambda$ (inversion from

corrugation minima in Fig. 1-a to maxima in Fig. 1-d) and at the $y$-positions $0\,\lambda$ and $\pm 5\,\lambda$ (inversion from corrugation maxima to minima). The phase inversion results in the stretching of the proton layer as regions of initial corrugation minima stay behind the regions of initial maxima (Fig. 1-d). It subsequently creates low-density regions between them at the positions, where the initial amplitude of the corrugation was zero ($\pm 1.25\,\lambda$ and $\pm 3.75\,\lambda$).

Different situation occurs in the case of LH interaction. After the shock hits the interface, the proton layer enters into the deuterium one and eventually propagates through it, as can be seen in the time evolution at the right hand side of Fig. 1. Now the phase on the remaining interface (at $x$-position around $2\,\lambda$ in Fig. 1-g and -h) is kept (maxima stay at the $y$-positions $\pm 2.5\,\lambda$ and minimum at $0\,\lambda$) as predicted by the RMI theory. Deuterium layer becomes (relativistically) transparent to the incident laser pulse and the radiation pressure is acting on the detached proton layer around $x$-positions $3\,\lambda$ (Fig. 1-g) and $5\,\lambda$ (Fig. 1-h). The detached proton layer then undergoes phase inversion. However, the driving mechanism is essentially different from that in the HL case and can be explained as follows. The momenta delivered to the particles by the laser pulse in both rectangles presented in Fig. 1-e are approximately the same (neglecting effects of Gaussian shape of the pulse around axis). However, the number of protons in the central rectangle (around $y$-position $0\,\lambda$) and lateral rectangle differ, i.e., less particles receive the same amount of momenta from the laser pulse in the case of lateral rectangle. Therefore, they can reach higher energies, propagate with higher velocity and eventually overtake the particles initially located inside the central rectangle.

To highlight the positions of the high-energy particles at later time ($t = 14\, T$), the energies of the particles are being displayed as colors in Fig. 2 instead of density as in Fig. 1. The laser pulse (depicted with grey color) is also included in this figure.

In the HL case (Fig. 2-a), the protons on the regions around initial maxima ($0\,\lambda$ and $\pm 5\,\lambda$) are accelerated to higher energies than around initial minima ($\pm 2.5\,\lambda$), which stay behind. Central and lateral bunches are being developed at the positions of initial maxima. The laser pulse propagates through the (relativistically) transparent low-
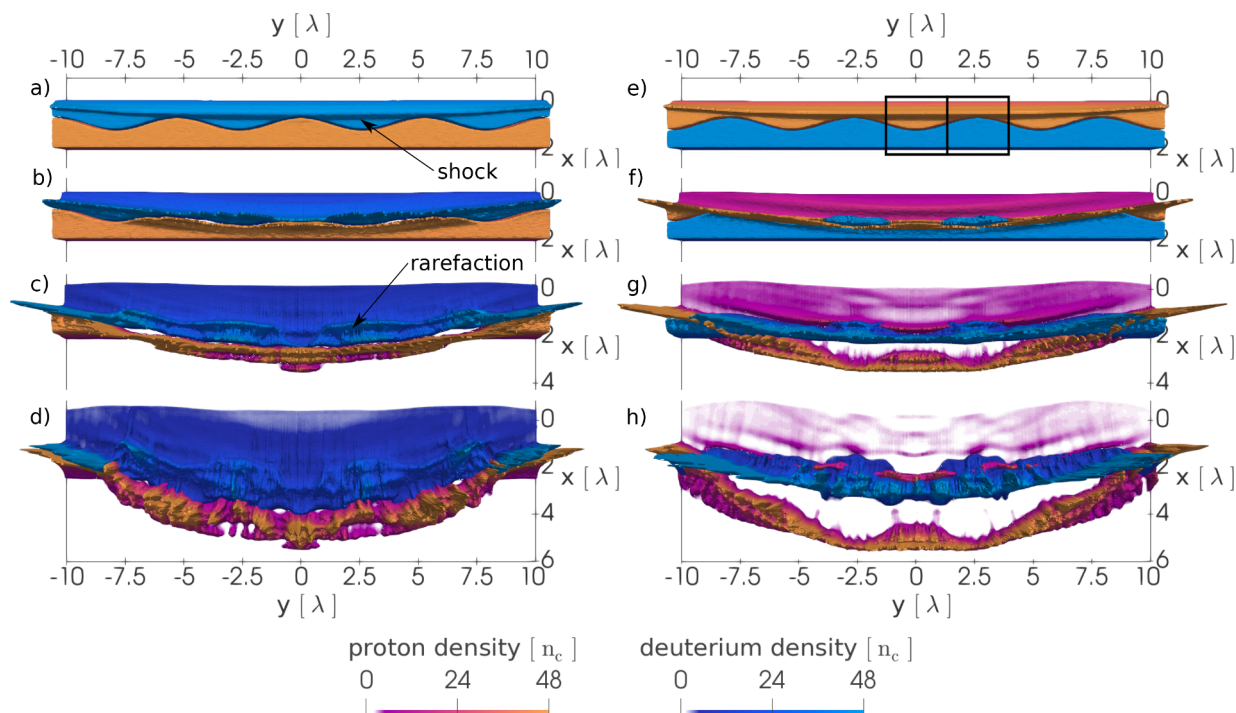


**Fig. 1.** The development of the instability. Presented cases: HL (left column) and LH (right column). Blue and red scales represents deuterium and proton densities with maximum value set to the initial density. Full density is indicated by the vertical height. Time instants at rows: 1.25 *T*, 3 *T*, 5.5 *T* and 8 *T*. (For interpretation of the references to colour in this figure legend, the reader is referred to the web version of this article.)
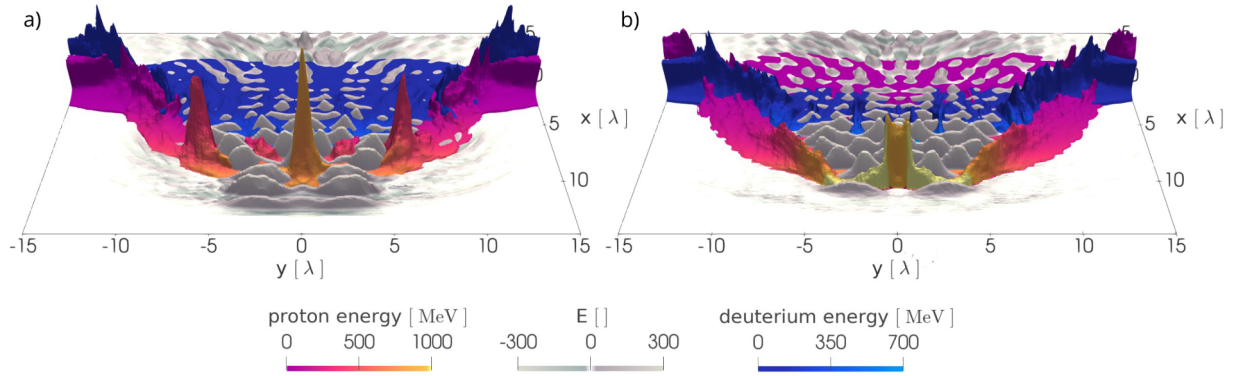
**Fig. 2.** Spatial distributions at time $t = 14\ T$. The ion local mean energy, represented by red and blue color scales, their density, represented by the vertical height and the laser pulse electric field in the z-direction (represented by both the vertical height and by the grey scale). Simulated cases: a) HL, b) LH. (For interpretation of the references to colour in this figure legend, the reader is referred to the web version of this article.)

density regions. The propagating electric field creates areas of high ponderomotive potential. Electrons are then pushed to the area of lower ponderomotive potential (i.e., lower electric field $E$) around the axis by the ponderomotive force, subsequently reducing the perpendicular movement of the ions. This field is not enfolding the lateral bunches (around $y$-positions $\pm\ 5\lambda$) which then rapidly dissipate in time and only central bunch is present at time $t = 47\ T$ as will be shown in Fig. 9-a. Supplementary videos of time evolution of this case can be found in Appendix A.

In the LH case (Fig. 2-b) the central bunch reaches lower energies than lateral areas (around $y$-positions $\pm\ 2.5\lambda$), corresponding to the previous discussion about rectangles in Fig. 1-e. This situation is opposite to the HL case. The detached proton layer can confine the laser pulse and can be accelerated as a bubble [4], till the low-density regions appears in the lateral areas (initial maxima at the y-positions $\pm\ 2.5\lambda$). Therefore, the maximal reached energy is still slightly higher at time $t = 14\ T$ in the LH case (light yellow color in Fig. 2-b) than in the HL case (Fig. 2-a). However, due to the occurrence of the low-density regions at the positions of initial zeros of the corrugation (HL case) instead of maxima (LH case), more narrow bunch with higher density and also more narrow enfolding field develop in the HL case. This behavior is crucial for long term acceleration as will be shown later.

### 3.2. Beam energy and quality

In the HL case, well collimated quasi-monoenergetic proton bunch is developed as can be seen in Fig. 3-a, where time evolution of proton energies is shown.

Although the energy spread is increasing after time $t = 47\ T$, the

bunch structure is still kept till the end of the simulation. Moreover, the average bunch energy is gradually shifting closer to the maximum energy during time. The average beam energy at time $t = 47\ T$ reaches 1882 MeV and bandwidth (at FWHM) is 69 MeV (Fig. 3-b). Therefore, the energy spread is about 3.7%. Angular distribution of the ions in the beam (red part of Fig. 3-b) is shown in Fig. 3-c. This graph implies low angular spread of $2\theta = 0.\ 65°$ (at FWHM). Therefore, the solid angle is $\Omega = 2\pi(1 - \cos(\theta)) = 0.1$ mrad. The normalized rms transverse emittance of these particles is $\epsilon_{rms} = \sqrt{\langle y^2 \rangle \langle p_y^2 \rangle - \langle y p_y \rangle^2}\ /\ m_p c = 0.046$ mm·mrad. Where $m_p$ and $p_y$ are proton mass and momentum in the (transverse) y-direction. $\epsilon_{rms}$ is proportional to the area of the ellipse containing particles in the phase space ($y - p_y$). Referring definition and further discussion can be found in Ref. [60]. This emittance is one order of magnitude lower than in the case of conventional proton accelerators [61], but still one order of magnitude higher than the emittance reported in Ref. [62] for much lower energy range of protons up to 10 MeV.

The transverse emittance can be also defined in real space via the beam divergence $\Theta_{div} = \sqrt{\sum_{i=1}^{N} \frac{(\Theta_i - \langle \Theta \rangle)^2}{N}}$ as in Ref. [63]

$$\epsilon_y = \frac{4}{N} \sqrt{\sum_{i=1}^{N} (y_i - \langle y \rangle)^2} \times \sqrt{\sum_{i=1}^{N} (\Theta_i - \langle \Theta \rangle)^2}. \tag{2}$$

That yields the values for protons at the FWHM of the bunch (Fig 3-b): $\Theta_{div} = 0.038$ rad and $\epsilon_y = 0.218$ mm·mrad. Assuming the whole high-energy proton beam (from 1748 MeV, i.e., the beginning of the bunch waist, to the maximum beam energy of 2770 MeV) the values rise to $\Theta_{div} = 0.051$ and $\epsilon_y = 0.372$ mm·mrad. This transverse emittance is still two order of magnitude lower compared to the one in Ref. [63], in which protons reached similar energies to our case (1.67 GeV) in the
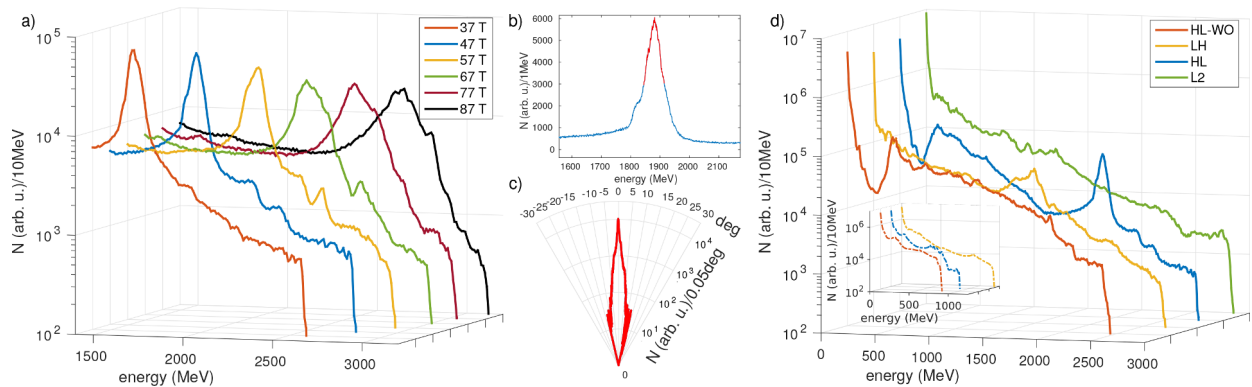


**Fig. 3.** Properties of the ion beam. a) Time evolution of the tail of the proton energy spectra in the HL case, b) proton energy spectra of the HL case at time $t = 47\ T$, with highlighted FWHM section used for c) angular distribution, d) proton energy spectra (corresponding deuteron energy spectra in inset) for various targets (see details in the text) at time $t = 47\ T$.

simulation with underdense hydrogen target.

Approximately $0.32 \times 10^6$ quasi-particles have energy within the assumed energy range, which means about 6.7% of $4.8 \times 10^6$ quasi-particles initially located inside the laser spot area (i.e., $\pm 5\lambda$). That yields $1.43 \times 10^{12}$ real particles and charge of 229 nC, assuming a projection of the initial 2D flat target of $2 \times 40\,\mu m^2$ into a 3D cuboid of $2 \times 40 \times 40\,\mu m^3$. Around 40.4% of the laser pulse energy is converted into the particles propagating in the forward direction (protons: 28.7%, deuterons: 6.1%, electrons: 5.6%). Around 3.4% of the laser pulse energy is converted into the proton particles in the energy range of $1882 \pm 69$ MeV (corresponding to the FWHM red part of Fig. 3-b).

### 3.3. Effects of different laser pulse polarisation and corrugation wavelength

Linear s-polarisation and single corrugation wavelength was used for the simulations so far. Other polarisations and corrugation wavelengths are investigated in this section, as they can affect laser-plasma interaction. The blue color line is used in graphs throughout the paper to highlight the HL case with the default parameters described in the Section 2.

The employment of the circular polarisation (C-pol) instead of linear one can mitigate the instability development, inhibit a strong electron heating and stabilize the foil as was shown, e.g., in Refs. [33,36,37]. In the case of linear polarisation, the differences between p-polarisation (P-pol) and s-polarisation (S-pol) may become especially significant in the 2D geometry, as the laser polarisation is in or out of the simulation plane, respectively.

The effects of the laser pulse polarisations on the early laser-plasma interactions (at time $t = 14\,T$) of our case are visualised in the terms of proton density, proton local mean energy and laser pulse electric field in Fig. 4.

In the case of S-pol (our default case) the instability develops, resulting into the generation of three bunches (with distinctive central one), where the radiation pressure is taking place. Laser pulse then can propagate only through the low-density regions between them (Fig. 4-a). The instability develops also in the case of P-pol (Fig. 4-b). However, the lateral bunches has already dissipated and most of the foil is becoming (relativistically) transparent to the incoming laser pulse. Only

the central bunch still holds, but in a significantly smaller form compared to the S-pol case. This behavior can be explained by artificially greater electron heating in the simulation plane in the P-pol case, while the S-pol case provides more isochoric heating into all 3 spatial directions as was demonstrated in Refs. [64,65]. Moreover, the target will become (relativistically) transparent earlier in the P-pol case [65], which affects the generation of low-density regions and then of the bunch itself as was described in our simulations in the Section 3.1. The extra heating of electrons in the P-pol case is visible in the electron energy spectra in Fig. 4-d as the electrons are accelerated to higher energy with higher temperature (which can be inferred from the flatter slope of the curve compared to the S-pol case).

On the contrary the instability is mitigated in the case of C-pol (Fig. 4-c). The laser pulse is confined by the bubble shaped foil and radiation pressure is properly acting on the whole area of the laser focal spot. The electron heating is reduced and protons are accelerated to higher energy than both S-pol and P-pol cases by the radiation pressure as can be seen in Fig. 4-d. However, due to the lack of instability development no distinctive bunch structure is found in the proton energy spectra for the C-pol case.

At the later time $t = 47\,T$ the P-pol case becomes mostly (relativistically) transparent to the laser pulse with only a few structures in the electron density as can be seen in Fig. 5-a and -c. On the contrary, the distinctive bunch structure is kept in the electron density in the S-pol case (Fig. 5-b). The radiation pressure acceleration of the bunch is ongoing, while the area around bunch is (relativistically) transparent as can be seen in Fig. 5-d. Note that the energy of electrons is relatively low inside the bunch (which means its thermal expansion is reduced) and is significantly higher in the transparent plasma where the electrons are heated and are oscillating directly in the laser field.

The extraordinary electron heating in the P-pol case becomes even more apparent in the electron spectra at time $t = 47\,T$ (Fig. 6-a) with reaching of the transparency regime. On the contrary, the proton energies are only slightly higher in the P-pol case, which corresponds to the discussion in Ref. [64] for the transparency regime. The stabilisation effect of circular polarisation is also visible in the deuteron spectra in Fig. 6-b as the deuterons are accelerated to significantly higher energies than in the cases with linear polarisations. The distinctive bunch
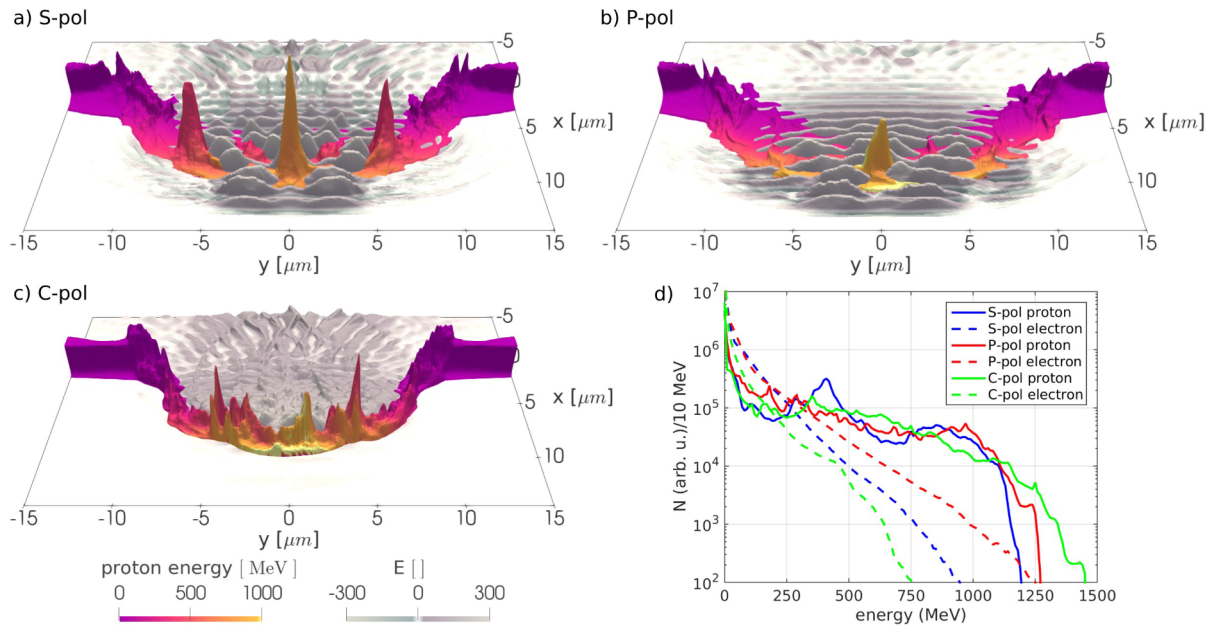


**Fig. 4.** Spatial distributions and energy spectra at time $t = 14\,T$ for different laser pulse polarisations: a-c) The proton local mean energy, represented by red color scales, its density, represented by the vertical height and the laser pulse electric field in the polarisation dependent direction (represented by both the vertical height and by the grey scale), d) proton and electron energy spectra for the corresponding cases. (For interpretation of the references to colour in this figure legend, the reader is referred to the web version of this article.)
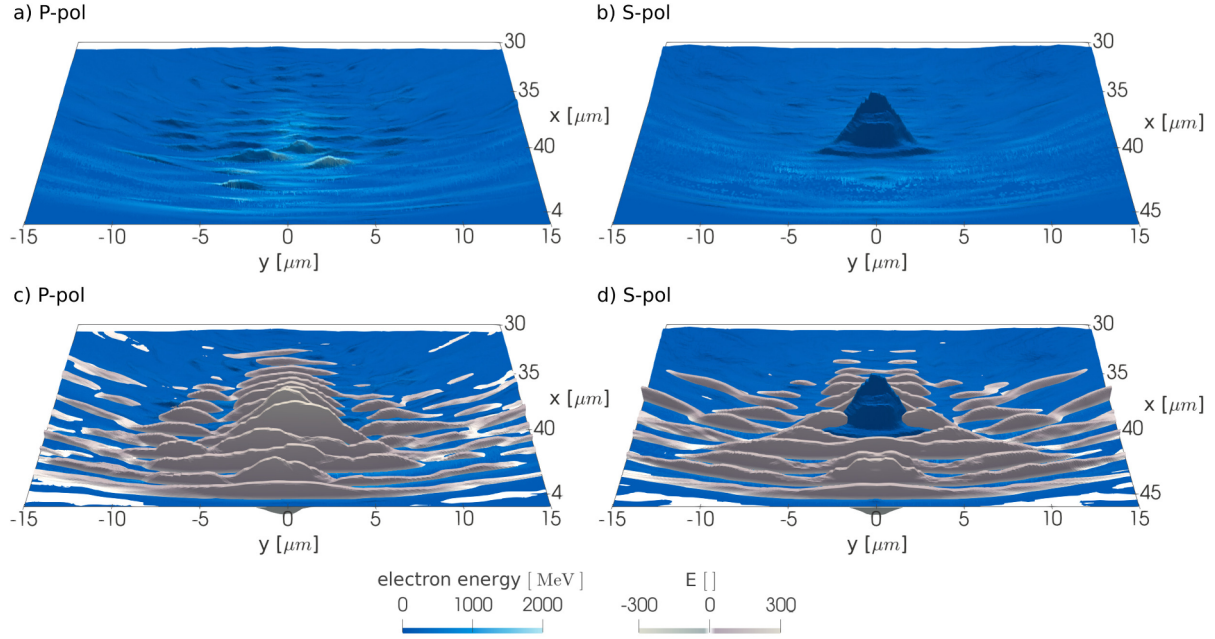
**Fig. 5.** Spatial distributions at time $t = 47\ T$ for different laser pulse polarisations: electron local mean energy, represented by blue color scales, its density, represented by the vertical height and the laser pulse electric field in the corresponding direction (represented by both the vertical height and by the grey scale). (For interpretation of the references to colour in this figure legend, the reader is referred to the web version of this article.)

structure is visible only in the proton spectra for linear s-polarisation, which is then employed in the simulations hereinafter. The dependence on linear polarisation clearly distinguishes our scheme from similar ones described in the introduction [32–35] as the circular polarisation plays a crucial role in them.

Another parameter significantly affecting the ion acceleration in our scheme is the wavelength of the interface corrugation $\lambda_C$. As was demonstrated in Section 3.1, the bunches are generated at the positions of corrugation maxima and are dependent on the development of low-density regions, located at the corrugation zeros. Therefore, a change of the corrugation wavelength may significantly modify the geometry of the system with a constant finite focal spot of diameter $D_L$. The increase of the ratio $D_L/\lambda_C$ by 0.5 then corresponds to the addition of another two corrugation points (maxima / minima / zeros) into the system as can be seen in the scheme in Fig. 7.

The HL simulation described in Section 3.1 corresponds to the ratio $D_L/\lambda_C = 2.0$ with 4 corrugation zeros. The low-density regions developed at the zeros further from the central axis provide a channels converging the laser pulse toward the central axis as can be seen in Fig. 2-a and in the scheme in Fig. 7. Therefore, an efficient bunch

should not be generated for the ratio $D_L/\lambda_C < 1$, where this phenomena cannot occur. For the same reason the bunch structure should significantly deteriorate for the ratio $D_L/\lambda_C > 2.5$ as another diverging channel is being applied. This idea corresponds to proton spectra shown in Fig. 6-c and is also valid for ratios $D_L/\lambda_C$ which are not multiples of 0.5 as shown in Fig. 6-d. The average bunch energy and maximum proton energy in simulation is rising with the corrugation wavelength (decreasing with $D_L/\lambda_C$) till $D_L/\lambda_C > 1$. The lowest energy spread was achieved in the case of $D_L/\lambda_C = 2$ (i.e. the HL case from the Section 3.2). The energy spread is rising with both increasing and decreasing corrugation wavelength. Two phenomena play roles in this case. The number of particles in the central bunch between the positions $-1/4\lambda_C$ and $+1/4\lambda_C$ (zeros closer to the central axis) is increasing with $\lambda_C$ as well as the enfolding field is broadened (see Fig. 8). There, the proton local mean energy and density for cases $D_L/\lambda_C = 3.0$, $D_L/\lambda_C = 2.5$, $D_L/\lambda_C = 1.5$ and $D_L/\lambda_C = 1.0$ corresponding to Fig. 2-a at time $t = 14$ T are shown. On one hand, if the corrugation wavelength is too small as shown in Fig. 8-a, more bunches of similar low density are actively developed. On the other hand, if the corrugation wavelength is too large, the enfolding field is too broad and the central bunch spreads
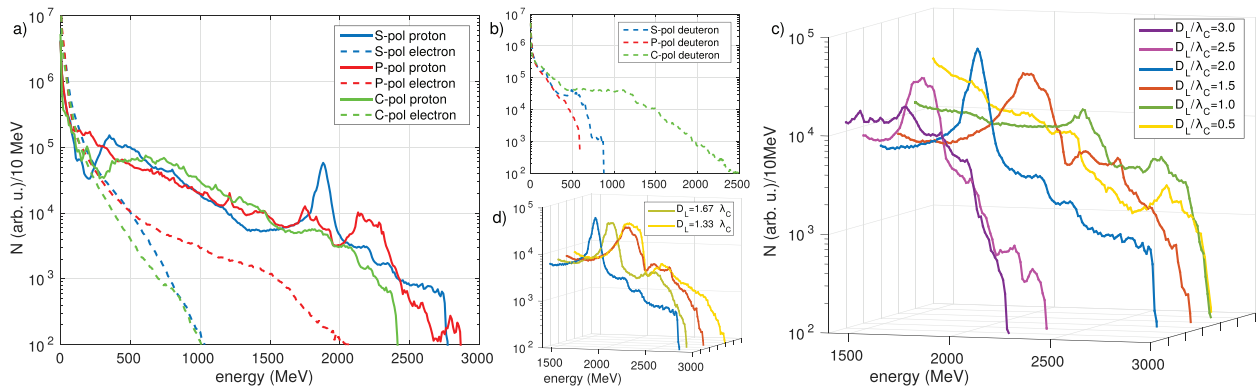


**Fig. 6.** Energy spectra at time $t = 47\ T$ for various parameters. a) Proton and electron energy spectra for simulation study cases with different laser pulse polarisations, b) corresponding deuteron energy spectra, c-d) the tail of the proton energy spectra of various corrugation wavelengths $\lambda_C$ for the focal spot diameter $D_L = 10\ \mu$m.
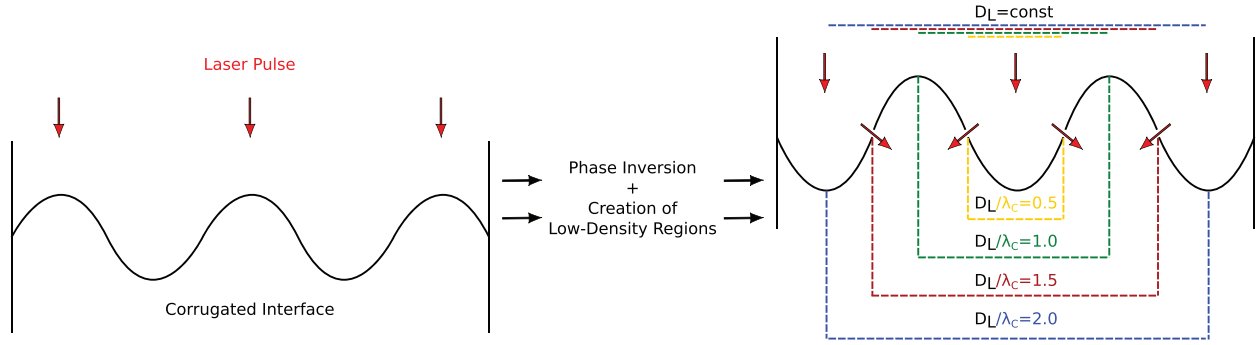
**Fig. 7.** Scheme of the different geometric interaction for various corrugation wavelengths $\lambda_C$.

in space as shown in Fig. 8-d. Therefore, an optimum corrugation wavelength is around $D_L/\lambda_C = 2.0$ which is then used for comparison with similar types of target in the following section.

### 3.4. Comparison with similar types of targets

To point out the effects of double-layer target and modulation on its interface, another two simulations are performed. Namely, double-layer deuterium-hydrogen target without modulation, referred as HL-WO, and pure hydrogen target of the same thickness ($2\lambda$), referred as L2. The reference time was chosen to be $t = 47\,T$ as in the previous discussion. Proton energy spectra of all the simulated cases are shown in Fig. 3-d and corresponding proton density and energy spatial distributions are presented in Fig. 9.

In the HL and LH cases (with the interface modulation) a bunch structure is created in the spatial plot (Fig. 9-a and -b) and corresponding quasi-monoenergetic peak is developed in the proton energy spectra (Fig. 3-d). The trend of a more narrow bunch in the HL case compared with the LH case, initialized by different positions of the low-density regions of the foil, also continues in the later time. This results into more narrow peak in the energy spectra with higher average energy in the HL case (1890 MeV compared to 1490 MeV) in Fig. 3-d. Maximal reached energy is also slightly higher in the HL case (2770

MeV compared to 2700 MeV). Proton bunch is more shifted in space towards the front of the overall proton cloud and less spread in the $x$-direction in the HL case (compare Figs 9-a and -b).

On the contrary, HL-WO and L2 cases develop a bubble structure (Fig. 9-c and -d), with no significant peaks in the energy spectrum (Fig. 3-d). The maximum proton energy of the simulated cases is reached in the L2 case (2850 MeV). This case is the best match for the radiation pressure acceleration regime described by Eq. (1) assuming single layer target with no induced instability. The symmetric bubble structure holds till the reference time and proportionally small amount of protons near the axis are accelerated to the highest maximal energies (Fig. 9-d). Oppositely, the bubble shape is getting distorted in the HL-WO case (Fig. 9-c), due to the multi-ion-species effects, resulting into significantly lower maximum energy (2430 MeV).

At the same reference time deuterium ion reached significantly lower maximal energies than protons in our simulations (see inset in Fig. 3-d). Their energies are lower than 1200 MeV (i.e., 600 MeV per nucleon) and the highest energy is reached in the LH case. It corresponds to the observation of proton bunch being detached from the deuterium layer, reducing further acceleration of deuterium ions.

The development of the transverse SWI is shown in Fig. 10-a. Here the full-front Gaussian laser pulse (8 $T$ longer) is used instead of the pulse with the steep front. The rest of the simulation parameters,
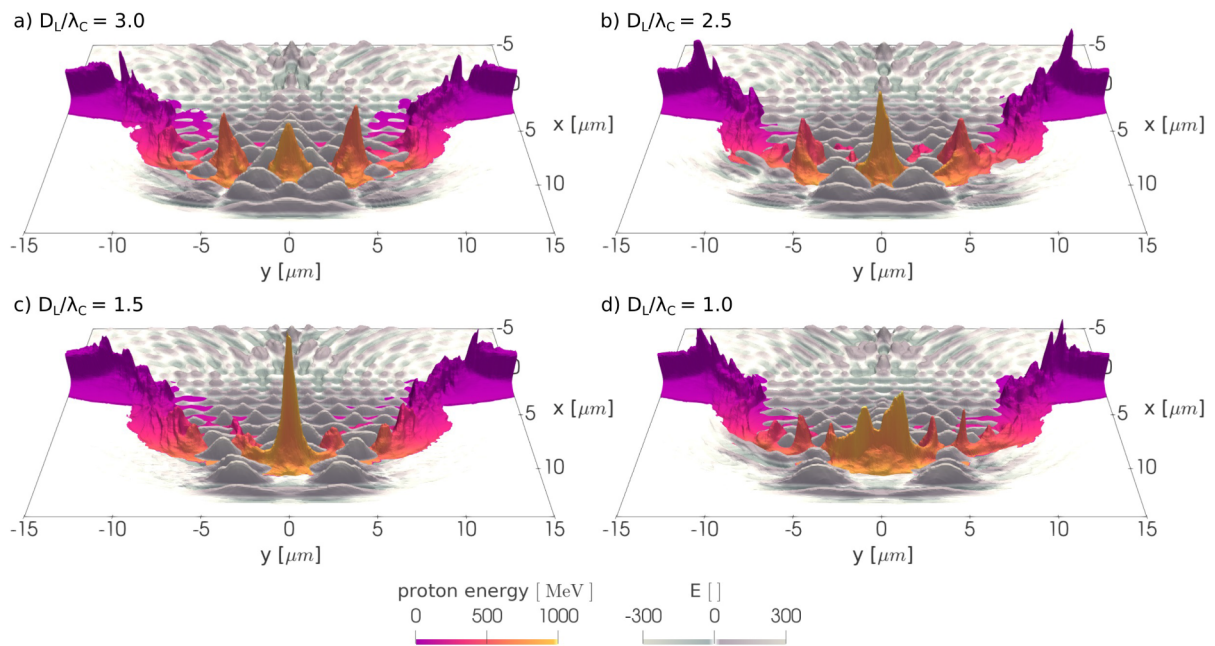


**Fig. 8.** Spatial distributions at time $t = 14\,T$ for different corrugation wavelengths. The proton local mean energy is represented by red color scales, proton densities are represented by vertical height. The laser pulse electric field (in the z-direction) is represented by both the vertical height and by grey scale. (For interpretation of the references to colour in this figure legend, the reader is referred to the web version of this article.)
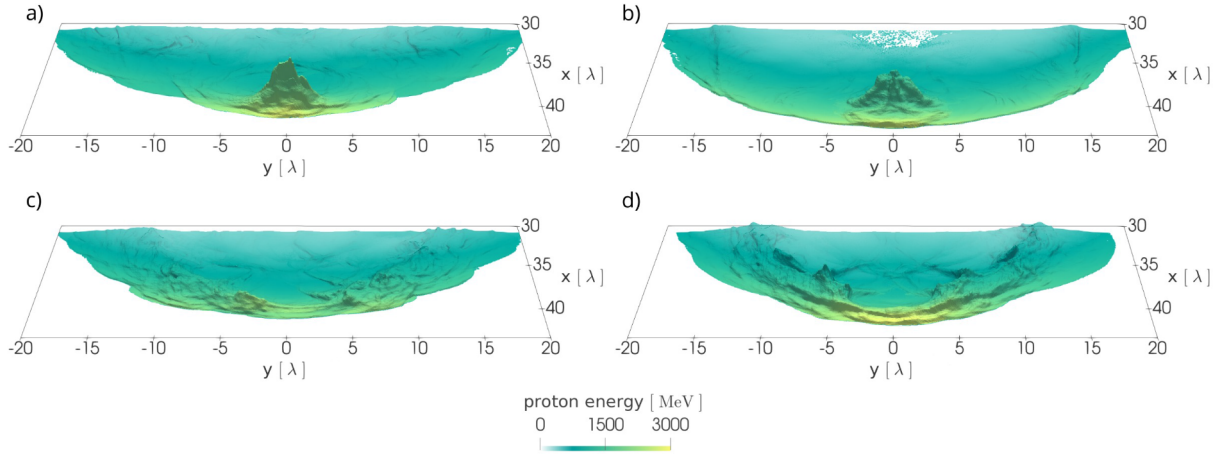
**Fig. 9.** Spatial distributions at time $t = 47\ T$. The proton density is represented by the vertical height and proton energy is represented by the blue to yellow scale. The simulated cases are: a) HL, b) LH, c) HL-WO, d) L2 (see parameters of all the targets in the text). (For interpretation of the references to colour in this figure legend, the reader is referred to the web version of this article.)

including the corrugation, are same as in the previous HL case. This simulation case is referred as HL-FF (full front). The foil is disrupted into relatively high number of small bunches and low-density regions (compared to 3 large bunches at the same time instant in Fig. 2-a).

On the first hand, the foil disruption enhances the acceleration of deuterons as they are more mixed with the protons and are kept together for longer time. Deuterons are then accelerated to maximum energy more comparable with protons (1600 MeV and 1920 MeV for deuterons and protons, respectively) than in the case of the steep-front pulse (870 MeV and 2770 MeV) as can be seen in Fig. 10-b at the reference time 47 $T$. The data for the HL-FF case are shown at time postponed by 8 $T$, i.e., the peak intensity of both laser pulses reaches the target at the same time instant.

On the other hand, the foil disruption significantly reduces the potential of the radiation pressure acceleration of protons. In this case the maximal proton energy is reduced to 1920 MeV and only a relatively small peak in medium energies (with average energy of 690 MeV) is created (Fig. 10-b). This behavior corresponds to previously made simulations with full pulse and single layer targets [4]. Moreover, the proton spectrum is also similar to another simulation of the steep-front laser pulse (the same as in previous HL and LH cases) with pure 2 $\lambda$ thick hydrogen target with the same modulation introduced on its front surface instead of the interface (referred as L2-SM). Where the average energy of the peak is 800 MeV and the maximum energy reaches 2010 MeV (Fig. 10-b).

## 4. Conclusions

In conclusion, collisionless relativistic instability with RMI-like features is observed in our simulations, using double-layer targets with initial interface modulation and high-intensity steep-front laser pulse. Evolution of this instability is described in the heavy-light (HL) and light-heavy (LH) cases, resulting into a development of bunch structures in the density distribution and proton spectra.

Well-collimated, quasi-monoenergetic proton bunch is observed for the HL case, with the average energy in the multi-GeV range, energy spread down to 3.7%, solid angle of 0.1 mrad, divergence of 0.038 rad and transverse rms emittance down to 0.046 mm·mrad (at FWHM). The emittance is one order of magnitude lower compared to that of conventional accelerators. The energy conversion of the laser pulse into the proton particles inside this bunch is around 3.4% and overall conversion into all particles is over 40%.

Optimal parameters for the ultra-low energy spread are acquired using corrugation wavelength of half of the laser focal spot diameter and linear (s- in the 2D geometry) polarisation.

The bunch is more distinctive in the proton spectrum and its average energy is significantly higher compared to other simulated cases with the same target composition. These other cases are either dominated by essentially different type of instabilities (development of short-wavelength instability using full-front laser pulse or introduction of the modulation on the surface of a single layer target) or the instability and bunch structures are not developed (targets without initial
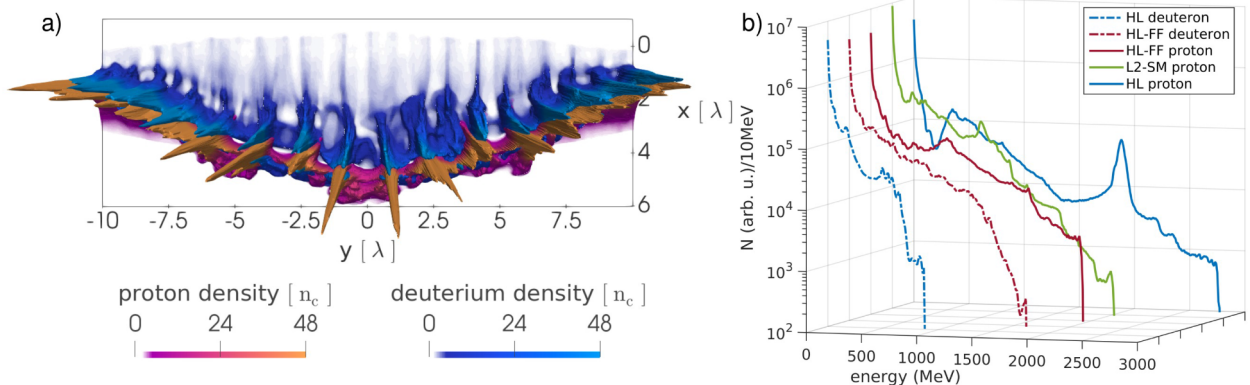


**Fig. 10.** Short-wavelength instability. a) Spatial distributions in the HL-FF case at time $t = 14\ T$. Blue and red scales represent deuterium and proton densities with maximum value set to the initial density. Full density is indicated by the vertical height. b) Proton and deuteron energy spectra for HL, HL-FF and L2-SM cases at time $t = 47\ T$. (For interpretation of the references to colour in this figure legend, the reader is referred to the web version of this article.)

modulation using steep-front laser pulse, reducing the development of short-wavelength instability).

## Declaration of Competing Interest

The authors declare that they have no known competing financial interests or personal relationships that could have appeared to influence the work reported in this paper.

## Acknowledgements

## Appendix A. Data visualisation and virtual reality

Several visualization methods were used to create visual outputs from the above discussed simulation data. Firstly, raw data were imported in ParaView [66] software to interpret them and to create visual outputs (figures and videos) describing the simulation mechanisms (see Fig. A.11-a). Secondly, data have been presented in web-based interactive 3D application [39] (see Fig. A.11-b), which runs in a regular web browser and utilizes VR (virtual reality) mode to offer scientists a completely new point of view of their simulations.

Here we present the videos (accessible online) of the time evolution of the simulated HL case mentioned above and in Fig. A.11 visualised in ParaView:

**VID1.mp4**

and in the web-based interactive 3D application:

**VID2.mp4**

The second option comes together with a challenge to find the best workflow that would enable visualization of such a large datasets in a web browser while maintaining high frame rates for smooth experience not only while using the VR headset. We have evaluated existing technologies like VTK.js library developed directly for scientific visualization in browser as well as Three.js javascript 3D library. Unfortunately, both libraries could not render our datasets with hundreds of timeframes with sufficient performance. The main issues were minutes-long loading times together with insufficient frame rates for large animated datasets. Thus, we have developed custom WebGL solution [39], a framework that not only renders the dataset on the GPU in real-time at high frame rates, but also provides orthogonal views, textual and numeric information, alongside a graphical user interface containing timeline animation controls and layer visibility management, with additional graphical elements based on D3.js for plotting animated graphs and legends. In order to import simulation data to this application, they are transformed into binary buffers in a node.js script so the visualization engine can directly send them to GPU with no need for further pre-processing. Currently we are working on an implementation of our transformation pipeline to the Jupyter notebook [67] toolchain to allow more users to create high-performance web-based VR-enabled visualizations.
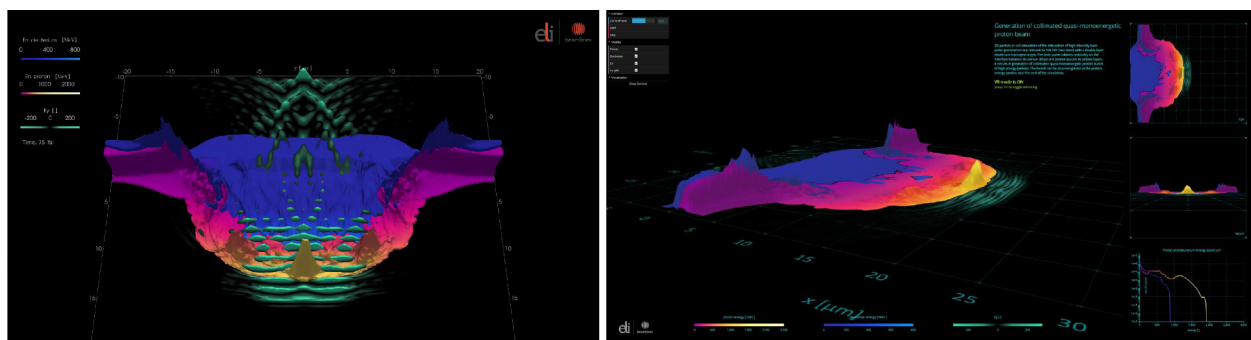


**Fig. A.11.** Data visualisation. Time evolution of the simulated HL case visualised in: a) ParaView, b) web-based interactive 3D application.

## Supplementary material

Supplementary material associated with this article can be found, in the online version, at 10.1016/j.hedp.2020.100844

# References

[1] A. Higginson, R.J. Gray, M. King, R.J. Dance, S.D. Williamson, N.M. Butler, R. Wilson, R. Capdessus, C. Armstrong, J.S. Green, S.J. Hawkes, P. Martin, W.Q. Wei, S.R. Mirfayzi, X.H. Yuan, S. Kar, M. Borghesi, R.J. Clarke, D. Neely, P. McKenna, Near-100 MeV protons via a laser-driven transparency-enhanced hybrid acceleration scheme, Nat. Commun. 9 (724) (2018) ., https://doi.org/10.1038/s41467-018-03063-9.

[2] T. Esirkepov, M. Borghesi, S.V. Bulanov, G. Mourou, T. Tajima, Highly efficient relativistic-ion generation in the laser-piston regime, Phys. Rev. Lett. 92 (175003) (2004), https://doi.org/10.1103/PhysRevLett.92.175003.

[3] S.S. Bulanov, E. Esarey, C.B. Schroeder, S.V. Bulanov, T.Z. Esirkepov, M. Kando, F. Pegoraro, W.P. Leemans, Radiation pressure acceleration: the factors limiting maximum attainable ion energy, Phys. Plasmas 23 (056703) (2016), https://doi.org/10.1063/1.4946025.

[4] F. Pegoraro, S.V. Bulanov, Photon bubbles and ion acceleration in a plasma dominated by the radiation pressure of an electromagnetic pulse, Phys. Rev. Lett. 99 (065002) (2007), https://doi.org/10.1103/PhysRevLett.99.065002.

[5] Rayleigh, Investigation of the character of the equilibrium of an incompressible heavy fluid of variable density, Proc. Lond. Math. Soc. 14 (1882) 170–177, https://doi.org/10.1112/plms/s1-14.1.170.

[6] G. Taylor, The instability of liquid surfaces when accelerated in a direction perpendicular to their planes. I, Proc. R. Soc. Lond. Ser.A. Math. Phys. Sci. 201 (1065) (1950) 192–196, https://doi.org/10.1098/rspa.1950.0052.

[7] S.V. Bulanov, E.Y. Echkina, T.Z. Esirkepov, I.N. Inovenkov, M. Kando, F. Pegoraro, G. Korn, Unlimited energy gain in the laser-driven radiation pressure dominant acceleration of ions, Phys. Plasmas 17 (063102) (2010), https://doi.org/10.1063/1.3428741.

[8] E.Y. Echkina, I.N. Inovenkov, T.Z. Esirkepov, F. Pegoraro, M. Borghesi, S.V. Bulanov, Dependence of the ion energy on the parameters of the laser pulse and target in the radiation-pressure-dominated regime of acceleration, Plasma Phys. Rep. 36 (1) (2010) 15–29, https://doi.org/10.1134/S1063780X10010022.

[9] S.V. Bulanov, V.S. Khoroshkov, Feasibility of using laser ion accelerators in proton therapy, Plasma Phys. Rep. 28 (5) (2002) 453–456, https://doi.org/10.1134/1.1478534.

[10] S.V. Bulanov, T.Z. Esirkepov, F.F. Kamenets, Y. Kato, A.V. Kuznetsov, K. Nishihara, F. Pegoraro, T. Tajima, V.S. Khoroshkov, Generation of high-quality charged particle beams during the acceleration of ions by high-power laser radiation, Plasma Phys. Rep. 28 (12) (2002) 975–991, https://doi.org/10.1134/1.1528239.

[11] T. Esirkepov, S.V. Bulanov, K. Nishihara, T. Tajima, F. Pegoraro, V.S. Khoroshkov, K. Mima, H. Daido, Y. Kato, Y. Kitagawa, K. Nagai, S. Sakabe, Proposed double-layer target for the generation of high-quality laser-accelerated ion beams, Phys. Rev. Lett. 89 (175003) (2002), https://doi.org/10.1103/PhysRevLett.89.175003.

[12] S.V. Bulanov, T. Esirkepov, V.S. Khoroshkov, A.V. Kuznetsov, F. Pegoraro, Oncological hadrontherapy with laser ion accelerators, Phys. Lett. Sect. A: Gen. Atomic Solid State Phys. 299 (2–3) (2002) 240–247, https://doi.org/10.1016/S0375-9601(02)00521-2.

[13] S.V. Bulanov, J.J. Wilkens, T.Z. Esirkepov, G. Korn, G. Kraft, S.D. Kraft, M. Molls, V.S. Khoroshkov, Laser ion acceleration for hadron therapy, Phys. Usp. 57 (12) (2014) 1149–1179, https://doi.org/10.3367/ufne.0184.201412a.1265.

[14] M. Roth, T.E. Cowan, M.H. Key, S.P. Hatchett, C. Brown, W. Fountain, J. Johnson, D.M. Pennington, R.A. Snavely, S.C. Wilks, K. Yasuike, H. Ruhl, F. Pegoraro, S.V. Bulanov, E.M. Campbell, M.D. Perry, H. Powell, Fast ignition by intense laser-accelerated proton beams, Phys. Rev. Lett. 86 (3) (2001) 436–439, https://doi.org/10.1103/PhysRevLett.86.436.

[15] S. Atzeni, M. Temporal, J.J. Honrubia, A first analysis of fast ignition of pre-compressed ICF fuel by laser-accelerated protons, Nucl. Fusion 42 (3) (2002), https://doi.org/10.1088/0029-5515/42/3/101.

[16] R.D. Richtmyer, Taylor instability in shock acceleration of compressible fluids, Commun. Pure Appl. Math. 13 (2) (1960) 297–319, https://doi.org/10.1002/cpa.3160130207.

[17] E.E. Meshkov, Instability of the interface of two gases accelerated by a shock wave, Fluid Dyn. 4 (5) (1969) 101–104, https://doi.org/10.1007/BF01015969.

[18] Y. Zhou, Rayleigh - Taylor and Richtmyer - Meshkov instability induced flow, turbulence, and mixing. I, Phys. Rep. 720–722 (2017) 1–136, https://doi.org/10.1016/j.physrep.2017.07.005.

[19] C.A. Palmer, J. Schreiber, S.R. Nagel, N.P. Dover, C. Bellei, F.N. Beg, S. Bott, R.J. Clarke, A.E. Dangor, S.M. Hassan, P. Hilz, D. Jung, S. Kneip, S.P. Mangles, K.L. Lancaster, A. Rehman, A.P. Robinson, C. Spindloe, J. Szerypo, M. Tatarakis, M. Yeung, M. Zepf, Z. Najmudin, Rayleigh-Taylor instability of an ultrathin foil accelerated by the radiation pressure of an intense laser, Phys. Rev. Lett. 108 (225002) (2012), https://doi.org/10.1103/PhysRevLett.108.225002.

[20] Y. Yang, Q. Zhang, D.H. Sharp, Small amplitude theory of Richtmyer-Meshkov instability, Phys. Fluids 6 (5) (1994) 1856–1873, https://doi.org/10.1063/1.868245.

[21] K. Nishihara, J.G. Wouchuk, C. Matsuoka, R. Ishizaki, V.V. Zhakhovsky, Richtmyer-Meshkov instability: theory of linear and nonlinear evolution, Philos. Trans. R. Soc. A 368 (1916) (2010) 1769–1807, https://doi.org/10.1098/rsta.2009.0252.

[22] C. Matsuoka, K. Nishihara, T. Sano, Nonlinear dynamics of non-uniform current-vortex sheets in magnetohydrodynamic flows, J. Nonlinear Sci. 27 (2) (2017) 531–572, https://doi.org/10.1007/s00332-016-9343-4.

[23] Y. Zhou, T.T. Clark, D.S. Clark, S. Gail Glendinning, M. Aaron Skinner, C.M. Huntington, O.A. Hurricane, A.M. Dimits, B.A. Remington, Turbulent mixing and transition criteria of flows induced by hydrodynamic instabilities, Phys. Plasmas 26 (080901) (2019), https://doi.org/10.1063/1.5088745.

[24] J.J. Hester, The crab nebula: an astrophysical chimera, Annu. Rev. Astron.

[25] J.D. Lindl, R.L. Mccrory, E.M. Campbell, Progress toward ignition and burn propagation in inertial confinement fusion, Phys. Today 45 (9) (1992) 32–40, https://doi.org/10.1063/1.881318.

[26] A.L. Velikovich, Analytic theory of Richtmyer-Meshkov instability for the case of reflected rarefaction wave, Phys. Fluids 8 (6) (1996) 1666–1679, https://doi.org/10.1063/1.868938.

[27] J.G. Wouchuk, K. Nishihara, Linear perturbation growth at a shocked interface, Phys. Plasmas 3 (10) (1996) 3761–3776, https://doi.org/10.1063/1.871940.

[28] C.E. Niederhaus, J.W. Jacobs, Experimental study of the Richtmyer-Meshkov instability of incompressible fluids, J. Fluid Mech. 485 (2003) 243–277, https://doi.org/10.1017/S002211200300452X.

[29] G. Fraley, Rayleigh - Taylor stability for a normal shock wave - density discontinuity interaction, Phys. Fluids 29 (2) (1986) 376, https://doi.org/10.1063/1.865722.

[30] J.G. Wouchuk, K. Nishihara, Asymptotic growth in the linear Richtmyer-Meshkov instability, Phys. Plasmas 4 (4) (1997) 1028–1038, https://doi.org/10.1063/1.872191.

[31] F. Mohseni, M. Mendoza, S. Succi, H.J. Herrmann, Relativistic effects on the Richtmyer-Meshkov instability, Phys. Rev. D - Part. Fields Gravitation Cosmol. 90 (12) (2014) ., https://doi.org/10.1103/PhysRevD.90.125028.

[32] M.L. Zhou, X.Q. Yan, G. Mourou, J.A. Wheeler, J.H. Bin, J. Schreiber, T. Tajima, Proton acceleration by single-cycle laser pulses offers a novel monoenergetic and stable operating regime, Phys. Plasmas 23 (043112) (2016), https://doi.org/10.1063/1.4947544.

[33] X.Q. Yan, H.C. Wu, Z.M. Sheng, J.E. Chen, J. Meyer-Ter-Vehn, Self-Organizing GeV, nanocoulomb, collimated proton beam from laser foil interaction at 7-1021w/cm2, Phys. Rev. Lett. 103 (13) (2009), https://doi.org/10.1103/PhysRevLett.103.135001.

[34] J.L. Liu, M. Chen, Z.M. Sheng, C.S. Liu, W.B. Mori, J. Zhang, Stable laser-produced quasimonoenergetic proton beams from interactive laser and target shaping, Phys. Rev. Spec. Top. Accel Beams 16 (12) (2013), https://doi.org/10.1103/PhysRevSTAB.16.121301.

[35] M. Chen, A. Pukhov, T.P. Yu, Z.M. Sheng, Enhanced collimated GeV monoenergetic ion acceleration from a shaped foil target irradiated by a circularly polarized laser pulse, Phys. Rev. Lett. 103 (024801) (2009), https://doi.org/10.1103/PhysRevLett.103.024801.

[36] O. Klimo, J. Psikal, J. Limpouch, V.T. Tikhonchuk, Monoenergetic ion beams from ultrathin foils irradiated by ultrahigh-contrast circularly polarized laser pulses, Phys. Rev. Spec. Top. Accel. Beams 11 (3) (2008), https://doi.org/10.1103/PhysRevSTAB.11.031301.

[37] A.P. Robinson, M. Zepf, S. Kar, R.G. Evans, C. Bellei, Radiation pressure acceleration of thin foils with circularly polarized laser pulses, New J. Phys. 10 (013021) (2008), https://doi.org/10.1088/1367-2630/10/1/013021.

[38] M. Nishiuchi, H. Sakaki, T.Z. Esirkepov, K. Nishio, T.A. Pikuz, A.Y. Faenov, I.Y. Skobelev, R. Orlandi, H. Sako, A.S. Pirozhkov, K. Matsukawa, A. Sagisaka, K. Ogura, M. Kanasaki, H. Kiriyama, Y. Fukuda, H. Koura, M. Kando, T. Yamauchi, Y. Watanabe, S.V. Bulanov, K. Kondo, K. Imai, S. Nagamiya, Acceleration of highly charged GeV Fe ions from a low-Z substrate by intense femtosecond laser, Phys. Plasmas 22 (3) (2015), https://doi.org/10.1063/1.4913434.

[39] M. Danielova, P. Janecka, J. Grosz, A. Holy, Interactive 3D Visualizations of Laser Plasma Experiments on the Web and in VR, in: J. Madeiras Pereira, R.G. Raidou (Eds.), EuroVis 2019 - Posters, The Eurographics Association, 2019, p. ., , https://doi.org/10.2312/eurp.20191145.

[40] T.D. Arber, K. Bennett, C.S. Brady, A. Lawrence-Douglas, M.G. Ramsay, N.J. Sircombe, P. Gillies, R.G. Evans, H. Schmitz, A.R. Bell, C.P. Ridgers, Contemporary particle-in-cell approach to laser-plasma modelling, Plasma Phys. Controlled Fusion 57 (113001) (2015), https://doi.org/10.1088/0741-3335/57/11/113001.

[41] C.P. Ridgers, J.G. Kirk, R. Duclous, T.G. Blackburn, C.S. Brady, K. Bennett, T.D. Arber, A.R. Bell, Modelling gamma-ray photon emission and pair production in high-intensity laser-matter interactions, J. Comput. Phys. 260 (2014) 273–285, https://doi.org/10.1016/j.jcp.2013.12.007.

[42] S.V. Bulanov, T.Z. Esirkepov, M. Kando, J. Koga, K. Kondo, G. Korn, On the problems of relativistic laboratory astrophysics and fundamental physics with super powerful lasers, Plasma Phys. Rep. 41 (1) (2015), https://doi.org/10.1134/S1063780X15010018.

[43] V.A. Vshivkov, N.M. Naumova, F. Pegoraro, S.V. Bulanov, Nonlinear electrodynamics of the interaction of ultra-intense laser pulses with a thin foil, Phys. Plasmas 5 (7) (1998) 2727–2741, https://doi.org/10.1063/1.872961.

[44] S.A. Reed, T. Matsuoka, S. Bulanov, M. Tampo, V. Chvykov, G. Kalintchenko, P. Rousseau, V. Yanovsky, R. Kodama, D.W. Litzenberg, K. Krushelnick, A. Maksimchuk, Relativistic plasma shutter for ultraintense laser pulses, Appl. Phys. Lett. 94 (20) (2009), https://doi.org/10.1063/1.3139860.

[45] S. Palaniyappan, B.M. Hegelich, H.C. Wu, D. Jung, D.C. Gautier, L. Yin, B.J. Albright, R.P. Johnson, T. Shimada, S. Letzring, D.T. Offermann, J. Ren, C. Huang, R. Hörlein, B. Dromey, J.C. Fernandez, R.C. Shah, Dynamics of relativistic transparency and optical shuttering in expanding overdense plasmas, Nat. Phys. 8 (10) (2012) 763–769, https://doi.org/10.1038/nphys2390.

[46] W.Q. Wei, X.H. Yuan, Y. Fang, Z.Y. Ge, X.L. Ge, S. Yang, Y.F. Li, G.Q. Liao, Z. Zhang, F. Liu, M. Chen, L. Zhao, H.B. Zhuo, Y.T. Li, Z.M. Sheng, J. Zhang, Plasma optical shutter in ultraintense laser-foil interaction, Phys. Plasmas 24 (113111) (2017), https://doi.org/10.1063/1.5008843.

[47] M. Matys, O. Klimo, J. Psikal, S.V. Bulanov, Simulation studies on transmissivity of silicon nitride plasma shutter for laser pulse contrast enhancement, 45th EPS Conference on Plasma Physics, EPS 2018, 2018-July (2018), pp. 1332–1335.

[48] M. Jirka, O. Klimo, Y.-J. Gu, S. Weber, Enhanced photon emission from a double-layer target at moderate laser intensities. Sci. Rep. 10 (8887) (2020), https://doi.org/10.1038/s41598-020-65778-4.

[49] S.V. Bulanov, I.N. Inovenkov, V.I. Kirsanov, N.M. Naumova, A.S. Sakharov, Nonlinear depletion of ultrashort and relativistically strong laser pulses in an underdense plasma, Phys. Fluids B 4 (7) (1992) 1935–1942, https://doi.org/10.1063/1.860046.

[50] S.V. Bulanov, V.I. Kirsanov, N.M. Naumova, A.S. Sakharov, H.A. Shah, I.N. Inovenkov, Stationary shock-front of a relativisticaily strong electromagnetic radiation in an underdense plasma, Phys. Scr. 47 (2) (1993) 209–213, https://doi.org/10.1088/0031-8949/47/2/014.

[51] C.D. Decker, W.B. Mori, K.C. Tzeng, T. Katsouleas, The evolution of ultra-intense, short-pulse lasers in underdense plasmas, Phys. Plasmas 3 (5) (1996) 2047–2056, https://doi.org/10.1063/1.872001.

[52] G.A. Mourou, T. Tajima, S.V. Bulanov, Optics in the relativistic regime, Rev. Mod. Phys. 78 (2) (2006), https://doi.org/10.1103/RevModPhys.78.309.

[53] Y. Wan, C.H. Pai, C.J. Zhang, F. Li, Y.P. Wu, J.F. Hua, W. Lu, Y.Q. Gu, L.O. Silva, C. Joshi, W.B. Mori, Physical mechanism of the transverse instability in radiation pressure ion acceleration, Phys. Rev. Lett. 117 (234801) (2016), https://doi.org/10.1103/PhysRevLett.117.234801.

[54] Y. Wan, C.H. Pai, C.J. Zhang, F. Li, Y.P. Wu, J.F. Hua, W. Lu, C. Joshi, W.B. Mori, V. Malka, Physical mechanism of the electron-ion coupled transverse instability in laser pressure ion acceleration for different regimes, Phys. Rev. E 98 (013202) (2018), https://doi.org/10.1103/PhysRevE.98.013202.

[55] D. Margarone, A. Velyhan, J. Dostal, J. Ullschmied, J.P. Perin, D. Chatain, S. Garcia, P. Bonnay, T. Pisarczyk, R. Dudzak, M. Rosinski, J. Krasa, L. Giuffrida, J. Prokupek, V. Scuderi, J. Psikal, M. Kucharik, M. De Marco, J. Cikhardt, E. Krousky, Z. Kalinowska, T. Chodukowski, G.A. Cirrone, G. Korn, Proton acceleration driven by a nanosecond laser from a cryogenic thin solid-hydrogen ribbon, Phys. Rev. X 6 (4) (2016), https://doi.org/10.1103/PhysRevX.6.041030.

[56] A.P. Robinson, R.M. Trines, N.P. Dover, Z. Najmudin, Hole-boring radiation pressure acceleration as a basis for producing high-energy proton bunches, Plasma Phys. Controlled Fusion 54 (11) (2012), https://doi.org/10.1088/0741-3335/54/11/115001.

[57] J. Psikal, M. Matys, Dominance of hole-boring radiation pressure acceleration regime with thin ribbon of ionized solid hydrogen, Plasma Phys. Controlled Fusion 60

[58] (4) (2018), https://doi.org/10.1088/1361-6587/aaa7fa.

[58] R. Courant, K. Friedrichs, H. Lewy, On the partial difference equations of mathematical physics, IBM J. Res. Dev. 11 (2) (2010) 215–234, https://doi.org/10.1147/rd.112.0215.

[59] P. Mora, Physics of relativistic laser-plasmas, Plasma Phys. Controlled Fusion 43 (12A) (2001) A31–A37, https://doi.org/10.1088/0741-3335/43/12A/303.

[60] K. Floettmann, Some basic features of the beam emittance, Phys. Rev. Spec. Top. Accel. Beams 6 (3) (2003) 80–86, https://doi.org/10.1103/PhysRevSTAB.6.034202.

[61] T. Zhang, S.X. Peng, W.B. Wu, H.T. Ren, J.F. Zhang, J.M. Wen, T.H. Ma, Y.X. Jiang, J. Sun, Z.Y. Guo, J.E. Chen, Practical 2.45-GHz microwave-driven Cs-free H - ion source developed at Peking University, Chin. Phys. B 27 (10) (2018), https://doi.org/10.1088/1674-1056/27/10/105208.

[62] T.E. Cowan, J. Fuchs, H. Ruhl, A. Kemp, P. Audebert, M. Roth, R. Stephens, I. Barton, A. Blazevic, E. Brambrink, J. Cobble, J. Fernández, J.C. Gauthier, M. Geissel, M. Hegelich, J. Kaae, S. Karsch, G.P. Le Sage, S. Letzring, M. Manclossi, S. Meyroneinc, A. Newkirk, H. Pépin, N. Renard-LeGalloudec, Ultralow emittance, multi-MeV proton beams from a laser virtual-cathode plasma accelerator, Phys. Rev. Lett. 92 (20) (2004), https://doi.org/10.1103/PhysRevLett.92.204801.

[63] Y.J. Gu, Z. Zhu, X.F. Li, Q. Yu, S. Huang, F. Zhang, Q. Kong, S. Kawata, Stable long range proton acceleration driven by intense laser pulse with underdense plasmas, Phys. Plasmas 21 (6) (2014), https://doi.org/10.1063/1.4882437.

[64] J.L. Liu, M. Chen, J. Zheng, Z.M. Sheng, C.S. Liu, Three dimensional effects on proton acceleration by intense laser solid target interaction, Phys. Plasmas 20 (6) (2013), https://doi.org/10.1063/1.4812458.

[65] D.J. Stark, L. Yin, B.J. Albright, F. Guo, Effects of dimensionality on kinetic simulations of laser-ion acceleration in the transparency regime, Phys. Plasmas 24 (5) (2017), https://doi.org/10.1063/1.4982741.

[66] J. Ahrens, B. Geveci, C. Law, ParaView: an end-user tool for large-data visualization, Visualization Handbook, Elsevier Inc., 2005, pp. 717–731, https://doi.org/10.1016/B978-012387582-2/50038-1.

[67] T. Kluyver, B. Ragan-kelley, F. Pérez, B. Granger, M. Bussonnier, J. Frederic, K. Kelley, J. Hamrick, J. Grout, S. Corlay, P. Ivanov, D. Avila, S. Abdalla, C. Willing, Jupyter Notebooks - a Publishing Format for Reproducible Computational Workflows, IOS Press, 2016, https://doi.org/10.3233/978-1-61499-649-1-87.

## C.4 Relativistic plasma aperture for laser intensity enhancement

The following article is reproduced from M. Jirka, O. Klimo, and M. Matys (2021) Relativistic plasma aperture for laser intensity enhancement. *Physical Review Research* **3**, 033175.

# Relativistic plasma aperture for laser intensity enhancement

M. Jirka, O. Klimo, and M. Matys

*ELI Beamlines Centre, Institute of Physics, Czech Academy of Sciences, Za Radnici 835, 25241 Dolni Brezany, Czech Republic*
*and Faculty of Nuclear Sciences and Physical Engineering, Czech Technical University in Prague, Brehova 7, 115 19 Prague, Czech Republic*

A substantial increase in local laser intensity is observed in the near field behind a plasma shutter. This increase is caused by the interference of the diffracted light at the relativistic plasma aperture and it is studied both analytically and using numerical simulations. This effect is only accessible in the regime of relativistically induced transparency and thus it requires a careful choice of laser and target parameters. The theoretical estimates for the maximum field strength and its spatial location as a function of target and laser parameters are provided and compared with simulation results. Our full 3D particle-in-cell simulations indicate that the laser intensity may be increased roughly by an order of magnitude, improving the feasibility of strong field QED research with the present generation of lasers.

## I. INTRODUCTION

Nowadays, the most powerful laser systems can reach intensity on the order of $10^{22}$ W/cm$^2$ and the dynamics of laser-plasma interaction becomes strongly relativistic [1–3]. One example is the onset of relativistic transparency in the interaction with the overdense target [4]. The laser light cannot propagate in the overdense target, as its frequency is lower or equal to the frequency of the electron plasma oscillations. However, when the intense laser field is applied, the electron mass increases due to the relativistic motion reducing the plasma frequency. It results in a decrease of the effective target density and thus the intense part of the laser field can propagate through the plasma.

Such an effect is especially important in the interaction with a thin overdense foil, as it affects the temporal envelope of the laser pulse [5–8]. Therefore, it has an impact on ion acceleration and radiation generation [9,10]. It was shown that in the case of an ultraintense laser pulse, a relativistic plasma aperture is created in an ultrathin foil and the laser pulse is diffracted [11]. Since the plasma electrons are driven by the diffraction pattern of the laser field, the spatial structure of the accelerated electron beam can be controlled by varying the laser pulse parameters [11]. As the electron dynamics consequently affects the spatial-intensity distribution of the accelerated ions, such an approach could be used for optically controlled ion acceleration [12–14].

Here we study the increase of the laser field intensity caused by the interference of the light diffracted at the relativistic plasma aperture for the case of linearly polarized laser pulse. It is investigated both analytically and using 2D and 3D

particle-in-cell (PIC) simulations. It is shown that due to the relativistic motion of the electrons, the laser intensity can be locally increased by almost an order of magnitude. However, this effect is only accessible in the regime of relativistically induced transparency and thus it requires a careful choice of the laser and target parameters. If the target is either under- or overdense, the relativistic plasma aperture cannot be created and the diffraction structure responsible for the field intensity enhancement is not present. The theoretical estimates for the maximum field strength and its spatial location are provided as a function of laser pulse and target parameters and compared with simulation results.

## II. INTERACTION WITH A PLASMA SHUTTER

In the following text, we study the process of laser intensity enhancement in the interaction of an ultraintense laser pulse ($\sim 10^{22}$ W/cm$^2$) with an ultrathin ($\sim 10$ s nm) plasma layer having the electron plasma density $n_\mathrm{p}$ greater than the value of the relativistic critical density $n_{\mathrm{c}\gamma} = \gamma n_\mathrm{c}$, where $\gamma$ is the relativistic Lorentz factor (of an electron having the charge $e$ and mass $m_e$) and $n_\mathrm{c} = \omega_0^2 m_e/(4\pi e^2)$ represents the nonrelativistic critical plasma density. The ion motion is neglected. We assume a laser pulse linearly polarized along the $y$ axis propagating in the negative $x$ direction focused to a spot of radius $w_0$. It has a Gaussian temporal envelope of full width at half maximum (FWHM) duration $\tau$ in the laser intensity. Its amplitude is characterized by the Lorentz invariant parameter $a_0 = eE_0/(m_e\omega_0 c)$, where $E_0$ is the amplitude of the electric field, $\omega_0$ is the laser angular frequency, and $c$ is the speed of light [15].

When a relativistically overdense shutter ($n_\mathrm{p} > n_{\mathrm{c}\gamma}$) is assumed, the front part of the laser pulse is reflected from the foil surface. However, as the laser pulse intensity grows to its maximum value, the laser pulse starts to penetrate the target. The dominant mechanism allowing target penetration differs depending on the target thickness and density. In the case of the ultrathin foil, the electrons are pushed away due

---

to the radiation pressure of the incoming laser pulse. If the thicker target is assumed, it is rather the increasing relativistic mass of electrons that causes the foil to become relativistically transparent so the rest of the laser pulse can pass through the foil. Therefore, the laser field strength at which the plasma layer becomes transparent depends on the density and thickness of the foil as well as on the laser wavelength $\lambda$. In both cases, the laser pulse acquires a steep front edge as a result of the interaction [5–7] that can be utilized, e.g., for enhanced photon emission due to the improved temporal contrast or for enhancement of ion acceleration from structured targets due to reduced development of transverse short-wavelength instabilities [16,17]. Here we study the interaction with the ultrathin foil. For $a_0 \gg 1$ and an unperturbed plasma slab of thickness $l \ll \lambda$, the laser pulse strength required for penetration of the foil (meaning that the laser pulse is able to push all electrons away from the initial position of the foil by the radiation pressure) can be estimated as [5,18,19]

$$a_0^{\max} = \frac{n_p \pi l}{n_c \lambda}. \tag{1}$$

Naturally, the laser pulse penetrates the target near the laser axis at first. With the increase of the laser pulse strength at later times, the target becomes transparent at all points where the condition Eq. (1) for laser penetration is satisfied.

However, even for $a_0 < a_0^{\max}$, the laser pulse may penetrate through the foil at least partially due to the skin effect [20]. The relativistically corrected skin depth is $l_{\text{skin}} = \sqrt{\gamma} c/\omega_p$, where $\omega_p = \sqrt{4\pi n_p e^2/m_e}$ is the plasma frequency [15]. The radiation pressure of the laser pulse will first squeeze the plasma layer of initial thickness $l$ to a thin slab of thickness $d$ while the density will grow by a factor of $l/d$. The corresponding skin depth is $c/\omega_0 \sqrt{\gamma n_c d/(n_p l)}$. As shown later in the text, the amplitude of the resulting field is enhanced due to the interference of the transmitted and scattered beams. Since the strength of the scattered beam should be non-negligible to noticeably contribute to the interference, we consider the target to be transparent if the intensity of the transmitted (scattered) beam is at least of the order of $\exp(-3/2)$ of the incident intensity. It is a free parameter and this particular choice illustrates well the studied case (10 s nm targets, intensity $10^{22}$ W/cm$^2$). If the target is very thin, the oscillating border of the plasma aperture cannot fully develop and affect the interaction. In such a case, the scattering process is not effective. For targets thicker than the skin depth, the scattered intensity is below the order of $\exp(-2)$ of the incident intensity. Therefore, in both cases, the interference enhancement is low and not interesting. Thus, assuming the intensity of the incident laser pulse is reduced by a factor of $\exp(-3/2)$ after passing through the squeezed plasma layer of a thickness $d$, we obtain

$$2k_0 \sqrt{\frac{l d n_p}{\gamma n_c}} = \frac{3}{2}, \tag{2}$$

where $k_0 = \omega_0/c$. Based on Eq. (1), the field strength $a_0^t = n_p \pi (l - d)/n_c \lambda$ is required for pushing the electrons along distance $l - d$ of the unperturbed target of density $n_p$ to create a squeezed plasma layer. After finding the value of $d$ from Eq. (2) and inserting into $a_0^t$, one may obtain the characteristic
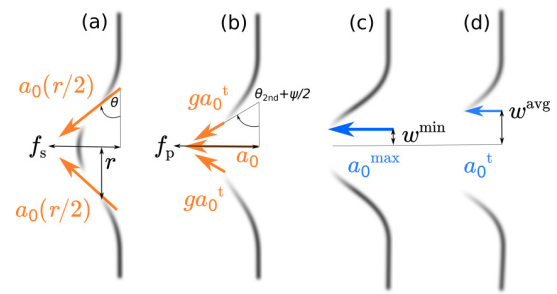


FIG. 1. Schematic of target geometry during the interaction with (a) *s*-polarized and (b) *p*-polarized laser pulse. (c) Minimal and (d) characteristic aperture radius for penetration of the foil.

amplitude of the field required for penetration of the target [as a penetration we consider intensity drop by a factor of $\exp(-3/2)$]:

$$a_0^t = \frac{4/3\sqrt{2} k_0^2 l^2 n_p}{(3/4 + 8/3\sqrt{2} k_0 l) n_c}. \tag{3}$$

For the ultrathin foils with the thickness of the order of 10 nm assumed in this paper, $a_0^t \approx 0.5 a_0^{\max}$. While the most intense part of the laser pulse propagates through the thin plasma slab and a relativistic aperture is formed, the electrons at the borders of the aperture oscillate in the direction of the resulting electric field, which is given by the interference of the incident laser wave with the wavefronts reflected from a relativistically overdense plasma slab [11]. In the case of *s* polarization (the laser electric field is perpendicular to the plane of incidence), target electrons are simultaneously driven toward the laser beam axis by the ponderomotive force of the two nodes created at the target front side twice per laser period [11]. It results in an increase of the target density on the axis and therefore two separate relativistic plasma apertures are created in the vicinity of the laser beam axis at first, see Fig. 1(a) [11]. It agrees with a double lobe profile of the transmitted laser field observed in three-dimensional simulations and the corresponding asymmetry measured in the distribution of accelerated electrons and ions [11,12,21,22]. We assume that at the radial position $r$, i.e., at the outer edge of the relativistic plasma aperture, the laser pulse strength is equal to $a_0^t = a_0 \exp(-r^2/w_0^2)$. As the high density along the beam axis prevents the transmission of the beam close to the axis, the strength of the field passing through one aperture can be estimated as $a(r/2) = a_0 \exp[-r^2/(2w_0)^2]$. The resulting field at the rear side of the target is created by the interference of two transmitted beams, each having the above-mentioned strength. Therefore, the amplitude of the diffracted field is approximately given by

$$a_0^s = 2a(r/2) = 2a_0 \exp[-r^2/(2w_0)^2]. \tag{4}$$

When *p* polarization is assumed (the laser electric field is parallel to the plane of incidence), the aperture is created on the axis at first, see Fig. 1(b). Contrary to the previous case, dense electron bunches are driven alternatively from two opposite edges of the aperture toward the laser axis at the frequency $2\omega_0$ [23]. The photons of the transmitted laser pulse are thus scattered by these relativistic electron bunches

generating a number of high harmonics. The intensity of the $n$th harmonic can be approximated by a power-law $I_n \propto n^{-8/3}$ [24,25]. Assuming that laser field of strength $a_0^t$ is scattered by the electron bunches at two opposite sides of the aperture, the interference of the generated harmonics will create a field of strength $2g a_0^t$, where $g = \sqrt{\sum_{n=2}^{N} n^{-8/3}}$ is the fraction of the incoming field scattered into $N$ harmonics. Due to their further interference with the field propagating along the laser axis, the resulting field amplitude can be approximated as

$$a_0^p = 2g a_0^t + a_0. \qquad (5)$$

However, in both cases, the field amplification is expected to be limited by the target thickness that has to be smaller than the relativistically corrected skin depth $l_{skin}$. Since Eq. (3) is maximized at $l = l_{skin}$ for a given target density and laser wavelength, such a choice presents through Eqs. (4) and (5) the upper limit for the resulting field strength.

The longitudinal position of the maximum field strength at the rear side of the target can be estimated from the knowledge of the aperture size and propagation direction of the transmitted or scattered light, see Fig. 1. The minimal aperture radius of the foil can be estimated as

$$w^{min} = w_0 \sqrt{\left| \ln \frac{a_0^{max}}{a_0} \right|}, \qquad (6)$$

as illustrated in Fig. 1(c).

In the case of $s$ polarization, the target surface is perturbed by the action of created electromagnetic nodes. The propagation direction $\theta$ (with respect to the laser axis) of the transmitted beam at the rear side of the target is given by the deformation of the target surface caused by radiation pressure and, therefore, it strongly depends on laser and target parameters [26,27]. However, $\tan\theta$ can be estimated as the ratio of the laser pulse strengths at the axis and at the radial distance, which are sufficiently strong to penetrate the target. Below the strength limit required for target penetration, the foil deformation is given by the distribution of intensity isosurfaces of the incoming laser beam. In such a case, the angle can be estimated as $\tan\theta = \tau c/(\sqrt{2\ln 2}w_0)$. When the plasma aperture is created, the ratio of longitudinal and radial distances given by isosurfaces has to be weighted by the maximum $a_0^{max}$ and the characteristic value $a_0^t$ of field strengths required for penetration, which results in

$$\tan\theta = \frac{\tau c}{\sqrt{2\ln 2}w_0} \frac{w^{min}}{w^{avg}}, \qquad (7)$$

where

$$w^{avg} = w_0 \sqrt{\left| \ln \frac{a_0^t}{a_0} \right|} \qquad (8)$$

is considered, see Fig. 1(d). Assuming that the laser pulse starts to penetrate once $a_0^{max}$ is achieved, one can expect the interference maxima to occur at the distance

$$f_s = w^{min} \tan\theta \qquad (9)$$

from the initial target position.

In the case of $p$ polarization, the maximum field strength is created by the constructive interference of scattered har-

monics with the field of the propagating laser beam. Thus, its location depends on the propagation direction of scattered photons which is a function of electron beam momentum. However, the angle of the electron bunch propagation direction evolves with time. At the beginning, the electrons are driven along the $y$ axis. At later times, the angle of propagation $\psi$ can be estimated again from the geometrical properties of the Gaussian laser pulse as

$$\tan\psi = \frac{\tau c}{\sqrt{2\ln 2}w_0}. \qquad (10)$$

The laser photons are scattered into a number of harmonics, each having a different angle of propagation measured with respect to the electron beam direction. Among them, the second harmonic has a dominant contribution for the interference pattern and the corresponding angle can be estimated as [28]

$$\theta_{2nd} = \arccos\left[ \frac{1 + \beta\cos(\psi/2)}{2\beta} \right], \qquad (11)$$

where $\beta = \sqrt{1 - 1/(\gamma^{avg})^2}$, $\gamma^{avg} = \sqrt{1 + (a_0^t)^2/2}$, and $\psi/2$ is the average value of the angle at which the electron bunch propagates. Thus, the maximum field strength is expected to be achieved at the distance of

$$f_p = w^{avg} \tan(\theta_{2nd} + \psi/2). \qquad (12)$$

## III. 2D AND 3D SIMULATION RESULTS

We compare our theoretical predictions with 2D and 3D PIC simulations performed in the code EPOCH [29,30]. The 2D simulation box resolved with $10\,125 \times 4\,500$ cells is spanning from $-30\,\mu m$ to $15\,\mu m$ in the $x$ direction and from $-10\,\mu m$ to $10\,\mu m$ in the $y$ direction. The laser pulse of the peak intensity $I_0 = 10^{22}$ W/cm$^2$ ($a_0 = 69$) enters the simulation box at a boundary $x = 15\,\mu m$ and is focused to a spot of radius $w_0 = 1.5\,\mu m$ located at $x = 0\,\mu m$. It has a wavelength $\lambda = 805$ nm and a Gaussian temporal envelope of FWHM duration $\tau = 30$ fs in laser intensity. We performed simulations for both $s$ and $p$ polarization of the laser pulse. The Al$^{13+}$ solid foil with the corresponding free electron density $450 n_c$ and the thickness $10 - 60$ nm is located at the focal spot. The initial particle temperature is set to zero.

The distributions of the transmitted laser intensity and the density of target electrons are shown in Figs. 2 and 3 for $s$ and $p$ polarization, respectively. The black contours correspond to the relativistic critical plasma density $n_{c\gamma}^{avg} = \gamma^{avg} n_c$. In the first figure, it is shown that during the penetration of the target having a thickness of 30 nm, the laser field has a two-lobe structure (at $x = -1.6\,\mu m$), later creating a symmetric field distribution at $x = -2.4\,\mu m$. This is a significant difference from the latter case, in which an asymmetric field diffraction pattern is created due to the interference of the penetrating laser field with the field scattered by the dense electron bunches which are driven alternately from two opposite sides of the aperture (see contours of the critical density near $x = -0.6\,\mu m$, $y = 2\,\mu m$ and $x = -1\,\mu m$, $y = -2\,\mu m$ in Fig. 3).

The longitudinal position of the maximum field strength generated by the interference pattern at the rear side of the target is shown in Fig. 4(a). The expected values calculated from Eqs. (9) and (12) ($x$ axis) are compared to the results
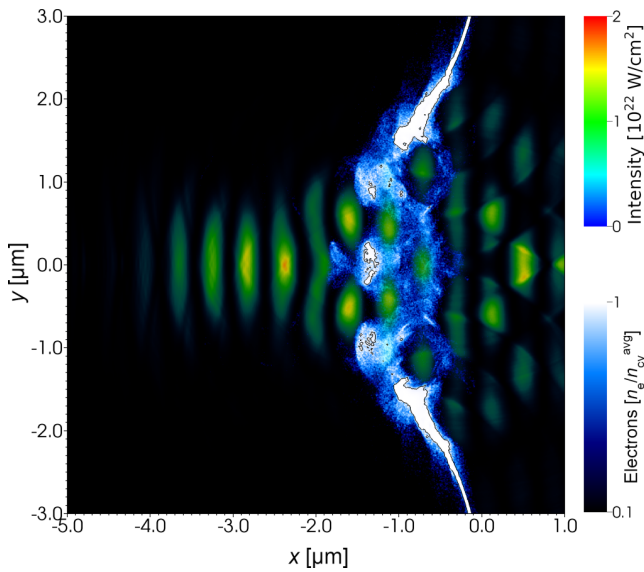
FIG. 2. The intensity of the *s*-polarized laser pulse and the density of target electrons for $I_0 = 10^{22}$ W/cm$^2$ and $\lambda = 805$ nm. Target thickness is 30 nm. Black contours in electron density represent the relativistic critical density $n_{c\gamma}^{avg}$.

obtained from PIC simulations (*y* axis) for different target thicknesses. The solid line is added to guide the eye for the perfect agreement between the theory and simulation results. As expected, according to the theory, the focal distance becomes shorter as the target thickness grows.

In Fig. 4(b), we compare the ratio of the first ten harmonics of the scattered light to the incident field of amplitude $E_0$ in the case of a *p*-polarized laser beam. The respective harmonics are obtained by filtering out all other frequency components in the Fourier transform of the laser electric field. The results
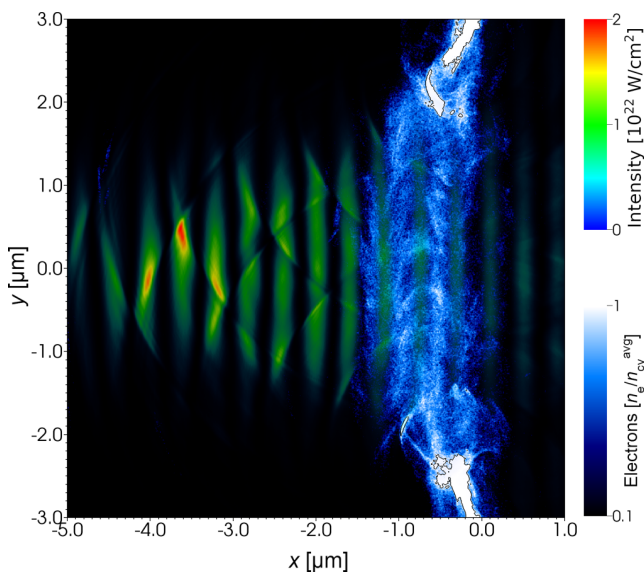


FIG. 3. The intensity of the *p*-polarized laser pulse and the density of target electrons for $I_0 = 10^{22}$ W/cm$^2$ and $\lambda = 805$ nm. Target thickness is 30 nm. Black contours in electron density represent the relativistic critical density $n_{c\gamma}^{avg}$.
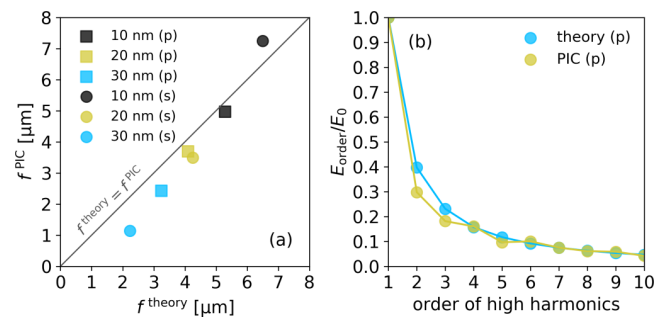


FIG. 4. (a) Longitudinal position of the maximum field strength at the rear side of the target given by Eqs. (9) and (12) and obtained from PIC simulation. (b) The ratio of the first ten harmonics of the scattered light to the incident field of strength $E_0$ obtained from PIC simulations and compared to the theory described in Refs. [24,25] for *p*-polarized laser beam.

obtained from the simulation with a 30 nm target are in good agreement with the theory described in Refs. [24,25] which was used for calculating the resulting field amplitude $a_0^p$ in Eq. (5). It can be seen that the field strength for higher harmonics is small and it can be neglected. This justifies our choice of $N = 10$ in Eq. (5). The electric field distributions in $k_x - k_y$ phase space (**k** is the wave vector) for (a) *s* and (b) *p* polarization are shown in Fig. 5 for the same laser and target parameters. This spectrum is calculated only for the field which penetrates through the target. There is a clear evidence of high harmonics propagating at an angle in case of *p* polarization in contrast to *s* polarization. The $k_x$ spectrum is broad as the maximum intensity due to interference is very well localized, corresponding to a short spatial profile of the pulse in the longitudinal direction. The $k_x$ and $k_y$ are normalized to the vacuum wave number of the laser $k_0 = 2\pi/\lambda$.

Figure 6 presents the comparison of the resulting field amplitude as a function of target thickness for both types of a linearly polarized laser beam. The simulation results show that the peak intensity of the diffracted field gradually grows with the target thickness as predicted by Eqs. (4) and (5). The thicker the target is, the stronger the field required for penetration, and thus the resulting diffracted field achieves higher amplitude. However, increasing the target thickness beyond
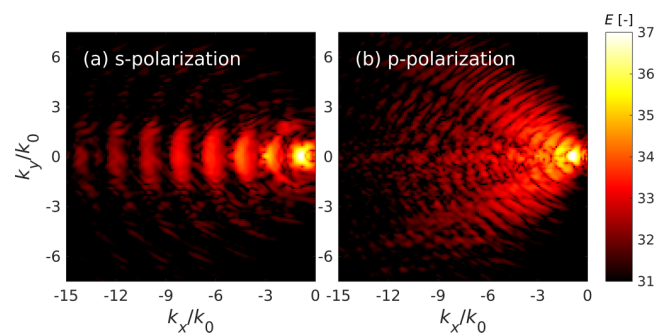


FIG. 5. The electric field intensity distribution in $k_x - k_y$ phase-space for (a) *s* and (b) *p* polarization at the same time step as in Figs. 2 and 3. The laser of intensity $I_0 = 10^{22}$ W/cm$^2$ and wavelength $\lambda = 805$ nm irradiates the 30-nm-thick target.
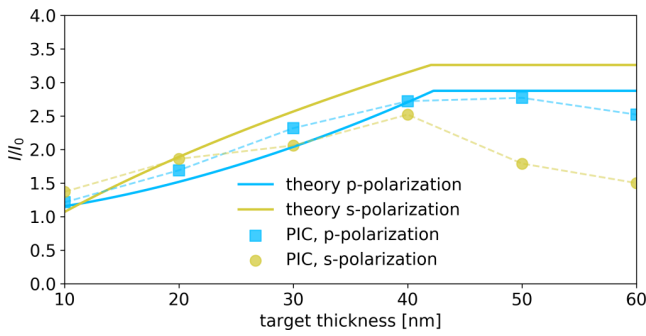
FIG. 6. Maximum intensity $I$ achieved in the interaction of the $s$- and $p$-polarized Gaussian laser beam characterized by $I_0 = 10^{22}$ W/cm$^2$ with the target of different thickness. Lines represent the expected values given by Eqs. (4) and (5), markers show the results obtained from PIC simulations. The relativistically corrected skin depth is 42 nm.

the relativistically corrected skin depth $l_{\text{skin}} = 42$ nm results in more pronounced laser energy absorption in the target and thus the intensity of the diffracted field becomes reduced. The obtained results are therefore in good agreement with the theory as it has a natural limit for target thickness given by the relativistically corrected skin depth. This absorption is not taken into account in the theory and thus the theoretical curve stays constant. In the case of $p$ polarization, the first ten harmonics were considered in Eq. (5).

To check the validity of our results and get more realistic information on the field amplification due to the interference of the laser field, we carried out an additional 3D simulation for different laser and target parameters ($\lambda = 1$ $\mu$m, $\sin^2$ temporal envelope, foil thickness 20 nm, $n_{\text{p}} = 835n_{\text{c}}$). The simulation box of dimensions $44\mu$m $\times$ $17\mu$m $\times$ $17\mu$m was resolved with $8\,800 \times 680 \times 680$ cells. The temperature of all particles was set to 5 keV. As shown in Fig. 7, the characteristic structures of the diffracted laser field in a plane perpendicular or parallel to the polarization axis (see Figs. 2 and 3) are also present in the 3D case. The horizontal and vertical slices of the laser beam correspond to $p$ and $s$ polarization from 2D, respectively. The horizontal plane in 3D contains the electric field vector of the linearly polarized laser beam. The laser field amplification due to the diffraction on an evolving plasma aperture in the 3D case can be roughly estimated as $(a_0^s + a_0^p)/a_0$ (resulting in intensity enhancement by a factor of $[(a_0^s + a_0^p)/a_0]^2$), where $a_0^s$ and $a_0^p$ correspond to the field contributions from $s$- and $p$-polarization components which were studied above in the 2D case, respectively. This approach predicts the maximum amplification of the laser intensity by a factor of 7.0 at a distance 3.7 $\mu$m behind the shutter, which is comparable to the maximum value 7.1 obtained from 3D simulation at a distance 4.3 $\mu$m, see Fig. 8, having in mind that in the simulation it is not guaranteed that the field interference maxima in both planes appear simultaneously at the same position. According to the analysis of 3D simulation, the processes in $s$ and $p$ planes previously studied in the 2D case happen simultaneously and independently, while there is no dominant process responsible for intensity enhancement. Thus, this enhancement can be estimated as a combination of these two processes. The relativistic electron bunches respon-
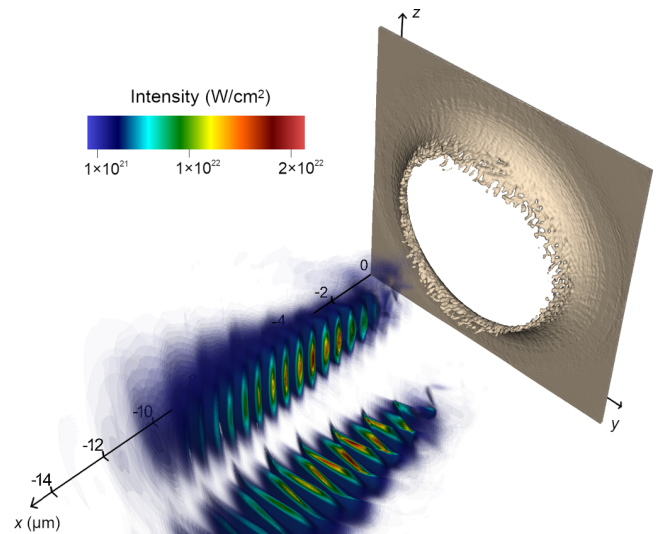


FIG. 7. The distribution of the laser intensity in horizontal and vertical slices of the laser pulse after the interaction with a foil as obtained from 3D simulation.

sible for scattering the laser field observed in the 2D case for $p$ polarization are also present in 3D simulation, see Fig. 8. We also note that in the case of long laser pulses, the ion motion should be considered in the theoretical model as it can affect the formation process of the relativistic plasma aperture and the consequent laser intensity enhancement.

So far, we have assumed an idealized laser pulse. However, the laser systems are subject to a limited contrast [31]. Due to the interaction of the laser pulse pedestal with the target, the preplasma is formed before the main laser pulse arrives and
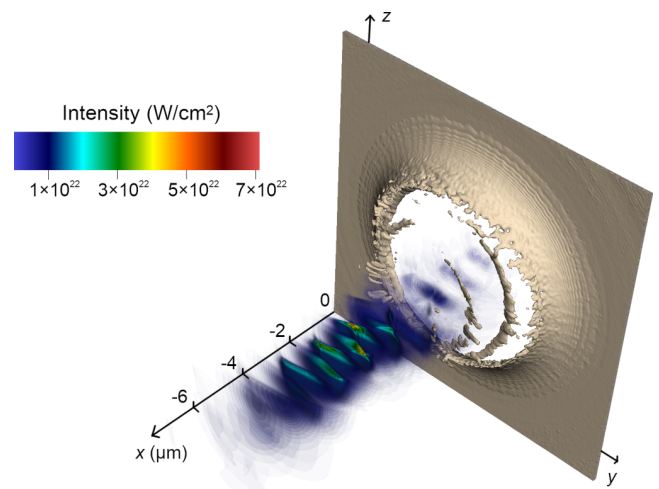


FIG. 8. The distribution of the laser intensity in the horizontal slice of the laser pulse as obtained from 3D simulation at the moment of reaching the maximum value.

thus it can significantly affect the interaction dynamics. Considering the above-mentioned laser intensity, the pedestal of the main laser pulse can completely destroy the nm-scale foil. The foil expands to several microns along the propagation axis and therefore its density is below the relativistically corrected critical value for the main laser pulse. As a result, the main laser pulse propagates in the expanded plasma without any significant distortion or focusing. To avoid such a scenario in a real experiment, one might consider the interaction with two foils. The pedestal of the main laser pulse interacts with the first foil only. The main laser pulse then propagates through the created underdense plasma and interacts with the second foil. Such a setup allows creating a relativistic plasma aperture in the second foil, which is essential for laser pulse diffraction, resulting in the increase of the laser intensity in the near field. This setup may also provide an additional intensity increase by laser self-focusing in the pre-expanded first foil, as we partially discussed in Ref. [32]. As the prepulse is mitigated by this configuration, this feature would be especially important in the interaction with additional (nano)structured and ultrathin targets, which would be pre-expanded otherwise. The application of the single and double foil configurations in the improvement of ion acceleration from an additional target was demonstrated by simulations in Ref. [33]. As the laser intensity can be increased by almost one order of magnitude, such a setup also allows enhancing gamma radiation and pair production using the present lasers.

## IV. CONCLUSION

In conclusion, we have studied the process of laser pulse diffraction on the relativistic plasma aperture created in the interaction with an overdense ultrathin foil. Such a setup allows amplifying the laser intensity due to the interference of the transmitted and/or diffracted beam. We provide theoretical estimates for obtaining the maximum field strength and its spatial location as a function of the laser and target parameters. Using 3D numerical simulations, we have verified that the laser intensity can be increased at least seven times when proper laser and target parameters are used. This setup, based solely on relativistic plasma optics, thus presents a viable approach for obtaining localized laser intensity enhancement, which might be interesting for applications like ion acceleration, generation of gamma rays, and electron positron pair creation.

[1] S.-W. Bahk, P. Rousseau, T. A. Planchon, V. Chvykov, G. Kalintchenko, A. Maksimchuk, G. A. Mourou, and V. Yanovsky, Generation and characterization of the highest laser intensities ($10^{22}$W/cm$^2$), Opt. Lett. **29**, 2837 (2004).

[2] V. Yanovsky, V. Chvykov, G. Kalinchenko, P. Rousseau, T. Planchon, T. Matsuoka, A. Maksimchuk, J. Nees, G. Cheriaux, G. Mourou, and K. Krushelnick, Ultra-high intensity-high 300-TW laser at 0.1 Hz repetition rate, Opt. Express **16**, 2109 (2008).

[3] A. S. Pirozhkov, Y. Fukuda, M. Nishiuchi, H. Kiriyama, A. Sagisaka, K. Ogura, M. Mori, M. Kishimoto, H. Sakaki, N. P. Dover, K. Kondo, N. Nakanii, K. Huang, M. Kanasaki, K. Kondo, and M. Kando, Approaching the diffraction-limited, bandwidth-limited petawatt, Opt. Express **25**, 20486 (2017).

[4] J. C. Fernández, D. Cort Gautier, C. Huang, S. Palaniyappan, B. J. Albright, W. Bang, G. Dyer, A. Favalli, J. F. Hunter, J. Mendez, M. Roth, M. Swinhoe, P. A. Bradley, O. Deppert, M. Espy, K. Falk, N. Guler, C. Hamilton, B. M. Hegelich, D. Henzlova, K. D. Ianakiev, M. Iliev, R. P. Johnson, A. Kleinschmidt, A. S. Losko, E. McCary, M. Mocko, R. O. Nelson, R. Roycroft, M. A. Santiago Cordoba, V. A. Schanz, G. Schaumann, D. W. Schmidt, A. Sefkow, T. Shimada, T. N. Taddeucci, A. Tebartz, S. C. Vogel, E. Vold, G. A. Wurden, and

L. Yin, Laser-plasmas in the relativistic-transparency regime: Sci. Appl. Phys. Plasmas **24**, 056702 (2017).

[5] V. A. Vshivkov, N. M. Naumova, F. Pegoraro, and S. V. Bulanov, Nonlinear electrodynamics of the interaction of ultra-intense laser pulses with a thin foil, Phys. Plasmas **5**, 2727 (1998).

[6] S. A. Reed, T. Matsuoka, S. Bulanov, M. Tampo, V. Chvykov, G. Kalintchenko, P. Rousseau, V. Yanovsky, R. Kodama, D. W. Litzenberg, K. Krushelnick, and A. Maksimchuk, Relativistic plasma shutter for ultraintense laser pulses, Appl. Phys. Lett. **94**, 201117 (2009).

[7] S. Palaniyappan, B. Manuel Hegelich, H.-C. Wu, D. Jung, D. C. Gautier, L. Yin, B. J. Albright, R. P. Johnson, T. Shimada, S. Letzring, D. T. Offermann, J. Ren, C. Huang, R. Hörlein, B. Dromey, J. C. Fernandez, and R. C. Shah, Dynamics of relativistic transparency and optical shuttering in expanding overdense plasmas, Nat. Phys. **8**, 763 (2012).

[8] W. Q. Wei, X. H. Yuan, Y. Fang, Z. Y. Ge, X. L. Ge, S. Yang, Y. F. Li, G. Q. Liao, Z. Zhang, F. Liu, M. Chen, L. Zhao, H. B. Zhuo, Y. T. Li, Z. M. Sheng, and J. Zhang, Plasma optical shutter in ultraintense laser-foil interaction, Phys. Plasmas **24**, 113111 (2017).

[9] A. Henig, D. Kiefer, K. Markey, D. C. Gautier, K. A. Flippo, S. Letzring, R. P. Johnson, T. Shimada, L. Yin, B. J. Albright,

K. J. Bowers, J. C. Fernández, S. G. Rykovanov, H.-C. Wu, M. Zepf, D. Jung, V. Kh. Liechtenstein, J. Schreiber, D. Habs, and B. M. Hegelich, Enhanced Laser-Driven Ion Acceleration in the Relativistic Transparency Regime, Phys. Rev. Lett. **103**, 045002 (2009).

[10] D. Kiefer, M. Yeung, T. Dzelzainis, P. S. Foster, S. G. Rykovanov, C. L. S. Lewis, R. S. Marjoribanks, H. Ruhl, D. Habs, J. Schreiber, M. Zepf, and B. Dromey, Relativistic electron mirrors from nanoscale foils for coherent frequency upshift to the extreme ultraviolet, Nat. Commun. **4**, 1763 (2013).

[11] B. Gonzalez-Izquierdo, R. J. Gray, M. King, R. J. Dance, R. Wilson, J. McCreadie, N. M. H. Butler, R. Capdessus, S. Hawkes, J. S. Green, M. Borghesi, D. Neely, and P. McKenna, Optically controlled dense current structures driven by relativistic plasma aperture-induced diffraction, Nat. Phys. **12**, 505 (2016).

[12] B. Gonzalez-Izquierdo, M. King, R. J. Gray, R. Wilson, R. J. Dance, H. Powell, D. A. Maclellan, J. McCreadie, N. M. H. Butler, S. Hawkes, J. S. Green, C. D. Murphy, L. C. Stockhausen, D. C. Carroll, N. Booth, G. G. Scott, M. Borghesi, D. Neely, and P. McKenna, Towards optical polarization control of laser-driven proton acceleration in foils undergoing relativistic transparency, Nat. Commun. **7**, 12891 (2016).

[13] A. Higginson, R. J. Gray, M. King, R. J. Dance, S. D. R. Williamson, N. M. H. Butler, R. Wilson, R. Capdessus, C. Armstrong, J. S. Green, S. J. Hawkes, P. Martin, W. Q. Wei, S. R. Mirfayzi, X. H. Yuan, S. Kar, M. Borghesi, R. J. Clarke, D. Neely, and P. McKenna, Near-100 MeV protons via a laser-driven transparency-enhanced hybrid acceleration scheme, Nat. Commun. **9**, 724 (2018).

[14] S. D. R. Williamson, R. Wilson, M. King, M. Duff, B. Gonzalez-Izquierdo, Z. E. Davidson, A. Higginson, N. Booth, S. Hawkes, D. Neely, R. J. Gray, and P. McKenna, Self-referencing spectral interferometric probing of the onset time of relativistic transparency in intense laser-foil interactions, Phys. Rev. Appl. **14**, 034018 (2020).

[15] P. Gibbon, *Short Pulse Laser Interactions with Matter* (Imperial College Press, Singapore, 2005).

[16] M. Jirka, O. Klimo, Y.-J. Gu, and S. Weber, Enhanced photon emission from a double-layer target at moderate laser intensities, Sci. Rep. **10**, 8887 (2020).

[17] M. Matys, K. Nishihara, M. Kecova, J. Psikal, G. Korn, and S. V. Bulanov, Laser-driven generation of collimated quasi-monoenergetic proton beam using double-layer target with modulated interface, High Energy Density Phys. **36**, 100844 (2020).

[18] S. S. Bulanov, C. B. Schroeder, E. Esarey, and W. P. Leemans, Optimized laser pulse profile for efficient radiation pressure acceleration of ions, Phys. Plasmas **19**, 093112 (2012).

[19] S. S. Bulanov, E. Esarey, C. B. Schroeder, S. V. Bulanov, T. Zh. Esirkepov, M. Kando, F. Pegoraro, and W. P. Leemans, Radiation pressure acceleration: The factors limiting maximum attainable ion energy, Phys. Plasmas **23**, 056703 (2016).

[20] E. G. Gamaliy and R. Dragila, Interaction of ultrashort laser pulses at relativistic intensities with solid targets: Relativistic skin effect, Phys. Rev. A **42**, 929 (1990).

[21] L. Yin, B. J. Albright, K. J. Bowers, D. Jung, J. C. Fernández, and B. M. Hegelich, Three-Dimensional Dynamics of Breakout Afterburner Ion Acceleration using High-Contrast Short-Pulse Laser and Nanoscale Targets, Phys. Rev. Lett. **107**, 045003 (2011).

[22] R. J. Gray, D. A. MacLellan, B. Gonzalez-Izquierdo, H. W. Powell, D. C. Carroll, C. D. Murphy, L. C. Stockhausen, D. R. Rusby, G. G. Scott, R. Wilson, N. Booth, D. R. Symes, S. J. Hawkes, R. Torres, M. Borghesi, D. Neely, and P. McKenna, Azimuthal asymmetry in collective electron dynamics in relativistically transparent laser–foil interactions, New J. Phys. **16**, 093027 (2014).

[23] M. J. Duff, R. Wilson, M. King, B. Gonzalez-Izquierdo, A. Higginson, S. D. R. Williamson, Z. E. Davidson, R. Capdessus, N. Booth, S. Hawkes, D. Neely, R. J. Gray, and P. McKenna, High order mode structure of intense light fields generated via a laser-driven relativistic plasma aperture, Sci. Rep. **10**, 105 (2020).

[24] T. Baeva, S. Gordienko, and A. Pukhov, Theory of high-order harmonic generation in relativistic laser interaction with overdense plasma, Phys. Rev. E **74**, 046404 (2006).

[25] M. R. Edwards and J. M. Mikhailova, The x-ray emission effectiveness of plasma mirrors: Reexamining power-law scaling for relativistic high-order harmonic generation, Sci. Rep. **10**, 5154 (2020).

[26] B. Gonzalez-Izquierdo, R. Capdessus, M. King, R. Gray, R. Wilson, R. Dance, J. McCreadie, N. Butler, S. Hawkes, J. Green, N. Booth, M. Borghesi, D. Neely, and P. McKenna, Radiation pressure-driven plasma surface dynamics in ultra-intense laser pulse interactions with ultra-thin foils, Appl. Sci. **8**, 336 (2018).

[27] A. McIlvenny, H. Ahmed, C. Scullion, D. Doria, L. Romagnani, P. Martin, K. Naughton, A. Sgattoni, D. R. Symes, A. Macchi, P. McKenna, M. Zepf, S. Kar, and M. Borghesi, Characteristics of ion beams generated in the interaction of ultra-short laser pulses with ultra-thin foils, Plasma Phys. Control. Fusion **62**, 054001 (2020).

[28] L. D. Landau and E. M. Lifshitz, *The Classical Theory of Fields*, 4th ed. (Butterworth-Heinemann, Oxford, 1980).

[29] C. P. Ridgers, J. G. Kirk, R. Duclous, T. G. Blackburn, C. S. Brady, K. Bennett, T. D. Arber, and A. R. Bell, Modelling gamma-ray photon emission and pair production in high-intensity laser–matter interactions, J. Comput. Phys. **260**, 273 (2014).

[30] T. D. Arber, K. Bennett, C. S. Brady, A. Lawrence-Douglas, M. G. Ramsay, N. J. Sircombe, P. Gillies, R. G. Evans, H. Schmitz, A. R. Bell, and C. P. Ridgers, Contemporary particle-in-cell approach to laser-plasma modelling, Plasma Phys. Control. Fusion **57**, 113001 (2015).

[31] S. Weber, S. Bechet, S. Borneis, L. Brabec, M. Bučka, E. Chacon-Golcher, M. Ciappina, M. DeMarco, A. Fajstavr, K. Falk, E.-R. Garcia, J. Grosz, Y.-J. Gu, J.-C. Hernandez, M. Holec, P. Janečka, M. Jantač, M. Jirka, H. Kadlecova, D. Khikhlukha, O. Klimo, G. Korn, D. Kramer, D. Kumar, T. Lastovička, P. Lutoslawski, L. Morejon, V. Olšovcová, M. Rajdl, O. Renner, B. Rus, S. Singh, M. Šmid, M. Sokol, R. Versaci, R. Vrána, M. Vranic, J. Vyskočil,

A. Wolf, and Q. Yu, P3: An installation for high-energy density plasma physics and ultra-high intensity laser–matter interaction at ELI-beamlines, Matter Radiat. at Extremes **2**, 149 (2017).

[32] J. Nikl, M. Jirka, M. Matys, M. Kucharik, and O. Klimo, Contrast enhancement of ultra-intense laser pulses by relativistic plasma shutter, in *High Power Lasers and Applications*, edited by T. J. Butcher, J. Hein, P. Bakule, C. L. Haefner, G. Korn, and L. O. Silva (SPIE, 2021).

[33] M. Matys, S. V. Bulanov, M. Kecova, M. Kucharík, M. Jirka, P. Janecka, J. Psikal, J. Nikl, J. Grosz, G. Korn, and O. Klimo, Ion acceleration enhancement by laser-pulse shaping via plasma shutter, in *Laser Acceleration of Electrons*, edited by S. S. Bulanov, J. Schreiber, and C. B. Schroeder (SPIE, 2021).

## C.5   Design of plasma shutters for improved heavy ion acceleration by ultra-intense laser pulses

The following article is reproduced from M. Matys, S. V. Bulanov, M. Kucharik, M. Jirka, J. Nikl, M. Kecova, J. Proska, J. Psikal, G. Korn and O. Klimo (2022). Design of plasma shutters for improved heavy ion acceleration by ultra-intense laser pulses. *New Journal of Physics* **24**, 113046.

**PAPER • OPEN ACCESS**

# Design of plasma shutters for improved heavy ion acceleration by ultra-intense laser pulses

View the article online for updates and enhancements.

# New Journal of Physics

The open access journal at the forefront of physics

**PAPER**

# Design of plasma shutters for improved heavy ion acceleration by ultra-intense laser pulses

M Matys[1,2,*] ⓘ, S V Bulanov[1,3] ⓘ, M Kucharik[2] ⓘ, M Jirka[1,2] ⓘ, J Nikl[1,2] ⓘ, M Kecova[1] ⓘ, J Proska[2] ⓘ, J Psikal[1,2] ⓘ, G Korn[1] ⓘ and O Klimo[1,2] ⓘ

[1] ELI Beamlines Centre, Institute of Physics, Czech Academy of Sciences, Za Radnici 835, 25241 Dolni Brezany, Czech Republic
[2] Faculty of Nuclear Sciences and Physical Engineering, Czech Technical University in Prague, Brehova 7, Prague 115 19, Czech Republic
[3] Kansai Photon Science Institute, National Institutes for Quantum Science and Technology, 8-1-7 Umemidai, Kizugawa-shi, Kyoto 619-0215, Japan
* Author to whom any correspondence should be addressed.

**E-mail:** Martin.Matys@eli-beams.eu

## Abstract

In this work, we investigate the application of the plasma shutters for heavy ion acceleration driven by a high-intensity laser pulse. We use particle-in-cell and hydrodynamic simulations. The laser pulse, transmitted through the opaque shutter, gains a steep-rising front and its peak intensity is locally increased at the cost of losing part of its energy. These effects have a direct influence on subsequent ion acceleration from the ultrathin target behind the shutter. In our 3D simulations of silicon nitride plasma shutter and a silver target, the maximal energy of high-*Z* ions increases significantly when the shutter is included for both linearly and circularly polarized laser pulses. Moreover, application of the plasma shutter for linearly polarized pulse results in focusing of ions toward the laser axis in the plane perpendicular to the laser polarization. The generated high energy ion beam has significantly lower divergence compared to the broad ion cloud, generated without the shutter. The effects of prepulses are also investigated assuming a double plasma shutter. The first shutter can withstand the assumed sub-ns prepulse (treatment of ns and ps prepulses by other techniques is assumed) and the pulse shaping occurs via interaction with the second shutter. On the basis of our theoretical findings, we formulated an approach toward designing a double plasma shutter for high-intensity and high-power laser pulses and built a prototype.

## 1. Introduction

Laser driven ion acceleration is one of the most promising and widely studied features of ultra-intense laser matter interaction, finding applications in various areas [1–5]. Especially heavy ions are useful in material science as a radioisotope source and a stage to explore exotic nuclei [6, 7], in nuclear science involving heavy ion collisions, e.g. for hot and dense matter research [8] and schemes like fission-fusion nuclear reaction [9, 10]. The heavy ions driven by intense laser can also be used as an injector into conventional accelerators for further research [11]. These promising applications drive the goal for improving the laser-accelerated ion beam energy and quality. Introduction of PW-class lasers set up a new records in ion acceleration, e.g. energy of 58 MeV was reached for protons in 2000 [12], employing the target normal sheath acceleration (TNSA) mechanism [13]. The straightforward way to boost the maximal ion energy is to increase the laser pulse intensity. In this way, another mechanisms may get involved especially in combination with the use of ultrathin or low-density targets. Namely, radiation pressure acceleration (RPA) [14] presents a promising mechanism. Its experimental indications have already been observed [15–18]. The trend of mechanism blending in high-intensity interaction was demonstrated in 2018 by the experiment involving a hybrid RPA-TNSA regime induced by the onset of the relativistic transparency, setting a new record in proton acceleration of 94 MeV [19]. The interplay between different ion acceleration mechanisms depends on the
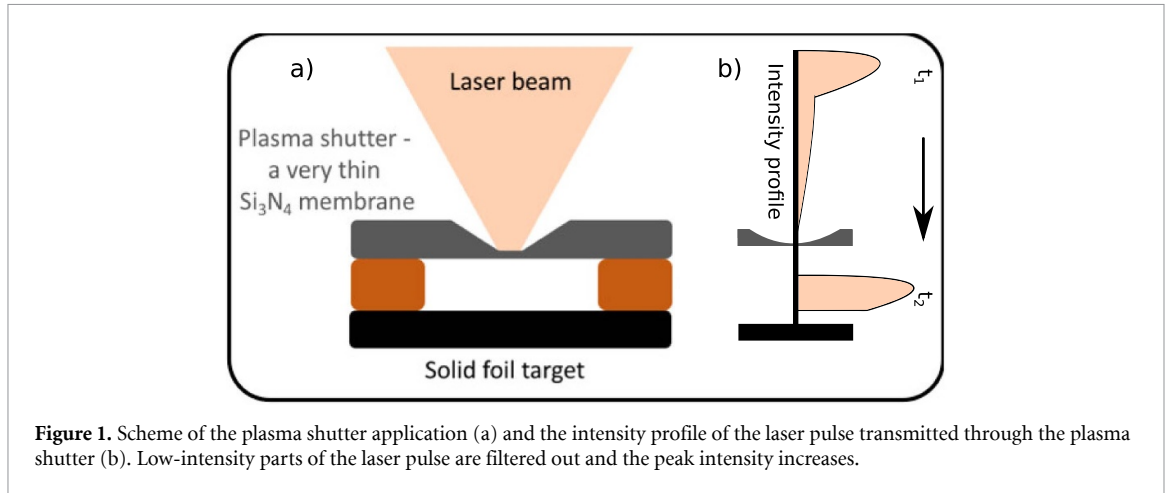
**Figure 1.** Scheme of the plasma shutter application (a) and the intensity profile of the laser pulse transmitted through the plasma shutter (b). Low-intensity parts of the laser pulse are filtered out and the peak intensity increases.

target and laser parameters [20]. For example, the increase of laser intensity for relatively low-density solid targets, like cryogenic hydrogen [21], can result in the shift of the origin of the ions accelerated to the highest energies from the target rear side toward its interior, as demonstrated in [22]. It was also demonstrated in experiment, that energies per nucleon of the bulk carbon ions can reach significantly higher values than the energies of contaminant protons [23]. For heavy ions the RPA regime is still-to-be-shown experimentally. Nevertheless, the highest energies are gradually being achieved by using ultrathin targets, e.g. the recent record for gold ion acceleration (exceeding 7 MeV/nucleon) was achieved with lowering the target thickness down to 25 nm [10]. For silver ions, energy exceeding 20 MeV/nucleon was achieved lowering the target thickness down to 50 nm [24].

Aside the increase of the laser pulse intensity and modification of the target thickness, the maximal energy and quality of laser-accelerated ions can be enhanced by using structured targets, e.g. double-layer [25–30], with nano-structures at its surface [31], nano-holes [32, 33] or a specific geometry, like a transverse Gaussian shape [34], a dual parabola [35], with a few micron-size holes [36] and a pizza-cone target [37].

Another approach is the shaping of the incoming laser pulse. Techniques like double planar plasma mirrors [38] and others are currently commonly used especially for the improvement of the laser pulse contrast. In addition to these techniques, the laser pulse can be also shaped via its nonlinear evolution as it propagates/burns through an underdense plasma [39–41], a near critical density plasma [42–47, 48] or an overdense plasma [49–53]. In addition to the prepulse treatment, the nonlinear pulse evolution can also result in steepening of the pulse front and (local) intensity increase. The positive effect of these phenomena on ion acceleration in the case of near critical density plasma was demonstrated by experiments and simulations, e.g. in [43] using a carbon-nanotube foam attached to a solid diamond-like carbon foil, resulting in increase of maximal carbon energy. In this paper we study the high-density (overdense) approach using plasma shutter of thickness relevant to PW-class laser systems.

In the context of ion acceleration, the plasma shutter is usually a thin solid foil or membrane which is attached to the front surface of the target with a gap between them (see a scheme in figure 1(a)). Therefore, it presents an obstacle which needs to be overcome by the laser pulse and by its accompanying prepulses before the interaction with the main target. Having solid (overdense) density, the plasma shutter is initially opaque for the low-intensity prepulse and beginning of the main pulse. The shutter subsequently becomes relativistically transparent to the rising intensity of the main pulse front. Assuming a thick (semi-infinite) shutter, its electron density $n_e$[4] can satisfy relation $n_e < \gamma n_c$, where $\gamma$ is the relativistic Lorentz factor (the relation for ultrathin shutter is introduced in the next paragraph). The critical density is defined in CGS units as $n_c = m_e \omega^2 / 4\pi e^2$, where $\omega$ is laser angular frequency, $m_e$ and $e$ are electron mass and charge, respectively. Therefore, the plasma shutter can directly produce a steep-rising front at the beginning of the transmitted laser pulse by filtering out the low intensity parts [49]. This observation leads to the direct application for ion acceleration as it reduces the target pre-expansion before its interaction with the high-intensity part of the laser pulse. The filtering out of the sub-ns prepulse was demonstrated in experiments and supplementary particle-in-cell (PIC) simulations [50, 52]. The main target remained

---

[4] Note that electron density $n_e$ can be locally increased by the radiation pressure. Therefore, a significantly higher initial laser intensity is required for a semi-infinite target to become relativistically transparent than would be given by the initial target density [54,55]. On the other hand, the density of thin targets can rapidly decrease by the target expansion and by expelling electrons out of the laser beam axis by the ponderomotive force.

overdense in these experiments when the plasma shutter was included, resulting in the increase of ion energy. This prepulse reduction can be especially important for the use of nanostructures/nanoholes in the target, as they diminish for low-contrast lasers otherwise [33]. Moreover, the steepening of the main pulse itself becomes important with the increasing intensity as it significantly affects the laser-electron dynamics in ultrathin targets as is shown in this work. The steep-rising front of the intensity profile can also mitigate the development of transverse short-wavelength instabilities usually ascribed to Rayleigh-Taylor instability [56–58] or electron-ion coupled instability [59, 60]. The mitigation of its development was demonstrated in [28] by numerically steepening of the pulse front. The steep front can also enhance the photon emission from under-dense targets [61]. The ultra-thin shutter also provides ideal conditions for the research of the relativistic induced transparency itself [51], leading to the formation of a relativistic plasma aperture [62]. The incident laser light is diffracted at this aperture having effects on electron [62] and ion [63] distributions. The diffraction of the laser pulse on such an aperture and its constructive interference with generated high harmonics can lead to a local intensity amplification [53]. Therefore, the use of the plasma shutter (or a series of them as discussed in section 3.5) can provide three positive effects as is sketched in figure 1(b): (1) mitigation of prepulses, (2) generation of the steep-front laser pulse, (3) local increase of the peak intensity. The negative effect is the partial lost of the laser pulse energy, depending on the shutter thickness. Note, that the use of a single plasma shutter for prepulse reduction inherently decreases its density, making the later two effects less significant (as discussed below). Therefore, a series of plasma shutters (each focusing on different effect) can provide a way to use the full potential of such interaction.

The interplay between a relativistic ($a_0 > 0$) laser pulse and a thin plasma shutter depends on two main parameters, the dimensionless amplitude of the laser electric field $a_0 = eE_0/m_e\omega c$ and the areal density of the target $\epsilon_0 = \lambda l/4\pi l_s^2 = \pi \frac{n_e}{n_c} \frac{l}{\lambda}$, where $E_0$ is the electric field amplitude, $c$ is speed of light in vacuum, $\lambda$ is the wavelength of the incident laser pulse, $l$ is the thickness of the plasma shutter and $l_s$ is the skin depth defined as $l_s = c/\omega_{pe}$ for the plasma electron angular frequency $\omega_{pe}$. The thin plasma shutter becomes relativistically transparent to parts of incident laser pulse fulfilling the condition $a_0 \gg \epsilon_0$ [49]. Therefore, the increase of the shutter thickness reduces the energy of transmitted laser pulse. On the opposite, the local peak intensity of transmitted laser pulse increases with the shutter thickness [53], saturating around the relativistically corrected skin depth $l_{sc} = \sqrt{\gamma}c/\omega_{pe}$. Therefore, the thickness of the plasma shutter needs to be optimized assuming both of these effects for efficient ion acceleration as they act against each other. More laser pulse energy will be transmitted through the thinner plasma shutter, but the intensity increase will be lower and vice versa.

The transmitted laser pulse (shaped by the plasma shutter) is subsequently used for ion acceleration from the target placed behind the plasma shutter. The optimal target thickness $l$ for ion acceleration via RPA mechanism [14] (for which $a_0 = \epsilon_0$) can be expressed as:

$$\frac{l}{\lambda} = \frac{a_0}{\pi} \frac{n_c}{n_e}. \tag{1}$$

In this work, we investigate the application of the plasma shutters for heavy-ion acceleration driven by a high-intensity laser pulse using 3D and 2D PIC simulations. Firstly, we assume an idealized situation with a plasma shutter being opaque for the high-intensity part of the laser pulse without any prepulse treatment. The main laser pulse, transmitted through the opaque plasma shutter, gains a steep-rising front and its peak intensity is locally increased at the cost of losing part of its energy, depending on the shutter thickness as was recently demonstrated in [53] (e.g. over 50% of the main pulse energy was lost for the effect of local pulse intensity increase by the factor of 7 in [53]). Therefore, we investigate a possible application of such shaped pulse for ion acceleration from the ultrathin target located behind the plasma shutter, where the advantages of pulse profile modifications need to overcome the laser pulse energy loss. Subsequently we investigate a more realistic scenario including interaction with a sub-ns prepulse with intensity relevant to nowadays PW-class laser systems. For this scenario we propose the use of two (or eventually multiple) shutters for ion acceleration having different purposes. The first shutter will be used for the prepulse treatment in the way already demonstrated in [50, 52], becoming transparent to the main pulse and thus allowing high percentage of transmitted pulse energy (up to 99% in [50]). The second shutter, being opaque for the main pulse, can directly shape the main pulse [53]. The whole double-shutter scenario is investigated using a combination of 2D hydrodynamic (simulating the prepulse interaction with the first shutter) and PIC simulations.

The parameters like target and shutter thicknesses, length of the gap between them, and the effects of the pulse-front steepness are investigated using 2D PIC simulations for the case of a silicon nitride plasma shutter and a silver target. The silver target was chosen for demonstration of our heavy-ion scheme assuming a PW-class laser, because its optimal thickness for RPA mechanism (equation (1)), is relatively high compared to materials with higher $Z$, as this thickness decreases with increasing target density. Therefore, the targets with thickness of the order of the optimal one (lower 10 s of nm) are reasonably thick for future

experiments (silver targets with thickness around 50 nm have been already used [24]). The relatively high thickness also makes the 3D PIC simulations less computationally demanding, as the target can be still resolved by at least a few cells even for higher cell size.

In the follow-up 3D simulations of our 2D reference case, the maximal energy of silver ions increases by 35% when the plasma shutter is included (2D simulations with a lower-*Z* target (aluminium) were also performed, resulting in similar but less significant increase). Moreover, the steep-rising front of the laser pulse leads to formation of high-density electron bunches. This structure (which also appears in the generated electric and magnetic fields) focuses ions toward the laser axis in the plane perpendicular to the laser polarization. The generated high-energy ion beam has significantly lower divergence compared to the broad ion cloud, generated without the shutter. In the later case, the structures are pre-expanded with the low-intensity part of the laser pulse and the subsequent onset of the transverse instability mentioned above. The effects of prepulses are investigated using a combination of 2D PIC and hydrodynamic simulations assuming a double plasma shutter. The first shutter can filter out the assumed sub-ns prepulse (treatment of ns and ps prepulses by other techniques is assumed). Therefore, the processes of the steep-front generation and the local intensity increase can develop via interaction with the second non-expanded shutter. The increase of the maximal ion energy is demonstrated also in this case. A prototype of this double-shutter is presented.

The paper is organized as follows. The simulation method and parameters are described in section 2. Section 3, containing results, is divided into five subsections. Firstly, the modifications of the laser pulse transmitted through the plasma shutter, like its local intensity increase and energy loses, are studied in section 3.1. The optimal shutter and target thicknesses and length of the gap between them for ion acceleration are discussed in section 3.2. The influence of the generated steep-rising front on ion acceleration is investigated via 2D simulations using approximated pulse with different steepness in section 3.3. Then the whole picture is discussed via 3D simulations comparing the cases of silver target with and without the plasma shutter for linear and circular polarization in section 3.4. Lastly, the use of double plasma shutter is discussed using the combination of 2D hydrodynamic and PIC simulations, taking the prepulse into account, in section 3.5. The prototype of such a shutter is also presented in that section. The supplementary material contains a video of time evolution of the laser pulse interaction with the shutter and the silver target. An interactive custom WebGL application [64] of this 3D simulation is available online [65].

## 2. Simulation method and parameters

To demonstrate the advantages coming from implementation of the plasma shutter on ion acceleration we performed 2D and 3D PIC simulations using the code EPOCH [66].

The parameters of the 2D simulations are as follows. Linearly p-polarized (electric field lies in the plane of incidence) laser pulse incidents normally on the target. The radiation wavelength is $\lambda = 1\ \mu$m and the peak intensity is $I_{\max} = 10^{22}$ W cm$^{-2}$, thus yielding dimensionless amplitude $a_0 \approx 0.85 \sqrt{I (10^{18}\ \text{W cm}^2)\, \lambda^2\,(\mu\text{m})} \approx 85$. The critical plasma density is equal to $n_c \approx 1.115 \times 10^{21}$ cm$^{-3}$.

The laser pulse has a Gaussian spatial profile with beam width at the full width at half maximum (FWHM) equal to 3 $\lambda$. The temporal profile has $\sin^2(t)$ shape in intensity and beam duration is 64 fs. This pulse corresponds to a 30 fs long 1 PW laser pulse with Gaussian envelope. The laser pulse energy can be fully represented by the $\sin^2(t)$ profile in the PIC simulations, avoiding the numerical cut of the infinite exponential beginning of the Gaussian shape. Therefore, a further analysis of transmitted energy is more reliable.

The plasma shutter is made of a silicon nitride ($Si_3N_4$) solid foil. Full ionization of the foil is assumed with electron density $n_e = 835\ n_c$. In the reference case the thickness of the plasma shutter is set to 20 nm. Plasma shutters with thickness between 12 and 45 nm were also considered. Thus, the interplay between parameters $a_0$ and $\epsilon_0$ discussed in section 1 is as follows: $\epsilon_0 = a_0 = 85$ for shutter thickness $l \approx 32.5$ nm, for the reference case of $l = 20$ nm then $\epsilon_0 \approx 52.5$ and for the thickness equal to the relativistically corrected skin depth $l = l_{sc} = 42.7$ nm, $\epsilon_0 \approx 112$.

The target which is located behind the plasma shutter corresponds to commercial silver solid foil with thickness of 20 nm. For the discussion of optimal thickness see the section 3.2. Partial ionization of the target is assumed, which is in agreement with the experiments of similar type of laser with a silver target [24]. For simplicity, the target consists of electrons with density $n_e = 2100\ n_c$ and silver ions with charge number $Z = 40$ and mass number $A = 108$.

Two sets of simulations were performed. Firstly, the simulation was done with the box size of 44 $\lambda \times 17\ \lambda$ ($\times 17\ \lambda$ for 3D cases) focusing on laser pulse transmission through the plasma shutter. Plasma shutter is placed in the middle of the simulation box, referred to as position $x = 0$. This setup ensures that both the reflected and transmitted part of the laser pulse are fully captured in the simulation for comparison.

Subsequently, the simulation box is prolonged to the size of $60\,\lambda \times 17\,\lambda$ ($\times 17\,\lambda$ for 3D cases) including ion acceleration from the target. In this case the plasma shutter is placed at the position $x = 0$, situated $12\,\lambda$ from the simulation box boundary in the direction of the laser propagation. The transverse size of the plasma shutter and the target is $17\,\lambda$, i.e. the target is reaching the simulation box boundaries at positions $y = \pm 8.5\,\lambda$ where thermal boundary conditions for particles are applied.

In 2D simulations, the mesh has square cells of the size $0.003\,\lambda$. This is shorter than the plasma skin depth $c/\omega_{pe} \approx 0.0055\,\lambda$, where $\omega_{pe}$ is electron plasma frequency corresponding to electron density of the shutter (the cell size is also lower than the plasma skin depth of the target $c/\omega_{pe} \approx 0.0035\,\lambda$, using the electron density of the target). Since the 3rd order b-spline shape of the quasi-particles and current smoothing are used in our simulations, it is ensured that numerical heating is strongly reduced even for the cells larger than the plasma Debye length [66]. The number of electrons is set to correspond to 835 particles per cell inside the plasma shutter and 1050 inside the target, respectively. The numbers of ions correspond to their charge ratios.

In 3D simulations, the mesh has cuboid cells. The size of the cells is set to $0.005\,\lambda$ in the laser propagation direction ($x$-direction) and $0.025\,\lambda$ in transverse directions ($y$- and $z$-directions). Number of electrons per cell was reduced to 400 inside the plasma shutter and 1000 inside the target. The ratios for number of ions are kept the same as in the 2D case.

Temperatures of all particles are initialized to 5 keV inside the plasma shutter and to 0.5 keV inside the target, to further reduce numerical heating. The particle solver begins to move the particles just a few time steps before the arrival of the laser pulse front to the plasma shutter.
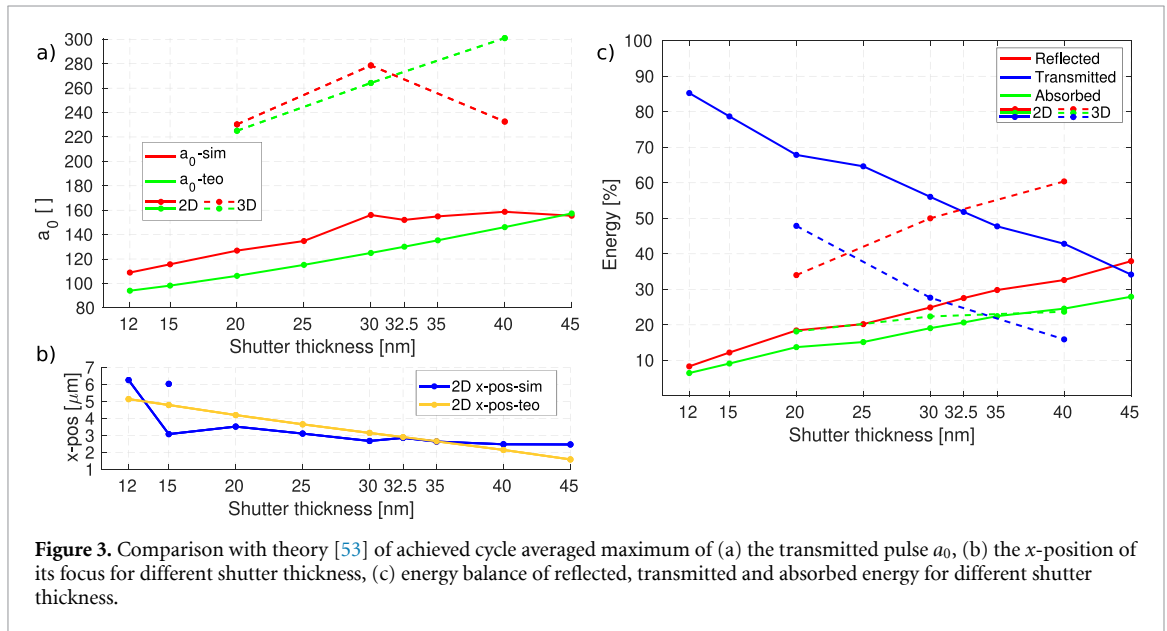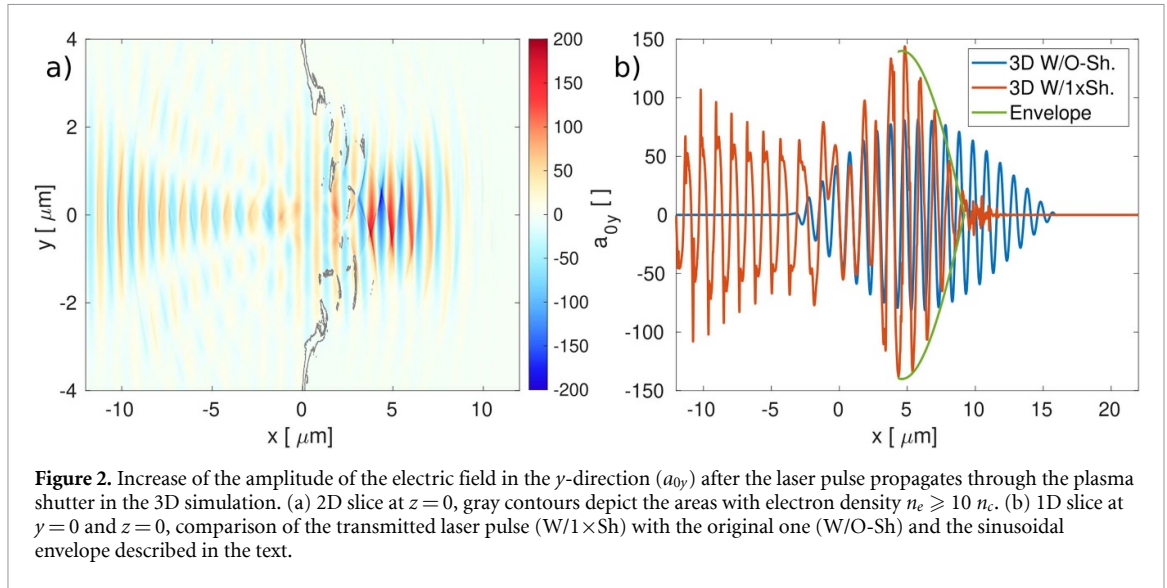
In order to include the effect of target pre-expansion done by the prepulse, the PIC simulations were combined with the output of hydrodynamic simulations performed in the code PALE (Prague Arbitrary Lagrangian–Eulerian) [67, 68], in section 3.5. This code employs a 2D cylindrical geometry in a moving Lagrangian framework. The robustness of the simulation is improved by performing periodic mesh smoothing followed by a conservative interpolation of the state quantities from the Lagrangian to the smoothed mesh [69]. The simulations involve a heat conductivity numerical model [70] and heat flux limiter, simple critical-density and wave-based laser absorption models [71], Spitzer–Harm heat conductivity model [72] and realistic Quotidian equation of State [73]. This code is commonly used for interpretation of experiments involving nanosecond pulses [74–76]. The simulation uses a 2D computational $r$–$z$ mesh containing $100 \times 100$ cells including a 40 nm thick and 25 $\mu$m long foil of solid aluminum at room temperature. The areal density is roughly the same as of the silicon nitride plasma shutter. Another set of simulations contains a corresponding 20 nm thick silver target. The computational cells are geometrically distributed in both dimensions to achieve high mesh resolution in the absorption region. A constant temporal intensity of $10^{12}$ W cm$^{-2}$ and Gaussian spatial laser beam profile with the focus radius $r_f = 2$ $\mu$m are considered.

## 3. Results

### 3.1. Laser pulse shaping via plasma shutter

The properties of the laser pulse transmitted through the plasma shutter of certain material depend on the thickness of the plasma shutter and differ with the dimensionality of the simulation. Therefore, the variables like intensity increase, position of the focus and the percentage of transmitted energy are discussed in this section.
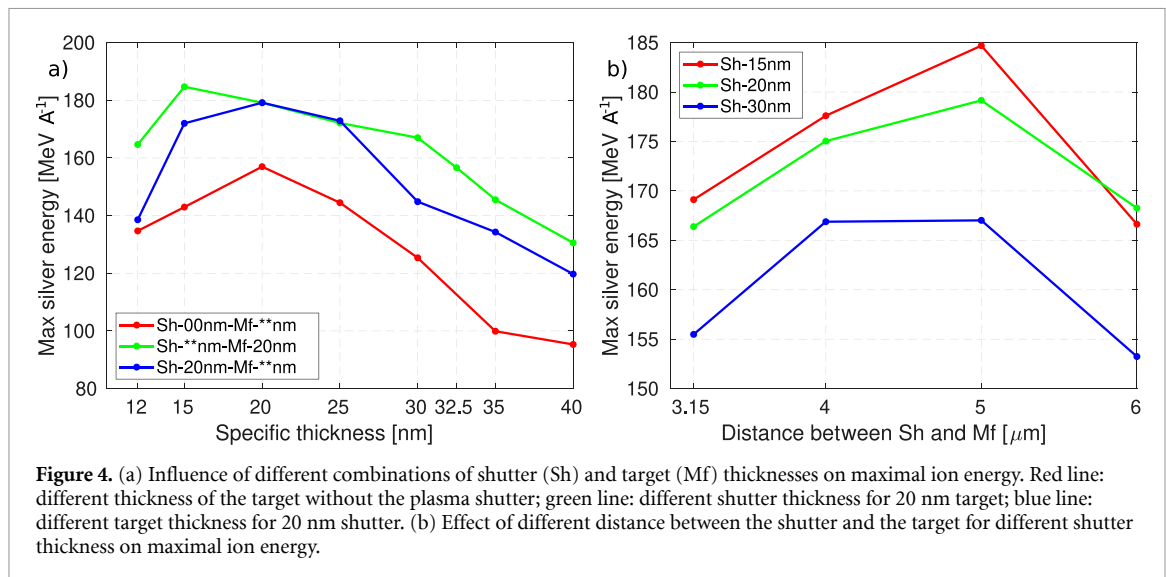
The properties of our reference case, using the 20 nm thick plasma shutter from the 3D simulation, which is then used for ion acceleration, are shown via 2D and 1D slices in figure 2 at time $t = 38$ T (from the beginning of the simulation). The electric field in the $y$-direction (parallel to the laser polarization) is presented in the form of $a_{0y} = eE_y/m_e\omega c$. The laser pulse with initial $a_0 = 85$ burns through the plasma shutter located at $x = 0$ $\mu$m. The relativistic aperture is developed as can be seen via contours of density $n_e \geqslant 10\,n_c$ in figure 2(a). It leads to the diffraction of the transmitting laser pulse and its local constructive interference with generated high harmonics as was described in [53]. The value of $a_{0y}$ can locally increase from the original $a_{0y} = 85$ to over $a_{0y} = 200$. The local maxima are located off-axis alternating $\pm$ in the $y$-direction, where the interference happens. The central 1D profile (at $y = 0$ and $z = 0$) is shown in figure 2(b). The transmitted laser pulse acquires the steep-rising front at the beginning. Its approximation using the equation $y = 140 \cdot \sin(\pi \cdot x/9.2)$ is depicted with the green color. Thus, the rising front is about 5 T shorter compared to the original pulse (depicted by the blue line) with duration of 19.2 T. Moreover, the steepness of the rising front is increased by the rise in the intensity. Note that the distribution of the laser pulse electric field (and also its energy) differs in space from the case without the shutter (pure Gaussian), being more dense around the central region as can be seen in figure 2(a). The integrated energy density of the transmitted laser pulse electric field in the central 1D profile (evaluated forwards from 0) is actually about 42% higher compared to the simulation without the shutter, even though a significant part of the laser pulse

**Figure 2.** Increase of the amplitude of the electric field in the *y*-direction ($a_{0y}$) after the laser pulse propagates through the plasma shutter in the 3D simulation. (a) 2D slice at $z = 0$, gray contours depict the areas with electron density $n_e \geqslant 10\ n_c$. (b) 1D slice at $y = 0$ and $z = 0$, comparison of the transmitted laser pulse (W/1×Sh) with the original one (W/O-Sh) and the sinusoidal envelope described in the text.



**Figure 3.** Comparison with theory [53] of achieved cycle averaged maximum of (a) the transmitted pulse $a_0$, (b) the *x*-position of its focus for different shutter thickness, (c) energy balance of reflected, transmitted and absorbed energy for different shutter thickness.

is reflected from the plasma shutter (figure 2(b)). On the contrary the total (whole space) transmitted pulse energy is about 50% lower as discussed below.

The comparison of maximal reached $a_0$ and the *x*-position of its focus from 2D PIC simulations with the theoretical model [53] for different shutter thicknesses are shown in the lower part of figure 3(a). The values represent the cycle averaged maximum of $a_0$ obtained from the simulation data. The intensity is rising with thickness, while the *x*-position of the focus is decreasing. After reaching a local maximum at 30 nm, the maximal $a_0$ is gradually saturating, reaching a global maximum at 40 nm and slowly decreasing afterwards. The *x*-position of the focus differs a little after saturation. This observations are in agreement with theory [53] for 'p' polarization as the electric field amplification should be saturated after the shutter thickness reaches the relativistically corrected skin depth $l_{sc}$, which is approx. 42.7 nm for our case. The prediction of the focus *x*-position for ultra-thin targets below 20 nm is challenging as the focus position changes with time and the interference pattern may produce several maxima at different positions. As an example, the second maxima for the case of 15 nm is shown by the blue dot. The predicted focus is roughly in the middle of these two values.

In 3D simulations, shown in the upper part of figure 3(a), the maximal $a_0$ fits well to the theory and rises with thickness between 20 and 30 nm cases. The saturation process is not observed in the simulation of 40 nm shutter as the maximal intensity decreases to value similar to the 20 nm case. The increase of the

**Figure 4.** (a) Influence of different combinations of shutter (Sh) and target (Mf) thicknesses on maximal ion energy. Red line: different thickness of the target without the plasma shutter; green line: different shutter thickness for 20 nm target; blue line: different target thickness for 20 nm shutter. (b) Effect of different distance between the shutter and the target for different shutter thickness on maximal ion energy.

maximal $a_0$ is almost two times higher in the 3D simulations compared to their 2D counterparts, which corresponds to the sum of two processes focusing the beam either in the polarization plane ('p') or out of it ('s') [53]. On the contrary, focusing in only one dimension occurs in the 2D cases. The highest value of $a_0$ is observed in the case of 30 nm, increasing from $a_0 = 85$ to $a_0 = 280$. Thus, yielding the intensity increase by the factor of $I_{max}/I_{init} = (a_{0max}/a_{0init})^2 \approx 10.85$. The absence of saturation effect in the case of 40 nm shutter in 3D can be ascribed to the combination of 's' and 'p' polarizations as the 's' part do not provide a saturation effect even in the 2D cases as was shown in [53]. Therefore, the optimal thickness for the highest local intensity increase in 3D is in our case around the condition of $a_0 = \epsilon_0$.
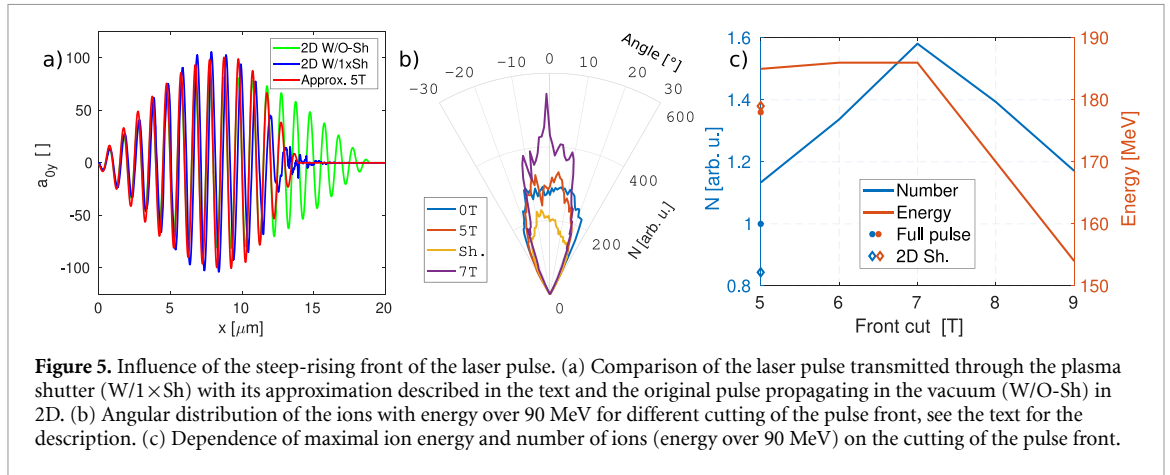
Another important parameter apart the intensity increase is the percentage of transmitted laser pulse energy. The energy balance for different thicknesses of the plasma shutter is investigated in figure 3(c). The simulation box is set to be able to contain the whole incident and transmitted laser pulse.

In 2D simulations (solid lines) the transmitted laser pulse energy is decreasing with thickness but stays above 50% for thicknesses where $a_0 \geqslant \epsilon_0$ (thickness $\leqslant$32.5 nm), as the plasma shutter becomes partially (relativistic) transparent before the intensity maximum reaches the plasma shutter [49]. In the 3D cases (dashed lines) the reflection and partially absorption are stronger than in the 2D cases, where the spherical apertures are not limited in the third dimension. About 50% of the laser pulse energy is transmitted in the case of 20 nm, decreasing to 28% for the 30 nm case and 16% for the 40 nm case. As the laser pulse energy loses (absorption and reflection) are significant with the increasing thickness in 3D, their influence needs to be taken into account for choosing the proper parameters for applications.

**3.2. Effects of different shutter and target thicknesses on ion acceleration in 2D**

For an efficient application of the transmitted laser pulse for ion acceleration, the benefits of the pulse shaping need to outweigh the loses of the laser pulse energy. Therefore, the combination of parameters of the plasma shutter (Sh) and the target (main foil - Mf) like their thickness and distance between them are investigated in figure 4.

The optimal thickness for reaching maximal silver ion energy of the target without the use of the shutter is 20 nm as is shown by the red line in figure 4(a). This value is slightly higher than the optimum predicted for RPA mechanism by equation (1), which corresponds to the thickness of 13 nm for the chosen silver target and laser pulse. The increase of the optimal target thickness can be ascribed to the early onset of the relativistic induced transparency in this ultrathin targets. Ion acceleration is then influenced by the hybrid RPA-TNSA mechanism described in [19]. The next step is to compare various shutter thicknesses for the 20 nm target, which is shown by the green line. The maximal ion energy is increased by including the plasma shutter into the simulation, when its thickness is lower than 32.5 nm (for this cases the transmitted laser pulse energy is still above 50% as discussed above). An interesting region for ion acceleration is found for shutter thicknesses between 15 and 30 nm where the maximal ion energy is slowly linearly decreasing with the shutter thickness. The maximum of 185 MeV A$^{-1}$ is reached in the case of 15 nm Sh. The thickness of 20 nm, where the maximal ion energy is just slightly lower (179 MeV A$^{-1}$) is chosen for further investigation as it can be more reliably represented in the 3D simulations with larger cells (keeping at least 4 cells per target

**Figure 5.** Influence of the steep-rising front of the laser pulse. (a) Comparison of the laser pulse transmitted through the plasma shutter (W/1×Sh) with its approximation described in the text and the original pulse propagating in the vacuum (W/O-Sh) in 2D. (b) Angular distribution of the ions with energy over 90 MeV for different cutting of the pulse front, see the text for the description. (c) Dependence of maximal ion energy and number of ions (energy over 90 MeV) on the cutting of the pulse front.

in our simulations). The blue line in figure 4(a) shows the dependence of maximal silver ion energy on the target thickness, when the shutter thickness is 20 nm. The maximum ion energy is reached for the same thickness of 20 nm as in the case without the Sh. Therefore, the plasma dynamics, including the onset of the relativistic induced transparency, is similar in both cases, as will be further discussed in section 3.4. In addition, the ion acceleration is less sensitive to the target thickness between 15 and 25 nm when the shutter is included than in the corresponding case without the shutter. This can be ascribed to the steep-rising front generated by the plasma shutter reducing the pre-expansion of the target. So far the distance between the shutter and the target was set to 5 $\mu$m, which roughly corresponds to the length of the rising front in figure 2(b). This distance is the optimum in our 2D cases as can be seen in figure 4(b) comparing different distances. Moreover, a plateau of similar maximal energies between 4 and 5 $\mu$m is developed for thicker plasma shutters, making the target fabrication more flexible.

Regarding to the parametric scan above, the thicknesses used for 2D and 3D simulations of ion acceleration are hereinafter 20 nm for both shutter and target which are located 5 $\mu$m apart. This set of parameters resulted in the increase of maximal ion energy from 157 to 179 MeV A$^{-1}$, when the plasma shutter is included. Note that similar but less significant increase was achieved with a lower-$Z$ material for the same laser pulse and shutter parameters. Namely, using a fully ionized aluminum foil with thickness of 80 nm, the maximal aluminum ion energy increased from 230 to 243 MeV A$^{-1}$. Further lowering of $Z$ of the target inherently results in increase of its optimal thickness according to equation (1), which may alter the laser-target dynamics of ultrathin targets described in this work.

### 3.3. Influence of the steep-rising front

As the generation of the steep-rising front of the incident laser pulse is an important feature in the subsequent laser-target dynamics, we run several 2D simulations approximating the generated pulse shape. The approximated pulse assumed an increased intensity of the central 1D profile from $a_0 = 85$ to $a_0 = 105$, which fits well the 1D profile obtained from the 2D simulation as can be seen in figure 5(a). The pulse then consists of two sinusoidal time envelopes. The beginning of the time profile is cut to zero for several periods (number of cut periods is denoted as Front cut #T in figure 5) and then rises to maximal $a_0$ with sinusoidal shape till the half of the original pulse. This way the steep front is generated. The envelope of the second half of the laser pulse remains unperturbed and decreases from the maximum to zero at the same timescale as the original pulse. The spatial profile is kept the same as of the original pulse, ignoring the appearance of the local off-axis maxima reaching higher value of $a_0 = 127$ (see the 2D slice from the 3D simulation in figure 2(a) for illustration). Thus, an average central on-axis maximum is introduced for the sake of brevity. The comparison of the 1D profile generated by the plasma shutter (blue) with this approximation assuming the cut of 5 T (red) and the original pulse (green), at time when the pulse is transmitted through the plasma shutter and the 1D profile stabilized, is shown in figure 5(a).

The introduction of the steep front has a positive effect on the divergence of high-energy ions (energy over 90 MeV A$^{-1}$, which is roughly half of the maximal energy reached). Their angular distribution for different front cutting is shown in figure 5(b). The use of the full pulse (0 T, blue) results in a relatively broad flat-top angular distribution without any significant peak. With the use of our steep-front approximation (cutting of 5 T, red) the distribution is divided into two lateral peaks. Increasing the steepness of the laser pulse front even further (cutting of 7 T, deep purple) results in a distinct single peak near the axis. The use of the plasma shutter in 2D (Sh., yellow) resulted in lower number of particles, which can be ascribed to a
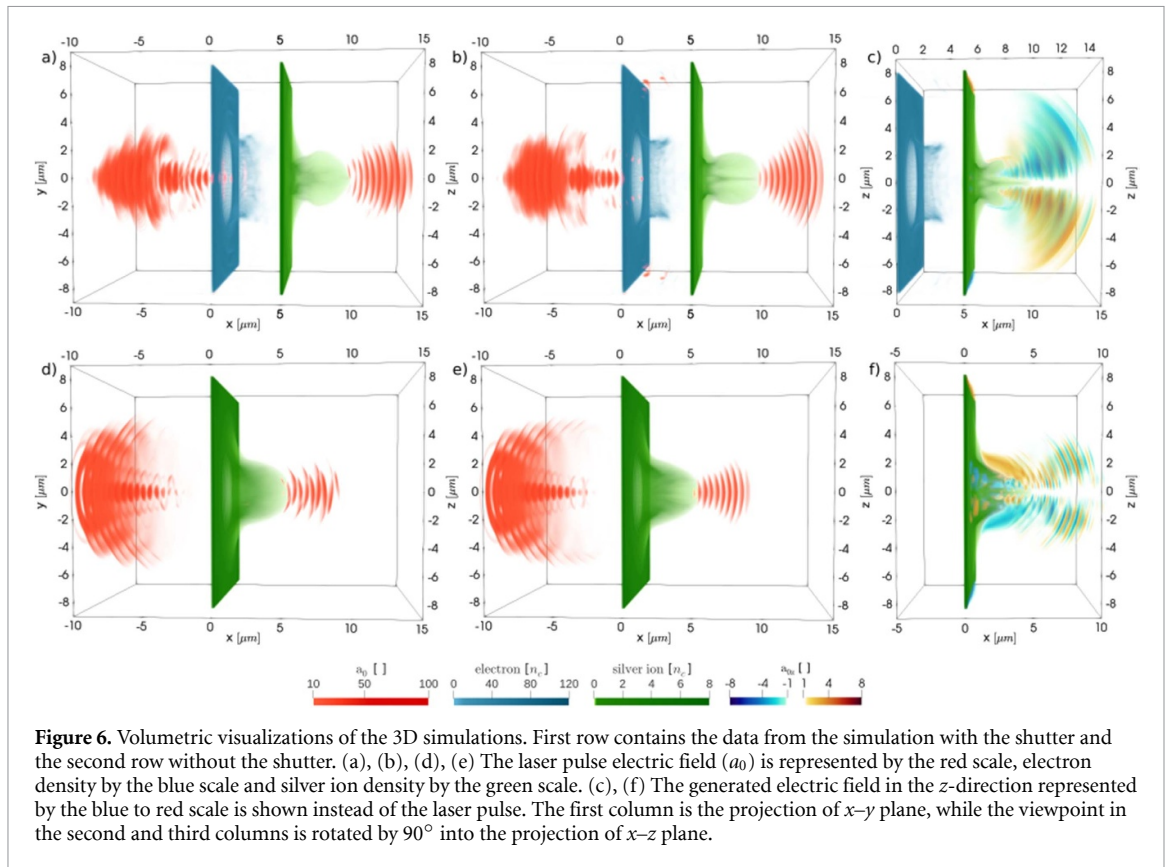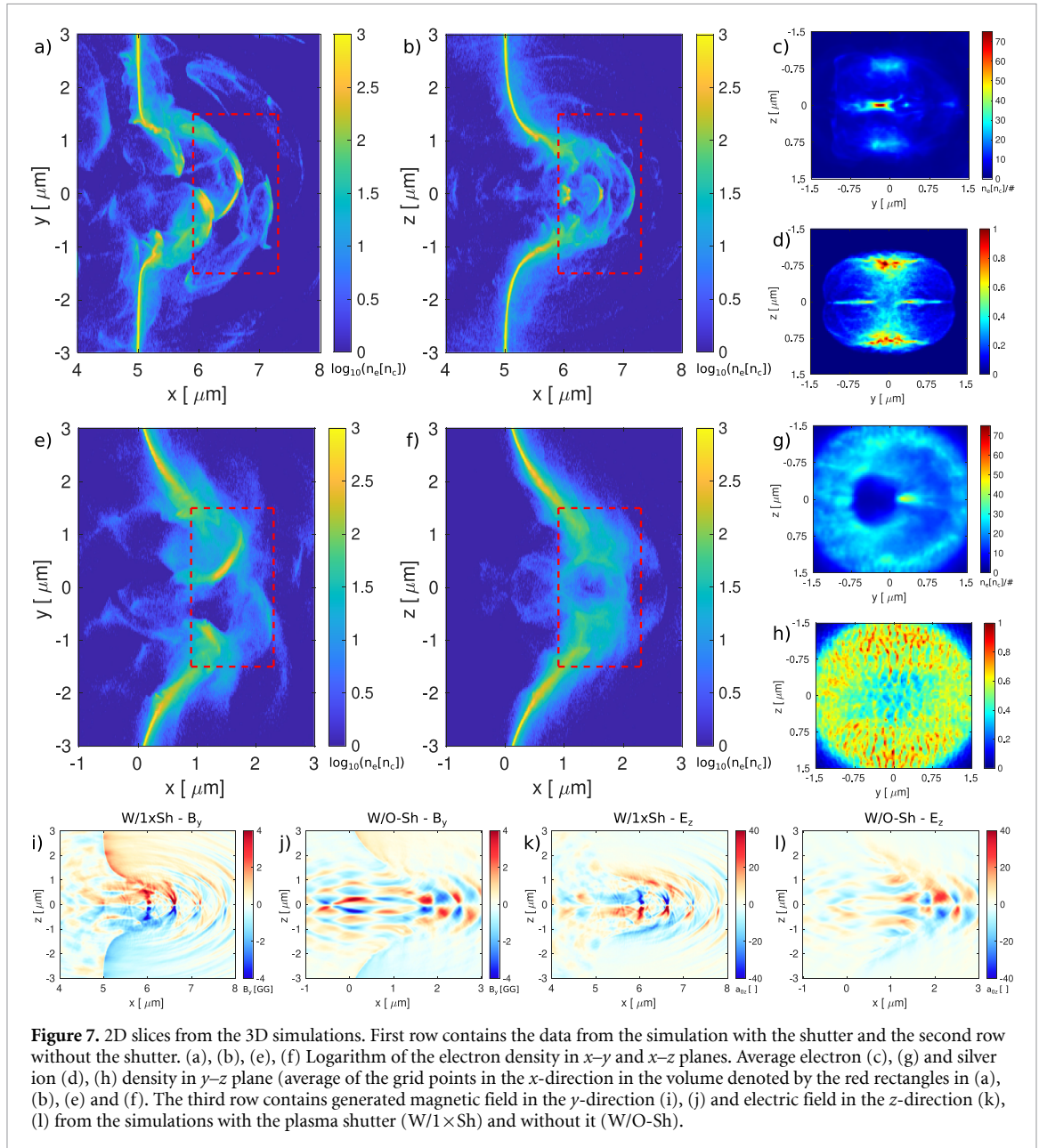
**Figure 6.** Volumetric visualizations of the 3D simulations. First row contains the data from the simulation with the shutter and the second row without the shutter. (a), (b), (d), (e) The laser pulse electric field ($a_0$) is represented by the red scale, electron density by the blue scale and silver ion density by the green scale. (c), (f) The generated electric field in the *z*-direction represented by the blue to red scale is shown instead of the laser pulse. The first column is the projection of *x*–*y* plane, while the viewpoint in the second and third columns is rotated by 90° into the projection of *x*–*z* plane.

different spatial profile, which is more localized compared to the Gaussian one, used in the approximations. Also the single peak generation is not so distinctive in this case in the 2D configuration. The benefits of the steep-rising front in the shutter case are more pronounced in 3D (see figure 8(f) in the next section), where the intensity is higher, so the front is steeper even for a similar time scale and is then closer to the 7 T case in 2D.

Another interesting effects of the steep-rising front is the increase of the number of high-energy ions in the region around the central axis (*y* between ±3 $\mu$m). This trend reaches maximum for the cutting of 7 T, as can be seen in figure 5(c) by the blue line and blue *y*-axis. Almost 1.6 more ions are located in this regions in the 7 T case compared to the use of the full uncut pulse (denoted by the single point). After this distinct maximum the number of particles drops. As mentioned before, the number of particles in the shutter case (denoted by diamond) is lower due to different pulse representation in the space. The red line and *y*-axis in figure 5(c) correspond to the maximal silver ion energy reached in the simulation. The development of the maximal energy is saturated till 7 T and has the same drop as the number of particles afterwards. These drops in the maximal energy and number of particles can explain the steeper reduce of the maximal energy of silver ions for green line in figure 4(a) with shutter thickness increasing over 30 nm. The thicker plasma shutter cuts too significant part of the laser pulse, reducing the maximal ion energy. The energy reached by the case with the plasma shutter (red diamond) is similar to the one reached with the full pulse (red star). Therefore, the ion acceleration dynamics corresponds to the lower value of $a_0 = 105$ from the on-axis 1D profile (figure 5(a)) and not to the off-axis local maxima of $a_0 = 127$ (figure 3(a)) observed in the previous chapters.

### 3.4. Ion acceleration in 3D

In this section, we will compare the silver target without the plasma shutter, placed at the laser focus at the *x*-position of 0 $\mu$m and the silver target with the plasma shutter. In the later case the shutter is placed at the laser focus at $x = 0$ $\mu$m and the silver target is located 5 $\mu$m behind it. The simulation setup is shown as 3D volumetric visualization of laser pulse ($a_0$, red), plasma shutter (electron density, blue) and target (silver ion density, green) in figure 6. The time instants are $t = 40$ T in the case with the plasma shutter (first row) and corresponding $t = 35$ T for the case without the shutter (second row) as the target is placed 5 $\lambda$ closer to the beginning of the simulation box. The first column is the projection of *x*–*y* plane, while the viewpoint in the second and third columns is rotated by 90° into the projection of *x*–*z* plane. Video of the time evolution of

**Figure 7.** 2D slices from the 3D simulations. First row contains the data from the simulation with the shutter and the second row without the shutter. (a), (b), (e), (f) Logarithm of the electron density in $x$–$y$ and $x$–$z$ planes. Average electron (c), (g) and silver ion (d), (h) density in $y$–$z$ plane (average of the grid points in the $x$-direction in the volume denoted by the red rectangles in (a), (b), (e) and (f). The third row contains generated magnetic field in the $y$-direction (i), (j) and electric field in the $z$-direction (k), (l) from the simulations with the plasma shutter (W/1×Sh) and without it (W/O-Sh).

the simulation with the plasma shutter is included as a supplementary material and an interactive custom WebGL application [64] of it is available online [65].

As can be seen in the figure 6(b), the application of the plasma shutter results into a narrow beam-like structure of accelerated silver ions (green) in the $x$–$z$ plane. This structure is hard to recognize in the case without the plasma shutter (figure 6(e)) and is missing in the $x$–$y$ plane (figures 6(a) and (d)). The difference in the electric field in the $z$-direction ($a_{0z}$, blue-red scale) at the corresponding times is shown in the third column. In the case without the plasma shutter (figure 6(f)) a relatively strong defocusing electric field is located around the outer surface of the ion cloud on positions $y = \pm 2$ $\mu$m. The focusing field with opposite polarity is also present inside the ion cloud around position $x = 3$ $\mu$m, $y = \pm 0.5$ $\mu$m. However, its influence is limited only to the small region. When the plasma shutter is included (figure 6(c)) the defocusing field acting on two lateral parts is reduced. On the contrary, the focusing field surrounding the central ion beam is well developed and prolonged over several microns.

The development of this heavy-ion beam-like structure is driven by the intense dynamics between the laser pulse and electron bunches at earlier stages, as can be seen in figure 7. The first row contains the visualization of the data from the case with the plasma shutter at time $t = 33$ T and the second row contains the data from the case without the plasma shutter at the corresponding time $t = 28$ T. The third row contains generated magnetic and electric fields in the directions perpendicular to these of the laser pulse for both simulated cases.

In the $x$–$y$ plane (i.e. the polarization plane of the laser pulse) in figures 7(a) and (e), the high-density bunches appear at the alternating $\pm y$ positions, roughly half of the laser pulse wavelength apart. The structure is more distinct in the case with the plasma shutter, where the electron density exceeds 400 $n_c$. Moreover, the diameter of the final aperture is smaller compared to the case without the plasma shutter. The target outside the central region of $y = \pm 1.5$ $\mu$m remains unperturbed. The differences can be ascribed to the generation of the steep-rising front and increased intensity when the plasma shutter is included (as was shown in figure 2). Therefore, the mostly unperturbed foil can still interact with the high-intensity part of the laser pulse and the dynamics is more intense. On the contrary, in the case without the plasma shutter, the foil (and consequently the generated bunches) needs to interact with a relatively long low-intensity time profile of the incoming laser pulse, causing their pre-expansion, before the arrival of the high-intensity part. The same bunch structure is reflected in the $x$–$z$ plane in figure 7(b) around the position $z = 0$. On the contrary, the structure is not observed in figure 7(f), as it is strongly pre-expanded. The figures 7(c) and (g) show the average electron density (its summation divided by the number of grid points in the $x$-direction) in the $y$–$z$ plane over the same volume denoted by the red rectangles in figures 7(a), (b), (e) and (f). Three distinct regions are presented in figure 7(c), two lobs around $z = \pm 0.75$ $\mu$m corresponding to the aperture diameter and a distinctive high-density lob around $z = 0$ $\mu$m. The lobs are prolonged in the $y$-direction, which corresponds to the spread by the laser pulse polarization. The lateral lobs were observed in [62] using a single foil of a lighter material, whereas the amount of electrons in the central lobe was strongly limited in that case. A less distinctive central lob with lower density is also present in the case without the plasma shutter (figure 7(g)). The effect of laser polarization on lateral lobs is weaker in this case, as they complete a ring shape of a similar density around the central lob.

The electron bunches in the case with the plasma shutter are also well coupled with the corresponding magnetic field in the $y$-direction ($B_y$) as can be seen in figure 7(i). The field exceeds 4 gigagauss at this timeframe (colors are saturated). This clear structure is not present in the case without the plasma shutter in figure 7(j), corresponding to the different electron distribution. The structuring of generated magnetic and electric fields using thin targets becomes a subject of interest recently, e.g. by using flat channel-like targets for improvement of laser-driven particle parameters like beam divergence [77].

The differences in the electron distribution then manifests itself also in the corresponding ion distributions in figures 7(d) and (h) via the generated electric field in the $z$-direction, which are shown in figures 7(k) and (l). In the case with the plasma shutter (figure 7(k)), two regions of electric fields with opposite influence on ions arises: (1) the parabolic shape structure which corresponds to the outer electron cloud around $y = \pm 0.75$ $\mu$m in figure 7(b) and (2) the region inside this cloud with opposite polarity of the electric field. In this inner region, the Coulomb force $F = qE$ focuses ions (with positive charge $q$) toward $z = 0$ as the electric field is negative for $z > 0$ and positive for $z < 0$. This field is present from the $x \approx 5.5$ $\mu$m (closely behind the initial target position at $x = 5$ $\mu$m) to the peak of the parabolic structure around $x \approx 7.5$ $\mu$m. The field (figure 7(k)) is stronger at the positions corresponding to the electron bunches in figure 7(b). Note that the colors are saturated for visualization purposes, the peak field reaches locally values of $a_{0z} \approx \pm 120$, even higher than the initial laser pulse with $a_{0y} = 85$. On the contrary, the parabolic structure with opposite polarity produces a de-focusing field pushing ions away from the central axis. The structures in electric field then correspond to the ion profile in the $y$-$z$ plane in figure 7(d) with two ion lobs pushed away from the central axis to positions $y = \pm 0.75$ $\mu$m and two thin ion stripes around $z = 0$, which follows the electron bunches in the $y$-direction (figure 7(a)).

The electric field in the case without the plasma shutter (figure 7(l)) contains similar de-focusing parabolic structure corresponding to a broader electron cloud in figure 7(f). On the contrary, the inner structure behind the target till $x \approx 1.5$ $\mu$m has opposite polarity around $z = 0$ than in the case with the plasma shutter and is thus de-focusing. It results in the low-density region around center in the corresponding ion distribution figure 7(h)). The ion distribution also contains the transverse instability. The typical longitudinal stripes along $z$-axis observed in the similar figures in 3D simulations and experiments for linear polarization (LP) in [63, 78, 79] are not so clearly visible in figure 7(h), as the inner field is weaker than the one of the parabolic structure (figure 7(l)). On the contrary, the inner field is the dominant part in the case with the plasma shutter (figure 7(k)), producing the stripe in the middle of figure 7(d). Therefore, the transverse instability is suppressed, when the plasma shutter is included, as can be seen by comparing the figures 7(d) and (h). This observation is in agreement with [28], where the steep-front laser pulse (which was assumed to be possibly produced by the plasma shutter) was used for mitigation of this kind of instabilities.

This development affects the final silver ion energy spectra and angular distribution as is shown in figure 8 at time $t = 70$ T, when the acceleration in all cases already ended.

The circular polarization (CP) is often proposed for the RPA dominated regimes of ion acceleration as an alternative to LP to increase the maximal ion energy, reduce energy spread and divergence of the ion beam [15, 34, 57, 58]. Therefore, additional 3D simulations with and without the plasma shutter using CP were
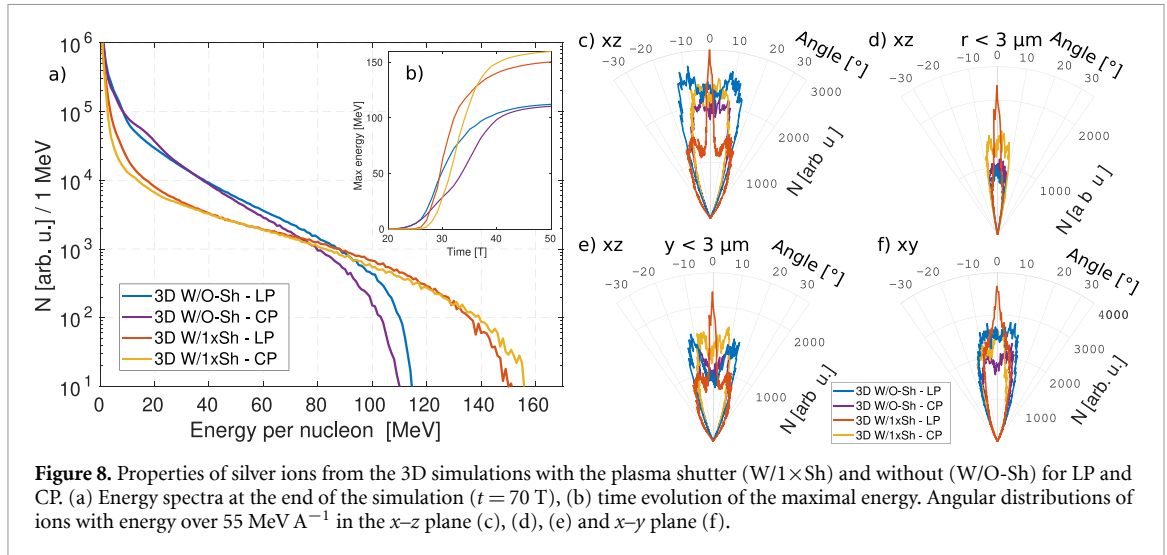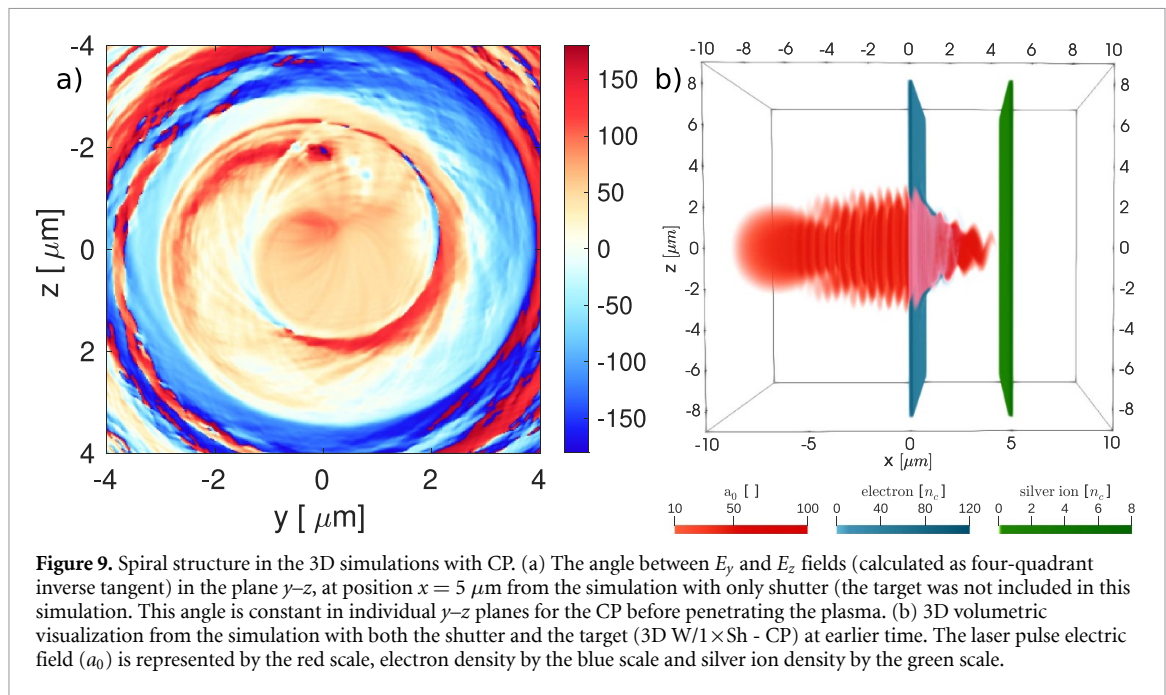
**Figure 8.** Properties of silver ions from the 3D simulations with the plasma shutter (W/1×Sh) and without (W/O-Sh) for LP and CP. (a) Energy spectra at the end of the simulation ($t = 70$ T), (b) time evolution of the maximal energy. Angular distributions of ions with energy over 55 MeV A$^{-1}$ in the $x$–$z$ plane (c), (d), (e) and $x$–$y$ plane (f).

made for comparison. Their results are also included in figure 8 via yellow and deep purple lines and discussed in the last paragraph of this section.

In the LP cases (blue and red lines), maximal energy rises from 115 to 155 MeV A$^{-1}$ (about 35%) when the plasma shutter is included in the simulation. The increase occurs, even though about 50% of the laser pulse energy is consumed by the plasma shutter as was shown in figure 3(b). The integrated number of high-energy ions is larger in the simulation with the shutter for energy above 65 MeV A$^{-1}$, although the total number of all accelerated ions is lower. The time evolution of the maximal energy of silver ions are shown in the inset of figure 8(b). The time was shifted by 5 T in the case without the plasma shutter as the target is shifted by 5 $\lambda$. The time profile is similar in both cases. The gradual change from the exponential rise, corresponding to the RPA [14] (which can be in principle unlimited [80]), to logarithmic rise can be spotted in both lines around the time $t = 30$ T. The target becomes partially (relativistically) transparent around this time, as can be inferred from the figure 6(b). The transmitted laser pulse front is about 10 $\mu$m ahead from the target at time $t = 40$ T. The RPA still significantly contributes to ion acceleration till time 33 T in the simulation with the shutter as the front of electron layer around the position $x = 7$ $\mu$m (figure 7(b)) is still compact. However, the density of the electron layer is decreasing, resulting in slower rise of maximal energy and partial transparency. Therefore, other mechanisms involving the relativistic transparency, like hybrid RPA-TNSA [19] and directed coulomb explosion [81] also take place at this stage. The rise of maximal energy in this stage (33–40 T) is noticeably lower compared to the previous stages. At time 40 T most of the laser pulse already left the area where the plasma is located as can be seen in figure 6(b). Only a small rise of ion energy is observed afterwards. Details on the influence of different acceleration mechanisms, supported by density profiles of electrons and silver ions, are included in the appendix.

The beam-like structure is reflected in the angular distribution of accelerated ions (energy above 55 MeV A$^{-1}$) in figures 8(c)–(f) at time $t = 70$ T. In the $x$–$z$ plane (comparing momenta in $x$ and $z$ directions) in figure 8(c), a narrow central bunch of particles is visible when the shutter is included (red). The divergence at the FWHM of the bunch is around 5°, whereas the case without the shutter generates a broad bunch divided into three directions with overall divergence over 35°. Another advantage of the use of the shutter is the space positioning of the ion bunch. In the case without the plasma shutter, the central part of the ion angular distribution is significantly reduced when a 'pinhole' is introduced filtering out the ions with radial position $r > 3$ $\mu$m away from the central axis, as can be seen in figure 8(d). If the filtering is done only in the y-direction, the lateral parts of the bunch prevails over the central part in the case without shutter (figure 8(e)). On the contrary, the central part prevails in the case with the shutter. The shutter has also a positive effect on the divergence at the FWHM in the $x$–$y$ plane figure 8(f)), which is reduced from over 28.5° to about 18.5°. This can be ascribed to the generation of the steep-rising front of the incident laser pulse as is discussed in the section 3.3.

In the CP cases, the silver ion spectra are similar to their LP counterparts (figure 8(a)). The increase of maximal ion energy when the plasma shutter is included is even slightly higher than for the LP (about 44%). In the simulations with the shutter, the change of the polarization affects mostly the tail of the silver ion spectra, which experiences slight increase of maximal energy from 155 to 164 MeV A$^{-1}$. The time evolution of maximal ion energy of the CP simulations (figure 8(b)) infers that the main acceleration phase starts later and lasts longer than in the LP cases. The CP inherently stabilizes the pulse interaction with the plasma

**Figure 9.** Spiral structure in the 3D simulations with CP. (a) The angle between $E_y$ and $E_z$ fields (calculated as four-quadrant inverse tangent) in the plane $y$–$z$, at position $x = 5 \ \mu$m from the simulation with only shutter (the target was not included in this simulation. This angle is constant in individual $y$–$z$ planes for the CP before penetrating the plasma. (b) 3D volumetric visualization from the simulation with both the shutter and the target (3D W/$1 \times$Sh - CP) at earlier time. The laser pulse electric field ($a_0$) is represented by the red scale, electron density by the blue scale and silver ion density by the green scale.

shutter (and the Mf) and thus delays the onset of relativistic transparency. It also results in lower amount of pulse energy being transmitted through the plasma shutter (38.4% compared to 47.9% for the LP). On the other hand, the effect of divergence reduction with the inclusion of the shutter is strongly reduced in the CP simulations. The divergence of the silver ion beam is higher compared to the LP simulation with the shutter (but still lower compared to the LP case without the shutter) as can be seen in figures 8(c)–(f)). In the simulations with the shutter the divergence increases from 5° to about 27° in the $x$–$z$ plane and from 18.5° to about 25° in the $x$–$y$ plane compared to the LP case. Note that the CP laser pulse transmitted through the shutter also generates a spiral-like, rotating laser diffraction structure as previously observed in [62, 82]. The spiral structure from our 3D simulations is shown in figure 9.

### 3.5. The use of a double plasma shutter and prepulse filtering

The interaction of the ultraintense pulse with the target having a step-like density profile may be hard to achieve even with nowadays technology. Therefore, we propose the use of a second plasma shutter, which will be used to mitigate the prepulses accompanying the main pulse.

We run a 2D hydrodynamic simulation of prepulse with intensity of $10^{12}$ W cm$^{-2}$ interacting with an aluminum shutter with areal density roughly the same as in the case of silicon nitride shutter. The 2D density profile from this simulation after 125 ps of interaction is then used as input data into a 2D PIC simulation in a form of a pre-expanded shutter, placed at the position $x = -5 \ \mu$m. The simulation also contains the previously used setup of the non-expanded plasma shutter at $x = 0 \ \mu$m and silver target at $x = 5 \ \mu$m (see figure 10(a)). This case is hereinafter referred to as W/$2 \times$Sh in analogy to the reference 20 nm cases without any shutter (W/O-Sh) and with one non-expanded shutter (W/$1 \times$Sh) used in previous sections. The remaining electron density of the expanded plasma shutter is still above the critical density. Therefore, the plasma shutter can efficiently filter out this kind of prepulses with duration (at least) up to 125 ps, justifying the step-like densities of the second plasma shutter and the silver target in the simulation of this case.

The silver ion energy spectra at the end of the simulation ($t = 70$ T) of the cases W/O-Sh (blue), W/$1 \times$Sh (red) and W/$2 \times$Sh (deep purple) from 2D simulations are shown in figure 10(b). When both shutters are used in the simulation, the maximum silver energy still increases from 157 to 167 MeV A$^{-1}$ compared to the simulation without the shutter. Note that the energy spectra of the cases of W/$1 \times$Sh and W/$2 \times$Sh are very similar for ions with energy up to 160 MeV A$^{-1}$ and only the most energetic ones are affected by the addition of the pre-expanded shutter. Therefore, maximal energy closer to the case of W/$1 \times$Sh (179 MeV A$^{-1}$) can be theoretically reached with optimal thickness, expansion and positioning of the pre-expanded shutter. The 2D simulations in figure 10(b) results in higher maximal energies than their 3D counterparts in figure 8(a). The simulations without shutter experience more significant drop of the maximal energies when the simulation dimension increases from 2D to 3D (42 MeV A$^{-1}$) compared to the simulations with the shutter (24 MeV A$^{-1}$). Therefore, the increase of the maximal energy in the W/$2 \times$Sh case compared to W/O-Sh case may be more significant in 3D even for the presented configuration.
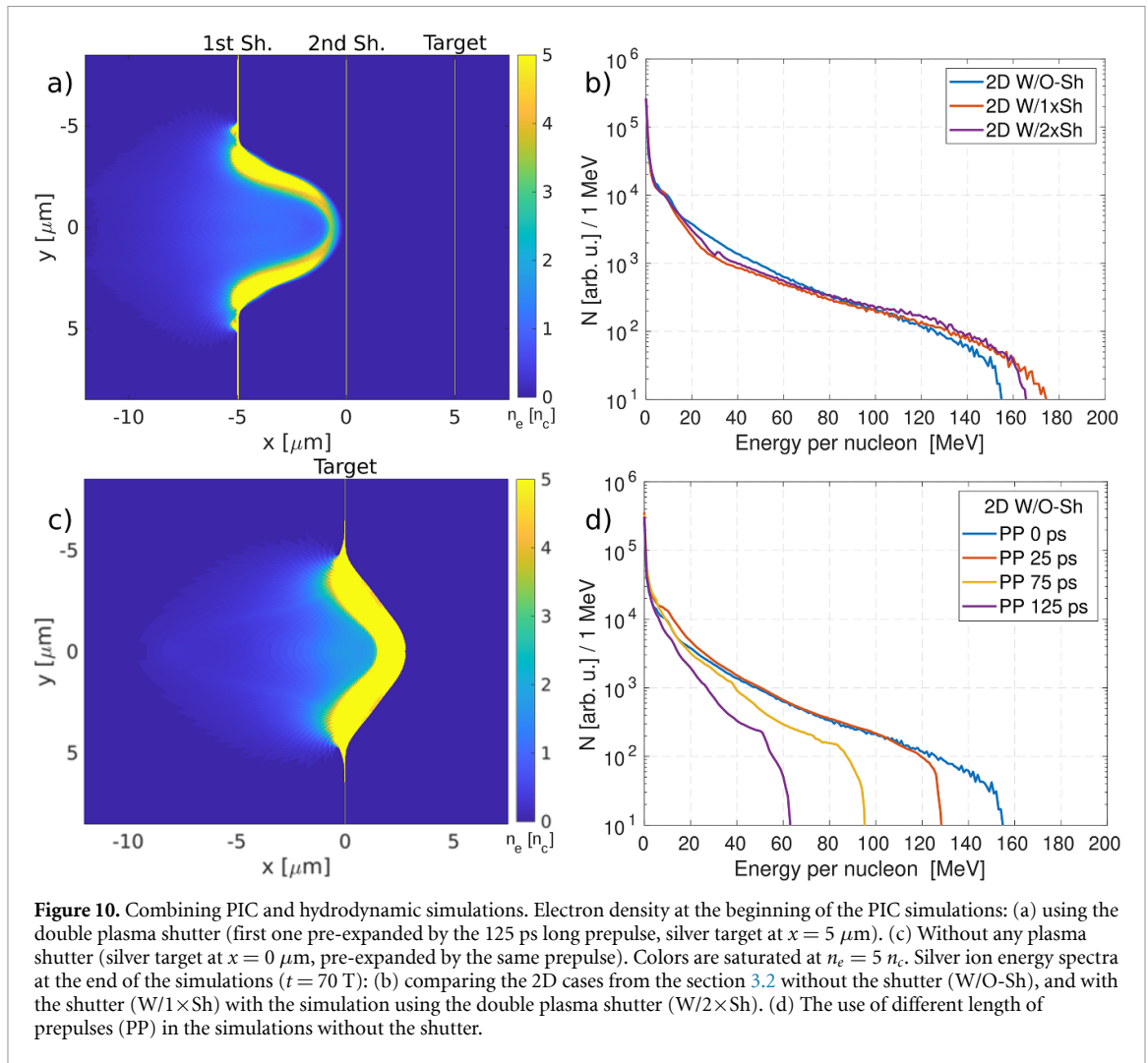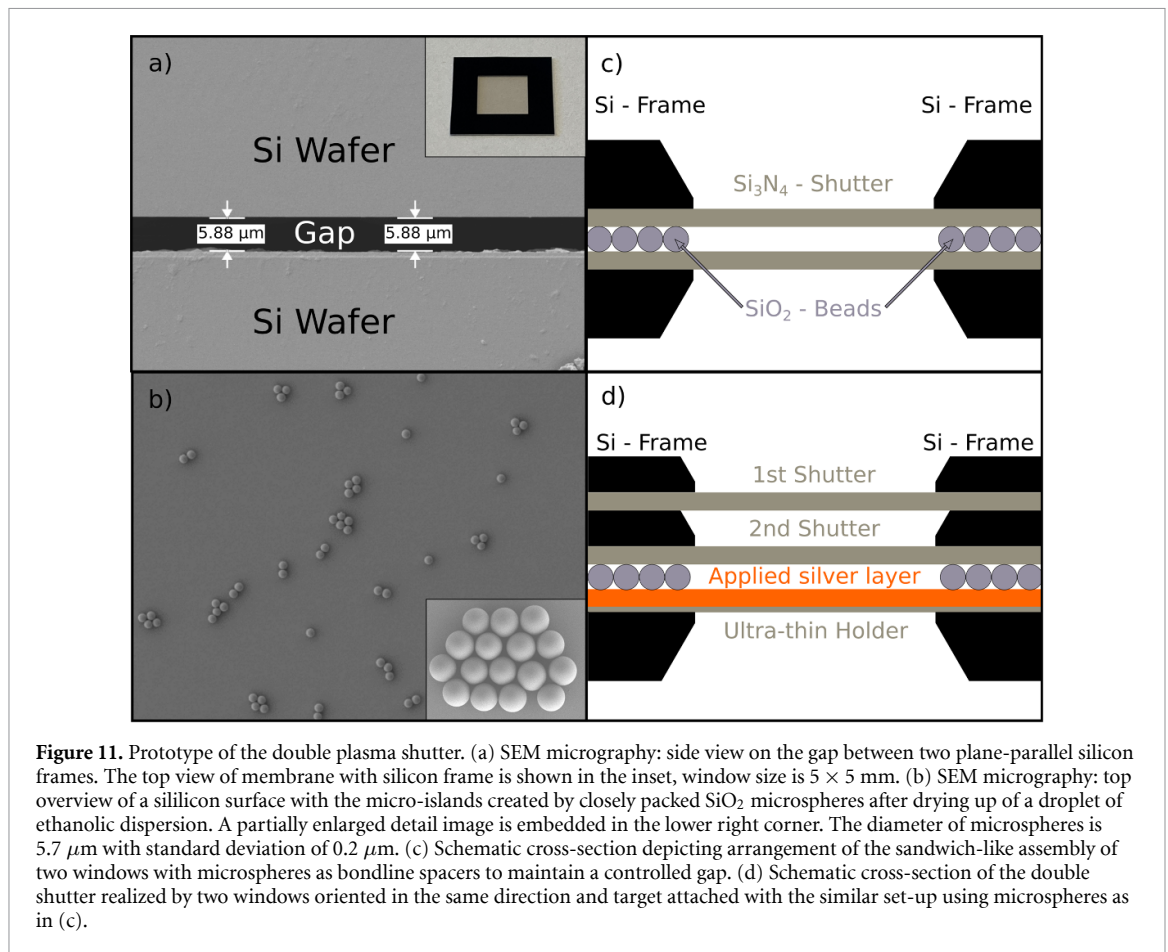
**Figure 10.** Combining PIC and hydrodynamic simulations. Electron density at the beginning of the PIC simulations: (a) using the double plasma shutter (first one pre-expanded by the 125 ps long prepulse, silver target at $x = 5$ $\mu$m). (c) Without any plasma shutter (silver target at $x = 0$ $\mu$m, pre-expanded by the same prepulse). Colors are saturated at $n_e = 5$ $n_c$. Silver ion energy spectra at the end of the simulations ($t = 70$ T): (b) comparing the 2D cases from the section 3.2 without the shutter (W/O-Sh), and with the shutter (W/1×Sh) with the simulation using the double plasma shutter (W/2×Sh). (d) The use of different length of prepulses (PP) in the simulations without the shutter.

One also needs to keep in mind, that the ion energy in the case W/O-Sh are overestimated compared to the W/2×Sh case, as no prepulse was assumed in this simulation. When the same prepulse of 125 ps is used in the hydrodynamic simulation with the silver target, the originally ultra-thin target of 20 nm expanded into a few microns of overdense plasma predeceased by a long preplasma (figure 10(c)). It results in a significant drop of the maximal energy compared to the previously optimized simulation. Several simulations with the density profiles obtained from the different time of hydrodynamic simulation with the prepulse were performed. The decrease of the maximal energy with the increase of the prepulse duration (PP) is shown in figure 10(d). Therefore, to fully understand the impact of the double plasma shutter scenario, one needs to compare the deep purple lines in figures 10(b) and (d), which captures the same physics. This comparison provides the increase of maximal energy from 64 to 167 MeV A$^{-1}$.

Our theoretical finding leads to the formulation of an idea of a double plasma shutter, which prototype was prepared at the Czech Technical University (see the photo in the inset of figure 11(a)). It consists of two commercial silicon nitride membranes separated by SiO$_2$ monodisperse microspheres. Therefore, a parallel surface between two layers is provided with the same spacing of 5.88 $\mu$m as can be seen in the snapshot from the scanning electron microscope (SEM) in figure 11(a). The two membranes have a thick protective frame made of silicon (thickness of 200 $\mu$m) with a thin window of silicon nitride (30 nm). The window is located at the edge of the one side of the membrane. Therefore, the double plasma shutter is created by these two windows facing each other as depicted in the scheme in figure 11(c). Multiple windows can be present on one shutter. Therefore, it can be used for high-repetition experiments using the target tower [83, 84]. For our laser and target parameters (requiring only a small gap between the shutter and target) another approach, with the two shutter windows oriented in the same direction (as shown in figure 11(d)), may be more practical. Note that for this implementation the manufactured frame of the shutter window should be thinner than in figure 11(c). The target can be attached either as the third window oriented in the same direction with the frame thickness corresponding to the required gap, using the microspheres

**Figure 11.** Prototype of the double plasma shutter. (a) SEM micrography: side view on the gap between two plane-parallel silicon frames. The top view of membrane with silicon frame is shown in the inset, window size is 5 × 5 mm. (b) SEM micrography: top overview of a sililicon surface with the micro-islands created by closely packed $SiO_2$ microspheres after drying up of a droplet of ethanolic dispersion. A partially enlarged detail image is embedded in the lower right corner. The diameter of microspheres is 5.7 $\mu$m with standard deviation of 0.2 $\mu$m. (c) Schematic cross-section depicting arrangement of the sandwich-like assembly of two windows with microspheres as bondline spacers to maintain a controlled gap. (d) Schematic cross-section of the double shutter realized by two windows oriented in the same direction and target attached with the similar set-up using microspheres as in (c).

(as in the previous scheme) or other spacer elements attached directly by the manufacturer. The microspheres option (shown in figure 11(d)) provides a possibility of an on-site modification of the gap size and the target structure for several experimental setups with prefabricated double shutter. The silver target can be either a standalone silver foil or a silver layer applied to an ultra-thin silicon nitride holder. The holder can be fabricated with thickness down to a few nm [85] to limit its effects on the silver ion acceleration. Note that the silver layer can be applied to either side of the holder, depending on the application.

## 4. Conclusion

In conclusion, we investigate the application of the plasma shutter for heavy ion acceleration driven by a high-intensity laser pulse using 3D and 2D PIC simulations. The laser pulse, transmitted through the plasma shutter, gains a steep-rising front and its peak intensity is locally increased at the cost of losing part of its energy, depending on the shutter thickness. These effects have a direct influence on subsequent ion acceleration from the ultrathin target located behind the plasma shutter. The parameters like target and shutter thicknesses, size of the gap between them, and the effects of the pulse-front steepness are investigated using 2D PIC simulations for the case of a silicon nitride plasma shutter, a silver target and a linearly polarized laser pulse. In the follow-up 3D simulations of our reference case, the maximal energy of silver ions increases by 35% when the plasma shutter is included. Moreover, the steep-rising front of the laser pulse leads to the formation of high-density electron bunches. This structure (which also appears in the generated electric and magnetic fields) focuses ions toward the laser axis in the plane perpendicular to the laser polarization. The generated high energy ion beam has significantly lower divergence compared to the broad ion cloud, generated without the shutter. In the absence of the plasma shutter, the structures are pre-expanded by the low intensity part of the laser pulse and the subsequent onset of transverse instability. This instability observed in ion density is thus efficiently reduced using plasma shutter. 3D simulations with the CP with and without the shutter are performed for comparison. The increase of maximal ion energy in the simulation with the plasma shutter is observed also for the CP (by 44%). The use of the CP in combination with the plasma shutter results in a slight increase of maximal ion energy, but also increase of the ion beam divergence compared to the corresponding simulation with a LP.

The efficiency of the processes introduced by the plasma shutter may be reduced by the previous shutter interaction with a long prepulse. Therefore, the effects of sub-ns prepulses are investigated using a combination of 2D PIC and hydrodynamic simulations assuming a double plasma shutter. The first shutter can withstand the assumed sub-ns prepulse (treatment of ns and ps prepulses by other techniques is assumed, alternatively increasing the thickness of the first shutter may filter out longer prepulses). Therefore, the processes of the steep front generation and the local intensity increase can develop via interaction with the second non-expanded shutter. The increase of the maximal ion energy compared to the simulation with a step-like density target without any shutter is demonstrated also in this case. Moreover, the comparison with a silver target pre-expanded by the same sub-ns prepulse as in the double shutter scenario results in an increase of maximal silver energy by the factor of 2.6 in the 2D simulations. A prototype of this double shutter is presented and the design of the whole shutter-target setup is discussed.

## Data availability statement

The data that support the findings of this study are available upon reasonable request from the authors.

## Acknowledgments

## Appendix. Details on the influence of different acceleration mechanisms

As the silver target is ultra-thin, several acceleration mechanisms (and their combination) are acting together during the laser target interaction. From the time evolution of maximal ion energy in figure A1(a) at least four different stages can be inferred. The time instants when the stages switch are highlighted by the grid in figure A1 (times 30, 33 and 40 T). The electron and silver ion density are shown in the respective time instants (and at time 36 T) in figure A2. The density of silver ions was multiplied by $Z = 40$ in order to visualize them with the same logarithmic color scale as electrons. The simulation data were recorded with time interval corresponding to laser period T.

The first stage is dominated by the RPA mechanism and last till 30 T. Around this time the laser pulse starts to penetrate through the target as can be seen comparing figures A1(b) and (c) and the temporal evolution of maximal energy stops having an exponential rise, connected to (in principle unlimited [80]) RPA and continues with slower rise afterwards. The shell structure (typical for RPA) is developed in the silver ion density distributions in figures A2(e) and (m). The RPA still significantly contributes to ion acceleration in the second stage till time 33 T. This can be seen from figures A2(f) and (n) as ions still keep a compact shell structure. The ions with highest energy (located at the front of the ion cloud) follow the front electron layer around the position $x = 7$ $\mu$m. However, the density of the electron layer is decreasing, resulting in slower rise of maximal energy in figure A1(a). The electron distribution now consists of high-density electron bunches and low-density regions around them (figures A2(b) and (j)), thus being partially (relativistically) transparent. Therefore, other mechanisms involving the relativistic transparency, like hybrid RPA-TNSA [19] and directed coulomb explosion [81] also take place at this stage.

**Figure A1.** (a) Time evolution of maximal ion energy. (b), (c) Electron density around the time of laser penetration from the 3D simulation with the shutter and LP (3D W/1×Sh - LP).



**Figure A2.** Electron and silver ion densities in the *x–z* and *x–y* slices of the 3D simulation with the shutter and LP (3D W/1×Sh - LP).
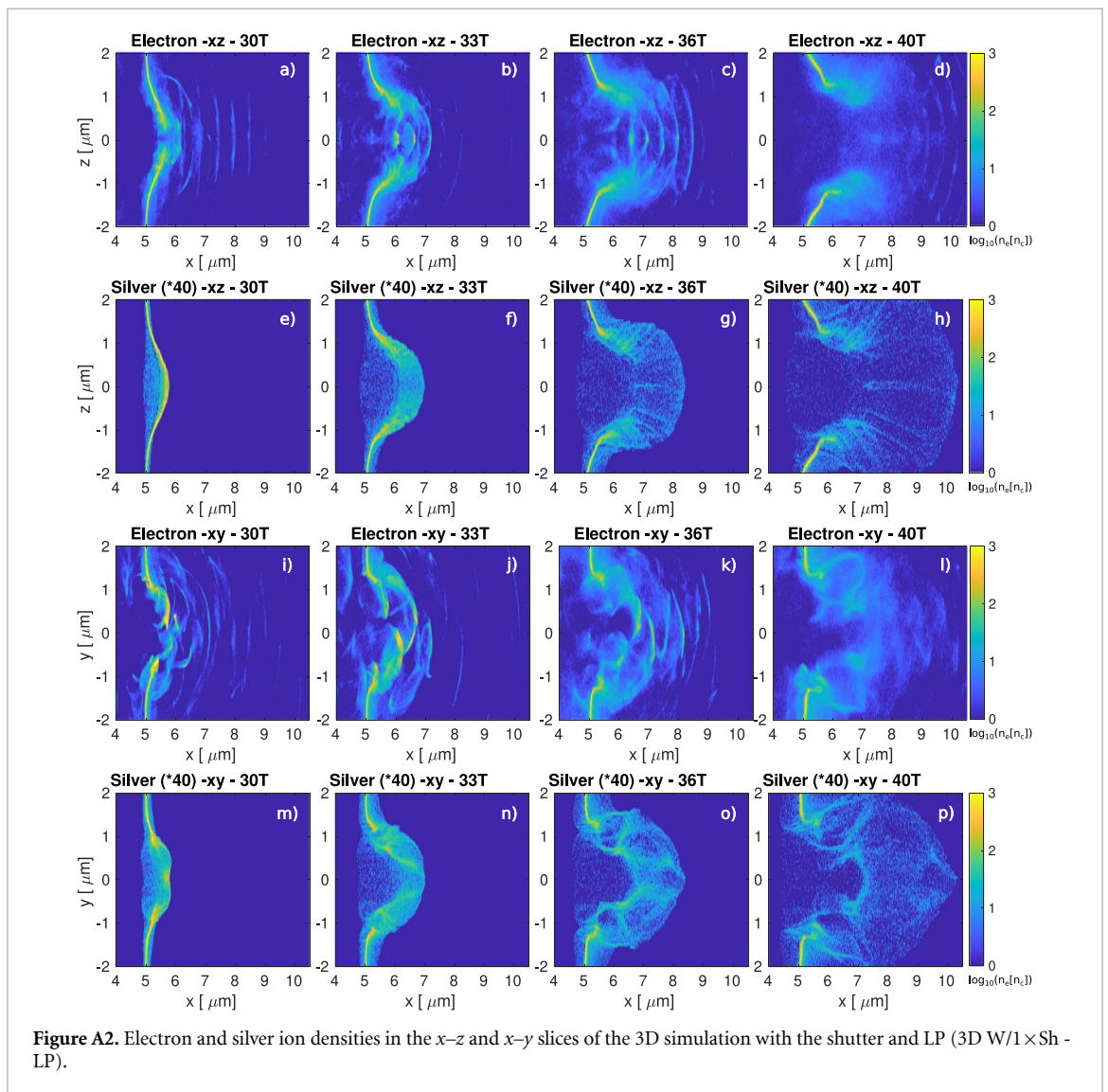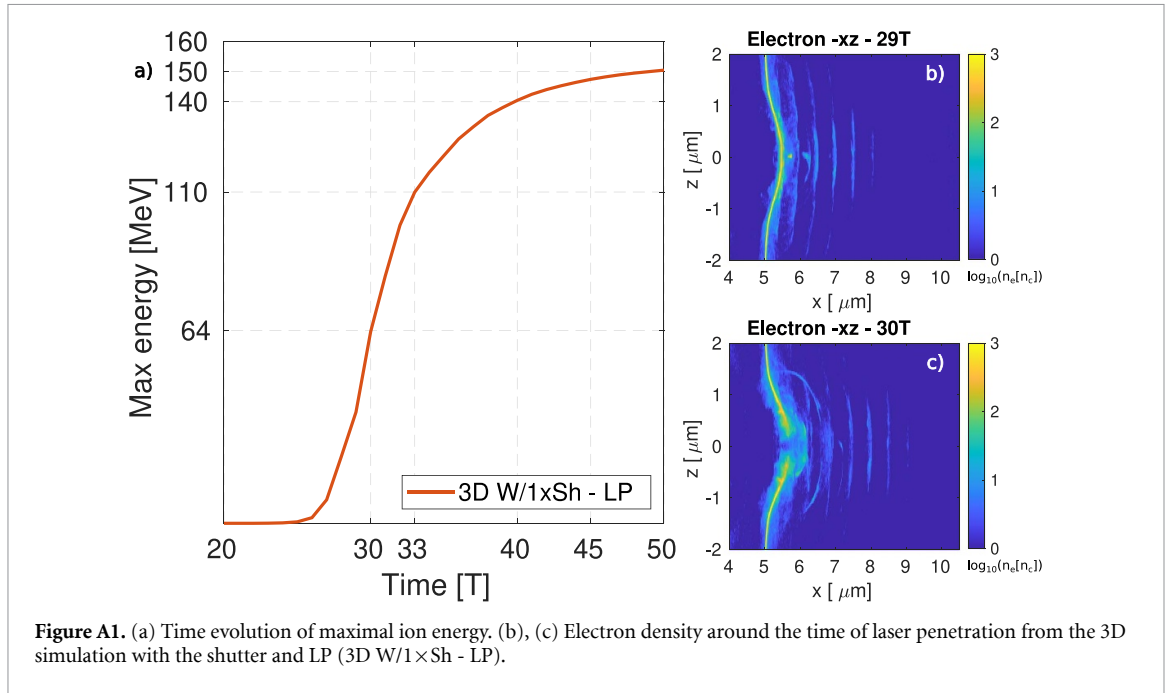
In the third stage between time instants 33 and 40 T the laser pulse propagates through the plasma as can be observed in figures A2(c) and (k). The influence of RPA thus drops significantly and regimes operating with relativistic transparency dominate in this stage. The rise of maximal energy in figure A1(a) is noticeably lower in this stage. At time 40 T most of the laser pulse already left the area where the plasma is located as can be seen in figure 6(b). The structures in electron density (figure A2(d)) and figure A2(l) expand and slowly disappear. Only a small rise of ion energy is observed afterwards in the last stage.

## ORCID iDs

M Matys ● https://orcid.org/0000-0002-6215-4246
S V Bulanov ● https://orcid.org/0000-0001-8305-0289
M Kucharik ● https://orcid.org/0000-0003-2828-9072
M Jirka ● https://orcid.org/0000-0003-4457-4471
J Nikl ● https://orcid.org/0000-0003-0131-0628
M Kecova ● https://orcid.org/0000-0002-2524-5552
J Proska ● https://orcid.org/0000-0002-2315-493X
J Psikal ● https://orcid.org/0000-0003-4586-1149
G Korn ● https://orcid.org/0000-0002-7093-5296
O Klimo ● https://orcid.org/0000-0002-0565-2409

## References

[1] Bulanov S V, Esirkepov T, Khoroshkov V S, Kuznetsov A V and Pegoraro F 2002 *Phys. Lett.* A **299** 240–7
[2] Bulanov S V, Wilkens J J, Esirkepov T Z, Korn G, Kraft G, Kraft S D, Molls M and Khoroshkov V S 2014 *Phys.-Usp.* **57** 1149–79
[3] Daido H, Nishiuchi M and Pirozhkov A S 2012 *Rep. Prog. Phys.* **75** 056401
[4] Macchi A, Borghesi M and Passoni M 2013 *Rev. Mod. Phys.* **85** 751–93
[5] Passoni M *et al* 2019 *Plasma Phys. Control. Fusion* **62** 014022
[6] Nishiuchi M *et al* 2015 *Phys. Plasmas* **22** 033107
[7] Nishiuchi M *et al* 2016 *Plasma Phys. Rep.* **42** 327–37
[8] Braun-Munzinger P, Koch V, Schäfer T and Stachel J 2016 *Phys. Rep.* **621** 76–126
[9] Habs D, Thirolf P G, Gross M, Allinger K, Bin J, Henig A, Kiefer D, Ma W and Schreiber J 2010 *Appl. Phys.* B **103** 471–84
[10] Lindner F H, Fitzpatrick E G, Haffa D, Ponnath L, Schmidt A K, Speicher M, Zielbauer B, Schreiber J and Thirolf P G 2022 *Sci. Rep.* **12** 4784
[11] Korzhimanov A V, Efimenko E S, Golubev S V and Kim A V 2012 *Phys. Rev. Lett.* **109** 245008
[12] Snavely R A *et al* 2000 *Phys. Rev. Lett.* **85** 2945–8
[13] Wilks S C, Langdon A B, Cowan T E, Roth M, Singh M, Hatchett S, Key M H, Pennington D, MacKinnon A and Snavely R A 2001 *Phys. Plasmas* **8** 542–9
[14] Esirkepov T, Borghesi M, Bulanov S V, Mourou G and Tajima T 2004 *Phys. Rev. Lett.* **92** 175003
[15] Henig A *et al* 2009 *Phys. Rev. Lett.* **103** 245003
[16] Kar S *et al* 2008 *Phys. Rev. Lett.* **100** 225004
[17] Scullion C *et al* 2017 *Phys. Rev. Lett.* **119** 054801
[18] Kim I J *et al* 2016 *Phys. Plasmas* **23** 070701
[19] Higginson A *et al* 2018 *Nat. Commun.* **9** 724
[20] Bulanov S S, Esarey E, Schroeder C B, Bulanov S V, Esirkepov T Z, Kando M, Pegoraro F and Leemans W P 2016 *Phys. Plasmas* **23** 056703
[21] Margarone D *et al* 2016 *Phys. Rev.* X **6** 041030
[22] Psikal J and Matys M 2018 *Plasma Phys. Control. Fusion* **60** 044003
[23] McIlvenny A *et al* 2021 *Phys. Rev. Lett.* **127** 194801
[24] Nishiuchi M *et al* 2020 *Phys. Rev. Res.* **2** 033081
[25] Bulanov S V and Khoroshkov V S 2002 *Plasma Phys. Rep.* **28** 453–6
[26] Bulanov S V, Esirkepov T Z, Kamenets F F, Kato Y, Kuznetsov A V, Nishihara K, Pegoraro F, Tajima T and Khoroshkov V S 2002 *Plasma Phys. Rep.* **28** 975–91
[27] Esirkepov T *et al* 2002 *Phys. Rev. Lett.* **89** 175003
[28] Matys M, Nishihara K, Kecova M, Psikal J, Korn G and Bulanov S V 2020 *High Energy Density Phys.* **36** 100844
[29] Wang P *et al* 2021 *Phys. Rev.* X **11** 021049
[30] Alejo A *et al* 2022 *Phys. Rev. Lett.* **129** 114801
[31] Margarone D *et al* 2012 *Phys. Rev. Lett.* **109** 234801
[32] Psikal J, Grym J, Stolcova L and Proska J 2016 *Phys. Plasmas* **23** 123121
[33] Cantono G, Permogorov A, Ferri J, Smetanina E, Dmitriev A, Persson A, Fülöp T and Wahlström C G 2021 *Sci. Rep.* **11** 5006
[34] Chen M, Pukhov A, Yu T P and Sheng Z M 2009 *Phys. Rev. Lett.* **103** 024801
[35] Liu J L, Chen M, Sheng Z M, Liu C S, Mori W B and Zhang J 2013 *Phys. Rev. Spec. Top.-Accel. Beams* **16** 121301
[36] Hadjisolomou P, Bulanov S V and Korn G 2020 *J. Plasma Phys.* **86** 905860304
[37] Gaillard S A *et al* 2011 *Phys. Plasmas* **18** 056710
[38] Lévy A *et al* 2007 *Opt. Lett.* **32** 310–2
[39] Bulanov S V, Inovenkov I N, Kirsanov V I, Naumova N M and Sakharov A S 1992 *Phys. Fluids* B **4** 1935–42
[40] Bulanov S V, Kirsanov V I, Naumova N M, Sakharov A S, Shah H A and Inovenkov I N 1993 *Phys. Scr.* **47** 209–13
[41] Decker C D, Mori W B, Tzeng K C and Katsouleas T 1996 *Phys. Plasmas* **3** 2047–56
[42] Wang H Y, Lin C, Sheng Z M, Liu B, Zhao S, Guo Z Y, Lu Y R, He X T, Chen J E and Yan X Q 2011 *Phys. Rev. Lett.* **107** 265002

[43] Bin J H *et al* 2015 *Phys. Rev. Lett.* **115** 064801
[44] Fedeli L, Formenti A, Cialfi L, Pazzaglia A and Passoni M 2018 Ultra-intense laser interaction with nanostructured near-critical plasmas *Sci. Rep.* **8** 3834
[45] Horný V, Chen S N, Davoine X, Lelasseux V, Gremillet L and Fuchs J 2022 High-flux neutron generation by laser-accelerated ions from single- and double-layer targets *Sci. Rep.* **12** 19767
[46] Park J *et al* 2019 Ion acceleration in laser generated megatesla magnetic vortex *J. Plasma Phys.* **26** 103108
[47] Hakimi S *et al* 2022 Laser–solid interaction studies enabled by the new capabilities of the iP2 BELLA PW beamline *J. Plasma Phys.* **29** 083102
[48] Yogo A *et al* 2008 Laser ion acceleration via control of the near-critical density target *Phys. Rev. E* **77** 016401
[49] Vshivkov V A, Naumova N M, Pegoraro F and Bulanov S V 1998 *Phys. Plasmas* **5** 2727–41
[50] Reed S A *et al* 2009 *Appl. Phys. Lett.* **94** 201117
[51] Palaniyappan S *et al* 2012 *Nat. Phys.* **8** 763–9
[52] Wei W Q *et al* 2017 *Phys. Plasmas* **24** 113111
[53] Jirka M, Klimo O and Matys M 2021 *Phys. Rev. Res.* **3** 033175
[54] Cattani F, Kim A, Anderson D and Lisak M 2000 *Phys. Rev. E* **62** 1234–7
[55] Goloviznin V V and Schep T J 2000 *Phys. Plasmas* **7** 1564–71
[56] Pegoraro F and Bulanov S V 2007 *Phys. Rev. Lett.* **99** 065002
[57] Klimo O, Psikal J, Limpouch J and Tikhonchuk V T 2008 *Phys. Rev. Spec. Top.-Accel. Beams* **11** 031301
[58] Robinson A P, Zepf M, Kar S, Evans R G and Bellei C 2008 *New J. Phys.* **10** 013021
[59] Wan Y *et al* 2016 *Phys. Rev. Lett.* **117** 234801
[60] Wan Y, Pai C H, Zhang C J, Li F, Wu Y P, Hua J F, Lu W, Joshi C, Mori W B and Malka V 2018 *Phys. Rev. E* **98** 013202
[61] Jirka M, Klimo O, Gu Y J and Weber S 2020 *Sci. Rep.* **10** 8887
[62] Gonzalez-Izquierdo B *et al* 2016 *Nat. Phys.* **12** 505–12
[63] Gonzalez-Izquierdo B *et al* 2016 *Nat. Commun.* **7** 12891
[64] Danielová M, Janečka P, Grosz J and Holý A 2019 *EuroVis 2019 - Posters* ed J Madeiras Pereira and R G Raidou (The Eurographics Association) (https://doi.org/10.2312/eurp.20191145)
[65] Matys M *et al* Virtual Beamline 2022 *ELI Beamlines* (available at: https://vbl.eli-beams.eu/mm-shutter/)
[66] Arber T D *et al* 2015 *Plasma Phys. Control. Fusion* **57** 113001
[67] Liska R, Kuchařík M, Limpouch J, Renner O, Váchal P, Bednárik L and Velechovský J 2011 ALE method for simulations of laser-produced plasmas *Finite Volumes for Complex Applications VI Problems & Perspectives* ed J Fořt, J Fürst, J Halama, R Herbin and F Hubert (Berlin: Springer) pp 857–73
[68] Kapin T, Kucharik M, Limpouch J, Liska R and Vachal P 2008 *Int. J. Numer. Methods Fluids* **56** 1337–42
[69] Kuchařík M, Shashkov M and Wendroff B 2003 *J. Comput. Phys.* **188** 462–71
[70] Liska R and Kuchařík M 2005 *Proc. Equadiff* **11** 213–22
[71] Velechovský J 2015 High-order numerical methods for laser plasma modeling *PhD Thesis* Czech Technical University in Prague
[72] Spitzer L and Härm R 1953 *Phys. Rev.* **89** 977–81
[73] More R M, Warren K H, Young D A and Zimmerman G B 1988 *Phys. Fluids* **31** 3059–78
[74] Badziak J, Krousky E, Kucharik M and Liska R 2016 *J. Instrum.* **11** C03043
[75] Picciotto A *et al* 2014 *Phys. Rev. X* **4** 031030
[76] Margarone D *et al* 2014 *Plasma Phys. Control. Fusion* **57** 014030
[77] Greplova Zakova M, Psikal J, Schillaci F and Margarone D 2021 *Plasma Phys. Control. Fusion* **63** 085005
[78] Sgattoni A, Sinigardi S, Fedeli L, Pegoraro F and Macchi A 2015 *Phys. Rev. E* **91** 013106
[79] Palmer C A J *et al* 2012 *Phys. Rev. Lett.* **108** 225002
[80] Bulanov S V, Echkina E Y, Esirkepov T Z, Inovenkov I N, Kando M, Pegoraro F and Korn G 2010 *Phys. Plasmas* **17** 063102
[81] Bulanov S S *et al* 2008 *Phys. Rev. E* **78** 026412
[82] Bulanov S V *et al* 2000 *J. Exp. Theor. Phys. Lett.* **71** 407–11
[83] Margarone D *et al* 2018 *Quantum Beam Sci.* **2** 8
[84] Chagovets T *et al* 2021 *Appl. Sci.* **11** 1680
[85] Yanagi I, Ishida T, Fujisaki K and Takeda K I 2015 *Sci. Rep.* **5** 14656

# Appendix D

# Author contribution statements

The core of this dissertation is based on the five selected publications (listed below) made in collaboration with other coauthors. Therefore, the contribution statements are given here.

I. M. Matys, J. Psikal, K. Nishihara, O. Klimo, M. Jirka, P. Valenta and S. V. Bulanov (2023). High-quality laser-accelerated ion beams from structured targets. *Photonics* **10**, 61.

II. J. Psikal and M. Matys (2018). Dominance of hole-boring radiation pressure acceleration regime with thin ribbon of ionized solid hydrogen. *Plasma Physics and Controlled Fusion* **60**, 044003.

III. M. Matys, K. Nishihara, M. Kecova, J. Psikal, G. Korn, S. V. Bulanov (2020). Laser-driven generation of collimated quasi-monoenergetic proton beam using double-layer target with modulated interface. *High Energy Density Physics* **36**, 100844.

IV. M. Jirka, O. Klimo and M. Matys (2021) Relativistic plasma aperture for laser intensity enhancement. *Physical Review Research* **3**, 033175.

V. M. Matys, S. V. Bulanov, M. Kucharik, M. Jirka, J. Nikl, M. Kecova, J. Proska, J. Psikal, G. Korn and O. Klimo (2022). Design of plasma shutters for improved heavy ion acceleration by ultra-intense laser pulses. *New Journal of Physics* **24**, 113046.

The author of this dissertation served as the first and also corresponding author for papers I., III. and V., and prepared the following contribution statements:

Paper I. The author wrote the bulk of the manuscript text, carried out the simulations included (with the exception of the 3D simulations in section 3.1, carried out by the author's supervisor), analyzed the results and served the role of the corresponding author.

Paper III. The author wrote the bulk of the manuscript text, carried out the simulations included, analyzed the results and served the role of the corresponding author.

Paper V. The author wrote the bulk of the manuscript text, carried out the PIC simulations included (hydrodynamic simulations were performed by other coauthors), analyzed the results and served the role of the corresponding author.

The first authors of the papers II. and IV. agree with the following contribution statements.

Paper II. The author of this dissertation collaborated with his supervisor on each aspect of the manuscript preparation, wrote parts of the manuscript text, carried out the simulations in sections 2 and 3, and the 2D counterparts of the 3D simulations in section 5 and analyzed the corresponding results. The author also helped with the preparation of the revised version of the manuscript (including response to referees) and with the final corrections of the paper.

Jan Pšikal

Paper IV. The author of this dissertation collaborated with his colleagues on the preparation of the manuscript, checked the theoretical model and carried out the 3D simulation and analyzed the intensity increase. The author also helped with the revised version of the manuscript (including response to referees) and with the final corrections of the paper.

Martin Jirka